Thèse de Doctorat

Thèse présentée à l'Université de Mons
pour l'obtention du grade de

Docteur en Sciences de l'Ingénieur et Technologie

par

Tommaso Carlesi

Development of an advanced experimental technique for the measurement of the turbulent heat flux in liquid metals

Membres du Jury

Président:	Prof. Marc Wuilpart, Université de Mons, (BE)
Membres extérieurs:	Prof. Martin Rohde, Technische Universiteit Delft (NL)
	Prof. Thomas Wetzel, Karlsruher Institut für Technologie (DE)
Membres intérieurs:	Prof. Christophe Caucheteur, Université de Mons, (BE), secretary
	Prof. Ward DE PAEPE, Université de Mons, (BE)
	Dr. Julio Pacio, Belgian Nuclear Research Center SCK CEN, (BE)
	Philippe Planquart, Von Karman Institute for Fluid Dynamics, (BE)
	Katrien van Tichelen, Belgian Nuclear Research Center SCK CEN, (BE)
	Prof. Delphine Laboureur, Von Karman Institute for Fluid Dynamics, (BE), co-supervisor
	Prof. Patrice Mégret, Université de Mons, (BE), supervisor

February, 2025

Thèse préparée dans le Service d'Electromagnétisme et de Télécommunications

"Felix, qui potuit rerum cognoscere causas"

Virgil

Abstract

One of the main challenges today is meeting the global energy demand while pursuing the carbon neutrality goals set by the Paris Agreement (COP21) and confirmed by the more recent COP28. Several successful energy scenarios by the International Energy Agency (IEA) depend on expanding the role of nuclear energy in electricity generation, which inherently increases nuclear waste production. A promising approach to address this challenge is nuclear waste transmutation, achievable through advanced fourth-generation reactors. A leading project in this field is MYRRHA (Multi-purpose hYbrid Research Reactor for High-tech Applications), a pool-type, fast-spectrum research reactor being developed at the Belgian nuclear research center, SCK CEN. MYRRHA employs lead-bismuth eutectic (LBE) as its primary coolant, which contributes to both its safety and operational efficiency.

Currently, the thermohydraulic behavior and modeling of liquid metals like LBE remain uncertain, especially in low-velocity regimes such as mixed and natural convection, which correspond to the accident conditions of the reactor. Addressing this issue requires accurately estimating the turbulent heat flux, which represents the heat transfer due to turbulence characterized by fast fluctuations of temperature and velocity in the fluid. While numerical simulations provide reliable estimates for fluids like water or air, validation data for low-Prandtl-number fluids, such as liquid metals, remain scarce. Consequently, new experiments are essential to establish a reference database for model validation. This PhD project thus aims to develop an advanced experimental technique capable of simultaneously measuring velocity and temperature fluctuations, i.e., the turbulent heat flux, in liquid metals.

Ultrasound Doppler Velocimetry (UDV) and Hot Film Anemometry (HFA) were selected for velocity measurements, while sheathed type K thermocouples (TC) and fiber Bragg gratings (FBGs) were used for temperature measurements. After initial calibration and characterization tests in liquid metals, these measurement techniques were applied in a differentially heated cavity used as a natural convection setup. The experimental results generally reached a good agreement with RANS and DNS simulations in terms of average fields for both fluids used, water and Galinstan. Nevertheless, velocity fluctuation measurements in Galinstan presented significant challenges, yielding results that reflect such uncertainties and limited the feasibility of directly quantifying turbulent heat flux values. Despite this, the experimental and numerical findings in this study provide valuable insights into the characteristic trends of liquid metal flows under natural convection conditions.

Acknowledgements

At the end of this journey, it feels inevitable to thank all the people who contributed to the success of this work.

First of all to all my supervisors, for their close guidance and their valuable counsel. To Prof. Delphine Laboureur, who followed me the closest and with whom I shared a full experience made of experiments, meals, and trips. To Prof. Patrice Mégret, for his continuous interest in a project far from his original background. To Philippe Planquart, for always finding the time to give me his recommendations. To Dr. Julio Pacio and Katrien Van Tichelen who always gave me their advice, perspective, and precious suggestions to help me stay on track. You each taught me lessons that I will carry with me for the rest of my life.

To all the jury members who helped shape and refine this manuscript. To all the people in the teams I collaborated with, impossible to mention one by one but that contributed to make this journey so rich and fullfilling. To all the technical staff of the Von Karman Institute, the University of Mons, and the SCK CEN, because sometimes demonstrations and practice are worth more than one thousand words.

To all the colleagues from VKI, UMONS and SCK that became friends with time, in particular Giuseppe, Gonçalo, Luca and Pietro, for the trips, the coffee breaks, the beers and the evenings we shared in every situation of our life. This journey would not have been half as fun and enriching without you. A special thanks goes to Maria, who kept me warm in her car during the daily commute to VKI, who shared with me the full French course experience and who even found the time to give me her technical advice whenever it was needed.

To my parents and all my friends at home, because it is only with solid roots that a tree can grow high. To Seiko, who contributed to the success of this PhD much more than she believes and who continues to improve the man that I am day after day.

Thank you.

Tommaso Carlesi
February 5, 2025

Contents

List of Figures **xi**

List of Tables **xvii**

Nomenclature **xix**

1 Introduction **1**
1.1 Context . . . 1
1.2 Turbulence in liquid metals . . . 4
1.3 Objectives . . . 8
1.4 Scope of the work . . . 8
1.5 Thesis structure . . . 9

2 Selection process of the measurement techniques **13**
2.1 Requirements of the sensor . . . 13
2.2 State-of-the-art overview on measurement techniques for liquid metal flows . . . 17
2.2.1 Temperature measurement techniques . . . 17
2.2.2 Velocity measurement techniques . . . 21
2.3 Choice of measurement techniques . . . 25
2.3.1 Thermocouple (TC) . . . 28
2.3.2 Fiber Bragg Gratings (FBG) . . . 29
2.3.3 Ultrasound Doppler Velocimetry (UDV) . . . 30
2.3.4 Hot Film Anemometry (HFA) . . . 31
2.4 Turbulent heat flux measurements . . . 33
2.4.1 Synchronization . . . 35
2.4.2 Positioning . . . 38
2.5 Conclusions . . . 39

3 Experimental setup and procedures **43**
3.1 Setup design . . . 44
3.1.1 Access for instrumentation . . . 47
3.2 Filling procedure and leaks . . . 50
3.3 Galinstan . . . 52

3.3.1 Galinstan compatibility . . . 52
3.3.2 Galinstan oxidation . . . 54
3.4 Boundary conditions . . . 56
3.5 Conclusions . . . 58

4 Numerical setup and results **61**
4.1 Governing equations . . . 62
4.2 Numerical domain . . . 63
4.3 Direct Numerical Simulations (DNS) . . . 64
4.4 Reynolds Averaged Navier-Stokes simulations (RANS) . . . 68
4.5 Results and discussion . . . 72
4.6 Conclusions . . . 79

5 Thermocouple and Fiber Bragg Gratings **81**
5.1 Working principle . . . 81
5.1.1 Thermocouple . . . 81
5.1.2 FBG . . . 84
5.2 Calibration . . . 86
5.2.1 Static calibration . . . 86
5.2.2 Dynamic calibration . . . 91
5.3 Effects of liquid metals on the FBG . . . 98
5.4 Conclusions . . . 103

6 Ultrasound Doppler Velocimetry **107**
6.1 Working Principle . . . 107
6.2 Water loop setup . . . 113
6.3 Seeding . . . 114
6.4 Uncertainty calculation . . . 118
6.5 Results and discussion . . . 122
6.5.1 Water loop . . . 122
6.5.2 Parametric study . . . 125
6.5.3 Preliminary results in the cavity . . . 128
6.6 Conclusions . . . 131

7 Hot wire - hot film anemometry **133**
7.1 Working principle . . . 133
7.1.1 Measurements in conductive fluids . . . 137
7.2 Calibration . . . 138
7.2.1 Static calibration . . . 138
7.2.2 Dynamic calibration . . . 140
7.3 Calibration setups . . . 141
7.3.1 Water loop setup . . . 142
7.3.2 Oil bath setup . . . 143
7.4 Results in the water loop . . . 145
7.4.1 Calibration . . . 145
7.4.2 Velocity measurements . . . 147

7.5 Results in the oil bath . . . 149
7.5.1 Acquisition procedure . . . 149
7.5.2 Processing methodologies . . . 152
7.5.3 Calibration results . . . 156
7.6 Effect of the hot film on the surroundings . . . 159
7.7 Spatial resolution . . . 163
7.8 Conclusions . . . 164

8 Results in the differentially heated cavity 165
8.1 Introductory remarks . . . 165
8.2 Water . . . 166
8.2.1 Average temperature . . . 167
8.2.2 Average velocity . . . 171
8.2.3 Fluctuations . . . 174
8.3 Galinstan . . . 176
8.3.1 Average temperature . . . 176
8.3.2 Average velocity . . . 178
8.3.3 Fluctuations of temperature . . . 180
8.3.4 Fluctuations of velocity . . . 184
8.3.5 Turbulent heat flux calculation . . . 186
8.4 Conclusions . . . 187

9 Conclusions 189
9.1 Objectives: achievements and contributions . . . 189
9.1.1 Measurement techniques . . . 189
9.1.2 Experimental setup . . . 191
9.1.3 Numerical simulations . . . 192
9.1.4 Experiments in liquid metals . . . 192
9.1.5 Primary objectives of the work . . . 193
9.2 Recommendations for future works . . . 194
9.2.1 Measurement techniques . . . 194
9.2.2 Experimental setup . . . 195
9.2.3 Numerical simulations . . . 197
9.2.4 Experiments in liquid metals . . . 197
9.3 LBE adaptation . . . 198

A Specifics on the Hot Film 201
A.1 Coating solutions for the hot film . . . 201
A.2 Settings . . . 203
A.3 Hot film in the tank setup . . . 205

B Experimental tests 209
B.1 Infrared camera analysis of the copper plates . . . 209
B.2 Leak tests in the cavity . . . 211

C Physical properties of materials **213**
C.1 Water 213
C.2 Galinstan (GaInSn) 214
C.3 Lead-Bismuth Eutectic (LBE) 214
C.4 Copper Cu-ETP 215
C.5 Stainless steel 316L 215

D Theory of 1st order systems **217**

E Differentially heated cavity **221**
E.1 Temperature measurements in water at different positions 221
E.2 Impact of the losses on the RANS simulations 222
E.3 UDV velocity hot profile in water 223

F Scientific outputs **225**
F.1 Journal Papers 225
F.2 Conferences, workshops and symposia 225

References **227**

List of Figures

1.1 Representative comparison of the viscous (δ_v) and thermal (δ_t) boundary layers with varying Prandtl numbers. U_0 and T_0 are respectively the free stream velocity and temperature and $T_w > T_0$ is the temperature of the wall. 6
1.2 Structure of this thesis 11

2.1 Summary of liquid metal flow characteristics relevant to the EPICURUS requirements 14
2.2 Overview of the selected techniques. Clockwise from the top left: Ultrasound Doppler Velocimetry (UDV), Hot Film (HF), Thermocouple (TC), and Fiber Bragg Grating (FBG). 26
2.3 Sensor and acquisition system chosen for the temperature measurements (TC). 28
2.4 Sensor and acquisition system chosen for the temperature measurements (FBG). 29
2.5 Sensor and acquisition system chosen for the velocity measurements (UDV). 30
2.6 Sensor and acquisition system chosen for the velocity measurements (HF). 31
2.7 Dimensions of the hot film used for this study 32
2.8 Scheme of the synchronization of the sensors 36
2.9 Positioning of the temperature sensors during the measurements with a schematic showing the key dimensions. 39
2.10 Sensor positioning of the hot film, TC and FBG on the same support. The key dimensions and distances are highlighted in the schematic. . . 40

3.1 Differentially heated cavity 44
3.2 Natual convection setup and components 46
3.3 Water cooling circuit for the cold side Peltier element 48
3.4 Access points of the instrumentation 49
3.5 Section of the cavity with the sensors 50
3.6 Cavity with GaInSn oxydes, before and after cleaning 55
3.7 Time evolution of the experimental temperature boundary conditions 57

3.8 Time evolution of the temperature of the water inside the cavity during the heat losses tests 58

4.1 Schematic of the numerical domain 64
4.2 Computational grid used for the fluid domain in the DNS simulations 66
4.3 Results of the grid independence study and the statistical convergence analysis 71
4.4 Mesh used in the conjugate heat transfer RANS simulations 72
4.5 Turbulent heat flux field calculated by non CHT, adiabatic walls DNS simulations in GaInSn. Section in one of the measurement xy planes $z = 12\,\mathrm{mm}$. 73
4.6 Comparison between non-dimensionalized values of velocity magnitude average fields in water and GaInSn 73
4.7 Comparison of the temperature and velocity magnitude fields over 3 planes at constant x and y 74
4.8 Comparison between RANS and DNS fields of the average temperature in GaInSn 75
4.9 Comparison between RANS and DNS averaged fields of the vertical velocity component U_y in GaInSn 76
4.10 Comparison between RANS and DNS fields of the turbulent kinetic energy (TKE) in GaInSn 77
4.11 Fields of the rms values for vertical component of the velocity and temperature calculated by CHT, adiabatic walls DNS simulations in GaInSn 78
4.12 Turbulent heat flux field calculated by CHT, adiabatic walls DNS simulations in GaInSn 78

5.1 Different thermocouple junction designs: a) exposed junction; b) grounded junction; c) sheathed junction 83
5.2 Schematic of the Bragg Gratings principle 84
5.3 Experimental setup of the comparative static calibration for temperature sensors 87
5.4 Static calibration curves of the temperature sensors 89
5.5 Difference between the sensors reading and the RTD reading plotted as a function of temperature to highlight possible second order effects 90
5.6 Schematic of the dynamic calibration setup for temperature sensors using the plunging method 94
5.7 Response time τ of the investigated temperature sensors in dependence of the immersion velocity u_{im} for the plunging process in different fluids 96
5.8 Response time of the investigated sensors in dependence of the immersion velocity u_{im} for the plunging process in molten salt, GaInSn, glycerin, paraffin oil and water at 45 °C and HITEC at 180 °C. 97
5.9 Comparison of the FBG spectra in molten salt and water 99

5.10 Time evolution of the signals of FBG and TC recorded at y=35 mm and y=40 mm of Position 1 in Figure 3.4. The cavity was filled with GaInSn. Despite the difference in the absolute value of the signals, the fluctuations around the mean are in very good agreement. 100
5.11 Effects of the liquid metal GaInSn on the FBG full spectrum 101
5.12 Effects of the liquid metal GaInSn on the FBG spectra 102

6.1 Schematic of the UDV velocity measurement in a pipe. 108
6.2 Comparison of the US cone shape for two different sensors 112
6.3 Schematic of the closed water loop, with pictures of each component included. 113
6.4 Ratio of velocity fluctuation amplitudes as a function of the Stokes number in water 116
6.5 Fully developed turbulent profiles of average velocity and turbulence intensity in a water pipe. Comparison between UDV, PIV, DNS and theoretical estimations. 123
6.6 Laminar profiles of average velocity in a water pipe 124
6.7 Cavity configurations adopted for UDV characterization 128
6.8 Echo modules of the UDV 10 MHz shown for different configurations . 130
6.9 Velocity profiles along position 1 in the cavity for the 10 MHz UDV sensor in four different configurations 130

7.1 Measurement chain of the Hot Wire - Hot Film Anemometry when used in Constant Temperature Anemometry mode. 134
7.2 Typical dynamic response of a hot film probe subjected to a square wave test 141
7.3 Configuration of the hot film and UDV in the closed water loop setup 142
7.4 Schematic and picture of the oil bath calibration setup 144
7.5 Velocity-voltage calibration of the hot film probe using the UDV as a reference sensor for velocity estimation 146
7.6 Measured dynamic response of the hot film 147
7.7 Comparison between the velocity profiles measured by the UDV and the fiber-film probe 148
7.8 Comparison between the conditions of the fiber-film probe before and after its usage in the closed water loop. Such condition is believed to be also a factor affecting the final measurement 149
7.9 Original raw voltage signal acquired by the hot film and zoomed view with the probe motion. 151
7.10 Nu-Re calibration methodology 153
7.11 Graphical summary of the Hollasch method 155
7.12 Velocity-temperature calibration results in water and GaInSn 156
7.13 Application of the Hollasch method to the dataset for water and GaInSn 158
7.14 Hot film voltage vs Temperature at velocity $U = 0$ 159
7.15 Voltage vs Temperature at different velocities. A second order fit was found to be the best and adopted for the relationship 159
7.16 Effect of the hot film probe on the temperature measurements 160

7.17 Effect of the distance between the hot film and the thermocouple . . . 161
7.18 Effect of the hot film probe on the reading of the thermocouple 162

8.1 Average temperature profiles in water along the y direction parallel to the hot wall (position 1) and to the cold wall (position 3). Comparison between TC, FBG and RANS 167
8.2 Average temperature profiles in water along the y direction parallel to the hot wall (position 1) and to the cold wall (position 3). Comparison between TC, FBG, HF and RANS 168
8.3 Average temperature profiles in water along the y direction parallel to the hot wall (position 1) and to the cold wall (position 3). Comparison between TC, FBG, HF and RANS simulations performed with different entity of the losses from the passive walls. 169
8.4 Average temperature profiles in water along the y direction parallel to the hot wall (position 1) and to the cold wall (position 3). Comparison between TC, FBG, HF and RANS. 170
8.5 Average velocity profile U_y along the y direction parallel to the cold wall (position 3). Comparison between UDV and RANS. 172
8.6 Average velocity field of RANS 3 of Table 8.2. The UDV ultrasound (US) cone for the 10 MHz sensor is represented close to the cold wall . 173
8.7 Average velocity profile U_y along the y direction parallel to the cold wall (position 3). Comparison between UDV and RANS 173
8.8 Energy spectrum of the temperature signal of the TC, FBG and HF at $y = 35$ mm along the cold profile (position 3). 174
8.9 Energy spectrum of the temperature signal in GaInSn along the y direction parallel to the hot wall (position 1) and to the cold wall (position 3). Comparison between FBG profiles. 175
8.10 Average temperature profiles in GaInSn along the y direction parallel to the hot wall (position 1) and to the cold wall (position 3). Comparison between TC, HF, RANS and DNS. 177
8.11 Average temperature profiles in GaInSn along the y direction parallel to the hot wall (position 1) and to the cold wall (position 3). Comparison between TC, HF, RANS and DNS 177
8.12 Average U_y velocity field of DNS 2 of Table 4.1. The UDV ultrasound (US) cones for the 10 MHz and the 8 MHz sensors are represented respectively close to the hot and cold wall 179
8.13 Average velocity profile U_y along the y direction parallel to the hot wall (position 1) cold wall (position 3). Comparison between UDV, RANS and DNS 179
8.14 Root mean square (rms) temperature profiles in GaInSn along the y direction parallel to the hot wall (position 1) and to the cold wall (position 3). Comparison between TC, FBG, HF and DNS. 180

8.15 Non-dimensionalized root mean square (rms) temperature profiles in GaInSn along the y direction parallel to the hot wall (position 1) and to the cold wall (position 3). Comparison between TC, FBG, HF and DNS. 181
8.16 Energy spectrum of the temperature signal of the TC, FBG, HF and DNS at $y = 10\,\mathrm{mm}$ along the hot profile (position 1) 182
8.17 Energy spectrum of the temperature signal of the HF and DNS in GaInSn at different heights along the hot profile (position 1) and the cold profile (position 3). 183
8.18 Root mean square (rms) values of the velocity fluctuations $u'_{\mathrm{y,rms}}$ in GaInSn along the y direction parallel to the hot wall (position 1) and to the cold wall (position 3). Comparison between UDV, DNS and RANS. 184
8.19 Energy spectrum of the velocity fluctuations signal in GaInSn along the y direction parallel to the hot wall (position 1) and to the cold wall (position 3). Comparison between UDV and DNS profiles. 186
8.20 Turbulent heat flux (THF) profiles in GaInSn along the y direction parallel to the hot wall (position 1) and to the cold wall (position 3). Comparison between available experimental data and DNS. 187

A.1 Settings used in the StreamwarePro 204
A.2 Tank setup used for the hot film calibration 205
A.3 Evolution in time of the voltage acquisition in the tank. 206

B.1 Setup used for the infrared camera tests 209
B.2 Infrared camera images for two different average temperatures of the plates 210
B.3 Evolution of pressure inside the cavity over time 211

D.1 Typical responses of a first order system to a step input 218

E.1 Average temperature profiles in water along the y direction parallel to the hot wall (position 1-2) and to the cold wall (position 3-4) 221
E.2 Average velocity U_y RANS profiles in water along the y direction parallel to the hot wall (position 1) and to the cold wall (position 3) . . . 222
E.3 Average velocity U_y RANS profiles in GaInSn along the y direction parallel to the hot wall (position 1) and to the cold wall (position 3) . 222
E.4 Average velocity profile U_y along the y direction parallel to the hot wall (position 1). Comparison between UDV and RANS. 223

List of Tables

2.1 Characteristics of fluctuations in GaInSn 15
2.2 Turbulence characteristics in GaInSn as predicted by theoretical calculations 17
2.3 Overview of velocity and temperature measurement techniques for liquid metals. The table presents the best reported volumetric (Δx) and linear (Δl) spatial resolutions, temporal resolution (Δt), measurement range, and suitability for turbulent heat flux measurements. 18
2.4 Main characteristics of the UDV sensors used for this work 30
2.5 Main characteristics of the Hot Film sensor used for this work 33
2.6 Summary of the literature review for the turbulent heat flux measurements 34
2.7 Delay and associated error on the THF value. 37
2.8 Delay and jitter values for different sources. 37
2.9 Turbulent structures characteristics 40
2.10 Summary of the sensors and acquisition systems chosen with their spatial (Δx) and temporal (Δt) resolution 41

3.1 Characteristics of the setup for the two different fluids used 47
3.2 Main thermophysical properties of Galinstan at 50 °C 52

4.1 Summary of the numerical simulations available for comparison with the experimental work. 67
4.2 Characteristics of the four meshes analyzed during the grid independence study 70
4.3 Characteristics of the RANS simulation used for the grid independence study. 70

5.1 Components used in the static calibration of TC and FBG 87
5.2 Static calibration results of the temperature sensors averaged over 60 samples, including their standard deviation and compared with the measured reference temperature 89
5.3 Intercept and slope of the linear regression of each sensor 89
5.4 RMSE values and corresponding uncertainty $u_{T_{fit}}$ of each sensor . . . 90
5.5 Total uncertainty of the two sensors 91

5.6 Thermal conductivity k, density ρ, specific heat capacity c_p, dynamic viscosity η, and Prandtl number Pr of all calibration fluids used . . . 95
5.7 Response time of the thermocouple for different exposed lengths when plunged in water with an immersion velocity of 150 mm/s. 98
5.8 Shift of the peak wavelength in respect of the value given by the Sense2020 software 102
5.9 Spatial and temporal resolution of temperature sensors for water and GaInSn 104

6.1 Comparison of the different particles analyzed for water and GaInSn for a US emitting frequency of 10 MHz 117
6.2 Summary of particles used in different setups 119
6.3 Relative uncertainties of measured quantities and their impact on the total uncertainty of the velocity 121
6.4 Summary of the optimal values of the analyzed UDV parameters for each setup 127
6.5 Tests performed to assess the effects of obstacles on the UDV velocity measurements 129
6.6 Summary of spatial and temporal resolutions obtained with the 10 MHz UDV 131

7.1 Hot film velocity limitations in water and GaInSn 139
7.2 Summary of spatial resolution and sampling frequency achieved with the Hot Film probe across various experimental setups. 164

8.1 Temperatures and non-dimensional parameters tested in this work for the different working fluids 166
8.2 Characteristics of the RANS simulations used for the comparison with the experimental study in water. 167

A.1 Characteristics of Coated Wires 202

C.1 Thermophysical properties of water 213
C.2 Thermophysical properties of GaInSn 214
C.3 Thermophysical properties of LBE 214
C.4 Thermophysical properties of Copper Cu−ETP 215
C.5 Thermophysical properties of Stainless steel 316L 215

Nomenclature

Abbreviations and acronyms

ABS	Acronitrile Butadiene Styrene
BC	Boundary Conditions
BFS	Backward Facing Step
BL	Boundary Layer
CAD	Computer-aided design
CCA	Constant Current Anemometry
CHT	Conjugate Heat Transfer
CIFT	Contactless Inductive Flow Tomography
CJC	Cold Junction Compensation
COP21	21st Conference of the Parties (Paris Agreement)
CTA	Constant Temperature Anemometry
CW	Cold Wire
DAQ	Data Acquisition
DHC	Differentially Heated Cavity
DNS	Direct Numerical Simulations
EMF	Electro-Motive Force
EP	Emissions per profile
FBG	Fiber Bragg Grating
FP	Flat Plate
GaInSn	Galinstan - Gallium-Indium-Tin

HCC	Heated Cavity Channel
HFA	Hot Film Anemometry
HWA	Hot wire Anemometry
HZDR	Helmholtz-Zentrum Dresden-Rossendorf
IEA	International Energy Agency
LBE	Lead Bismuth Eutectic
LCSR	Loop Current Step Response
LDV	Laser Doppler Velocimetry
LFV	Lorentz Force Velocimetry
LM	Liquid Metal
LMPLM	Low Melting Point Liquid Metal
MID	Magnetic-Inductive Flow meter
MYRRHA	Multi-purpose hYbrid Research Reactor for High-tech Applications
NBR	Nitrile Butadiene Rubber
NEA	Nuclear Energy Agency
NI	National Instrument
OECD	Organisation for Economic Co-operation and Development
OHR	Overheat ratio
OTDR	Optical Time Domain Reflectometry
PIV	Particle Image Velocimetry
PMP	Permanent Magnet Probe
PRF	Pulse Repetition Frequency
PTFE	Polytetrafluoroethylene
PVC	Polyvinyl Chloride
RANS	Reynolds Averaged Navier Stokes (equations)
RB	Rayleigh-Bénard
RS	Rotating Shaft
RTD	Resistance Temperature Detector

SCK CEN	Belgian Nuclear Research Center
SI	International System of Units
SST	Shear Stress Transport
TC	Thermocouple
TECF	Transient Eddy Current Flowmeter
THF	Turbulent Heat Flux
THFS	Turbulent Heat Flux Sensor
TI	Turbulence Intensity
TKE	Turbulent Kinetic Energy
TMF	Turbulent Momentum Flux
UDOP	UDV software
UDV	Ultrasound Doppler Velocimetry
URANS	Unsteady Reynolds Averaged Navier Stokes (equations)
US	Ultrasound
VC	Vertical Convection
VKI	Von Karman Institute
WT	Wind Tunnel

Greek letters

α	Thermal diffusivity	$[m^2/s]$
α_w	Temperature coefficient of resistance of the wire	$[1/°C]$
β	Thermal expansion coefficient	$[1/°C]$
ΔT	Temperature difference	$[°C]$
Δt	Temporal resolution	$[s]$
Δx	Volumetric spatial resolution	$[m^3]$
Δ	Difference, variation	[–]
δ	Phase shift	[–]
ϵ	Turbulent dissipation rate	$[m^2/s^3]$
ϵ_s	Strain	[–]

χ	Divergence angle of the UDV cone	[°]
ϕ	Generic quantity	[–]
η	Kolmogorov scale of turbulence	[m]
γ	Surface tension	[J/m^2]
Λ	Grating period of the Bragg mirror	[m]
λ_B	Bragg wavelength	[m]
λ_e	Emitting wavelength of the ultrasound	[m]
λ_T	Taylor scale of turbulence	[m]
μ	Dynamic viscosity	[kg/(m s)]
ν	Kinematic viscosity	[m^2/s]
ν_P	Poisson ratio	[–]
Ω	Leak rate	[bar L/s]
ω	Specific rate of dissipation	[1/s]
θ	Inclination angle of the UDV sensor	[°]
ρ	Density	[kg/m^3]
σ	Standard deviation	[–]
σ_A	Seebeck coefficient of the metal A	[V/°C]
$\boldsymbol{\tau}$	Viscous stress tensor	[kg/(m s^2)]
τ	Characteristic time	[s]
τ_v	Viscous time lag	[s]
Ψ	Non-dimensional ratio	[–]

Mathematical operators

$\cdot$	Dot product
∇	Nabla operator (vector differential operator)
$\otimes$	Outer product (tensor product)
∂	Partial derivative operator
$\|\|$	Absolute value
$\mathbf{I}$	Identity Matrix

Non-dimensional numbers

Gr	Grashof number
Pe	Péclet number
Pr	Prandtl number
Ra	Rayleigh number
Re	Reynolds number
St	Stokes number

Roman letters

A	Area	[m^2]
B	Hollasch non-dimensionalized voltage	[–]
c	Sound velocity	[m/s]
c_P	Specific heat capacity	[J/(kg °C)]
D	Diameter	[m]
d_v	Axial resolution of the UDV	[m]
D_w	Diameter of the wire	[m]
$\mathbf{e_z}$	unit vector in z component	[–]
E	Voltage	[V]
e	Internal energy per unit mass	[J/kg]
f	Frequency	[Hz]
f_D	Doppler frequency	[Hz]
f_e	Ultrasound emitting frequency	[Hz]
f_l	Frequency of the integral scale of turbulence	[Hz]
f_η	Frequency of the Kolmogorov scale of turbulence	[Hz]
$f_{cut-off}$	Cut-off frequency	[Hz]
g	Gravity	[m/s^2]
h	Convective heat transfer coefficient	[$W/(m^2°C)$]
I	Current	[A]
K	Thermal activity parameter	[–]

k	Thermal conductivity	[W/(m °C)]
l	Integral length scale of turbulence	[m]
L_c	Characteristic length	[m]
L_w	Length of the wire	[m]
L_{NF}	Length of the near field	[m]
m	Mass	[kg]
n	Refractive index	[/]
N	Length of a generic vector	[–]
P	Position of the seeding particle	[m]
p	Pressure	[Pa]
p_{rgh}	$p - \rho g h$ Pressure minus the hydrostatic pressure	[Pa]
$\mathbf{q}$	Specific heat flux vector	[W/m^2]
Q	Heat flux	[W]
q_t	Turbulent specific heat flux	[W/m^2]
S	Mean strain rate tensor	[1/s]
$\mathbf{r}$	Spatial coordinate (vector)	[m]
R	Resistance	[Ω]
r	Velocity fluctuations ratio	[–]
R_ρ	Density ratio	[–]
S	Strain tensor	
s	Distance	[m]
T	Temperature	[°C]
t	Time	[s]
t_{PRF}	Inverse of the pulse repetition frequency	[s]
U_i	Fluid velocity in the i direction ($U_1 = U_x$, $U_2 = U_y$, $U_3 = U_z$)	[m/s]
$\mathbf{u}$	Fluid velocity (vector)	[m/s]
u'	Velocity fluctuations $U(t) - U_{mean}$	[m/s]
U	Velocity	[m/s]

u	Uncertainty ..... [–]
u_τ	Friction velocity ..... [m/s]
V	Volume ..... [L]
x, y, z	Spatial coordinate (Cartesian) ..... [m]
x_i	Spatial coordinate in the i direction ($x_1 = x$, $x_2 = y$, $x_3 = z$) ..... [m]
Z	Acoustic impedance ..... [kg/(m^{2}s)]

Subscripts and superscripts

$bulk$	bulk value
c	characteristic value
eff	effective value
f	fluid
hot	Refers to the higher temperature level
im	immersion
i, j	component i, j of the vector
m	melting point
mag	magnitude
max	maximum value
$mean$	mean value
n	general index
p	particle
ref	reference value
rms	root mean square
s	solid
T	Transposed
t	turbulent value
tot	total quantity
w	wire
0	value at the initial condition

$'$	Turbulent fluctuations
$+$	Refers to wall quantity
$\overline{\quad}$	mean value over time

Chapter 1

Introduction

This Chapter introduces the context in which this thesis is developed and the main objectives of the research. Following an overview explaining the background of the work in Section 1.1, Section 1.2 examines the current approaches to addressing turbulence in liquid metals, identifying the challenges that this work aims to address to further understand the mechanics of turbulence in such flows. Subsequently, the limitations of this research are outlined in Section 1.4, establishing the boundaries and specific focus areas. The main objectives of the research are then presented in Section 1.3. Finally, Section 1.5 provides an outline of the thesis structure, including a brief description of each Chapter.

1.1 Context

One of the greatest challenges currently faced is meeting the increasing global energy demand while adhering to carbon neutrality targets and the maximum 1.5 °C temperature increase limit set for 2050 [1–3]. July 2023 set a new record as the hottest month ever recorded, followed closely by August 2023 as the hottest August on record. Additionally, in 2022, global carbon dioxide (CO_2) emissions from the energy sector reached an unprecedented high of 37 billion tonnes (Gt), surpassing pre-pandemic levels by 1%. Although both CO_2 emissions and fossil fuel demand are expected to peak this decade (with fossil fuels accounting for approximately 80 % of the global energy supply), further efforts are necessary to achieve the 1.5 °C target by 2050 [2, 3].

The International Energy Agency (IEA) has identified several key measures to realize the Net Zero Emission (NZE) Scenario, including an increase in renewable capacity, accelerated electrification, reduction of methane emissions, and investment in technologies like carbon capture, hydrogen, and energy infrastructure. While renewable sources are expected to dominate, contributing over 70 % of the global energy supply in the NZE, nuclear energy is anticipated to play a significant role, increasing its share from 5 % to 12 % and doubling installed power capacity from 413 GW in 2022 to 812 GW by 2050 [2, 4].

The recent COVID-19 pandemic and invasion of Ukraine by Russia have under-

scored the value of a diverse mix of non-fossil and domestic energy sources. Consequently, several countries, such as the United Kingdom, France, China, Poland, and India, have announced energy strategies that feature pivotal roles for nuclear power, while others, including Belgium and Korea, have recently revised plans to phase out existing nuclear plants [4].

However, the anticipated increase in nuclear power installation will lead to a corresponding increase in nuclear waste production. A promising solution to this issue is transmutation, i.e. the transformation of nuclear waste, specifically minor actinides, into shorter-lived waste to facilitate disposal. This process can be achieved by Liquid Metal Fast Reactors (LMFRs) of the fourth generation, utilizing fast neutrons [5]. This technology has garnered significant attention in recent years, leading to the initiation of various international research projects, such as SESAME [6], MYRTE [7], and PATRICIA [8]. These projects focus particularly on supporting the design of MYRRHA (Multi-purpose hYbrid Research Reactor for High-tech Applications), a groundbreaking accelerator-driven pool-type fast-spectrum research reactor under development at SCK CEN, the Belgian nuclear research center [9–11]. The primary objectives of MYRRHA are as follows:

- Addressing the nuclear waste issue: MYRRHA will be the first reactor of its kind to incorporate an accelerator-driven system that enables the use of fast neutrons for transmuting minor actinides and long-lived fission products. By reducing their radiotoxicity, this technology could potentially reduce the volume of high-level radioactive waste by 99 % and the storage time required to just 300 years [10].

- Providing a proof of concept and technology platform: MYRRHA can operate in subcritical mode, avoiding a self-sustaining chain fission reaction by coupling with a high-energy proton accelerator, which produces the necessary primary neutrons in the reactor core via spallation reactions. This design ensures reactivity control during minor actinide burning and offers the additional safety feature of immediate shutdown upon stopping the accelerator. The reactor is also equipped to operate in critical mode, with residual decay heat removal achieved through natural circulation without active systems or intervention.

- Serving as an irradiation facility: MYRRHA will support fusion material testing with its fast neutron environment, providing irradiation conditions similar to those of a fusion reactor. Additionally, the reactor will facilitate the production of novel therapeutic radioisotopes for targeted cancer treatment and advance research in nuclear physics, atomic physics, fundamental interactions, and solid-state physics [9–11].

Among its distinguishing characteristics, MYRRHA employs lead-bismuth eutectic (LBE) as the primary coolant. The choice of LBE was motivated by several factors:

- Its low melting temperature (125±1°C [12] at normal atmospheric pressure) enables a reduced core inlet temperature (around 270 °C), decreasing corrosion

risk and allowing for an increased core temperature difference. Furthermore, its high boiling temperature (1654±16°C [12]) permits operation of the primary circuit at atmospheric pressure, enhancing safety and improving plant thermal efficiency.

- LBE exhibits favorable heat transfer properties, with a specific heat capacity of $\approx 146.5\,\mathrm{J/(kgK)}$ and a density of $\approx 10\,500\,\mathrm{kg/(m^3)}$ measured at the working temperature of the reactor (see Appendix C. This combination results in a thermal capacity comparable to other typical nuclear reactor coolants, such as water or molten salts. However, LBE also has a high thermal conductivity, ranging from $10\,\mathrm{W/(mK)}$ to $15\,\mathrm{W/(mK)}$ as a function of temperature. This value is approximately one order of magnitude higher than that of water or molten salts. These favorable properties enable efficient heat removal from the core and contribute significantly to enhancing the passive safety of the reactor, even under accident conditions.
- When protons collide with the LBE target, a high yield of neutrons is produced via spallation [9–11] thanks to its high atomic number, supporting the chain reaction in the subcritical core.
- LBE has a low neutron absorption cross-section, rendering it virtually transparent to neutrons. This is a significant advantage in fast reactors where neutrons are kept at high energies rather than slowed down (thermalized), as high-energy neutrons are essential for sustaining fast fission reactions. This property is related to the high atomic number of LBE.
- The chemical stability of LBE precludes hazardous reactions upon contact with water or air, a significant advantage over other coolants such as liquid sodium. This enhances the safety of the coupling between the primary (LBE) and secondary (water) cooling circuits. However, a physical interaction between LBE at lower pressure and water at higher pressure can induce sudden boiling of the water, potentially leading to violent reactions. These potential interactions must be carefully assessed during the reactor design phase.
- Radiation shielding: LBE effectively attenuates γ radiation, contributing to the intrinsic safety of the reactor.

However, LBE also presents challenges, such as causing erosion or corrosion to structural materials in contact with it [10] and posing uncertainties regarding the behavior of mechanical components submerged in it, such as bearings, gears, and electrical cables [13]. In fact, the primary challenges in the development of MYRRHA are particularly associated with using liquid lead-bismuth eutectic as reactor coolant [10]. Several aspects of LBE use must therefore be addressed:

- Chemistry and conditioning
- Corrosion of materials
- Testing of components in LBE

- Development of instrumentation compatible with LBE

- Thermal hydraulics

This PhD research is primarily focused on the last two points, aiming to develop instrumentation capable of addressing thermohydraulic aspects of liquid metals. For the design and safety evaluation of MYRRHA, it is essential to predict the temperature of the primary coolant and reactor core components during normal operation (forced convection) as well as under accident scenarios (mixed and/or natural convection). Ensuring the removal of decay heat solely by natural circulation, without relying on external auxiliary systems, is crucial for reactor safety under accidental conditions [10]. Consequently, this PhD research is focused on studying natural convection regimes, particularly related to reactor accident scenarios.

1.2 Turbulence in liquid metals

Turbulence remains one of the *most important unsolved problems of classical physics* [14], and it is be expected that addressing this phenomenon in liquid metals introduces further complexities. Currently, experiments and Direct Numerical Simulations (DNS) serve as methodologies for obtaining reference data, as they do not require modeling assumptions.

In contrast, Reynolds-Averaged Navier-Stokes (RANS) simulations approach the turbulence problem expressing local quantities as a combination of a mean value $\overline{\phi}$ and the fluctuations around the mean $\phi^{'}$ as shown in Equation (1.1) for the generic quantity ϕ.

$$\phi = \overline{\phi} + \phi^{'} \tag{1.1}$$

The advantage is that is not necessary to model the fluctuations $\phi^{'}$ in detail, but it is important to consider their influence on the mean values $\overline{\phi}$. Applying this approach to both the local velocity ($\phi = U$) and temperature ($\phi = T$), the RANS momentum and energy balance equations are given by Equations (1.2) and (1.3), where ρ, μ, c_p, and k represent the primary thermophysical properties of the fluid: density, dynamic viscosity, heat capacity, and thermal conductivity, respectively. Additionally, U_i denotes the i-component of velocity and u_i' its fluctuations, T the temperature, and p the pressure.

$$\rho\left(\underbrace{\frac{\partial\bar{U}_i}{\partial t}}_{\substack{\text{time}\\\text{variation}}}+\underbrace{\bar{U}_j\frac{\partial\bar{U}_i}{\partial x_j}}_{\substack{\text{advection}\\\text{term}}}\right)=\underbrace{\rho\bar{f}_i}_{\substack{\text{volume}\\\text{force}}}+\frac{\partial}{\partial x_j}\left(\underbrace{\mu\frac{\partial\bar{U}_i}{\partial x_j}}_{\substack{\text{diffusion}\\\text{term}}}\underbrace{-\rho\overline{u_i^{'}u_j^{'}}}_{\textbf{TMF}}\right)-\underbrace{\frac{\partial\bar{p}}{\partial x_i}}_{\text{pressure}} \tag{1.2}$$

$$\rho c_P\left(\underbrace{\frac{\partial\bar{T}}{\partial t}}_{\substack{\text{time}\\\text{variation}}}+\underbrace{\bar{U}_j\frac{\partial\bar{T}}{\partial x_j}}_{\substack{\text{advection}\\\text{term}}}\right)=\underbrace{E}_{\substack{\text{energy}\\\text{source}}}+\frac{\partial}{\partial x_j}\left(\underbrace{k\frac{\partial\bar{T}}{\partial x_j}}_{\substack{\text{conduction}\\\text{term}}}\underbrace{-\rho c_P\overline{u_j^{'}T^{'}}}_{\textbf{THF}}\right) \tag{1.3}$$

The full derivation of the equations is explained in detail in all fluid mechanic textbooks, see e.g. [15], and more details are also reported in this thesis in Chapter 4. Several terms are identified on the left- and right-hand sides of Equations (1.2) and (1.3). In the momentum equation (Equation (1.2)), a term known as the Turbulent Momentum Flux (TMF) or Reynolds Stress Tensor (RST) is introduced, arising from the product of velocity fluctuations as a result of the averaging process. Similarly, the Turbulent Heat Flux (THF) in Equation (1.3) is associated with the fluctuations $\mathbf{u}^{'}$ and $T^{'}$. The THF represents a convective heat transfer mechanism linked to rapid turbulent fluctuations in the local fluid velocity and temperature. For clarity, the formulation of these terms is presented again in Equations (1.4) and (1.5).

$$TMF=\rho\overline{u_i^{'}u_j^{'}} \tag{1.4}$$

$$THF=\rho c_P\overline{u_i^{'}T^{'}} \tag{1.5}$$

Note that the Turbulent Momentum Flux (TMF, or Reynolds Stress Tensor) and Turbulent Heat Flux (THF) are both vector quantities arising from the product of velocity and temperature fluctuations. Over recent decades, various closure laws have been developed and validated for modeling the TMF [16]. The most common approach assumes a linear relationship between this term and the mean rate of strain tensor, S_{ij}, which represents the rate of deformation of fluid elements due to velocity gradients [15]. Consequently, the constitutive relation involving the turbulent (or eddy) viscosity, ν_t, as expressed by Equation (1.6), is introduced.

$$\overline{u_i^{'}u_j^{'}}\propto\nu_t S_{ij} \tag{1.6}$$

This quantity, in turn, is evaluated as a function of other turbulent parameters, such as the turbulent kinetic energy, k, and its dissipation rate, ϵ (or its specific equivalent, ω), which are computed in RANS simulations. Conventionally, a similar approach is adopted for the closure of the THF term. However, relatively limited progress has been made in developing these closures, especially for flows with non-unity Prandtl numbers [16]. In its most common formulation, the THF is expressed as a function of the turbulent thermal diffusivity, α_t, according to Section 1.2

$$\overline{u_i' T'} \propto \alpha_t \frac{\partial \overline{T}}{\partial x_i}$$

To retrieve the value of α_t, the Reynolds analogy is typically applied, assuming similarity in the turbulent transport characteristics of momentum and heat. The relationship between the molecular momentum diffusivity ν (kinematic viscosity) and the thermal diffusivity α is generally expressed by the (molecular) Prandtl number, commonly defined as in Equation (1.7)

$$Pr = \frac{\nu}{\alpha} \tag{1.7}$$

It is therefore possible to apply the same definition at a turbulent level, therefore defining the turbulent Prandtl number Pr_t as in Equation (1.8) relating the turbulent viscosity ν_t and the turbulent thermal diffusivity α_t.

$$Pr_t = \frac{\nu_t}{\alpha_t} \tag{1.8}$$

The closure problem is therefore shifted to finding the unknown proportionality factor, $1/\,Pr_t$, between α_t and ν_t [17].

However, the application of the Reynolds analogy to close the THF term for fluids with non-unity molecular Prandtl numbers has well-known limitations. The value of Pr significantly affects the similarity assumption between turbulent momentum and heat transfer, as illustrated in Figure 1.1.

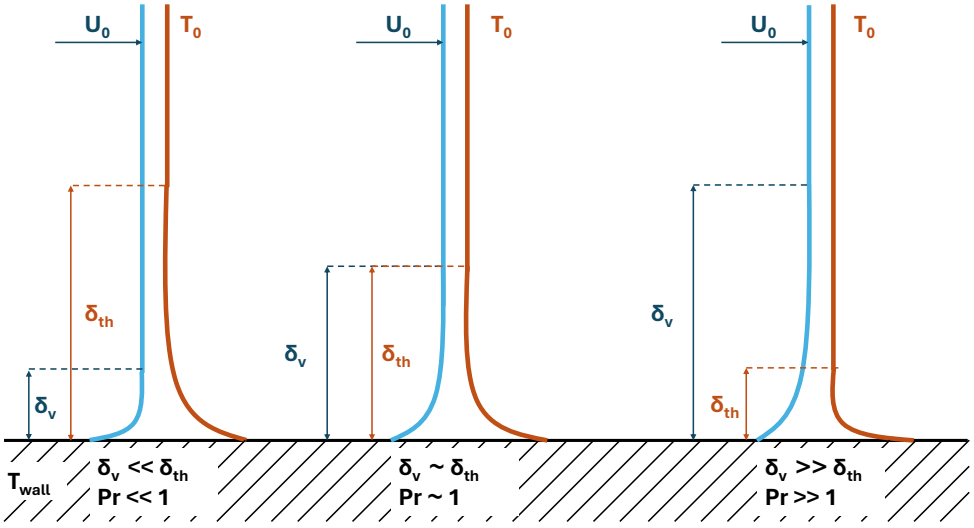

Figure 1.1 - *Representative comparison of the viscous (δ_v) and thermal (δ_t) boundary layers with varying Prandtl numbers. U_0 and T_0 are respectively the free stream velocity and temperature and $T_w > T_0$ is the temperature of the wall.*

Liquid metals are characterized by low Prandtl numbers, resulting in a significantly larger thermal boundary layer compared to the momentum (viscous) boundary layer. The absence of similarity between thermal and momentum boundary layers explains why thermal closures based solely on momentum statistics lack a robust justification in this framework. It is reasonable to assume that Pr_t will not be constant, but will depend on various flow features. Consequently, many different closures have been proposed for this problem:

- Constant Pr_t: A constant value is assigned to Pr_t. This value, commonly set to approximately $0.85 - 0.9$ for commercial software, has been set to 2 for liquid metals. However, DNS data have shown that such a value is strongly dependent on the local flow features, thereby not providing satisfactory results when treated as constant [16].

- Flow-dependent Pr_t: Pr_t is expressed as a function of integral flow features, such as Re and Pe. However, these models have proven to be highly tuned to the reference data and require a priori knowledge of integral flow parameters [16].

- Algebraic closures: The THF is directly related to the TMF and the temperature gradient, resulting in both implicit [18] and explicit [19] models.

- Second-order closures: The three components of the THF are solved using three different transport equations. This approach leads to a high-complexity model consisting of up to 7 equations and 18 empirical parameters that must be tuned [20].

It is clear that this issue can be discussed and complicated to a great extent. However, as the model becomes more complex, it becomes easier to lose the physical sense of the problem, risking the tuning of parameters for a given flow condition without a solid physical foundation. For this reason, experiments are still considered paramount for obtaining a general and reliable estimation of the THF. Several European Projects [21, 22] have already provided an overview of available experimental and numerical datasets and clear need for additional data was identified. In particular, natural and mixed convection in low Prandtl number fluids have been identified as areas lacking the most, primarily due to the additional effort required to simulate these flows, owing to the coupling of the momentum and energy equations.

Thus, experiments are critically needed in this flow regime, which corresponds to the accidental conditions of the reactor. Despite the existence of several measurement techniques for the velocity and temperature in liquid metals, the issue of the simultaneous measurements of their fast fluctuations is still open. Therefore, turbulent heat flux sensors are essential tools for obtaining a quantitative and reliable estimation of the thermal behavior of liquid metals.

1.3 Objectives

Considering the scenario previously described, the main objective of this thesis can be considered twofold:

1. Develop an advanced experimental technique EPICURUS (ExPerImental teChnique for tURbUlence in liquid metalS) suitable for the measurement of the turbulent heat flux in liquid metals, i.e., for the simultaneous measurement of the fast velocity and temperature fluctuations in harsh environments.
2. Provide reference data for the study of natural convection in liquid metals, especially focusing on the transitional and turbulent regime. These data will be used as a valuable reference dataset as well as for the improvements of numerical models.

In particular, these achievements will be a consequence of the following:

- Evaluate the state-of-the-art of the measurement techniques.
- Characterize all the chosen techniques when used in liquid metals.
- Design and develop a natural convection setup and the related procedures where liquid metals can be used and controlled under different conditions.
- Conduct numerical simulations to elucidate their limitations and identify the conditions under which experimental approaches may provide useful insights.
- Conduct experimental tests to evaluate the thermo-hydraulic behavior of low-Prandtl number fluids and compare the experimental results with numerical simulations.

1.4 Scope of the work

The primary objective of this work is to develop an experimental technique capable of measuring turbulent heat flux in liquid metals. Given the necessity for operation in harsh environments, the conditions that the sensor must withstand has to be well defined and taken into account. This work will conduct tests in natural convection using two different fluids:

- **Water**: This fluid is utilized for benchmark tests, to evaluate the setup, its design, and procedure, as well as to assess the comparability between experimental and numerical results.
- **Galinstan (GaInSn)**: This eutectic alloy is composed of $Ga_{67}In_{20.5}Sn_{12.5}$ (wt%), with a melting temperature of approximately $T_m \approx 10\,^{\circ}\mathrm{C}$ [23], making it liquid at ambient temperature. At $T = 50\,^{\circ}\mathrm{C}$, its Prandtl number is $Pr_{\mathrm{GaInSn}} = 0.022$, which is very similar to $Pr_{\mathrm{LBE}} = 0.025$. This similarity guarantees thermohydraulic similarity with LBE while simplifying its use due

to the possibility to operate at ambient temperatures. Detailed information about its properties, applications, and associated challenges will be provided in Chapter 3.

With this background, the experimental activities presented in this work are confined to the following conditions:

- The sensor will be employed in water and GaInSn, therefore high-temperature applications (i.e., above $T = 80\,°C$ for the purposes of this thesis) are not prioritized. However, considerations regarding the adaptability of the sensors for LBE conditions will be noted, and recommendations for future use will be provided at the end of the work.
- The sensors will not be used directly in MYRRHA or any other nuclear reactor but only in facilities supporting their design. For this reason, the effect of neutron fluxes and radiation on the sensors is not taken into account.
- The chemical composition, purity, and properties of the liquid metal alloy GaInSn are not measured, and literature properties are assumed. Variability in metal composition or impurities is not examined in this work.
- The wetting issue of liquid metals is not addressed. Despite being sometimes a key concern in sensing, analyses on the wetting of the probes are not carried out. However, precautions to minimize non-wetting effects are taken and described.

1.5 Thesis structure

This thesis is structured into nine Chapters, as summarized in Figure 1.2. Each Chapter provides a brief introduction to the topic addressed, outlines the core developments of the work, presents the innovative findings, and concludes with a summary of the results obtained in that Chapter and key points relevant for proceeding with the reading of the thesis.

A brief overview of each Chapter is presented as follows:

- **Chapter 1** introduces the general topic and the framework of the project. It particularly addresses the current approaches to turbulence in liquid metals as treated in the literature, emphasizing the importance of understanding the available turbulent models and their underlying assumptions to contextualize the thesis.
- **Chapter 2** reviews the state of the art in instrumentation for measurements in liquid metals. It evaluates the characteristics of turbulence in liquid metals relevant to this work. By integrating these two aspects, the Chapter analyzes various techniques to identify suitable methods for the present research.
- **Chapter 3** details the experimental setup and the procedures developed for managing GaInSn in the laboratory. This Chapter provides significant insights necessary for constructing the complete experimental campaign.

- **Chapter 4** presents a detailed description of the numerical setup adopted, highlighting the strengths, differences, and limitations of the two approaches utilized: Direct Numerical Simulations (DNS) and Reynolds-Averaged Navier-Stokes (RANS). A comparison of the results obtained from both approaches is also included.
- **Chapter 5** focuses on the characterization of temperature sensors (thermocouples and Fiber Bragg Gratings), with particular attention to the static and dynamic calibration of these sensors and their response when used in liquid metals.
- **Chapter 6** discusses the characterization of the Ultrasonic Doppler Velocimetry (UDV) sensor in various experimental setups. It addresses challenges related to flow seeding, optimization of parameters, and uncertainty analysis in detail.
- **Chapter 7** concentrates on the characterization of the hot film sensor. Similar to previous Chapters, static and dynamic calibration are emphasized, along with results obtained from its use in different experimental setups.
- **Chapter 8** builds upon the chosen and characterized techniques as well as the experimental and numerical setups established, presenting all relevant results obtained for natural convection in a differentially heated cavity with water and GaInSn. The Chapter highlights the most significant findings related to the measurement of turbulent heat flux and fluctuations characteristics.
- **Chapter 9** summarizes the main conclusions drawn from this work, addressing both the feasibility and limitations of turbulent heat flux measurements in liquid metals, as well as insights gained regarding the natural convection regime. Recommendations for future work are also provided, particularly focusing on potential adaptations of the sensors for use in Lead-Bismuth Eutectic (LBE) environments.
- Additionally, publications and other materials produced during this project are included in the appendix.

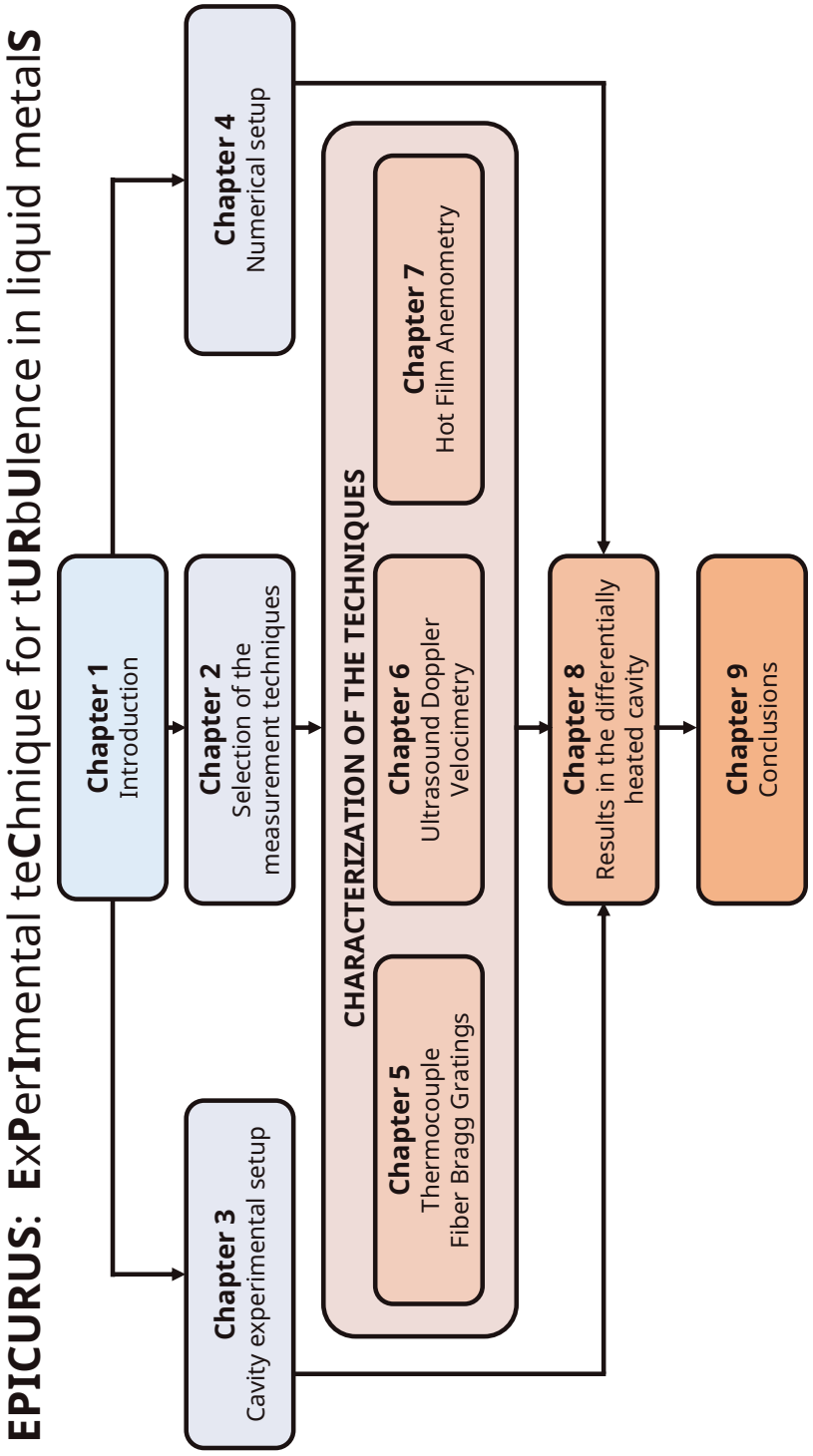

Figure 1.2 - *Structure of this thesis*

Chapter 2

Selection process of the measurement techniques

Chapter 1 introduced the topic of turbulence in liquid metals and outlined the motivations behind this work. Building on this, the current Chapter starts to address this issue in more practical terms, quantifying the phenomena related to temperature and velocity in liquid metals. Such work is carried out with a combination of literature review, theoretical calculations and DNS numerical simulations in Section 2.1. The requirements for a reliable turbulent heat flux sensor are therefore retrieved and compared with the state-of-the-art sensors in Section 2.2 where temperature and velocity measurements are treated separately. Following this analysis, the measurement techniques chosen for this work are presented in Section 2.3. To conclude, Section 2.4 is sepcifically dedicated to the issue of measuring the turbulent heat flux, focusing on the synchronization and the positioning of the sensors.

2.1 Requirements of the sensor

To accurately measure the fast temperature and velocity fluctuations that produce the Turbulent Heat Flux (THF), the Turbulent Heat Flux Sensors (THFSs) must meet specific requirements in terms of:

- spatial and temporal resolution,
- temperature and velocity measurement range and sensitivity,
- capability of withstanding harsh environments, such as high temperatures and strong chemical corrosion.

These characteristics must be translated into physical specifications that the sensor must satisfy to reliably perform measurements in liquid metals. As mentioned in Chapter 1, this work involves two primary working fluids: water and GaInSn. Furthermore, the ultimate goal of the project, beyond the scope of this PhD, is to

conduct measurements in Lead Bismuth Eutectic (LBE). In general, the measurement conditions in liquid metals (especially in LBE) are considered more challenging and demanding compared to those in water. As this Chapter will show, the requirements for spatial and temporal resolution are generally met in water if they are also satisfied in liquid metals. Therefore, the liquid metal environment serves as the reference for sensor selection. However, a distinction is still made between low-temperature environments (primarily for GaInSn) and high-temperature environments (mainly for LBE) as well as for natural convection and forced convection flows. Since this work does not involve high temperature or forced convection measurements, the main focus is on GaInSn compatibility, with attention given to LBE adaptations as described in Section 9.3.

First, it is crucial to understand what needs to be measured, specifically the characteristics of temperature and velocity fluctuations that occur in liquid metals. Figure 2.1 provides a schematic overview of these flow features, still separating different type of flows.

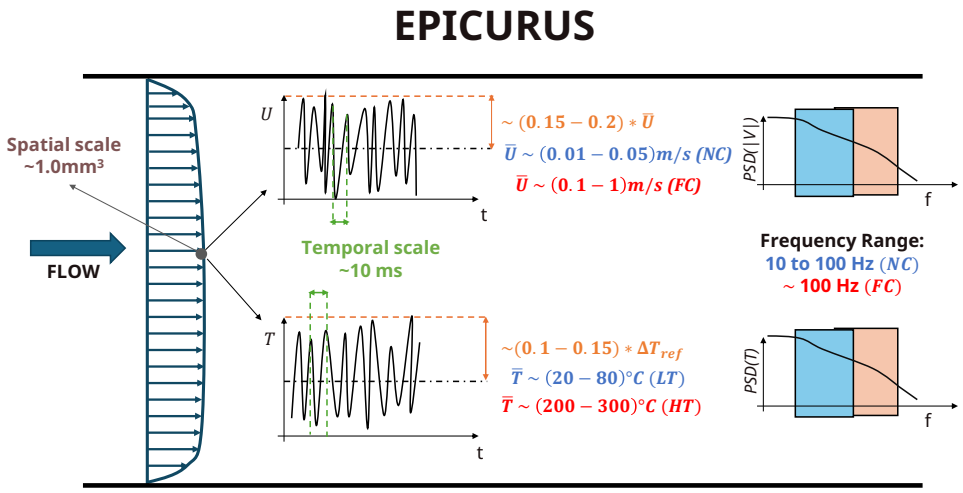

Figure 2.1 - *Summary of liquid metal flow characteristics relevant to the EPICURUS requirements. The flow regimes are categorized into natural convection (NC) and forced convection (FC), and high temperature (HT) and low temperature (LT) conditions.*

The expected **frequencies** of the temperature and velocity fluctuations in liquid metals range between 10 Hz to 100 Hz in the natural convection regime and may exceed 100 Hz in the forced convection regime [12, 24–29]. Table 2.1 presents a summary of the fluctuation characteristics observed in the DNS simulations performed with GaInSn in natural convection [30], whose details are elaborated in Chapter 4.

The reported frequency represents the maximum frequency observed in the turbu-

Table 2.1 - *Characteristics of fluctuations in GaInSn as predicted by DNS simulations [30]*

Variable	Max frequency	Amplitude	Reference value
Temperature	60 Hz	10 % of reference value	$T_{\max} - T_{\text{mean}}$
Velocity	30 Hz	16 % of reference value	U_{mean}

lence spectrum, beyond which all the turbulent vortex energy is dissipated into heat. Overall, the results align well with previous studies in the literature. Given that the flow regime can cause the target quantities to change up to 60 times per second, it is crucial to set the sampling frequency to at least twice the physical frequency to avoid aliasing effects and maintain signal integrity. Therefore, strict **time response** requirements for the sensor are imposed (ideally below 10 ms) to ensure it can capture fluctuations even in the fastest cases. This also translates into a need for a small sensor size to satisfy spatial resolution constraints.

The smallest turbulence scale of interest sets the required **spatial resolution**, which is directly linked to the sensor size. In DNS simulations, the Kolmogorov scale, i.e. the smallest scale in turbulent flows where viscous forces dominate and kinetic energy dissipates as heat, is estimated to be approximately 10^{-4} m to 10^{-5} m for GaInSn in natural convection [30]. Although these scales are too small to be resolved experimentally, focusing on larger turbulent structures, such as the Taylor scale, provides a reasonable compromise. This leads to the recommendation of a sensor spatial resolution on the order of 0.5 mm^3 to 1 mm^3, sufficient to yield valuable insights into flow characteristics [25, 30].

The **amplitude** of the fluctuations is another important factor. Lower frequencies are generally easier to capture, but smaller amplitudes can pose challenges due to the higher accuracy and sensitivity required by the instrumentation. Velocity fluctuations in liquid metals can vary according to the regime, but for natural convection typical values about 15 % to 20 % of the absolute velocity can be assumed in first approximation. The expected velocities range are of several cm/s [12, 24, 26–30] for GaInSn (but down to mm/s for water [31, 32]), meaning that fluctuations are likely in the mm/s range. DNS results summarized in Table 2.1 align with prior literature values. For temperature, the experimental range in this work spans 20 °C to 80 °C, with previous studies reporting temperature fluctuations around 10 % to 15 % of the non-dimensionalized temperature [12, 27–30, 33]. Using water could result in lower fluctuation amplitudes (at a given Gr number), potentially making measurements more challenging.

The general turbulence characteristics of a flow can also be roughly estimated using theoretical calculations [34, 35]. Knowing the characteristic length of the domain L_c and the temperature difference ΔT driving the flow in natural convection, it is possible to calculate the characteristic velocity U_c as in Equation (2.1), assuming a balance between buoyant and viscous forces in the flow.

$$U_c = \sqrt{g\beta\Delta T L_c} \tag{2.1}$$

In the case of this work, with $L_c = 60\,\text{mm}$, $\Delta T = 60\,^\circ\text{C}$ (see Chapter 3) and assuming GaInSn as working fluid, $U_c = 0.056\,\text{m/s}$. Assuming a turbulent intensity (TI) of 16 % as retrieved from the DNS simulations in Table 2.1, it is possible to estimate several important turbulence length scales:

- **Integral length scale** l: the range in which the turbulence is produced. It is also characterized by the frequency of the integral scale f_l.
- **Taylor length scale** λ_T: the inertial subrange, where turbulence is transported to smaller scales still without dissipation. It is the limit scale where the structures still have the memory of the characteristics of the parent average flow and tend to isotropic behaviour.
- **Kolmogorov scale** η: the dissipation scale where the small turbulent structures are dissipated in the form of heat.

Assuming the setup characteristics mentioned before and GaInSn as working fluid, the integral length and time scales of turbulence can be estimated as in Equations (2.2) to (2.4), passing through the rms value of velocity u'_{rms} that represents the amplitude of the fluctuations around the mean.

$$u'_{\text{rms}} = U \times \text{TI} = 9 \times 10^{-3}\,\text{m/s} \tag{2.2}$$

$$l = L_c \times \text{TI} = 9.6 \times 10^{-3}\,\text{m} \tag{2.3}$$

$$f_l = \frac{u'_{\text{rms}}}{l} = 6\,\text{Hz} \tag{2.4}$$

With these values, the turbulent Reynolds number can be calculated as in Equation (2.5) where $\nu = 2.841 \times 10^{-7}\,\text{m}^2/\text{s}$ is the kinematic viscosity of GaInSn at 50 °C.

$$Re_t = \frac{u'_{\text{rms}} \times l}{\nu} \approx 300 \tag{2.5}$$

Using the relationships between the integral and Kolmogorov scales, the smallest turbulence scale η and the associate frequency f_η can be estimated through Equations (2.6) and (2.7).

$$\eta = l\left(Re_t^{-\frac{3}{4}}\right) = 1.3 \times 10^{-4}\,\text{m} \tag{2.6}$$

$$f_\eta = \frac{u'_{\text{rms}}}{\eta} = 68\,\text{Hz} \tag{2.7}$$

The results of these theoretical calculations are summarized in Table 2.2.

Interestingly, these values are of a similar order of magnitude as those calculated from DNS simulations (Table 2.1), confirming consistency between theoretical estimates, DNS results, and literature data on the turbulence characteristics, at least in a first approximation. While Kolmogorov scales are too small to be resolved with current instrumentation, turbulence can be analyzed via frequency and spectrum

Table 2.2 - *Turbulence characteristics in GaInSn as predicted by theoretical calculations [34, 35]*

Turbulence scale	Frequency	Length
Integral	6 Hz	9.6×10^{-3} m
Kolmogorov	68 Hz	1.3×10^{-4} m

analysis, as the turbulent frequencies are within the range of the sensors. The spatial resolution will likely only capture the larger turbulent structures, within the inertial subrange.

Though no equivalent calculation exists specifically for thermal fluctuations, in low Pr number fluids, the thermal fluctuation frequency can be expected to be higher than the velocity frequency, according to what predicted by DNS results in Table 2.1 [30].

2.2 State-of-the-art overview on measurement techniques for liquid metal flows

This Section gives an overview of the state-of-the-art techniques used to measure velocity and temperature in liquid metals. The development of a turbulent heat flux sensor (THFS) will be a direct consequence of the selection of the most suitable instruments currently available. Therefore, this section analyzes and compares existing measurement techniques through their advantages and disadvantages when used in liquid metals. Characteristics and suitability of each sensor will then be analyzed and consequent choices will be made in Section 2.3. An overview of all the techniques considered is given in Table 2.3.

For each measurement technique considered, the best values found in the literature for their spatial and temporal resolution are reported, along with their applicability to the THF measurements conducted in this work. More details and references are given in the following Sections of this Chapter.

2.2.1 Temperature measurement techniques

In this section, the temperature measurement techniques evaluated for this work are introduced. Each technique is explained briefly, followed by a summary of its performance and limitations as reported in the literature, particularly in the context of liquid metals.

- **Infrared camera**: it measures temperature by detecting infrared radiation emitted by the surface of objects. The camera converts this radiation into a thermal image where temperature variations are displayed as different colors or intensity levels, making it non-invasive and ideal for surface temperature mapping [36]. When applied in liquid metals, infrared cameras find most of their application for industrial processes involving liquid metal fusion [37–40].

Table 2.3 - *Overview of velocity and temperature measurement techniques for liquid metals. The table presents the best reported volumetric (Δx) and linear (Δl) spatial resolutions, temporal resolution (Δt), measurement range, and suitability for turbulent heat flux measurements.*

Technique	**Δl**[a)] [mm]	**Δx** [mm^3]	**Δt** [ms]	**Range**	**THF**
Infrared Camera [39]	2×10^{-2}	4×10^{-4} mm^{2}[b)]	1×10^{-2}[c)]	750 °C to 4000 °C	X
RTD [36]	0.5	1.25×10^{-1}[d)]	3×10^{2}	−260 °C to 1000 °C	X
Thermocouple [41]	0.08	5.12×10^{-4}[d)]	2 to 3	−200 °C to 1260 °C	✓
Distributed Fiber [42, 43]	5.12	2.1[e)]	7 to 8	−100 °C to 400 °C	X
FBGs [44, 45]	<1	5×10^{-2}[e)]	7 to 8	−100 °C to 300 °C	✓
Local LFV [46, 47]	10	1×10^{3}[d)]	1×10^{3}[c)]	10^{-1} m/s to 1 m/s	X
TECF [48]	10.6	1.5×10^{3}[e)]	1 to 10[c)]	10^{-2} m/s to 10 m/s	X
UDV [49, 50]	10 to 12	2.5 to 16[e)]	1.7×10^{1}[c)]	10^{-3} m/s to 1 m/s	✓
Pitot [51]	1 to 2	1 to 8[d)]	1[c)]	5×10^{-2} m/s to 1 m/s	✓
PMP [52, 53]	1.6	4.1[d)]	6.5[c)]	10^{-3} m/s to 1 m/s	✓
CIFT [54, 55]	5 to 10	1.25×10^{2} to 1×10^{3}[d)]	1×10^{3}[c)]	2×10^{-2} m/s to 1 m/s	X
Neutron Radiography [56, 57]	≈ 1	1.75 mm^{2}[b)]	1×10^{1}[c)]	10^{-2} m/s to 10^{-2} m/s	X
HWA/HFA [58, 59]	1.25	2×10^{-2}[e)]	0.1 to 0.2[c)]	10^{-3} m/s to 1 m/s	✓

a) Due to the strong spatial inhomogeneity within the measurement volume of some techniques, this parameter represents the largest linear dimension of the measurement volume, expressed in mm.

b) In the case of imaging techniques providing a 2D picture of the flow, the spatial resolution is expressed in mm^2

c) This temporal resolution was reported in the reference papers as a sampling acquisition rate f_s and converted to time t through $t = 1/f_s$

d) The spatial resolution was reported in the reference papers either as the characteristic dimension of the sensor or its one-dimensional resolution d_s, converted to volumetric resolution d_v through $d_v = d_s^3$

e) The spatial resolution was reported in the reference papers as either the length of the sensitive part or the one-dimensional resolution l_s of the sensor. The volumetric resolution d_v was calculated through $d_v = \pi r_s^2 l_s$, given either the radius of the sensitive part or the radial resolution of the sensor r_s

Despite the existence of some commercial devices able to record at a rate of up to 100 kHz with spatial resolution of 20 µm [39], their main liability lies in their relatively high uncertainty [38] ($\approx$ 10 %) related to the fact that their measurement range is often wide and focused on high temperature applications (750 °C to 4000 °C). Even if this value can be improved with the use of a more complex setup and two-color techniques [38, 40], their measurements are limited to the surface temperature of the metal and it is therefore not interesting for the local measurements goal that is targeted in this work.

- **RTD (Resistance Temperature Detector)**: RTDs operate based on the principle that the electrical resistance of metals, such as platinum, increases in a linear way with temperature. The resistance change is measured and correlated with temperature, offering high accuracy and stability over a wide range of temperatures (−260 °C to 1000 °C) [36]. Standard sensors can be as small as 1 mm of diameter [36], but nowadays customized commercially available sensors can arrive down to 0.5 mm of diameter. Despite their small dimensions and wide measurement range, the current applications of these sensors in liquid metals are primarily limited to bulk temperature measurements [32, 60]. This is due to the continued dominance of thermocouples for local measurements, particularly because of the relatively slow time response of RTDs, typically exceeding 0.3 s [36].

- **Thermocouples**: these sensors consist of two different conductors, i.e., metals with a different Seebeck coefficient, joined at one end to form a junction. When there is a temperature difference between this junction and the other ends of the wires (the reference junction), a voltage is generated along the wires. This voltage is then used to determine the temperature at the measurement point [36]. Their extensive use in all applications, from industrial processes to scientific research for an extremely wide range of temperatures, makes it difficult to provide an exhaustive reference list. The need of sheathed sensors for the use in liquid metals is now acknowledged by the work of several authors [52, 61–63] and the type K is normally preferred because of their constant Seebeck coefficient over a wide range of temperatures [12, 36]. However, different types have also been used in harsh environments [58, 64]. Commercially available sheathed type K thermocouples can be as small as 80 µm of external diameter and the literature addressing their time response is very vast, addressing sensors with response time from 2 ms to 3 ms [41, 65, 66] to 10 s [67], strongly depending on the characteristics of the sensor chosen. In fact, several studies have successfully utilized thermocouples for measuring fluctuations in liquid metals, including type E chromel-constantan thermocouples with a diameter of 300 µm [68, 69] and ungrounded type K thermocouples with a diameter of 250 µm [52]. On the other hand, they only allow pointwise measurements and being an intrusive sensor, perturbations of the flow are inevitable. Despite of that, their robustness, versatility and wide temperature range make them the most common instrument used in liquid metals for temperature measurements. For this reason, the research nowadays is focused on much more detailed aspects of their

use in liquid metals like measurement accuracy, secondary effects, e.g. the ones due to positioning and bending, and calibration drift phenomena [61].

- **Distributed fiber sensors**: Distributed fiber optic sensors measure physical changes like temperature and strain along the length of an optical fiber by detecting variations in backscattered light. When light travels through the fiber, impurities and molecular-level structural variations cause scattering. These scattering events produce a unique backscatter pattern for each fiber. Physical changes, such as temperature shifts or strain, alter this backscatter pattern in a predictable manner, enabling the fiber to function as a sensor. By monitoring these changes, temperature variations along the fiber can be accurately measured [70]. Optical fiber technologies, widely used in telecommunications [71], have found growing applications in sensing due to their lightweight nature, resistance to corrosion, and immunity to electromagnetic interference [70]. After over 40 years of development, distributed fiber-optic sensing has advanced in terms of measurement range, spatial resolution, and sensitivity. These qualities make this technology a candidate for applications in this work. Distributed fiber-optic sensing primarily uses three types of scattering phenomena:
  - *Rayleigh scattering*: an elastic scattering phenomenon where light is scattered by inhomogeneities in the fiber. Rayleigh scattering is sensitive to strain but also responds to temperature changes. The Optical Time Domain Reflectometry (OTDR) technique monitors the time and intensity of the backscattered light, which changes with temperature, enabling indirect temperature measurement. A calibration process is required to differentiate temperature effects from strain.
  - *Raman scattering*: in Raman-based distributed sensors, temperature is determined by the temperature dependence of the spontaneous Raman scattering process. This occurs due to thermally-driven molecular vibrations, producing two frequency-shifted components from the incoming light. The intensity of the anti-Stokes component increases with temperature, while the Stokes component remains relatively unchanged. By comparing these two components, distributed temperature sensing can be achieved.
  - *Brillouin scattering*: an inelastic scattering process where light interacts with acoustic waves within the fiber. Brillouin scattering is sensitive to changes in thermodynamic quantities like temperature and density, making it useful for sensing both temperature and strain.

  Although all three scattering effects are widely used in various sensing applications [70, 72], Rayleigh scattering is the only method reported in literature for temperature sensing in liquid sodium environments [42, 43, 73, 74], including nuclear reactors [75], making it the most relevant technique for this work. Rayleigh-based sensors have been applied in extreme environments up to 400 °C, achieving spatial resolutions of 5.12 mm and time constants between 7.1 ms to 8.9 ms [42, 43]. However, these applications typically use stainless steel-coated fibers, which increase sensor size and degrade time response. Additionally, the

focus in literature is on distributed measurements over long distances (typically greater than 1 m, sometimes up to the km) and longer time scales (hours to days), making them unsuitable for the high temporal resolution required in this work.

- **Fiber Bragg Gratings (FBGs)**: FBGs are optical sensors inscribed within a fiber where periodic variations in the refractive index cause selective reflection of specific wavelengths of light centered on the so-called Bragg wavelength. As the temperature varies, the spacing between these gratings shift and the effective refractive index of the core changes, altering the wavelength of the reflected light. This shift can be correlated almost linearly with temperature, providing accurate localized temperature readings [70]. They are currently applied since several years for monitoring of structures, temperature, pressure, and vibrations measurements in different environments and biomedical applications [70, 76, 77]. In more recent times, they have also found applications in more harsh environments like nuclear reactors, for instance for flow-induced vibrations in LBE [78], and for temperature [79, 80] or strain [81] measurements. In fact, one of their characteristics is the fact of being sensitive to both strain and temperature and for this reason one of the main challenges addressed in literature is the differentiation between the effects given by strain and temperature [82–84]. A part of the intrinsic advantages of the fibers already listed before, these sensors can be inscribed for a length <1 mm over a fiber with an external diameter of 125 µm, therefore giving a total measurement volume smaller than $1\,\mathrm{mm}^3$ [70]. Their small size is also associated with short response times, which can vary depending on the application and potential coating, within a range from 4.8 ms to 9 s [85–89]. This particular aspect has also been the focus of two publications by the author [44, 45]. Some applications even use the sensors with a similar principle to the one of the hot wire for the measurement of velocity in fluids [90, 91] but this application is not considered in the current work.

The main findings of this section are summarized in Table 2.3 to ease the comparison among the different techniques. Section 2.3 will present more in depth the techniques chosen and the main reasons that led to their choice.

2.2.2 Velocity measurement techniques

This section examines all the techniques considered for measuring velocity fluctuations in liquid metals. Several experimental methods, which have been well-established for use in air and water, were excluded due to their incompatibility with liquid metals. For instance, Particle Image Velocimetry (PIV) and Laser Doppler Velocimetry (LDV) necessitate optical access, which is unfeasible because of the opacity of liquid metals. However, some techniques originally developed for water or air measurements can be adapted for the liquid metals environment; these adaptations are presented herein. Subsequently, specific techniques designed explicitly for use in liquid metals are evaluated.

- **Lorentz Force Velocimetry (LFV)**: originally born as a flow meter typically used for integral velocity measurements, this sensor bases the measurement of the bulk velocity through the direct measurement of the mechanical force induced on an external permanent magnet by the liquid metal flow [92]. Such force will be proportional to the velocity of the liquid and its flow rate can therefore be calculated. It is a non-intrusive technique but mostly adopted in forced convection applications, e.g., pipe flows, and mainly for bulk measurements [93, 94]. In principle, the technique can be made local by the use of a permanent magnetic much smaller than the vortical structures of the flow and by accepting to be able to measure only in regions very close to the walls [47, 95] due to the limitations given by the power of the magnet. In this configuration a spatial resolution of $1\,\mathrm{cm}^3$ and a temporal resolution of $1\,\mathrm{Hz}$ are achieved [46, 47].

- **Eddy current flowmeters**: the basic design of the detector consists in three coils, one excitation coil fed by an AC current and two detection coils. The sensor has to be placed inside the flow and it is able to measure the flow rate in a certain volume around the sensor itself depending on the frequency of the injected current and on the electrical conductivity of the fluid and therefore the temperature. The information about the velocity can be related to both the voltage and the phase difference between both detection coils [96, 97]. Further development of the technique led to the transient eddy current flow meter (TECF) [48], that can reduce the sensitivity to changes of the electrical conductivity of the fluid, reaching temporal resolutions in the order of the ms [98]. On the other hand, the sensor still results to be relatively big with an outer diameter of $10.6\,\mathrm{mm}$ [48] and therefore very intrusive and not adapt for the current work.

- **Ultrasound Doppler Velocimetry (UDV)**: In this technique, UDV transducers send a pulsed ultrasonic signal into the liquid metal, which is reflected by microscopic particles, such as oxydes or impurities. The position and velocity of these particles are determined by measuring the transit time of the ultrasound and the phase shift of the echo from subsequent pulses. This allows the beam-parallel velocity distribution along the ultrasonic beam to be calculated [50, 99]. The UDV technique has become an established method for velocity measurements in opaque fluids and has been widely used in various experimental setups and applications [49, 100–104].Being fully non-intrusive, the sensor can be flush-mounted on the wall of the facility, with its spatial and temporal resolutions depending on the sensor dimensions, setup, and chosen settings. Axial resolutions up to $0.1\,\mathrm{mm}$ are commonly reported [50, 102]. However, the transversal resolution is primarily limited by the diameter of the piezosensor, resulting in a significantly larger measurement volume in this direction. This spatial inhomogeneity within the measurement volume necessitates careful consideration when applying this technique. Specifically, it may be necessary to account for spatial averaging effects during data processing and subsequent comparison with other measurement techniques. Previous studies indicate ac-

quisition rates up to 60 Hz are achievable [49, 51]. The main advantages of UDV are its suitability for opaque fluids, non-intrusive nature, and distributed measurement capabilities along the sensor axis. However, its success in liquid metals is not always consistent, with influencing parameters such as sensor wetting (for good acoustic coupling, particularly in high-temperature applications) and the optimal characteristics of scatterers in the fluid still not fully understood [51].

- **Pitot tube**: it is another well-established technique for the velocity measurements based on a differential measurement between dynamic and static pressure in a flow. It has been used for water and air measurements for decades, also coupled with temperature sensors to allow the simultaneous measurement of velocity and temperature [105]. The probe is generally simple, robust and accurate and depending on the pressure sensor used it can also reach high acquisition frequency. Its use in liquid metals has been exploited with moderate success up to reaching an accuracy of 5 mm/s with an acquisition rate of up to 1 kHz when combined with piezo-resistive transducers [51, 62, 63, 106]. The spatial resolution depends on the size of the orifices, with diameters ranging from 1 mm to 2 mm having been adopted in liquid metals [62]. Naturally, the probe must be larger than the orifice itself, making it a highly intrusive measurement technique. Moreover, due to the high surface tension of liquid metals, the pressure difference required to fill the tubes orifices increases significantly with the degree of miniaturisation. Some authors also highlight that the use of these sensors in liquid metals can be significantly affected by electromagnetic forces. These forces can induce additional losses in fluid kinetic energy, making the pressure readings no longer a direct indicator of fluid velocity [103, 107].

- **Permanent Magnet Probes (PMP)**: it consists of a ringshaped permanent magnet with radial magnetization direction and thermocouples. When the magnet is placed in a liquid metal flow with a certain velocity, an electro-motive force (EMF) is induced according to Faraday's law of induction. If two electrodes are placed within the induced electric field, a potential can be measured and if it is measured by thermocouples instead of regular wires, information about the temperature can also be retrieved. [52, 108]. The technique is one of the most promising and recently developed among the ones here reported and successfully allowed simultaneous temperature and velocity measurements in liquid metal flows [52, 53, 107, 109]. Similar to a Pitot, its spatial resolution is given by the diameter of the tip and the most recent found in the literature reported a value of 1.6 mm [52, 53]. The sampling rate mainly depends on the acquisition system and can be up to 5000 Hz but in literature a realistic probe frequency cutoff has been calculated to be 154 Hz, therefore limiting the acquisition rate to this value. The probe showed good accuracy and the possibility to measure a wide range of velocities but the voltages induced are in the order of few μV therefore good care should be taken to minimize the electromagnetic noise, select a suitable acquisition system and correct the measurements in post-processing. Some authors also mention wetting of the probe as a possible issue in liquid metals [52].

- **Flow Mapping Techniques**:
  - *Contactless Inductive Flow Tomography (CIFT)*: In this technique, the three dimensional behaviour of the flow can be reconstructed by measuring the flow-induced perturbation of a magnetic field [110]. A static magnetic field is imposed outside of the liquid metal container and an electric current is generated inside the melt because of its relative motion in comparison with the magnetic field. This electric current, in turn, generates a magnetic field that is measurable outside of the facility. Through the resolution of a linear inverse problem, it is possible to retrieve the three-dimensional flow structure inside the vessel. This technique is part of the techniques specifically developed for liquid metal flows since it relies on the electromagnetic properties of the flow itself. The interest of the scientific community in its application grew recently [54, 55, 111] since it has shown good results in Rayleigh-Bénard setup at very low velocities of about 20 mm/s [29] with sampling frequency up to 1 Hz and spatial resolution in the order or 5 mm to 10 mm. This technique is a promising technique for the acquisition of the entire 3D velocity field at once without any perturbation of the flow. On the other hand, it is extremely susceptible to external electromagnetic intereference and suitable countermeasure must be taken into account. Moreover, it is not meant to be a local measurement technique and it is therefore not considered suitable for the turbulent measurement applications of this thesis.
  - *Neutron Radiography*: this imaging technique is based on the general principle of radiography, allowing the visualization of the structure of an object by measuring the differences in attenuation rates of rays passing through the various materials that constitute the object [112]. Originally developed for the study of multiphase flows, neutron radiography requires tracers for flow visualization when used for velocity measurements [56, 112, 113]. Acquisition rates up to 100 Hz and spatial resolutions below 1 mm have been achieved in previous applications [56, 57]. In principle, neutron particle image velocimetry (NeuPIV) could be implemented [113], following similar principles to PIV. However, the requirement for specialized facilities complicates the experimental setup. For completeness, X-rays could be considered as an alternative to neutrons, but their high attenuation coefficient in liquid metals significantly limits their use in large facilities. In fact, while neutron attenuation depends on the material, X-ray attenuation increases with atomic number [112].
- **Hot Wire Anemometry (HWA)**: it is based on the cooling effect of a flow on a heated body, usually a cylindrical wire. The wire is connected to one arm of a Wheatstone bridge and heated by an electrical current. In the Constant Temperature Anemometry (CTA), the temperature of the wire remains constant through the whole measurement and thus, the current flowing through the wire (i.e., the heating power) changes to maintain the temperature constant. The voltage measured across the wire can therefore be related to the velocity of the

flow. The technique has been used for decades for turbulence measurements and spectral analysis in different types of flows, mostly in air [114, 115]. Its first application in water dates back to the beginning of the 20$^{\text{th}}$ century [116], but only in the 1970s the technique started to be reliable and widely used due to the technological advancements that allowed the development of coated wires and hot-film probes [117, 118]. At the same time, some first attempts were made for the use of these same probes in liquid metals, very often combined with thermocouples for temperature measurements and corrections [119–121]. Velocities comparable to those observed in natural convection, in the range of 1 cm/s to 12 cm/s, were successfully measured [119, 122]. Further advancements in technology allow to exploit the potential of the probe reaching good repeatability and accuracy [58, 64] but to the knowledge of the author their use for turbulence measurement in liquid metals has not been explored thoroughly in recent times even if attempts have been made previously [123]. The main focus was on the retrieval of non-dimensional correlations [119, 121–123] and only a few authors performed a spectral analysis [124, 125] of the signal. Thanks to their working principle, typical cut-off frequencies of the probe for use in conductive fluids are in the order of 10 kHz [59] and their sampling rate is only limited by the acquistion system used. The probe itself can be very small, with an active length on the order of mm and a diameter in the range of 7 µm to 100 µm, allowing for measurement volumes smaller than 1 mm^3. However, the entire support structure and prongs can be highly intrusive in the fluid. The probe is also generally very fragile, requiring extreme care during calibration. These factors present significant challenges when using the probe in liquid metals, where the harsh environment and high temperatures can not only damage the probe but also impact the repeatability of the measurements [58, 119].

The main findings of this section are summarized in Table 2.3 to facilitate comparison among the different techniques. Section 2.3 will present a more in-depth discussion of the techniques selected and the rationale behind their choice.

2.3 Choice of measurement techniques

Based on the considerations outlined in Section 2.1, this Section identifies the most suitable techniques for turbulent heat flux measurements within the scope of this work. The requirements established in Tables 2.1 and 2.2 are compared with the capabilities of the measurement techniques summarized in Table 2.3. This analysis leads to the selection of specific techniques for temperature and velocity measurements, which are subsequently summarized in Figure 2.2.

Two techniques for the velocity measurements (Ultrasound Doppler Velocimetry and Hot Film) and two techniques for the temperature measurements (Thermocouples and Fiber Bragg Gratings) were chosen. The following sections outline the rationale behind the chosen equipment, with a focus on the selected sensors, acquisition systems, and the complete measurement chain utilized for the experiments. Additionally, the reasons for discarding alternative techniques are discussed.

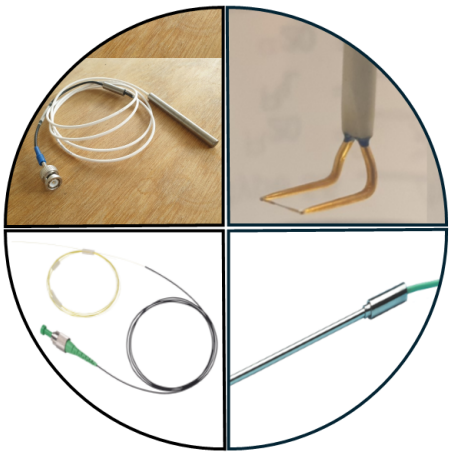

Figure 2.2 - *Overview of the selected techniques. Clockwise from the top left: Ultrasound Doppler Velocimetry (UDV), Hot Film (HF), Thermocouple (TC), and Fiber Bragg Grating (FBG).*

Regarding temperature measurement techniques, the infrared camera was considered out of the scope of this work, being more suited for surface imaging than for local measurements. Similar considerations were made for distributed temperature sensing with optical fibers. Despite the potential for local measurements, their main field of application lies in long-distance measurements, discouraging their use for local fluctuation measurements. The RTD did not have many prior studies supporting its use for local fluctuation measurements, likely due to its relatively slow response time, and was also discarded.

Eventually, two temperature sensors were chosen for this work: thermocouples and Fiber Bragg Gratings (FBGs). Thermocouples have been successfully used in liquid metals for years, and once material compatibility issues are resolved, they are a suitable candidate for temperature fluctuations measurements in GaInSn or LBE, in terms of temporal and spatial resolution, and measurement range, as highlighted by the comparison between Tables 2.1 and 2.3. FBGs offer advantages in terms of cost-efficiency, lightweight design, corrosion resistance, and immunity to electromagnetic interference. Previous studies have shown that FBGs can often replace and outperform thermocouples in many applications, offering similar or smaller dimensions and fewer material compatibility issues. The growing field of optical fiber sensing also presents an opportunity for this work to contribute to the use of FBGs in liquid metals. Details about the chosen thermocouples and FBG sensors are provided in Section 2.3.1 and Section 2.3.2.

Regarding velocity measurement techniques, after discarding optical techniques due to their inapplicability in liquid metals, several alternatives were still considered. Flow mapping techniques were considered out of scope for this thesis due to their focus on visualizing structures in opaque fluids rather than local measurements. Local Lorentz Force Velocimetry (LFV) was examined in greater detail but ultimately discarded due to setup complexity and insufficient spatial resolution. However, the author believes that local LFV could be a promising candidate for future local and fast measurements in specific setups.

Despite being a suitable candidate for simultaneous local velocity and temperature measurements, the Pitot tube was not selected for this work. It is challenging to reduce the sensor size below 1 mm while maintaining the desired temporal resolution, particularly in liquid metals, where material compatibility issues arise. The high surface tension of liquid metals could also hinder the filling of the Pitot tube up to the sensitive part, compromising measurement reliability. Additionally, the substantial post-processing corrections necessary to account for the effects of viscosity, turbulence, velocity gradients, and the proximity of walls for accurate velocity measurements in liquid metals diminish the simplicity that characterizes this technique [62]. Lastly, the predicted velocities in natural convection flows like the one studied here are incompatible with the sensitivity of the Pitot tube, which requires relatively high velocities to function properly in liquid metals.

The last technique discarded was the PMP sensor. While the technique has proven suitable for this kind of measurement, it has not yet been fully applied to THF measurements. However, the required know-how in sensor production, expertise in its use, and the lack of available setup led to its exclusion from this work.

Ultimately, the hot film anemometer and Ultrasound Doppler Velocimetry (UDV) were selected as the most suitable techniques for this experiment. This selection was based on an analysis presented in Section 2.2.2, which highlighted their general compatibility with the requirements while also acknowledging their respective limitations. The hot film has already passed the proof-of-principle stage and has proven applicable in liquid metals. The choice of a hot film over a hot wire lies in its greater mechanical strength and its possibility of being electrically isolated from the flow [126]. The main challenges will be finding a suitable probe and calibration setup and exploiting the technique to its full potential for turbulence measurements in liquid metals. The intrusiveness of the support and prongs can be mitigated through careful facility design and probe selection, without significantly affecting the spatial resolution, which is mainly determined by the sensor dimensions. UDV has proven to be one of the best techniques for velocity measurements when optical access is unavailable. Its temporal resolution is in principle compatible with the sensor requirements. On the other hand, careful consideration must be given to its spatial resolution, which can exhibit significant inhomogeneity in all three dimensions. If the axial resolution is infact respecting the requirements of Section 2.1, the radial resolution is bigger, requiring careful assessment of the measurements volume. However, prior studies in the literature provide a solid foundation for further improvement. Moreover, its ability to measure along a line is a desirable feature in environments where non-pointwise measurements are difficult. Additionally, previous in-house experience and the avail-

ability of sensors make UDV a promising technique for further exploration. The main limitations are likely to arise from low velocities and environmental conditions, which cannot be fully predicted in advance. Nevertheless, there is no reason to believe these challenges cannot be overcome. To the knowledge of the author, UDV has never been used for turbulent measurements, and this work could provide an opportunity to push the capabilities of the sensor to their limits. Details about the selected sensors are provided in Section 2.3.4 and Section 2.3.3.

Once the sensors are chosen, an appropriate acquisition system must be paired with them. Beyond intrinsic limitations set by the Nyquist theorem, no special considerations are needed for the acquisition systems. A wise choice of commercially available systems should suffice. The following sections also present the acquisition systems selected for each sensor.

2.3.1 Thermocouple (TC)

The selected thermocouple is a Type K sheathed thermocouple with a diameter of 250 µm and a total length of 500 mm, supplied by TC Direct (code 406-477), as shown in Figure 2.3(a).

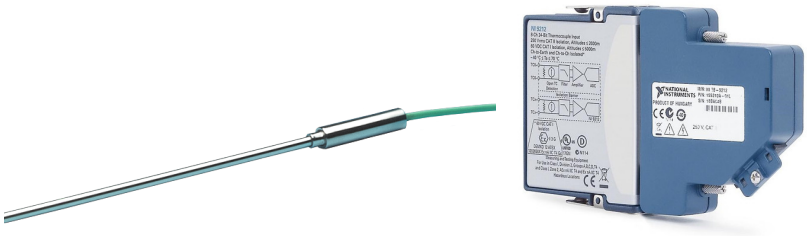

(a) Sheathed type K TC, Ø250 µm (b) NI9212

Figure 2.3 - *Sensor and acquisition system chosen for the temperature measurements (TC).*

The sheathed design was chosen due to its increasing standardization for use in liquid metals, as well as its compatibility with higher-temperature applications such as LBE without requiring further adaptations. To optimize both spatial and temporal resolution, the smallest commercially available size by TC Direct was selected. An even smaller Type K sheathed thermocouple (100 µm) was initially tested but proved too fragile, breaking during operation. As a result, it was deemed unsuitable for further testing and replaced by the more robust 250 µm version. For data acquisition, the NI9212 acquisition card from National Instruments, shown in Figure 2.3(b), was selected. The system includes an isothermal terminal block, which allows for a declared measurement accuracy of up to 0.29 °C [127], and offers a maximum acquisition frequency of 95 Hz. Although faster thermocouple acquisition systems are available, the decision to use this particular system was mainly driven by the ability to synchronize

data acquisition via the software configuration. The acquisition card is connected to a NI9178 Compact DAQ chassis, which provides a plug-and-play USB interface that can be directly connected to a PC and controlled through a custom LabView routine.

The final configuration used for the measurements, in combination with the FBG sensor, is shown in Figure 2.9, with more details about the complete measurement chain provided in Section 2.4.

2.3.2 Fiber Bragg Gratings (FBG)

The FBG sensor utilized in this study was custom-made by the University of Mons by lateral illumination of interfering ultraviolet laser beams. This fabrication technique allowed for precise customization of sensor dimensions and accurate positioning of the sensitive grating. The sensor was constructed using SM1500 (4.2/125) bend insensitive, photosensitive silica optical fiber obtained from Fibercore Ltd., featuring a diameter of 0.125 mm and an acrylate coating. The sensor is shown in Figure 2.4(a).

(a) FBG, Ø0.125 mm (b) Benchtop Bayspec WaveCapture interrogator

Figure 2.4 - *Sensor and acquisition system chosen for the temperature measurements (FBG).*

The grating was inscribed at the tip of the uncoated fiber aligned parallel to its edge, intentionally designed to be as short as feasible to achieve the best possible spatial resolution, resulting in a final total length of less than 1 mm. The distance between the grating and the end of the fiber is therefore ideally zero. The fiber was left uncoated, as the grating is expected to remain undamaged up to temperatures of 300 °C. Nonetheless, preliminary tests were conducted to confirm its durability under these conditions.

Signal acquisition was performed by the Bayspec WaveCapture interrogator, enabling data acquisition up to a frequency of 5 kHz and allowing a wavelength resolution

of 1 pm [128]. The acquisition system was connected to a PC through a USB connector and the acquisition was carried out through the software BaySpec Sense 2020 [129].

The final configuration used for the measurements, in combination with the TC sensor, is shown in Figure 2.9, with more details about the complete measurement chain provided in Section 2.4.

2.3.3 Ultrasound Doppler Velocimetry (UDV)

For the UDV measurements, two sensors were chosen because of their different emitting frequency, the TR0805LS and the TR1005LS commercial sensors from Signal Processing. A picture of TR1005LS is shown in Figure 2.5(a).

(a) TR1005LS sensor

(b) DOP4000 acquisition system

Figure 2.5 - *Sensor and acquisition system chosen for the velocity measurements (UDV).*

Their main characteristics are also reported in Table 2.4.

Table 2.4 - *Main characteristics of the UDV sensors used for this work*

Parameter	**Value**
Emitting US frequency	8 MHz-10 MHz
Piezo element diameter	5 mm
Case diameter	8 mm
Case material	Stainless Steel 316L
Case length	90 mm
Front material	Epoxy
Impedance	$\approx 50\,\Omega$
Cable	RG174
Connector type	BNC
Max. pressure	5 bar
Insertion loss	16 dB-12 dB

In general, the higher the ultrasound (US) frequency, the smaller the averaging volume, leading to improved spatial resolution. However, higher frequencies also increase signal attenuation as the US waves travel through the metal. In this case, due to the small dimensions of the setup, it was possible to select the highest available US frequency without significant drawbacks. More details regarding the physical mechanisms behind this are provided in Section 6.1.

The acquisition was performed using the DOP4000 system from Signal Processing, shown in Figure 2.5(b), chosen for its ease of use, sensor compatibility, and the ability to synchronize with external devices [130]. The positioning and use of the sensor in the various setups are described in Section 3.1.1 and Chapter 6, with further information on the complete measurement chain available in Section 2.4.

2.3.4 Hot Film Anemometry (HFA)

The sensor chosen for the tests is a particular probe made for measurement in water developed by DANTEC. Different providers were considered as main suppliers, e.g., AREMCO, BUKO, TSI, but DANTEC was considered the best in terms of quality-price, customer support, and reliability. The specific DANTEC probe chosen is the 55R14, reported in Figure 2.6(a).

(a) 55R14 hot film probe (b) StreamLine DANTEC system 90CN10/C10

Figure 2.6 - *Sensor and acquisition system chosen for the velocity measurements (HF).*

As shown in Figure 2.7, the probe consists of three layers, with the sensitive part being the middle one consisting of a thin film from which the name is derived.

In fact, fiber-film probes have cylindrical thin film sensors and may be used as a substitute for wire probes in liquids or in gas applications where probes more robust and less sensitive to contamination are needed.

The sensor has a core of quartz fiber with a diameter of 70 µm and it is 3 mm long in total. It is covered by a nickel-thin film of approximately 0.1 µm in thickness obtained by cathode sputtering providing an effective sensitive length of 1.25 mm.

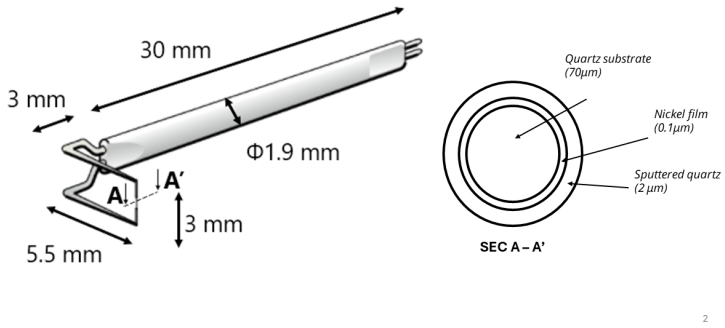

Figure 2.7 - *Dimensions of the hot film used for this study*

With this technique, the film forms in a continuous process and results in a homogeneous thin film of high purity and good adherence to the substrate. The films have high-temperature coefficients of resistance and possess high mechanical and electrical stability.

Above this, another layer of quartz with a thickness of 2 µm is sputtered to provide electrical insulation and oxidation protection, increasing the robustness of the probe. The ends are copper and gold plated and the fiber is soldered onto the prong ends. Being made for water applications (i.e., for conductive liquids), the joints and the prongs are lacquer-coated soldered to obtain perfect electrical insulation from the surroundings [59]. A summary of this information is reported in Table 2.5.

The particular 90° geometry was considered the best to be coupled with the temperature sensors in the cavity. In fact, the sensor is turned 90°, making the probe suitable for measurements in places that are not easily accessible otherwise. On the other hand, the probe will be used with the prongs perpendicular to the main flow direction, which is not recommended due to the potential for prong vibrations that could affect the measurements. However, the low velocities encountered in the cavity are not expected to pose a problem in this regard. Moreover, the manual states that the most important point is that the calibration and the measurements are performed with the same relative orientation between prongs and flow [59]. The probe is declared to be suitable for measurements in conductive liquids up to 150 °C, from low to high velocities, and capable of measuring mean and fluctuations values [59]. The support used was the 55H21 from Dantec, with a length of 235 mm and a diameter of 4 mm from which a BNC cable of approximately 0.8 m connects the probe to the anemometer where the voltage signal is read [59].

As mentioned in 2.2.2, the output voltage of the hot film is obtained through the balancing of a Wheatstone bridge. The necessary circuitry and electronics are contained in the StreamLine DANTEC system 90CN10/C10 [131] and the acquisition was carried out by a National Instrument acquisition card NI9215 [132]. To

Table 2.5 - *Main characteristics of the Hot Film sensor used for this work*

Parameter	**Value**
Sensor material	nickel and quartz
Wire diameter D_w	70 µm
Wire length L_w	1.25 mm
Thickness of quartz coating	2 µm
Sensor resistance at 20 °C	7.715 Ω
Temperature coefficient of resistance	0.38 %/°C
Max ambient temperature	150 °C
Min. velocity	0.01 m/s
Max. velocity	10 m/s [a)]
Frequency limit (63% response)	30 kHz
Designed for	Water

a) The minimum velocity given here is the one recommended by the manufacturer for the use of the probe in water [59]. However, it is also declared that *if a probe is calibrated and used under the same orientation with respect to the gravity field, it may be used at even lower velocities.*, which is the case for this work. Moreover, such limitation is given by the onset of natural convection, therefore depending by several external parameters, e.g., the fluid used and the sensor over temperature. Calculations in this sense are extensively performed in Chapter 7.

run the measurements and set the correct parameters for the hot film, the software StreamWare Pro by DANTEC was used [131].

2.4 Turbulent heat flux measurements

Once suitable techniques for a specific application are selected, the additional challenge posed by the turbulent heat flux (THF) measurements is the need for simultaneous acquisition of velocity and temperature fluctuations at the same spatial point. As discussed in the previous sections, the various sensors not only have different intrinsic physical characteristics but also employ distinct acquisition systems to capture their respective signals. This necessitates a synchronization system that is precise enough to ensure that synchronization is maintained over the duration of acquisition (minimizing jitter). Additionally, the positioning of the sensors is crucial, as they must measure temperature and velocity at "the same point." This means they need to be sufficiently close to resolve meaningful turbulence structures, while also being spaced apart enough to prevent interference during measurements.

For this reason, this section reviews literature that examines velocity and temperature measurements in various fluids and setups. A summary of their main characteristics is presented in Table 2.6, highlighting the aspects most relevant to this work.

First, the table presents the fluid and experimental setup used in each study. Following that, the measurement techniques employed for velocity and temperature,

Table 2.6 - *Summary of the literature review for the turbulent heat flux measurements. The table includes the fluid and setup used, the measurement techniques employed for velocity and temperature along with their acquisition frequencies, and addresses key aspects of the synchronization issue between the different systems and the spatial distance between the sensors.*

Reference	**Setup**	**Fluid**	**Velocity**		**Temperature**		**Synch.**	**Spatial**
			Tech.	**Freq.**	**Tech.**	**Freq.**		**Distance**
Das et al. [133]	DHC a)	Air	PIV	X	TC	X	X	X
Zwirner et al. [50]	DHC	GaInSn	UDV	X	TC	X	X	X
Belleoud et al. [139]	DHC	Air	PIV,LDV	X	TC	X	X	X
Ivey [140]	DHC	Water	PIV	X	NTC	X	X	X
Godaux [135]	VC b)	Water	HW	X	TC	X	X	X
Laube et al. [141]	Pipe	GaInSn	Coriolis, MID	X	TC	X	X	X
Leporini et al. [134]	DHC	Air	PIV	6.1 Hz	TC	X	X	X
Aubert et al. [32]	RS c)	Water	PIV,LDV	1500 Hz	RTD	X	X	X
T Caudwell [142]	DHC	Air	PIV	1 Hz	T-LIF	1 Hz	X	X
A. Weppe [136]	DHC	Air	PIV	25 Hz	TC	20 Hz to 40 Hz	X	X
Vliet and Liu [143]	VC	Air	HF	5 Hz	TC	5 Hz	X	1.27 mm
Schaub et al. [52]	BFS d)	GaInSn	PMP	500 Hz	TC	500 Hz	X	0.5 mm
Buckingham [144]	WT e)	He-Xe	HW	75 Hz	TC	75 Hz	X	1.5 mm
Omprakash et al. [145]	DHC	Water	PIV	5 Hz/X	TC	95 Hz	Setup	X
K.H. Sohn [146]	FP f)	Air	HW	2 kHz to 5 kHz	CW	2 kHz to 5 kHz	Setup	0.35 mm
Hishida and Nagano [147]	Pipe	Air	HW	6 kHz	CW	6 kHz	Setup	0.7 mm
Abu-Mulaweh et al. [148]	BFS	Air	LDV	10 Hz to 100 Hz	CW	10 Hz to 100 Hz	Postpro	2 mm
Eyler and Sesonske [149]	Pipe	Mercury	HF	0.1 Hz to 1000 Hz	CW	0.1 Hz to 1000 Hz	Setup	0.46 mm

a) Differentially Heated Cavity
b) Vertical Convection
c) Rotating Shaft
d) Backward Facing Step
e) Wind Tunnel
f) Flat plate

along with their respective acquisition frequencies, are outlined. The last two columns focus on critical aspects of this section: the synchronization between velocity and temperature measurements, as well as the spatial distance between the two sensors. It is important to note that not all columns can be filled with data from the literature due to various reasons. For instance, some studies focus on examining both temperature and velocity fields with varying objectives, such as average field characterization [32, 133, 134], analysis of boundary layer features [135], wall heat flux measurements [136, 137], and development of non-dimensional correlations [50, 138]. In such cases, detailed information on acquisition frequencies or sensor positioning may not be required.

2.4.1 Synchronization

Focusing on the synchronization aspect, it is noted that other authors interested in fluctuations or root mean square (rms) values either do not report details regarding sensor synchronization [139, 144] or utilize specific probes that can acquire both temperature and velocity through the same acquisition system, thereby simplifying the issue but not providing insights for the current study [142, 145–147, 149–151]. Some studies mention addressing synchronization issues in post-processing without specifying how [148]. The author believes that the synchronization issue should be resolved as much as possible during the setup and acquisition phase, with only minor refinements made in post-processing. Only one study has been identified that explicitly addresses this issue, using two different techniques (PMP and TC) for velocity and temperature measurements. However, a definitive solution has not been achieved, and thus the final calculation of turbulent heat flux remains incomplete [52]. In conclusion, the synchronization issue is not adequately addressed in the literature. For this reason, a specific measurement chain has been developed in this work, with its conceptual scheme presented in Figure 2.8. An external signal generator provides a 5 V signal that triggers both the UDOP system of the UDV and the NIcDAQ9178 system, which connects to the NI9212 (thermocouple) and NI9215 (hot film) acquisition cards. Once the signal is received, the acquisition starts, and each sensor operates independently until it is stopped manually or automatically, such as when a predefined number of samples is reached. Simultaneously, the FBG sensor is also acquiring data; however, due to limitations in the available hardware version, it was not possible to trigger the acquisition of this system externally (neither as a master nor a slave). Consequently, the FBG acquisition is initiated separately, and synchronization with the thermocouple signal is achieved post-acquisition using the cross-correlation function. While this method is not ideal, it was the only feasible option with the available equipment. Additionally, it is essential to consider two phenomena that could affect synchronization:

- **Delay at Start:** The fact that all systems are triggered simultaneously does not guarantee that the acquisitions begin concurrently. The inherent delays in both the electronics and software must be accounted for.
- **Jitter in Frequency Acquisition:** Jitter refers to small, unwanted variations or fluctuations in the timing of data sampling, which occur when the time

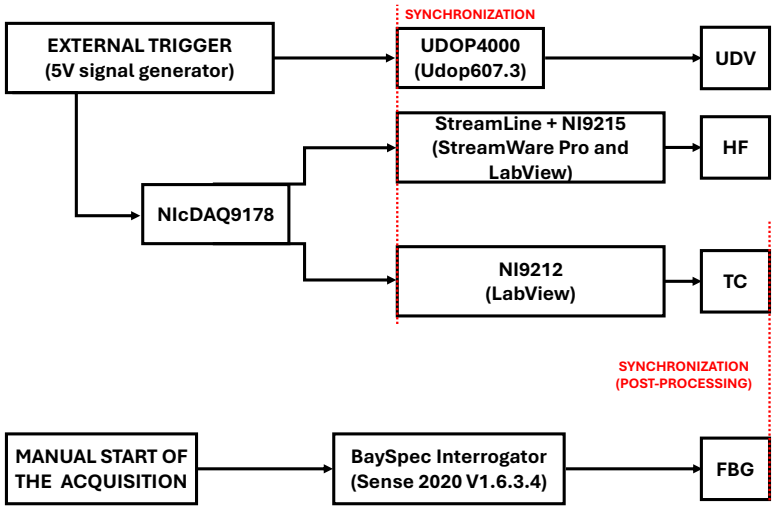

Figure 2.8 - *Scheme of the synchronization of the sensors. The thermocouple, the UDV and the hot film are triggered by the same external signal generator that allows to start the measurements all together. In particular, the thermocouple and the hot film also share the same acquisition software written in LabView. The FBG is working on a completely independent measurement chain and its signal is therefore synchronized in post-processing.*

intervals between consecutive samples deviate from their expected values. These variations can be caused by hardware imperfections, noise, or synchronization issues. In frequency acquisition, jitter can degrade the quality of measurements, leading to errors such as phase noise or signal distortion, which complicate the accurate reconstruction of the original signal or the execution of precise measurements.

When discussing synchronization, it is essential to compare these values with the required precision to evaluate their potential impact on the overall measurements. To illustrate this, a conceptual experiment has been conducted.

1. Consider a temperature signal and a velocity signal, both represented as sinusoidal functions: $T(t) = B\sin(\omega_1 t)$ and $U(t) = A\sin(\omega_2 t)$.

2. The resulting Turbulent Heat Flux (THF) can be estimated using the relation $THF = \rho c_P \overline{u'T'}$ where $u' = U(t) - U_{\text{mean}}$ and $T^{'} = T(t) - T_{\text{mean}}$.

3. The value obtained from this calculation is considered the true value.

4. Next, a delay is introduced in one of the two signals, and the THF is recalculated to compare it with the "real" value. An estimation of the error resulting from

this process as a function of the delay between the two signals is presented in Table 2.7.

Table 2.7 - *Delay and associated error on the THF value.*

Delay [ms]	**Error [%]** $\frac{\mathbf{THF}-\mathbf{THF}_{\mathrm{delay}}}{\mathbf{THF}}$
0	0
1	14
3	42
5	70
10	140

This means that if the two signals are delayed by, for example, 3 ms due to one of the aforementioned effects, the resulting error in the THF will be approximately 14%. Therefore, an investigation into the start delay and jitter effect of each acquisition system was conducted. The findings are summarized in Table 2.8.

Source	**Delay [ms]**
UDOP start delay	$< 10^{-3}$ [152]
UDOP jitter	Variable but negligible
NI start delay	$\approx 10^{-3}$ [127, 132]
NI jitter	50 ppm [127, 132]
BaySpec start delay	Unknown
BaySpec jitter	Variable but negligible

Table 2.8 - *Delay and jitter values for different sources.*

It is important to note that the values reported without a reference were obtained through direct meetings or email exchanges with the hardware provider. Based on these values, it was possible to estimate the accumulated delay after a certain number of samples. Assuming an acquisition frequency of 100 Hz, which is consistent with the requirements outlined in Section 2.1 and the limitations of the equipment, the cumulative delays listed in the table would phase out the signals by 5×10^{-3} Hz with each sample. This indicates that a total delay of 1 ms accumulates after approximately 2000 samples, which corresponds to 20 s of acquisition time, setting a maximum continuous time of acquisition. It should be noted that this calculation is quite approximate, as some delays depend on the specific PC used for the acquisitions and cannot be accurately estimated a priori. Nonetheless, this simple calculation provides a rough estimation of the effect.

2.4.2 Positioning

The positioning of the sensors has been approached differently by various authors. Some studies did not focus on obtaining local measurements of the flow and consequently did not address the issue at all [32, 133, 134]. Many of the papers mentioned employ optical techniques for velocity measurements, such as PIV or LDV [136, 139, 140, 142, 145, 148]. For these techniques, the positioning of the probe is not a concern; instead, it is essential to establish the correct field of view and the addition of a temperature sensor does not pose any problems.

Scientific publication describing the use of two separate probes for temperature and velocity measurements typically report distances ranging from 0.35 mm to 2 mm [52, 143, 144, 148–151]. Some of these studies do not provide insights into their chosen distances [143, 144], while many others indicate that their choices were constrained by manufacturing limitations [148–151]. Notably, only one paper addresses the issue more rigorously, offering considerations about the distance between probes and the turbulence scales that can be resolved with such a setup [52], employing similar calculations as those presented in Section 2.1. It is important to note that the distances reported in the literature cannot be directly translated to the requirements for the present work.

In this study, the temperature sensors were positioned with their sensitive elements located at the very tip, as illustrated in Figure 2.9(a). The sensors were secured within a ceramic support tube, as schematized in Figure 2.9(b).

The ceramic tube, purchased from *frIatec*, was selected for its thermal properties, which do not affect the time response of the sensors and effectively insulate them from one another. Additionally, its chemical inertia makes it suitable for use with liquid metals. Moreover, it also acts as a mechanical support for the FBG reducing possible bending effects along the fiber while keeping the sensitive part outside without interference. The tube features two holes with a diameter of 0.5 mm to accommodate the two sensors. The external diameter of the tube is 2 mm, with the sensors positioned 1 mm apart. The length of the exposed tip is 2 mm, which has been shown to prevent any secondary effects while still reliably measuring the temperature [153]. When combined with the Hot Film sensor, the setup is illustrated in Figure 2.10(a).

The sensors were positioned as close together as possible to meet the spatial resolution requirements outlined in Section 2.1. This close placement was facilitated by the specific design of the sensors, such as the 90-degree bend of the hot wire. However, placing the sensors too closely can lead to mutual interference, a concern that is explored in detail in Chapters 5 and 7. As a final remark, it is noteworthy that, regardless of the distance between sensors, the literature lacks discussion on the potential disturbing effects one probe may have on another. This issue is specifically addressed in this work in Section 7.6. Similarly, the acquisition frequencies of the two sensors are also a critical consideration. If the sensors operate at different frequencies, the method for combining these signals to calculate the final value of the turbulent heat flux must be carefully considered. In this study, undersampling the higher frequency signals has been implemented as a viable solution. While this approach does result in a loss of information, oversampling the lower frequency signal through interpolation would have led to unacceptable approximations and extrapolation errors.

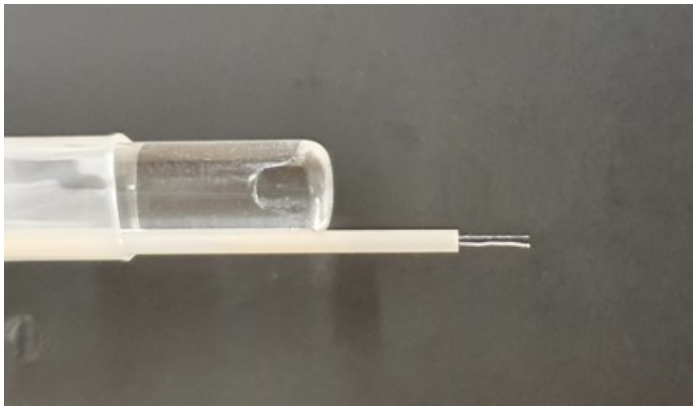

(a) FBG (top) and TC (bottom) glued inside the ceramic tube. Picture taken by the author before the start of the experimental campaign.

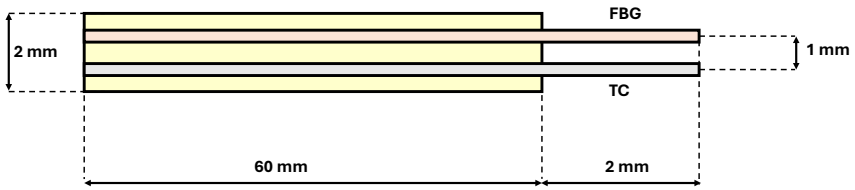

(b) Schematic of the two sensors in the ceramic tube

Figure 2.9 - *Positioning of the temperature sensors during the measurements with a schematic showing the key dimensions.*

2.5 Conclusions

To conclude this Chapter, this Section provides a summary of the key findings. Firstly, turbulence phenomena were investigated in Section 2.1 through a comprehensive literature review, DNS simulations, and theoretical calculations, which demonstrated overall good agreement among the various estimations. The characteristics of the targeted turbulence fluctuations have been gathered and are summarized in Table 2.9.

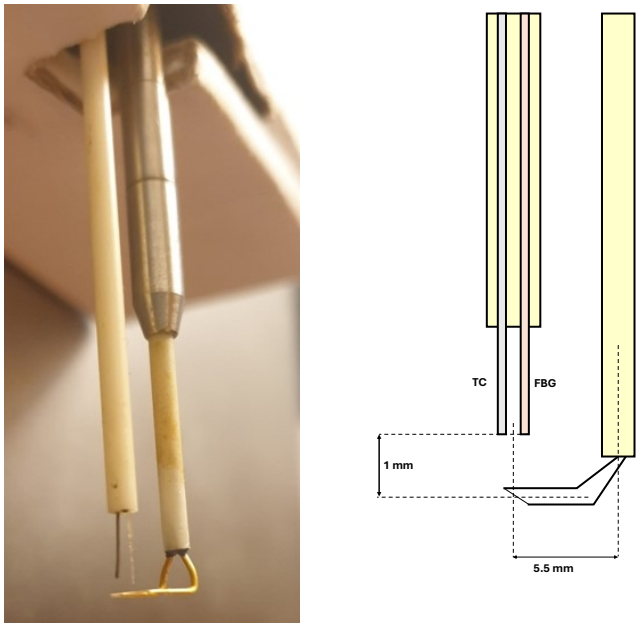

(a) HF+TC+FBG (b) Schematic of the configuration

Figure 2.10 - *Sensor positioning of the hot film, TC and FBG on the same support. The key dimensions and distances are highlighted in the schematic.*

Table 2.9 - *Turbulent structures characteristics*

Variable	Frequency	Amplitude	Dimension
Temperature	$\approx 60\,\text{Hz}$	$0.5\,^\circ\text{C}$ to $1\,^\circ\text{C}$	$\approx$ mm
Velocity	$30\,\text{Hz}$ to $60\,\text{Hz}$	$\approx$ mm/s	$\approx$ mm

It is crucial to note that these values represent estimations that may not be precise. However, they serve as a valuable foundation for understanding the targeted phenomena. Based on these estimations, sensors that are theoretically suitable for the measurements have been selected, and the choices are summarized in Table 2.10.

It is important to emphasize that these values should not be interpreted as definitive truths but rather as indicative of the capabilities of the equipment and its inherent limitations.

Additionally, in Section 2.4 a general assessment was performed concerning the positioning of the sensors and the synchronization of their measurements. All sensitive parts of the sensors were placed within a volume $< 1\,\text{mm}^3$ to meet the spatial resolution requirements. Furthermore, the error caused by non-synchronization and sensor jitter limited the maximum continuous acquisition time to approximately 1 min.

Table 2.10 - *Summary of the sensors and acquisition systems chosen with their spatial (Δx) and temporal (Δt) resolution*

Sensor	Model	Acquisition	Δx	Δt
TC	Sheathed type K, Ø0.250 mm	NIcDAQ9178 + NI9212	$\approx 0.02\,\text{mm}^3$	$\approx 10\,\text{ms}$
FBG	in-house made, Ø0.125 mm	BaySpec WaveCapture Interrogator	$\approx 0.05\,\text{mm}^3$	$< 10\,\text{ms}$
UDV	TR0805LS - TR1005LS	DOP4000	$2\,\text{mm}^3$ to $16\,\text{mm}^3$	$\approx 15\,\text{ms}$
HF	55R14	NIcDAQ9178 + NI9215 StreamLine 90CN10/C10	$\approx 0.02\,\text{mm}^3$	5 kHz to 10 kHz

After this duration, the sensors should be stopped and restarted to restore synchronization. This procedure allows to maintain effective synchronization while accurately measuring the targeted phenomena.

The selected approaches are expected to effectively address the measurement objectives. Although challenges may arise during the process, the proposed methods should be adequate for capturing the necessary data. The actual performance of the various sensors in different environments, as well as the true characteristics of the phenomena observed in liquid metal flows, will be evaluated in the subsequent Chapters aiming at the characterization of the different techniques.

Chapter 3

Experimental setup and procedures

Following Chapter 2, where the selected measurement techniques were presented, in this Chapter a detailed description of the experimental setup used for the investigation is provided in Section 3.1, including the main design choices. The procedures developed and adopted for its operation are then described in Section 3.2, with a particular focus on the attentions needed for the use of GaInSn in the lab in Section 3.3. Eventually, a detailed analysis of the experimental boundary conditions is reported in Section 3.4. Natural convection was selected as the primary flow regime due to the scarcity of validated turbulent models for natural convection and the critical need for experimental data in this regime, as exposed in Chapter 1. Additionally, natural convection offers advantages in terms of lower expected turbulent frequencies and operational simplicity [12]. In literature, mainly two types of heated cavities have been used for natural convection studies:

- Differentially heated cell: one vertical side of the cell is maintained at a constant higher temperature compared to the opposite side, while all other sides of the cell are adiabatic or subjected to constant heat flux. Gravity is considered and parallel to the active walls. [154–156]
- Rayleigh-Bénard convection cell: the bottom side of the cavity is maintained at a constant higher temperature compared to the top side with the gravity vector perpendicular to the active walls [33, 155, 157]

The flow features are different between the two cases, and the former setup has been chosen for the current experiment. Given the relatively limited research on this configuration [30, 155, 158] and the potential for novel findings on transitional Gr and Ra numbers, 3D turbulence patterns and boundary layer development, the author believes that a focused investigation in this area has significant potential to advance scientific knowledge. Moreover, this setup is more relevant to real-world engineering and industrial applications, such as natural ventilation in buildings, nuclear reactor safety, crystal growth, and geophysical flows [154, 155, 159].

3.1 Setup design

The differentially heated cavity employed in this study is presented in Figure 3.1 together with a schematic useful to highlight some of its main characteristics. This

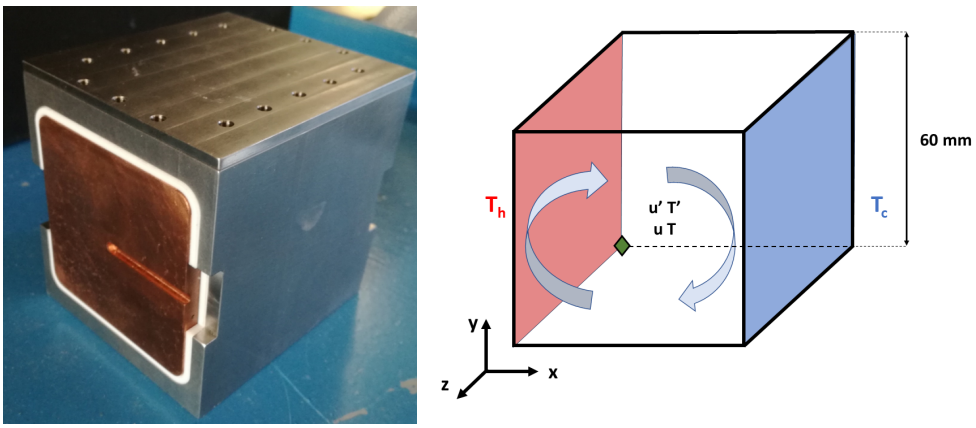

(a) Stainless steel cavity used as main experimental setup

(b) Schematic of the experimental setup

Figure 3.1 - *On the left, the cavity used for the experiments. One of the two copper plates used as active wall is visible. On the right, a schematic of the differentially heated cavity where the origin of the reference system is indicated by the green diamond. The left side (red) is kept at a hot temperature T_h while the cold side (blue) at the cold temperature T_c. The established temperature difference in the cavity initiates a buoyancy-driven natural convection flow. The characteristics of the flow strongly depend on the regime and the fluid employed.*

configuration usually results in a flow with characteristics similar to the isothermal vertical plate on its active walls, and for this reason, it is also referred to as vertical convection (VC) in some literature [50]. Inside the cavity, the imposed temperature difference triggers a natural convection loop rotating in the direction from the warmer side towards the colder side [154] with secondary oscillatory flows that can appear in the corners [155]. The flow inside the cavity can go through laminar and stable regimes to unsteady and turbulent, strongly depending on the working fluid, the geometry of the setup and the imposed flow regime [27, 28, 154, 155]. In all cases the main features of the flow are driven by the following non-dimensional numbers as defined in Equations (3.1) to (3.3):

$$Pr = \frac{\nu}{\alpha} \tag{3.1}$$

$$Gr = \frac{g\beta\Delta T L_c^3}{\nu^2} \tag{3.2}$$

$$Ra = Gr\,Pr = \frac{g\beta\Delta T L_c^3}{\nu\alpha} \tag{3.3}$$

- Prandtl Number Pr: it characterizes the relative thickness of the velocity boundary layer to the thermal boundary layer. It is defined as the ratio of momentum diffusivity (kinematic viscosity) to thermal diffusivity.
- Grashof Number Gr: it represents the ratio of buoyancy forces to viscous forces within the fluid. It is a key parameter in natural convection problems, indicating the strength of the buoyancy-driven flow. Higher values of Gr signify stronger buoyancy forces relative to viscous forces, leading to stronger natural convection therefore promoting instabilities and leading to fully turbulent flows.
- Rayleigh number Ra: it is closely related to buoyancy-driven natural convection flows and is used to characterize the flow regime. When below a certain critical threshold, the flow remains laminar, and heat transfer is dominated by conduction. Once this threshold is exceeded, the flow becomes turbulent, and convection takes over as the primary mode of heat transfer. Consequently, for a specific fluid with a fixed Pr, the Gr can also be used as a threshold indicator for the onset of convection.

Previous studies in mercury and low Prandtl number fluids have shown a critical Ra of about 10^5 to 10^7 where the transition to turbulence in buoyant flows in natural convection driven cavities is expected [27, 28, 160, 161]. Moreover, this range of non-dimensional numbers is also relevant for the MYRRHA reactor, particularly for the mixing and stratification phenomena in the three-dimensional upper plenum [162].

Within the framework of this PhD thesis, experimental investigations were conducted in a cubic cavity made of 316L stainless steel, with an internal edge length of 60 mm as illustrated in Figure 3.1(a) and Figure 3.1(b). An aspect ratio of unity was chosen for this study to minimize experimental complexity and ensure predictable flow behavior. Previous research has shown that significant variations in the physical phenomena leading to the quasi-steady state of the flow can occur as the aspect ratio approaches a value of 3 [155]. The selection of the 60 mm edge length was primarily driven by the desire to create a compact and easily manageable experimental setup. Moreover, this dimension, in combination with the imposed temperature difference, allowed for the achievement of relevant non-dimensional parameters, as discussed further. However, it is important to acknowledge that other cavity dimensions could be considered for future investigations, as discussed in Chapter 9. The thickness of the stainless steel external walls was 15 mm, 15 mm and 13 mm respectively in the x, y and z direction. Figure 3.2 shows the full setup as it is used during the tests. The increased complexity of the setup, necessary to address all design and practical issues, is evident. Each part indicated in Figure 3.2 will be explained in detail in the following sections. Tests were performed with the use of two different working fluids, water and Galinstan. An overview of the main parameters of the setup in the two cases is reported in Table 3.1. Natural convection was established through heated/cooled Peltier elements from Laird Thermal Systems [164] capable of reaching a maximum heating power of 800 W and a maximum cooling power of 340 W supplied by an EA-PSI 9000 2U [165]. Cooling systems were added in contact with the Peltier elements to avoid overheating. On the hot wall, a fan supplied with 12 V in DC was installed (component number 6 in Figure 3.2) while on the cold wall, the water cooling system

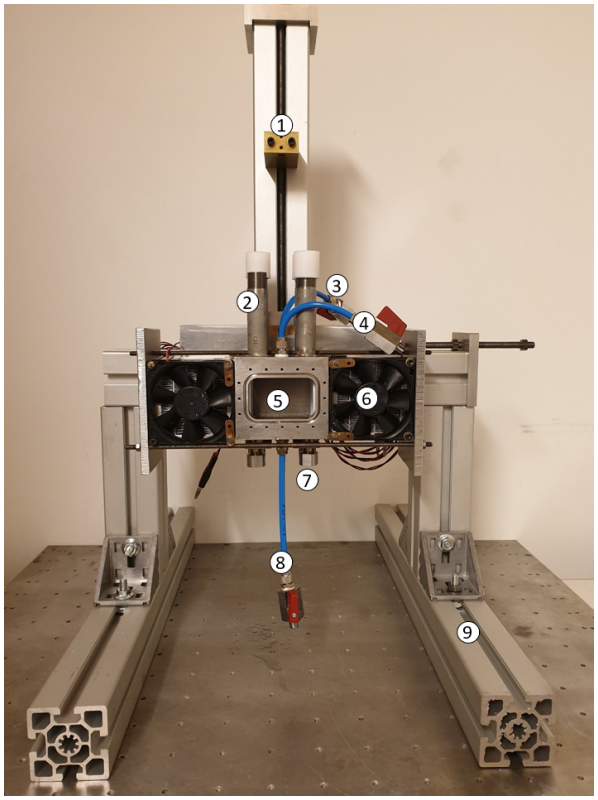

Figure 3.2 - *Natural convection setup: 1) Chariot for temperature instrumentation and hot film probe moved by an electrical Maxon Motor 110209 [163]; 2) TC + FBG + Hot Film access; 3) Valve to feed the fluid; 4) Valve to feed the inert gas; 5) Cavity 6) Fan; 7) UDV access; 8) Valve to empty the cavity; 9) Support; the whole setup is mounted on a optical table to ensure stability and precision during the measurements.*

shown in Figure 3.3 was chosen. This choice was made because the power dissipated on the cold side was much higher than on the hot side, due to the cooling system being in contact with the hot face of the Peltier element.

The two elements were positioned oppositely on each side of the cell in contact with two copper plates inserted in place holders in the cavity and supported by a Teflon structure visible in white in Figure 3.1(a). The high thermal conductivity of copper (390 W/(m K), one order of magnitude higher than the one of the stainless steel and the GaInSn) was enough to guarantee the desired isothermal conditions on the opposed walls as shown in Appendix B.1. The copper walls were coated with a 1 µm carbon coating deposited through magnetron sputtering at the University of Namur to ensure material compatibility during future tests with liquid metals (see Section 3.3.1). The following characteristics mainly led to its choice:

Table 3.1 - *Characteristics of the setup for the two different fluids used*

Parameter	Water	Galinstan
L_c (Characteristic length)	60 mm	60 mm
α (Thermal diffusivity)	$1.56 \times 10^{-7}\,\mathrm{m^2/s}$	$1.24 \times 10^{-5}\,\mathrm{m^2/s}$
β (Thermal expansion coefficient)	0.000 457/K	0.000 123/K
ΔT (Temperature difference)	50 K	42 K
ν (Kinematic viscosity)	$5.27 \times 10^{-7}\,\mathrm{m^2/s}$	$2.84 \times 10^{-7}\,\mathrm{m^2/s}$
Pr (Prandtl number)	3.4	0.021
Gr (Grashof number)	1.8×10^8	1.4×10^8
Ra (Rayleigh number)	6×10^8	3×10^6

- Max temperatures reachable: for this application, no more than 100 °C is needed but this coating can withstand up to 400 °C.
- Thermal conductivity: the added layer will increase the thermal resistance of the wall. However, due to its small thickness, it has been calculated that the thermal resistance of the layer will be in the order of 10^{-6} K/W and when compared to the one of the copper 10^{-2} K/W it will reasonably give negligible effects on the heat transfer properties of the wall.
- Electrical insulation: the chosen solution is not electrically conductive.
- Wettability: previous studies say that wetting is an issue with GaInSn but there is no reason to think that this particular coating should worsen the situation [166, 167].

The working fluid (either water or GaInSn) was fed through an opening on the top wall controlled by a ball-valve directly linked to a container filled with the fluid (component number 3 in Figure 3.2). Another ball-valve placed on the bottom of the cell was instead used to empty the cavity (component number 8 in Figure 3.2). One last ball-valve was used to feed Nitrogen used to work in low-oxygen environment during the liquid metal experiments (component number 4 in Figure 3.2) and this inlet was directly connected to a Nitrogen tank. More details about the procedures implemented for the use of all these valves are given in the following Sections.

3.1.1 Access for instrumentation

An important aspect of the experiment design was ensuring access for the instrumentation, as shown in Figure 3.2. In such a small setup, finding the optimal compromise between the available space and the ideal locations for the sensors is challenging, and practical implementation and manufacturing can be complex even once the best compromise is identified. Access for the instrumentation was meticulously designed based on previous Direct Numerical Simulations (DNS) performed in GaInSn [30], with details provided in Chapter 4. The simulations showed that the higher intensities in terms of THFs are concentrated close to the active walls, in particular in the upper part of the hot plate and and the lower part of the cold plate in a range of 5 mm from

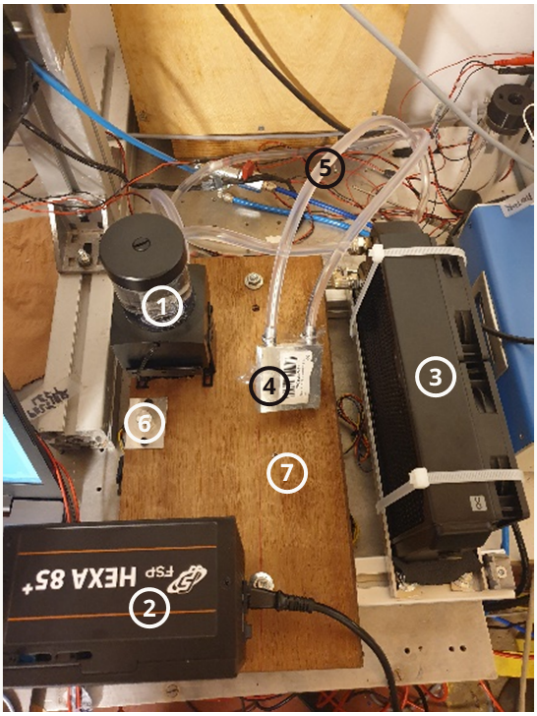

Figure 3.3 - *Water cooling circuit for the cold side Peltier element: 1) Water reservoir and water pump; 2) Controller and power supply 3) Fans for a max dissipation power of* 1000 W *4) Hollow alluminium plate to allow the flow of water. This part is in direct contact with the hot face of the Peltier element; 5) Water pipes connecting the plate (4) and the fans (3); 6) Control knob for the pump and the fans; 7) Wood support. The fan on the right side was replaced with this system.*

the hot/cold wall, as shown in Figure 3.4(a). The same distribution can be retrieved for the temperature fluctuations.

It is clear that close to the active walls the turbulent phenomena are more accentuated and the higher amplitudes reached by temperature and velocity are also easier to measure. Therefore, these are the most interesting zones where the sensors should be placed. Figure 3.4(b) gives a better overview of the four different locations where measurements of velocity and temperature are possible. The x and z coordinates of the measurements are limited to 4 combinations while the y direction is in principle fully accessible by all the sensors. The experimental access points were therefore placed in this range, in particular at $x = 4\,\text{mm}$ and $x = 56\,\text{mm}$, i.e., at a 4 mm distance respectively from the hot and cold wall. Such a distance was chosen as a compromise between the suggestions from the DNS simulations—which indicated that the most interesting phenomena were occurring within 5 mm of the active walls—and practical constraints. In fact, the UDV sensor described in Section 2.3.3 had an external diameter of 8 mm. To avoid overlap between the sensor and the wall, which would

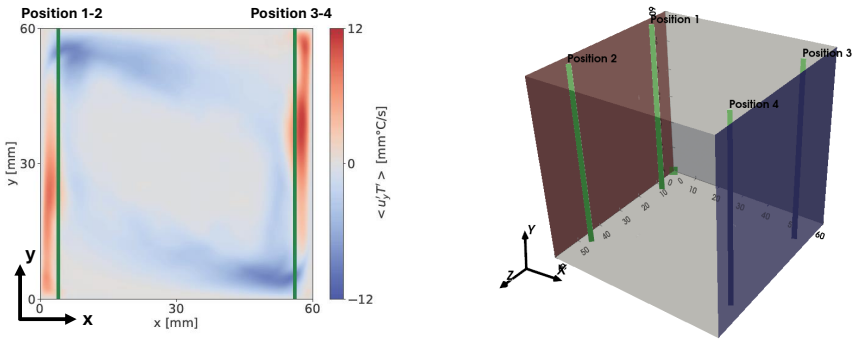

(a) Section $z = 12\,\text{mm}$

(b) Schematic of the setup and the 4 instrumentation access points.

Figure 3.4 - *On the left, a section of the turbulent heat flux field as calculated by the DNS [30] is shown. The two visible instrumentation access points are highlighted by the green lines. More details about these simulations are given in Section 4.3 On the right, a 3D schematic of the natural convection setup is reported. The green dot indicates the origin of the reference system whose axes are shown on the bottom left. The hot and cold walls are respectively indicated with red and blue colors. The four green lines represent the locations where measurements are possible, meaning that every sensor has access to every point on each line. The distance from the hot/cold wall of each green line is* 4 mm*, while the distance from the insulated walls is* 12 mm

have negatively impacted the measurements, it was necessary to position the sensor at this distance. Consequently, the entire setup was designed to allow all sensors to measure at this same distance. Moreover, the space from the adiabatic wall, i.e., the z coordinate, was chosen to ensure that the flow was not affected by the presence of the wall themselves. In particular, $z = 12\,\text{mm}$ and $z = 48\,\text{mm}$ were chosen, i.e., a 12 mm distance from the two opposed adiabatic walls.

For the sake of clarity, a picture of the inside of the cavity with the temperature sensors is shown in Figure 3.5.

The access for the temperature sensors (TC and FBG) and the hot film was guaranteed from the top, while the UDV was flush-mounted on the bottom wall. In this way, the UDV could acquire the profile of the y-component of the velocity while the other sensors could move along the vertical line through the moving chariot. At the same time, the UDV is placed such that the axis of the cylindrical sensor (i.e. the center of the ultrasonic beam) is in correspondence with the temperature sensor tip so that the last meaningful point of the velocity profile measured by the UDV coincides with the point where the temperature sensors acquire data. In this way, the theoretical need of measuring temperature and velocity at the same location to obtain the THF was satisfied the best way possible. The vertical movement of the probes is ensured by a Maxon stepper Motor 110209 [163] placed on the top of the

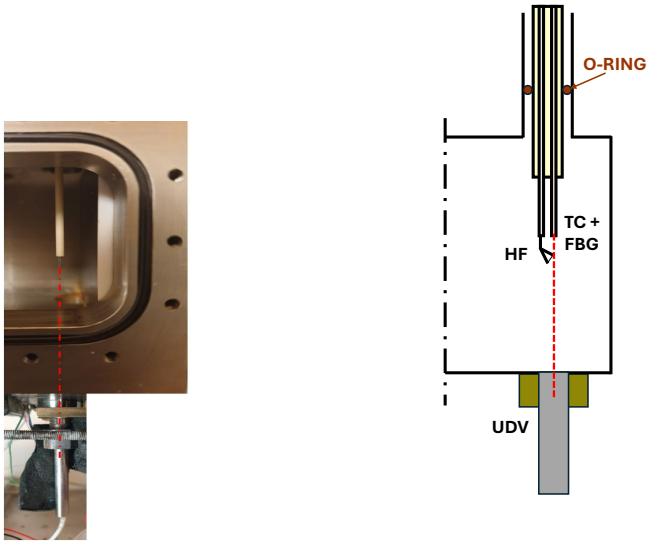

Figure 3.5 - *On the left, a section of the cavity with the temperature sensors inside and the UDV flush-mounted in the bottom. The hot film probe is attached to the same support as the temperature sensors but it is not shown in this figure. On the right, a schematic of the same setup with the hot film included.*

cell. The motor is controlled by a control system developed in the VKI and controlled by a LabView software. The system allow the vertical movement of the probes with a resolution lower than 1 µm. Since four ingresses were provided in the bottom of the cavity but only two UDV sensors were available, the other two ingresses had to be closed. For this purpose, a stainless steel bar with a thermocouple glued inside was used. This setup allowed the bar to be flush-mounted on the cavity floor, providing the evolution of temperature in the stainless steel, which corresponded to the zero point of the temperature profile acquired inside the cell.

3.2 Filling procedure and leaks

As discussed in Section 3.3.2, maintaining the purity of GaInSn, specifically ensuring it remains free of oxides, necessitated additional modifications to the cavity. To achieve a low-oxygen environment, it was decided to operate within a nitrogen atmosphere at a pressure slightly above ambient (approximately 1.2 bar). This configuration was chosen to allow any potential leaks to expel and prevent the ingress of oxygen into the setup.

To ensure the effectiveness of this approach, it was crucial to first verify the leak-tightness of the setup. A preliminary test was performed using water at 20 °C, during which no liquid leaks were detected from the cavity. Given that the surface tension of water at 20 °C is 72.8 mN/m and the surface tension of GaInSn at 58.5 °C is

590 mN/m, it can be confidently assumed that no leaks of GaInSn will occur during operation. Additionally, the dynamic viscosity of GaInSn at 58.5 °C is 1.85 mPa s, while the dynamic viscosity of water at 20 °C is 1.0518 mPa s. Therefore the leak rate in GaInSn is expected to be slower than in water [168].

Ensuring gas tightness proved to be significantly more challenging. The cell is equipped with three separate access points for valves, which can be utilized for either gases or liquids. Among these, one top access was designated for introducing and removing the inert gas (Nitrogen). The initial step involved creating a low-oxygen environment. This was achieved by evacuating the air from the cell using a vacuum pump and subsequently refilling it with Nitrogen at a pressure of 1.2 bar. This process was repeated at least three times to ensure the lowest possible oxygen concentration. Following this, it was crucial to assess how gas leaks might impact the pressure within the cavity. For this purpose, the pressure decay equation was used as a reference, as expressed in Equation (3.4) [168]:

$$\Omega = V \frac{\Delta p}{\Delta t} \tag{3.4}$$

Here, the leak rate Ω mbar L/s is related to the pressure drop Δp, the volume V, and the duration of the test Δt. Various approaches can be taken with this equation depending on the chosen parameters as inputs and outputs. In this case, the target pressure for the experiments was set at 1.2 bar inside the cavity. The pressure evolution was monitored over time with samples taken every 30 min. Given the cavity volume of 0.216 L, the gas flow rate was estimated to be approximately 1×10^{-3} mL/s, which also provided an estimate of the gas consumption. Additionally, the test indicated that it would take nearly 5 h for the pressure to drop from 1.2 bar to ambient pressure (1 bar). This duration is sufficient for conducting a complete experiment without the need for gas refilling during the test. The whole procedure and the outcome is discussed in more details in Appendix B.2.

Another important step in preparing the setup for operations was filling the cavity. Water did not pose any issues; however, transferring GaInSn from its original container to the experimental setup required careful handling to minimize exposure to air. The liquid metal was first transferred to a syringe, ensuring the suction point was not too close to the free surface where oxides had already started forming. The syringe was then connected to the top valve, and GaInSn was introduced into the cavity by slowly pushing it out of the syringe to avoid to incorporate air bubbles that could damage the instrumentation. To remove GaInSn from the cavity, the same syringe was connected to the bottom valve, which, when opened, allowed the GaInSn to flow naturally into the syringe.

It is to be noticed that all the instrumentation accesses described in Section 3.1.1 were proven to be leak-tight in order to sustain vacuum and the consequent nitrogen filling at 1.2 bar. The sealing was maintained also during the vertical movement of the instrumentation thanks to nitrile butadiene rubber (NBR) O-rings with specific diameters. While a measurement was performed, all the other 3 non-used instrumentation ingresses on the top were kept closed with a plastic cap.

3.3 Galinstan

While the preliminary tests of the project were carried out with distilled water, the following and most important ones used GaInSn as working fluid foreseeing LBE as future and final stage of the project. This low melting point liquid metal (LMPLM) is liquid at ambient temperature, presenting properties similar to mercury but with the big advantage of being not toxic and therefore not presenting major safety issues [169]. Thanks to its characteristics, it is often used in scientific works concerning liquid metals and electronics [170–172] and therefore reliable papers have been found addressing its properties [23, 173, 174] and general behaviour [175]. Its thermophysical properties calculated for an average temperature of 50 °C are reported in Table 3.2 and Appendix C but full relationships as function of temperature are available in literature [23, 173].

Table 3.2 - *Main thermophysical properties of Galinstan at* 50 °C

Property	**Value**
Thermal conductivity	$25.9\,\mathrm{W/(m\,K)}$
Dynamic viscosity	$1.86\,\mathrm{mPa\,s}$
Surface tension	$586\,\mathrm{mN/m}$
Density	$6329\,\mathrm{kg/m^3}$
Specific heat	$331\,\mathrm{J/(kg\,K)}$
Thermal expansion coefficient	$0.000\,123/\mathrm{K}$
Thermal diffusivity	$1.24 \times 10^{-5}\,\mathrm{m^2/s}$
Prandtl number (Pr)	0.021

It is particularly interesting to notice that its Pr number is extremely close to the targeted Pr of LBE $Pr = 0.025$.

3.3.1 Galinstan compatibility

Another factor to consider when working with liquid metals is the harsh environment, which is often exacerbated by the high temperatures required to maintain the liquid state. These conditions can lead to chemical corrosion and embrittlement phenomena. Even though working at low temperatures, i.e. $<100\,^\circ\mathrm{C}$, typically simplifies material selection since chemical reactions are less likely to occur or intensify, previous studies have identified some incompatibilities between GaInSn and other materials that still need attention[176, 177]. Compatibility with 316L stainless steel has been proved up to 200 °C [176]. Since the cavity is made of stainless steel 316L, no major compatibility problems arise for the walls of the cavity. The main issue is the use of copper plates as conductive materials for the active walls since even at ambient temperature copper tends to be corroded for an exposure time in the order of hours [176]. Several works solved the problem by coating the copper with nickel-chromium of different thickness [160, 177]. For instance, layers of 20 µm of NiP_{12} and 2 µm of chromium to prevent the material from dissolving in the GaInSn has been used [177], confirming previous findings that guaranteed compatibility between GaInSn and Ni−Cr up to 200 °C.

Unfortunately, in the cited studies, this layer was made by a local Swiss company whose name was not traceable anymore and therefore the same solution could not be adopted in this work. Other studies have addressed similar issues in mercury using 50 µm nickel-plated copper plates [160]. However, due to the different properties of the working fluid, this exact solution cannot be directly applied to GaInSn. Many companies have been contacted in order to ask for possible solutions. A summary of the possibilities taken into account is reported in Appendix A.1. In the end, as a compromise between cost and availability, the solution proposed by the University of Namur based on a carbon coating deposited through magnetron sputtering has been adopted (Section 3.1).

For the sake of completeness, a more general overview on material compatibility with GaInSn is also discussed here. Brass (CDA230), copper (CDA122), and aluminum (AL1100) cannot be used as they are corroded by GaInSn [176]. Additionally, gold, indium, nickel, platinum, and silicon should be avoided, with general corrosion increasing with temperature. Suitable coating layers for these metals include chromium, silver, or silicon carbide. Previous works have used graphene layers to separate GaInSn from Al. Similarly, layers of $Cr{-}C_{poor}$ (the most effective), Zr−C, and $Cr{-}C_{rich}$ have successfully protected Al, whereas Ti−C and Nb−C did not [176]. On the other hand, stainless steel (E-brite ferritic and austenitic), nickel-chromium alloys (inconel and hastelloy), titanium, and tungsten are compatible up to 200 °C. Regarding non-metal materials, they generally exhibit good compatibility. Specifically, acronitrile butadiene styrene (ABS), nitrile rubber (Buna N), and polyvinyl chloride (PVC) remain unchanged after GaInSn exposure at 25 °C, while acrylic, nylon, and Teflon remain unchanged after exposure at 100 °C [176]. Although previous studies were skeptical about compatibility with PTFE (and generally, plastics containing fluorine) [166], more recent studies (including this one) have proven compatibility at least up to 100 °C. The experimental setup used in this work employs 316L stainless steel for the main structure of the cavity, copper (coated) for the active walls, Teflon for the copper plate supports, and nitrile butadiene rubber (NBR) for the O-rings. All these materials were in direct contact with GaInSn for over 1000 h at temperatures reaching up to 80 °C and showed no signs of deterioration. Another issue worth mentioning with GaInSn is its wettability with various materials, which refers to its ability to maintain contact with a solid surface [166]. This behavior is governed by the balance between the adhesive forces between the liquid and solid, and the cohesive forces within the liquid. In the context of this thesis, wettability is particularly important for sensing, as proper coupling between the sensors and the fluid is essential for accurate measurements [178, 179]. Three main factors influencing wetting have been identified [166]:

- **Surface tension**: Higher surface tension of the liquid makes coupling with the solid more difficult, which is why wetting is often a challenge with liquid metals.
- **Solid surface**: High roughness or chemical interactions leading to oxidation of the solid surface can impede or worsen the wetting process.
- **Temperature**: Increasing the temperature generally facilitates the wetting process. Therefore, preheating the equipment is recommended when feasible.

In the framework of this thesis, it was not possible to adjust parameters like surface tension (since the liquid metal was predetermined) or solid surface (as probe characteristics were fixed by their design). Additionally, the setup and instrumentation were not designed to exceed 100 °C, limiting the ability to use temperature as a variable. As a result, the instrumentation was either lightly scrubbed with the liquid metal [166] or left in contact with the metal for several hours before use [58], both methods shown to be successful in previous studies.

3.3.2 Galinstan oxidation

A major issue with GaInSn is its fast oxidation that happens even with oxygen concentration below 1 ppm [175, 180–182] and in time ranges below 1 min [183]. Too many oxides can in fact affect the metal properties [167], the fluid behaviour [181] and ruin the instrumentation so their level must be kept as low as possible. On the other hand, some techniques like the UDV could even benefit from the presence of these oxides that seed the flow (see Chapter 6). Moreover, many studies in literature deal with microelectronics application of GaInSn therefore working with droplets of fluid and reasonably having big differences in fluid behaviour when too many oxides are present due to the high surface/volume ratio [175, 181]. Figure 3.6(a) shows the status of the setup after one full campaign where GaInSn was used. The oxides formed tend to adhere to the walls, making it impossible to continue testing without cleaning the setup. Fortunately, a 3 % solution of Mucasol©diluted in water effectively loosens the oxides. Simply filling the cavity with the solution and waiting a few hours allows the oxides to detach and be easily removed. For an even better result, cleaning with ethanol can be used as it evaporates more effectively than water. The chemical composition of the oxides is also still not fully clarified in literature. It is believed that most of them come from the oxidation of Gallium, therefore generating Ga_2O_3 and Ga_2O [171, 182] since other compounds like SnO_2 and In_2O_3 are not thermodynamically stable [182]. Some studies provide an empirical but effective description of gallium oxides, defining the oxide skin as a layer ranging from 0.5 nm to 2 nm [171, 181, 184, 185]. This oxide layer is visually indistinguishable from the pure fluid when the oxygen concentration exceeds 1 ppm [171, 186] and its formation is regulated by an irreversible diffusion process across the liquid surface affected by the presence of impurities in the liquid [185]. The thickness and aspect of such layer has not been seen to change when the oxidation was taking place at temperatures until 300 °C [184] while other studies conducted in $Ga_{0.93}$:$Hg_{0.07}$ seem to disagree finding thicker layers for temperatures between 83 °C to 122 °C [187]. Wetting issues were also addressed saying that the oxide skin can prevent the complete removal of liquid gallium alloys surfaces because it strongly adheres to most surfaces and does not allow the high surface tension of the liquid to keep the fluid intact [167, 188].

In previous literature studies, the best solution to this problem seem to be obtained with sofisticated gloveboxes capable of keeping oxygen and moisture levels below 1 ppm [175, 185]. Mainly because of time and budget limitations, it has been decided to adopt first cheaper and faster solutions trying to deal with the small amount of oxides that could form. For this reason, it has been decided to limit as much as possible the contact between GaInSn and air (i.e. oxygen). Some papers underline

(a) Cavity with GaInSn oxides (b) Cavity after cleaning with Mucasol©

Figure 3.6 - *When the bottom valve is opened to allow GaInSn to exit, the metal unavoidably comes into contact with air. Consequently, GaInSn oxides tend to form and adhere to the walls, necessitating thorough cleaning of the setup before it can be used again.*

the effectiveness of a hydrochloric acid vapor HCl used as a cover since in this case the surface oxide is replaced with other less intrusive alloys (e.g., $GaCl_3$ and $InCl_3$) [171, 182, 183, 189]. On the other hand, the toxicity of this gas would negate the primary motivation of replacing mercury with Galinstan [188]. Other works use acidified siloxane oils [183], electrochemical reduction methods [182, 190], ion exchange membranes [188] or even boiling deionized water [191] to remove the oxides and prevent their formation but the implications for this work in terms of complexity go beyond the scope of the project. Moreover, it is again important to notice that many of these applications actually deal with droplets of fluids therefore not guaranteeing the applicability of the same methods for larger scales. In conclusion, various techniques have been developed in the literature to address GaInSn and Ga oxides. The working principles of these techniques differ, making them not universally applicable to every situation and sometimes significantly increasing the complexity of the setup. In this work, the most feasible solution was identified as using an inert gas (Nitrogen) to fill the cell, maintaining the lowest possible oxygen concentration and necessitating to deal with the small amount of oxides that will inevitably form in the cavity. The typical Oxygen concentration in the 200 bar Nitrogen bottle used for the experiment was less than 0.01 ppm, therefore having a negligible impact on liquid metal oxidation.

3.4 Boundary conditions

To compare experiments with numerical simulations, it is essential to accurately assess the experimental boundary conditions. As noted in Section 3.1, natural convection was induced using Peltier elements from Laird Thermal Systems [164], with thermal coupling to copper plates ensured by a silicon-based thermal paste by Omega Engineering [192]. Determining the actual heat flux provided by the Peltier elements proved challenging due to the complex electronic control involved. The only known input was the electrical power supplied to the elements, which could typically be converted to heating or cooling power using datasheets. However, the expected hot face temperatures specified in the datasheet were not attainable under our experimental conditions. Consequently, a direct conversion between electrical power and heating power was not straightforward. As a result, empirical tests were performed in order to assess the real boundary conditions achieved during the tests.

First of all, since the approach was to rely on a single temperature monitoring point on each plate, it was important to make sure to have an uniform temperature over each copper plate. To do that, experiments with an infrared camera were performed and the main outcomes are shown in Appendix B.1. The copper plate was heated up (or cooled down) and the surface of the plate was recorded with the camera. A maximum gradient of 0.8 °C over the plate heated up at 80 °C was retrieved, but it went down to 0.2 °C when referring to the plate at 20 °C. Due to the high thermal conductivity of copper, monitoring could be limited to a single point at the geometric center of each plate.

Further tests in this sense were therefore performed in order to check if a proper steady state condition could be reached in the experimental setup. The experimental conditions were tested with water and GaInSn and the active elements were left running for several hours. One of the outcome of these tests performed with GaInSn is reported in Figure 3.7(a) and Figure 3.7(b). Figure 3.7(a) shows the evolution in time of the hot and cold copper plates of the setup over more than 3 h. The acquisition is shown when the cavity has already reached a steady state presenting an average $T_{hot} = 79.5\,°C$ and an average $T_{cold} = 37.5\,°C$, therefore giving an average fluid temperature of $T_{ave} = 58.5\,°C$. Over the time shown in the figure, T_{hot} and T_{cold} had a drift $< 0.01\,°C/min$. Figure 3.7(b) shows the resultant ΔT, which is considered the most critical parameter as it drives the flow. Since both T_{hot} and T_{cold} exhibited a small positive drift, the drift in their difference ΔT can be estimated to be even smaller than the one observed in each temperature individually. Consequently, considering that a single acquisition lasts no longer than 2 min, the conditions during the measurement can be regarded as steady.

It is worth emphasizing that in practice, the experimental boundary conditions will always fall somewhere between a constant heat flux and constant temperature [193], and it is impossible to precisely replicate it in a numerical simulations. In this sense, the thermal activity parameter K defined as in Equation (3.5) where f refers to the fluid and *wall* refers to the wall.

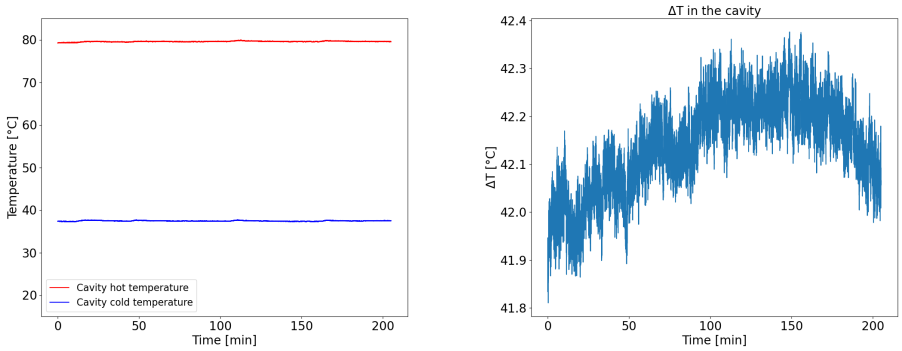

(a) Hot and cold temperature boundary conditions

(b) ΔT established in the cavity

Figure 3.7 - *Time evolution of the temperature boundary conditions during the measurements. These results were obtained with GaInSn as working fluid providing a total power of* 354 W *to the Peltier elements*

$$K = \sqrt{\frac{\rho_f c_{P,f} k_f}{\rho_{wall} c_{P,wall} k_{wall}}} \tag{3.5}$$

It can give a good indication of how much the oscillating temperature imposed in the boundary is propagating in the flow [25, 194, 195]. In particular, $K = \infty$ indicates an isoflux idealization with oscillating temperature boundary conditions while $K = 0$ refers to the isothermal idealization where $\rho_f c_{P,f}$ and k_f are negligible in respect of $\rho_w c_{P,wall}$ and k_{wall}. In literature, $K > 10$ is taken as a threshold value to establish if the temperature fluctuations at the wall are propagating in the fluid in numerical studies [25, 194, 195] and it is also strongly supported by several experimental works [195, 196].

In the case of this research, the value of K obtained with water and GaInSn considering copper as the active wall are respectively $K_{\text{water}} = 0.04$ and $K_{\text{GaInSn}} = 0.2$. Since both of them are close to zero, it is once again safe to assume that isothermal boundary conditions are reached during the tests.

The other issue regarding the boundary conditions is related to the remaining four adiabatic walls. Although adequate insulation is provided with a combination of Insulfrax©and aluminium foil, achieving perfect adiabatic conditions is challenging in practice especially when the temperature difference is increasing [155]. In fact, due to the many irregularities on the cavity surfaces, e.g., valves and openings for instrumentation, it was not possible to place effectively the insulation on every wall. As a result, the full adiabaticity of the cavity during the operations was not ensured. Consequently, some heat losses were anticipated from the setup, and an experiment was conducted to estimate the heat transfer coefficient. The cavity was initially heated to 90 °C and then filled with water at the same temperature. The cavity was then

allowed to cool down while the temperature of the water inside was recorded. The temperature evolution is reported in Figure 3.8.

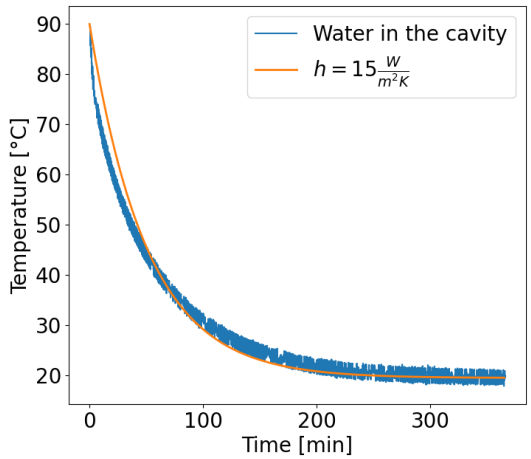

Figure 3.8 - *Time evolution of the temperature of the water inside the cavity. The system was brought to* 90 °C *and the temperature was recorded by a thermocouple in contact with the water.*

Based on the cooling law formulated by Newton (Appendix D) it was possible to estimate the value of τ and from that the resulting estimated convection heat transfer coefficient $h = 15\,\mathrm{W/m^2}$. For this calculation, the cavity was considered as a full block with properties calculated as the mass-weighted average of the water, copper and stainless steel. In particular, $m = 3.47\,\mathrm{kg}$, $c_P = 729\,\mathrm{J/(kg\,K)}$ and $A = 0.056\,\mathrm{m^2}$. The same experiment was repeated with GaInSn, delivering a slightly higher value of $h = 20\,\mathrm{W/m^2}$. It will be explained in Chapter 4 how these values will be handled in the numerical simulations.

3.5 Conclusions

In this Chapter, the rationale behind the choices made for the design of the experimental setup was analyzed, with a detailed explanation of the differentially heated cavity in Section 3.1. While not all choices were ideal, many were influenced by practical constraints related to manufacturing, accessibility of instrumentation, and compatibility.

Special attention was given to the handling of Galinstan in the lab treated in Section 3.3. Despite the increasing number of studies involving this material in recent literature, each experiment presents unique challenges, therefore requiring unique solutions. For this study, the implementation of a vacuum cycle and a nitrogen atmosphere to avoid the oxydation was adopted.

A thorough analysis of the boundary conditions was conducted in Section 3.4, as it was essential to establish a clear understanding of the experimental setup and the criteria for comparison with previous studies. This analysis will be particularly relevant when relating the outcomes to the numerical simulations introduced in Chapter 4. The primary objective of the CFD is to simulate conditions that closely approximate the actual experimental setup, considering acceptable to not simulate features like smooth corners, instrumentation accesses or insulation material. While this may limit the precision of the numerical results, it is acknowledged that simulating every detail of the setup is both complex and time-consuming. Therefore, the results must be interpreted with this in mind, and their reliability adjusted accordingly.

Chapter 4

Numerical setup and results

In fluid dynamics, numerical simulations are essential for predicting and analyzing fluid behavior. Two common approaches to simulating fluid flow are Reynolds-Averaged Navier-Stokes (RANS) and Direct Numerical Simulation (DNS), each with distinct advantages and limitations.

RANS is widely used for simulating turbulent flows due to its computational efficiency. By averaging the flow field over time, RANS simplifies the problem, though this approach introduces modeling assumptions that can lead to inaccuracies, especially in flows with complex configurations or unique properties, such as low Prandtl number fluids like liquid metals. Consequently, experimental validation is crucial to refine these models, ensuring that RANS can be effectively applied to such challenging cases.

DNS, in contrast, provides a more rigorous and accurate approach by directly solving the full set of Navier-Stokes equations without relying on modeling assumptions, thereby resolving the entire turbulence energy spectrum. This method yields highly precise results but is computationally demanding, limiting its use to simpler flow configurations.

In the framework of this thesis, numerical simulations serve as a vital tool for comparison with experimental results and estimation of quantities to be measured. This Chapter begins with a brief theoretical overview of the Navier-Stokes equations in Section 4.1. Following this, the specifics of the numerical domain are presented, detailing the assumptions made and the differences with the real experimental setup described in Chapter 3. Sections 4.3 and 4.4 then focus respectively on the DNS and RANS approaches, highlighting the codes used, the assumptions made, the meshing of the domain, and the different test cases available for comparison with experiments. Finally, Section 4.5 presents results comparing temperature and velocity fields, drawing conclusions on the reliability of both approaches.

4.1 Governing equations

The general governing equations of fluids motion are the Navier-Stokes equations as reported in Equations (4.1) to (4.3) in their vectorial form, representing respectively the continuity, momentum and energy equations [197, 198]:

$$\frac{\partial \rho}{\partial t} + \nabla \cdot (\rho \mathbf{u}) = 0 \tag{4.1}$$

$$\frac{\partial}{\partial t}(\rho \mathbf{u}) + \nabla \cdot (\rho \mathbf{u} \otimes \mathbf{u}) = -\nabla p + \nabla \cdot \boldsymbol{\tau} + \rho \mathbf{g} \tag{4.2}$$

$$\frac{\partial}{\partial t}(\rho E) + \nabla \cdot (\rho E \mathbf{u}) = -\nabla \cdot (p \mathbf{u}) + \nabla \cdot (\boldsymbol{\tau} \cdot \mathbf{u}) - \nabla \cdot \mathbf{q} + \rho \mathbf{g} \cdot \mathbf{u} \tag{4.3}$$

where:

- ρ is the fluid density,
- $\mathbf{u}$ is the velocity vector,
- t is the time.
- p is the pressure,
- $\boldsymbol{\tau}$ is the viscous stress tensor, defined as:

  $$\boldsymbol{\tau} = \mu \left[\nabla \mathbf{u} + (\nabla \mathbf{u})^T \right] - \frac{2}{3} \mu (\nabla \cdot \mathbf{u}) \mathbf{I}$$

  where μ is the dynamic viscosity, and $\mathbf{I}$ is the identity matrix. The first term corresponds to the symmetric part of the velocity gradient tensor, which represents the rate of strain in the fluid. The second term accounts for the isotropic contribution to the stress tensor due to fluid compression or expansion, assuming Stokes' hypothesis valid for Newtonian fluids, which states that the bulk viscosity is proportional to the dynamic viscosity, i.e., the contribution of the volume change to the stress is related to the mechanical pressure.
- μ is the dynamic viscosity,
- $\mathbf{g}$ is the gravitational acceleration vector.
- $E = e + \frac{1}{2}|\mathbf{u}|^2$ is the total energy per unit mass, which includes the internal energy e and kinetic energy,
- $\mathbf{q}$ is the heat flux vector, modeled as $\mathbf{q} = -k_f \nabla T$ with thermal conductivity of the fluid k_f and temperature T.

Moreover, some of the simulations reported here utilized Conjugate Heat Transfer (CHT) modeling, which simultaneously solves heat transfer in both solid and fluid regions. This approach captures the interaction between heat conduction in solids (e.g., walls) and convection in fluids at their interface, accounting for thermal coupling

at the solid-fluid boundary. In such cases, the heat conduction equation, as shown in Equation (4.4), is solved in the solid:

$$\rho c_{p,s} \frac{\partial T_s}{\partial t} = \nabla \cdot (k_s \nabla T_s) \tag{4.4}$$

where:

- ρ_s is the density.
- $c_{p,s}$ is the specific heat at constant pressure.
- T_s is the temperature field.
- k_s is the thermal conductivity.

Moreover, at the solid-fluid interface, the temperature and heat flux continuity conditions, expressed by Equations (4.5) and (4.6), are enforced for the temperature field, where n represents the direction normal to the wall.

$$T_f = T_s \tag{4.5}$$

$$k_f \frac{\mathrm{d}T_f}{\mathrm{d}n} = k_s \frac{\mathrm{d}T_s}{\mathrm{d}n} \tag{4.6}$$

The equations solved in the different numerical simulations are based on these fundamental equations, with additional simplifications introduced in each approach. These simplifications are further explained in Sections 4.3 and 4.4.

4.2 Numerical domain

The domain considered for the numerical simulations is a three-dimensional space that closely simulates the experimental setup described in Chapter 3. Not all elements were modeled in detail. Thus, a compromise had to be made between the simplicity of the simulations, including computational time, and the reliability of the results.

A schematic illustrating two views of the domain as utilized in the numerical simulations is presented in Figure 4.1.

While the main characteristics of the setup are represented, such as the presence of the different walls and the fluid with their correct dimensions, certain elements were omitted in the schematic. For instance, the stainless steel tubes at the top of the cavity, which are used for instrumentation access (as shown in Figure 3.2), were not simulated, nor was the support required for the UDV access from the bottom. Additionally, the Teflon holder of the copper plates, which separates the copper and stainless steel reducing the heat conduction between the two, was also not taken into account. The implications of these assumptions are analyzed in Chapter 8 during the comparison with experimental results.

Another important aspect to consider is that not all simulations presented here employed the Conjugate Heat Transfer method. In those cases, the solid walls, specifically the copper and stainless steel depicted in Figure 4.1, are not simulated, and the

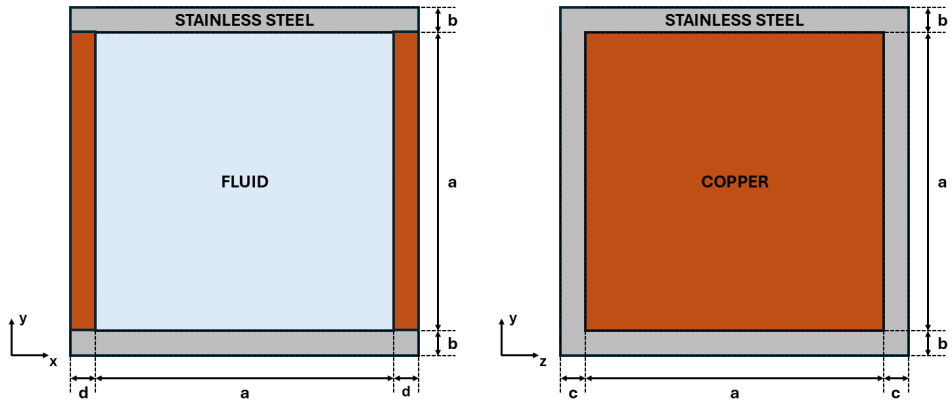

(a) Section of the cavity in the xy plane at $z = 30\,\text{mm}$

(b) Section of the copper plate in the yz plane at $x = 0\,\text{mm}$

Figure 4.1 - *Schematic of the numerical domain with* $a = 60\,\text{mm}$, $b = 13\,\text{mm}$, $c = d = 15\,\text{mm}$. *The fluid indicated can be either water or GaInSn, according to the simulation carried out.*

simulations are conducted solely within the fluid volume. This distinction is significant when setting the boundary conditions. In instances where the Conjugate Heat Transfer method is utilized, the boundary conditions are applied at the external solid walls, where they are effectively measured during experiments. Conversely, when the solid wall is not simulated, the boundary conditions are imposed directly at the edge of the fluid domain.

The various methods of dividing the domain into elements, i.e., meshing it, are described in Sections 4.3 and 4.4, as they vary depending on the adopted approach. It is important to note that in no case was possible to exploit the symmetry of the cavity. For example, utilizing the xy-plane at $z = 30\,\text{mm}$ as a plane of symmetry would incorrectly constrain the fluctuating velocity component across this plane to zero, as symmetry boundary conditions would be needed. Similar considerations apply to potential point symmetries at the center of the cavity. Since the impact on the full flow of this assumptions was not known, the full domain had to be simulated in all cases.

4.3 Direct Numerical Simulations (DNS)

Direct Numerical Simulations (DNS) were initially conducted by Mohammed Alsailani within the framework of the Research Master Program at the von Karman Institute (VKI), employing GaInSn as the working fluid [30]. Afterwards, these simulations were implemented for water and further improved in subsequent work [31], culminat-

ing in the inclusion of conjugate heat transfer effects by Szilveszter Fehér at the VKI [199].

The simulations were carried out using the open-source spectral element method code, NEK5000 v19.0, developed by Argonne National Laboratory [200]. The spectral element method is a hybrid finite-element method that utilizes high-degree polynomials as basis functions to resolve the solution within each element [201, 202]. This method presents numerous advantages, including a reduction in numerical dispersion/dissipation errors, decreased computational costs compared to traditional methods, and high scalability, making it computationally efficient for high-fidelity simulations [203].

The principle of pseudo-spectral methods involves the expansion of a variable in a finite series of orthogonal trial solutions, typically represented in the form of Chebyshev polynomials. In the pseudo-spectral method, these polynomials are evaluated at specific spatial locations known as Gauss-Lobatto points. The selection of these collocation points simplifies the computation of the nonlinear terms and facilitates the use of Fast Fourier Transforms. The primary advantage of pseudo-spectral methods is their accurate approximation of sufficiently smooth functions. However, they are limited to simple geometries, the grid refinement distribution in the boundary layers is exclusively trigonometric, and constructing an efficient code can be quite challenging.

For this reason, the code has been extensively validated against a variety of cases relevant to nuclear applications, including T-junctions, pipe flows, and jets [204]. In particular, validations have also been carried out both in 2D and in 3D, respectively for a differentially-heated cavity configuration and for Rayleigh-Bénard convection using available databases employing low Prandtl fluids [154, 205]. More details on the full analysis can be found in previous publications [30]. Further validation of the results and the performances of the code will be also given by the experimental analysis reported in this work.

The equations solved by the software can be derived from the Navier-Stokes equations of Equations (4.1) to (4.3) with the following assumptions:

- **Incompressibility:** In fluid flows where the Mach number is below 0.3, the density can be assumed constant, i.e.

$$\frac{\partial \rho}{\partial t} = 0$$

  and a value ρ_0 calculated at the temperature T_0 can be taken as reference value.

- **Boussinesq approximation:** The Boussinesq approximation is used to model buoyancy effects. Commonly adopted in natural convection scenarios, this assumption involves considering the density variations only in the source term of the momentum equation considering the flow incompressible elsewhere. The fluid density is approximated by the temperature change as in Equation (4.7):

$$\rho = \rho_0 \left[1 - \beta(T - T_0)\right] \tag{4.7}$$

Therefore, the model works by adding the buoyancy term as a source term in the momentum equation and it is applicable for small density differences in the domain [206].

Under these assumptions Equations (4.1) to (4.3) become Equations (4.8) to (4.10) taking also advantage of the simplification of the expression of the viscous stress tensor $\boldsymbol{\tau}$ given by the implementation of Equation (4.8).

$$\nabla \cdot \mathbf{u} = 0 \tag{4.8}$$

$$\frac{\partial \mathbf{u}}{\partial t} + \mathbf{u} \cdot \nabla \mathbf{u} = -\frac{1}{\rho_0}\nabla p + \frac{1}{\rho_0}\nabla \cdot (\mu \nabla^2 \mathbf{u}) + g\left(1 - \beta(T - T_0)\right)\mathbf{e_z} \tag{4.9}$$

$$\begin{aligned}\frac{\partial E}{\partial t} + \mathbf{u} \cdot \nabla E = &-\frac{1}{\rho_0}\nabla \cdot (p\mathbf{u}) + \frac{1}{\rho_0}\nabla \cdot \left((\mu \nabla^2 \mathbf{u}) \cdot \mathbf{u}\right) \\ &- \frac{1}{\rho_0}\nabla \cdot \mathbf{q} + g(1 - \beta(T - T_0)) \cdot \mathbf{u}\end{aligned} \tag{4.10}$$

As initial conditions for the equations, the velocity field was imposed as zero, and the temperature field was imposed as uniform and equal to the average of the imposed boundary conditions.

The fluid domain for the DNS simulations is discretized into a grid of $30 \times 30 \times 30$ elements, with 9 collocation points per spatial direction. Figure 4.2 shows a section of the computational grid adopted.

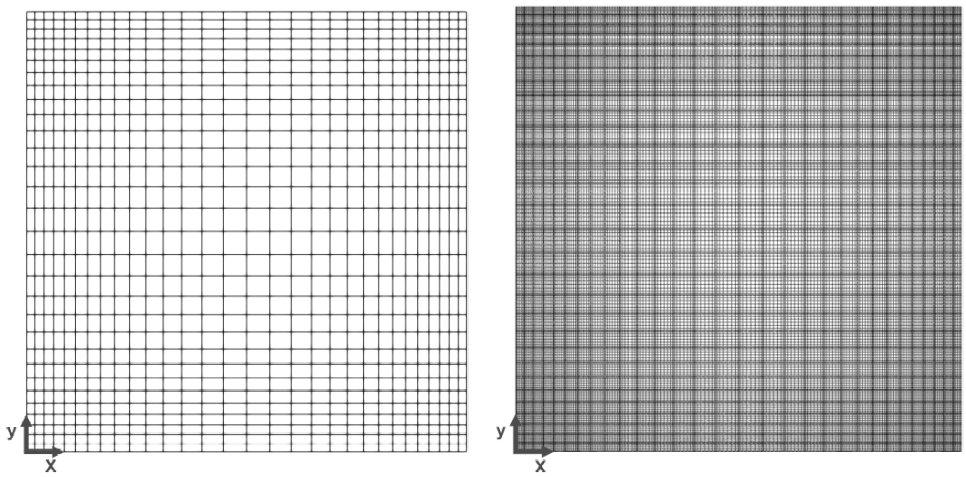

(a) Grid elements (b) Grid nodes

Figure 4.2 - *Computational grid used for the fluid domain in the DNS simulations [30].*

This approach implies that the numerical approximation of the solution is evaluated at 9 nodes within each element. The mesh size increases from the walls towards

the center of the domain with an expansion ratio of 1.075. The adequacy of the mesh was assessed by comparing it with the calculated Kolmogorov scales, ensuring that the typical distance between collocation points remained below five times the estimated Kolmogorov scales throughout the domain. Additional details on the grid sensitivity analysis and the statistical convergence study can be found in the report of Mohammed Alsailani [30].

Statistical convergence was ensured by monitoring some points inside the domain ensuring convergence for the mean quantities, similarly to what has been done for the RANS simulations in this work as shown in Section 4.4. Moreover, before sampling for the mean, the simulation is initialized for about 300 large-eddy-turn-over defined as L/U_{rms}.

In this context, various numerical simulations were conducted and are available for comparison in this work. A summary of the simulations used in this study is presented in Table 4.1.

Table 4.1 - *Summary of the numerical simulations available for comparison with the experimental work.*

Simulation	**Fluid**	**CHT**	**BC - T Active Walls**	**BC - T Passive Walls**	**BC - U**
DNS 1 [30, 31]	GaInSn	No	$T_{hot} = 80\,^{\circ}\mathrm{C}$ $T_{cold} = 20\,^{\circ}\mathrm{C}$	Adiabatic	No slip
DNS 2*	Water	No	$T_{hot} = 80\,^{\circ}\mathrm{C}$ $T_{cold} = 20\,^{\circ}\mathrm{C}$	Adiabatic	No slip
DNS 3 [199]	GaInSn	Yes	$T_{hot} = 79.7\,^{\circ}\mathrm{C}$ $T_{cold} = 39.2\,^{\circ}\mathrm{C}$	Adiabatic	No slip

The first two DNS simulations were conducted with the same numerical setup, differing only in the choice of working fluid. It is important to note that the boundary conditions applied in these cases were those initially targeted in this study, and they were directly imposed on the edges of the fluid volume. Indeed, the cavity walls were not included in these simulations (no CHT implemented), as the significance of such implementation became evident only later. Consequently, while these simulations are not suitable for a direct comparison with experimental data, they provided essential initial insights into the general behavior of liquid metals and the order of magnitude of key quantities, which were used for the calculations presented in Chapter 2. Additionally, preliminary considerations regarding sensor positioning, as discussed in Chapter 3, were based on these simulations.

In contrast, the simulation DNS 3 is the closest approximation to the experimental conditions, as it incorporates both the experimental boundary conditions and the cavity walls. However, all available DNS simulations assume adiabatic passive walls,

*The results of these simulations were not published

an assumption that is only theoretically accurate. Chapter 8 will demonstrate how incorporating the calculated thermal losses from Chapter 3 can enhance the agreement between numerical and experimental results.

4.4 Reynolds Averaged Navier-Stokes simulations (RANS)

RANS simulations were conducted using OpenFOAM, chosen primarily for its availability, extensive use, and the high level of expertise at the VKI. OpenFOAM is a free, open-source software that utilizes a C++ toolbox for the development of customized numerical solvers, as well as pre- and post-processing utilities for solving continuum mechanics problems, including computational fluid dynamics (CFD). It also provides libraries that create toolboxes accessible to both solvers and utilities. OpenFOAM primarily uses the Finite Volume Method (FVM), a technique that involves dividing the geometry into finite control volumes on which the continuity and momentum equations are applied and discretized. By calculating the fluxes over the system boundaries for each control volume, FVM can simulate diverse flow scenarios [207].

Given the importance of simulating both the fluid and solid domain, *chtMultiRegionSimpleFoam* was selected as the OpenFoam solver. This steady-state solver is designed for compressible, buoyancy-driven turbulent flows and can account for conjugate heat transfer (CHT), where the interaction between the fluid and solid phases is crucial.

The equations solved in the simulations can therefore be obtained from Equations (4.1) to (4.3) under the following assumptions:

- **RANS:** The Reynolds decomposition is applied, which decomposes the generic quantity ϕ into a time-averaged component $\overline{\phi}$, representing the actual signal, and a fluctuating component ϕ', which captures all the dynamics, as shown in Equation (4.11) [15]:

$$\phi = \overline{\phi} + \phi' \tag{4.11}$$

  By definition, the fluctuating components represent deviations from the average, so when averaged over a sufficiently long period, these deviations sum to zero $\overline{\phi'} = 0$

- **Steady state:** The fluid flow and thermal fields are time-independent, meaning they do not vary with time. This assumption allows the solver to focus on finding a solution where all transient effects have dissipated, resulting in a steady-state distribution of temperature, velocity, and pressure within the domain. Consequently, for any quantity ϕ

$$\frac{\partial \phi}{\partial t} = 0$$

As a consequence of the steady-state assumption, any time-dependent terms in the governing equations are neglected. This represents a primary limitation of RANS simulations, which can predict only time-averaged quantities. Additionally, turbulent quantities, such as turbulent kinetic energy (TKE), are estimated based on underlying assumptions and turbulence models, rather than being directly resolved.

- **Compressible:** Density variations due to temperature and pressure changes are considered. Although these changes are often small and can be neglected in most terms, they are significant in the momentum equation since the flow is entirely buoyancy-driven.

Under these assumptions it is possible to rewrite Equations (4.1) to (4.3) as Equations (4.12) to (4.14):

$$\nabla \cdot (\overline{\rho}\,\overline{\mathbf{u}}) = 0 \tag{4.12}$$

$$\nabla \cdot (\overline{\rho}\,\overline{\mathbf{u}} \otimes \overline{\mathbf{u}}) = -\nabla \overline{p} + \nabla \cdot \overline{\boldsymbol{\tau}} + \overline{\rho}\,\mathbf{g} - \nabla \cdot \left(\overline{\rho}\,\overline{\mathbf{u}' \otimes \mathbf{u}'}\right) \tag{4.13}$$

$$\nabla \cdot \left(\overline{\rho}\,\overline{E}\,\overline{\mathbf{u}}\right) = -\nabla \cdot (\overline{p}\,\overline{\mathbf{u}}) + \nabla \cdot (\overline{\boldsymbol{\tau}} \cdot \overline{\mathbf{u}}) - \nabla \cdot \left(\overline{\mathbf{q}} + \overline{\rho}\,c_p\,\overline{\mathbf{u}'T'}\right) + \overline{\rho}\,\mathbf{g} \cdot \overline{\mathbf{u}} \tag{4.14}$$

This decomposition introduces the term $\nabla \cdot \left(\overline{\rho}\,\overline{\mathbf{u}' \otimes \mathbf{u}'}\right)$ in Equation (4.13), commonly referred to as the Reynolds stress term, which represents the influence of turbulent velocity fluctuations on the mean flow [15], i.e., their macroscopic effect. Simultaneously, the term $\overline{\rho}\,c_p\,\overline{\mathbf{u}'T'}$ in Equation (4.14) represents the turbulent heat flux, signifying the transport of thermal energy caused by velocity and temperature fluctuations. This term is the central focus of this thesis, underscoring the necessity of simultaneous velocity and temperature measurements, which becomes clearer when considering the complete set of equations.

In particular, the Reynolds stress term requires additional modeling to close the RANS equations, which has led to the development of various turbulence models. In this study, the k-ω SST model has been adopted [208]. The k-ω SST (Shear Stress Transport) model combines the advantages of both k-ϵ and k-ω models by using the k-ω formulation near walls for improved accuracy in boundary layer regions, while switching to the k-ϵ model in the free stream to reduce sensitivity to freestream turbulence. This makes it particularly effective with a refined mesh at the wall, as in this case, due to its accurate capture of near-wall turbulence effects. The choice of the k-ω SST model was made after testing various models and observing the best alignment with experimental results. Regarding the treatment of temperature for the retrieval of the turbulent heat flux as explained in Section 1.2, in the framework of this thesis the most simple approach using a constant $Pr_t = 2$ was adopted [16], also supported by previous similar studies in liquid metal natural convection [162]. The limitations of such approach were already exposed in Section 1.2 and their impact on the final results will be further addressed in Chapter 8. Additional details on turbulence modeling are extensively covered in literature [15].

In the RANS simulations, the numerical domain replicates the actual configuration, with the fluid domain dimensions of 60 mm × 60 mm × 60 mm. This domain

is discretized using a non-uniform grid with an equal number of cells in each of the three spatial directions, with refinement applied near the walls. The solid walls are discretized with a uniform grid along the direction perpendicular to the fluid domain, with each cell corresponding to 1 mm of the physical domain.

The utility blockMesh provided by OpenFOAM was used to create four structured meshes with the characteristics reported in Table 4.2.

Table 4.2 - *Characteristics of the four meshes analyzed during the grid independence study. The table lists the number of cells in the fluid and solid domains, as well as the total number of cells, the y^+ and the time required to reach convergence.*

Mesh Type	**Fluid Cells**	**Solid Cells**	**Total Cells**	**Time**	**y^+**
Coarse mesh	1×10^3	5.4×10^3	6.4×10^3	30 min	7.8
Medium mesh	1.25×10^5	1.25×10^5	2.5×10^5	1 h	1.2
Fine mesh	1×10^6	1.1×10^6	2.1×10^6	8 h	0.15
Super fine mesh	8×10^6	9×10^6	17×10^6	60 h	0.075

A critical parameter for the design of the mesh and the consequent choice of the turbulent model is the y^+ defined as in Equation (4.15) [206]:

$$y^+ = \frac{y u_\tau}{\nu} \tag{4.15}$$

where u_τ is the friction velocity, y is the absolute distance from the wall and ν is the kinematic viscosity of the fluid. Its value at the wall for the different meshes analyzed is reported in the last column of Table 4.2. As the chosen $k-\omega$ SST model directly resolves the viscous sublayer without relying on wall functions, a $y^+ < 1$ is considered appropriate for this turbulence model [206].

The grid independence study was made on the reference case reported in Table 4.3.

Table 4.3 - *Characteristics of the RANS simulation used for the grid independence study.*

Fluid	**CHT**	**BC - T Active Walls**	**BC - T Passive Walls**	**BC - U**	**Turbulence model**
GaInSn	Yes	$T_{hot} = 79.7\,^\circ$C $T_{cold} = 39.2\,^\circ$C	$h = 35\,\mathrm{W/(m^2K)}$	No slip	$k-\omega$ SST

This case was selected as the implemented boundary conditions most closely matched the experimental setup. The choice of the heat transfer coefficient h, which is slightly higher than the experimental value found in Section 3.4, will be further discussed in Chapter 8. Average temperature profiles along the y-direction at the

position $x = 4\,\text{mm}$, $z = 12\,\text{mm}$ were selected as benchmark profiles, as they are also significant for the experimental analysis that will be conducted. The results for these profiles, obtained from the four different meshes, are presented in Figure 4.3(a).

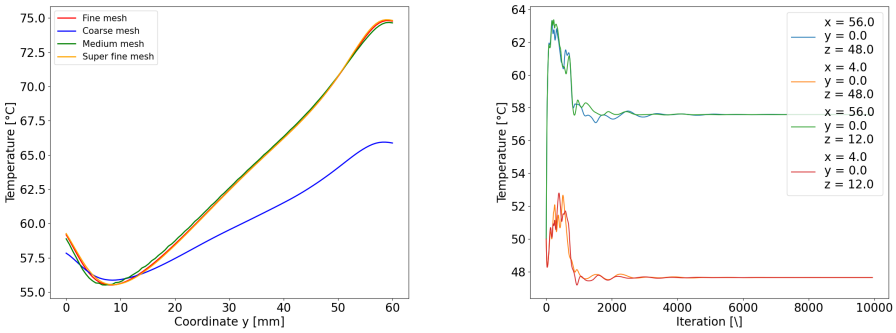

(a) Temperature profiles with different grids (b) Numerical probes evolution vs iteration

Figure 4.3 - *Results of the grid independence study and the statistical convergence analysis. On the left, temperature profiles along the y direction at* $x = 4\,\text{mm}$ *and* $z = 12\,\text{mm}$ *are compared, demonstrating that the medium and fine meshes provide grid independent results. On the right, the convergence behavior of the numerical probes at various locations for the selected mesh (fine mesh) is illustrated.*

It is evident that while the profiles from the coarse mesh of Figure 4.3(a) are significantly inaccurate, the results from the other three meshes converge closely, almost perfectly overlapping for the fine and super fine mesh. Ultimately, the fine mesh was selected because of its reasonable computational time and its compatibility with the turbulence models used. A visualization of the mesh section at $z = 30$ (comparable with Figure 4.1(a)) is shown in Figure 4.4.

From this point onward, references to "the mesh" in the text will pertain to this mesh. Additionally, numerical probes placed at various locations within the domain of this same mesh were monitored to ensure the statistical convergence of the simulation, as illustrated in Figure 4.3(b). Once statistical convergence is achieved, the values recorded by each probe stabilize, indicating that further changes are minimal and convergence has been effectively reached.

In this framework, several RANS simulations were conducted with varying boundary conditions, taking advantage of their relatively low computational cost. These simulations were especially useful for examining the sensitivity to parameters such as boundary conditions, mesh refinement, and turbulence models, ultimately guiding the choices presented in this Section. Although providing an exhaustive list of all simulations would not be beneficial at this stage, it is essential to emphasize that the RANS simulations were designed to encompass all DNS and experimental conditions, and even extend beyond them. Consequently, whenever RANS simulations are introduced, their relevant characteristics will be explicitly specified.

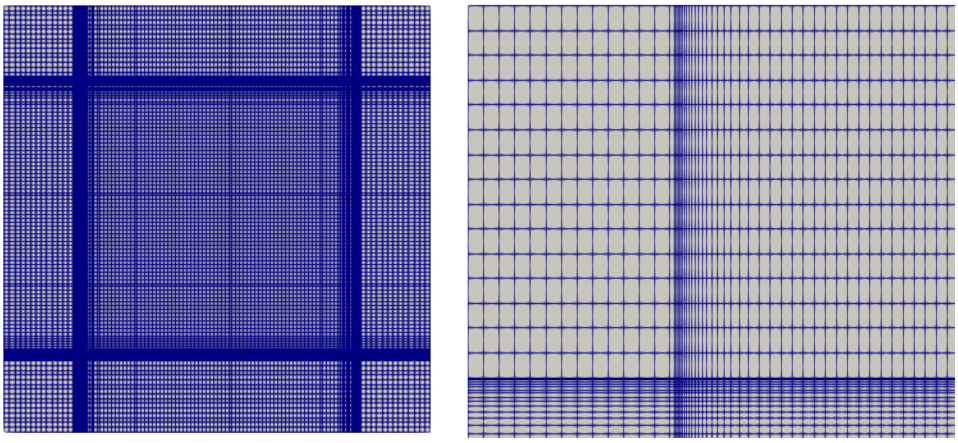

(a) Section of the full mesh at the xy plane $z = 30\,\text{mm}$

(b) Refinement of the mesh on the top left corner

Figure 4.4 - *Mesh used in the conjugate heat transfer RANS simulations*

4.5 Results and discussion

This Section focuses exclusively on numerical results, comparing the outputs of DNS and RANS simulations. Only the flow fields are analyzed here, as specific profiles and temporal evolutions are examined in greater detail in Chapter 8, where comparisons with experimental results are also included. In particular, the simulations considered in this analysis are those already presented in Tables 4.1 and 4.3. The primary objective of this Section is, therefore, to compare the performance of various numerical setups and to gain insights into the physics and order of magnitude of the fluctuating quantities involved.

The first DNS simulation in Table 4.1 was conducted using GaInSn under the initially targeted boundary conditions. One of the most significant outcomes is presented in Figure 4.5, which displays the Turbulent Heat Flux field corresponding to the vertical velocity component in the plane $z = 12\,\text{mm}$ where the measurements are carried out.

Through these simulations, an initial estimation of the temperature and velocity fluctuations in GaInSn under a natural convection setup similar to that used in the experiments was obtained, which facilitated the determination of optimal sensor placement. The maximum turbulent heat flux intensity appears close to the wall, particularly within a 5 mm range, which aligns with the sensor positions in the cavity (see Figure 3.4). These trends and values are revisited and validated at the end of this Section, where simulations that are more closely aligned with the experimental conditions are conducted.

The second DNS simulation in Table 4.1 was performed in water, using the same setup as the previous GaInSn simulation. Although the results could not be directly

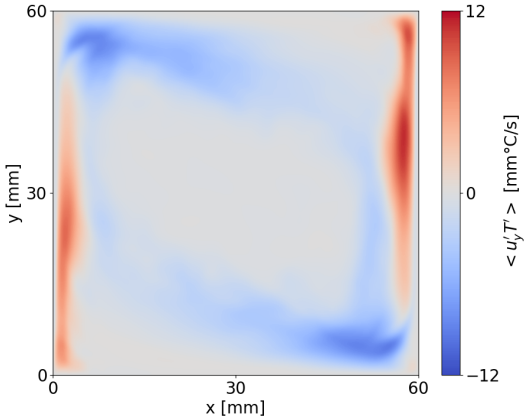

Figure 4.5 - *Turbulent heat flux field calculated by non CHT, adiabatic walls DNS simulations in GaInSn. Section in one of the measurement xy planes* $z = 12\,\mathrm{mm}$.

compared to experimental work due to the absence of CHT implementation, they served as a useful comparison between the behaviors of the two fluids. Figure 4.6 illustrates a comparison of the velocity magnitude fields for water and GaInSn, both obtained with the same numerical setup.

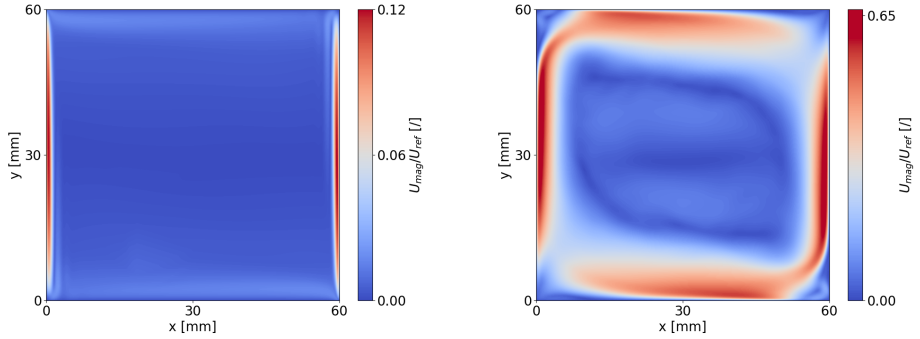

(a) Water (b) GaInSn

Figure 4.6 - *Comparison between non-dimensionalized values of velocity magnitude average fields in water and GaInSn in one of the measurement xy planes* $z = 12\,\mathrm{mm}$. *The scales of the two images are different to ease the visualization.*

The results are presented in a non-dimensional form, normalized by the characteristic velocity defined in Equation (2.1). The boundary layer thickness adjacent to the walls, where high-intensity magnitudes are observed and measurements are most

relevant, is notably thinner in water compared to GaInSn. In particular, for water, this region does not extend beyond $x = 1.5\,\text{mm}$ to $2\,\text{mm}$ from the wall. Given the current sensor placement at $x = 4\,\text{mm}$, , capturing fluctuations in water, if present, may be challenging. This point will be further addressed in the context of the water results in Chapter 8.

Upon analysis of the experimental data, the importance of implementing conjugate heat transfer in the simulations became evident. This necessity will be discussed in greater depth in Chapter 8. As a first point to highlight, Figure 4.7 shows a comparison between 3 different xy-planes sections of the fluid domain at different z coordinates taken from the DNS 3 from Table 4.1.

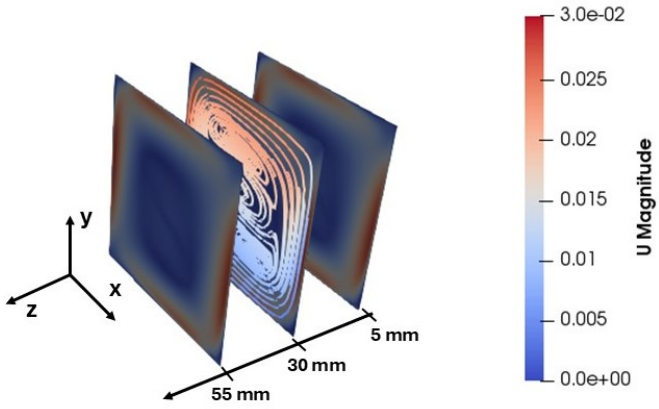

(a) Velocity magnitude U with streamlines in Galinstan

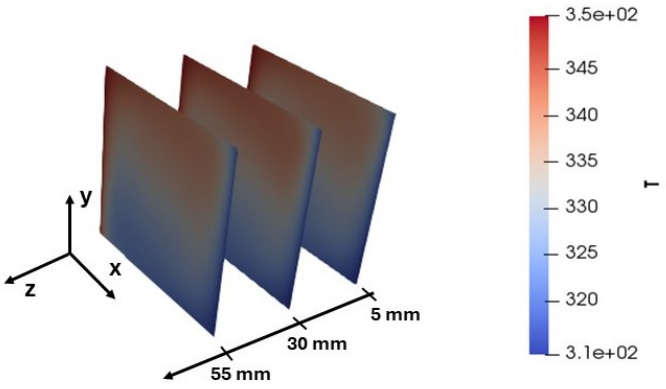

(b) Temperature in Galinstan

Figure 4.7 - *Comparison of the tempearature and velocity magnitude fields over 3 planes at constant x and y. The planes are chosen for the z-coordinates* 5 mm, 30 mm, 55 mm.

The three planes were selected to be maximally spaced to assess the sensitivity of the flow to the z-coordinate. Simultaneously, they were positioned sufficiently far from the passive walls to minimize wall influence. The results, in terms of both velocity magnitude and temperature, demonstrate minimal variation in the z-direction. This justifies the presentation of the results based solely on data from the $z = 12\,\text{mm}$ plane.

Figure 4.8 illustrates a comparison between DNS 3 and the RANS simulation from Table 4.3, with the primary distinction being the inclusion of thermal losses at the external walls.

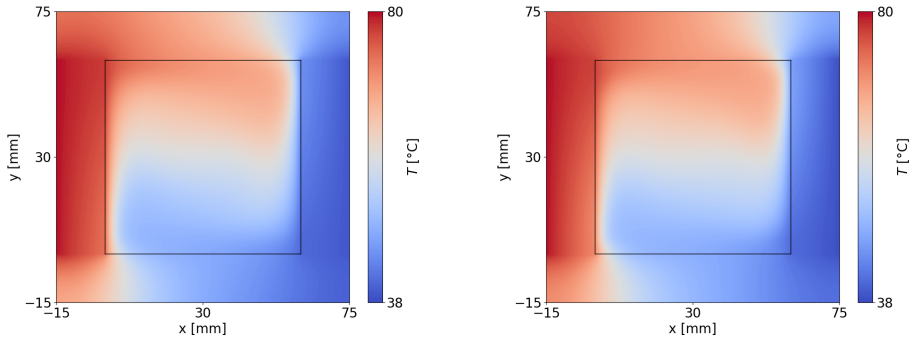

(a) RANS GaInSn

(b) DNS GaInSn

Figure 4.8 - *Comparison between RANS and DNS fields of the average temperature in GaInSn in one of the measurement xy planes $z = 12\,\text{mm}$. The solid wall temperature around the fluid is also shown and the cavity walls are highlighted in black.*

The figure also depicts the temperature field within the cavity walls, including both the stainless steel on the top and bottom and the lateral copper plates, which are distinguishable in the thermal fields due to their very different thermal conductivities.

A high degree of agreement is observed between the two simulations, suggesting that thermal losses do not significantly impact the overall temperature field. However, the precise influence of these losses on the measured profiles will be examined in greater detail in Chapter 8, where comparisons with experimental profiles are presented.

Another key comparison can be made between the velocity fields of these simulations. Specifically, Figure 4.9 focuses on the vertical velocity component, U_y, as it predominantly contributes to the overall velocity magnitude and is the component measured experimentally.

A good agreement between the order of magnitude of the velocity predictions from RANS and DNS simulations is observed, indicating the feasibility of using RANS for estimating average fields even in natural convection for liquid metals. However, a slight overestimation of the boundary layer thickness near the walls is noted, as well as more pronounced discrepancies in regions such as the upper left and lower right corners, where mixing and turbulence phenomena are expected to have a greater impact.

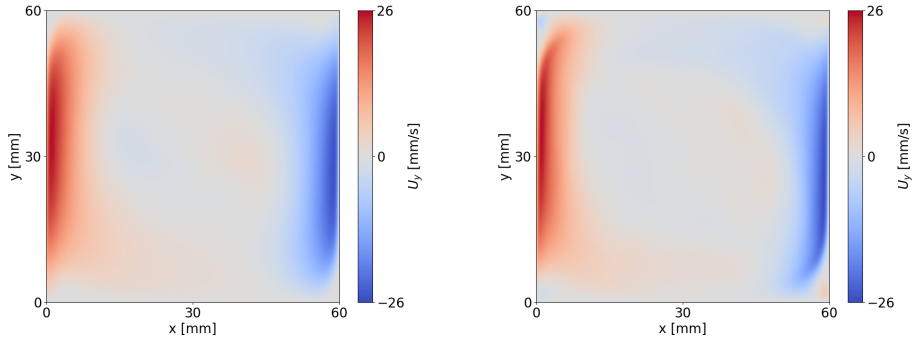

(a) RANS GaInSn

(b) DNS GaInSn

Figure 4.9 - *Comparison between RANS and DNS averaged fields of the vertical velocity component U_y in GaInSn in one of the measurement xy planes, $z = 12\,\mathrm{mm}$.*

These discrepancies may be attributed to the limitations of RANS turbulence models in accurately representing turbulence in liquid metals, which could also influence the average field in areas with higher turbulence levels.

Despite these limitations, both simulations provide a reliable estimation of the expected velocity magnitudes within the cavity, approximately 25 mm/s, a value slightly lower than the estimation provided in Chapter 2 using Equation (2.1). In particular, the comparison between Figure 4.9(b) and Figure 4.6(b) demonstrates that, near the active walls, the vertical velocity component U_y contributes most significantly to the total velocity magnitude, thus supporting the measurement focus on this component close to the wall.

Additionally, comparisons were conducted for quantities more closely associated with turbulence and fluctuations, among which the turbulent kinetic energy (TKE) is particularly significant. TKE, which relates to velocity fluctuations $u' = U(t) - U_{mean}$ as defined in Equation (4.16), serves as a key indicator of turbulence phenomena related to velocity and their distribution within the flow field.

$$\mathrm{TKE} = \frac{1}{2}\left(u'^2_{x,\mathrm{rms}} + u'^2_{y,\mathrm{rms}} + u'^2_{z,\mathrm{rms}}\right) \tag{4.16}$$

The generic root mean square (rms) component, denoted as ϕ_{rms}, is derived from a time-dependent quantity ϕ as follows where the mean is denoted by Equation (4.18).

$$\phi_{\mathrm{rms}} = \sqrt{\frac{1}{N}\sum_{i=1}^{N}\left(\phi_i - \overline{\phi}\right)^2} \tag{4.17}$$

$$\overline{\phi} = \frac{1}{N}\sum_{i=1}^{N}\phi_i \tag{4.18}$$

Figure 4.10 illustrates a comparison of the turbulent kinetic energy (TKE) fields. As anticipated, this result demonstrates the greatest discrepancies between RANS and DNS simulations.

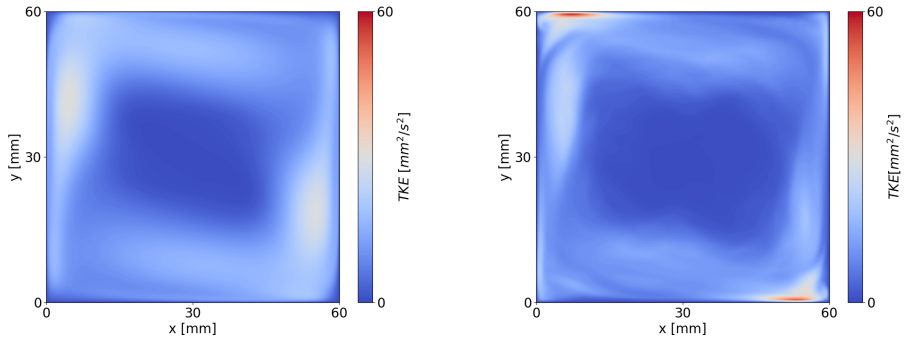

(a) RANS GaInSn

(b) DNS GaInSn

Figure 4.10 - *Comparison between RANS and DNS fields of the turbulent kinetic energy (TKE) in GaInSn in one of the measurement xy planes,* $z = 12\,\mathrm{mm}$.

Despite capturing the general trend of a higher turbulent kinetic energy (TKE) near the walls of the cell, it is evident that many features present in the DNS flows are not captured by the RANS simulations. Overall, the RANS TKE distribution appears significantly smoother, as is characteristic of the averaging process inherent in these simulations. Consequently, RANS simulations cannot be regarded as reliable for comparing turbulent results and quantities related to fluctuations within the context of this work.

Consequently, an analysis of the root mean square (rms) quantities is conducted using only the DNS conjugate heat transfer (CHT) simulations (DNS 3 of Table 4.1). Figure 4.11 presents the rms fields for both the vertical component of the velocity U_y and the temperature T.

The figure provides a good estimation of the magnitude of the fluctuations expected during the experiments, and a comprehensive comparison with the measured experimental values is detailed in Chapter 8. Notably, the highest intensity of the fluctuations is not observed at the same locations for velocity and temperature. The most significant instabilities for velocity are found when the flow, at its peak velocity, impacts the wall, effectively acting as an impinging jet. Conversely, the highest temperature fluctuations occur in the two corners, where flows at differing temperatures converge and mix.

Lastly, Figure 4.12 presents the turbulent heat flux calculated for the vertical velocity component.

This figure depicts the quantity considered the main goal of the thesis, and the final experimental measurements will specifically target it. Notably, it is insightful to compare this figure with Figure 4.5. The comparison reveals that, despite the

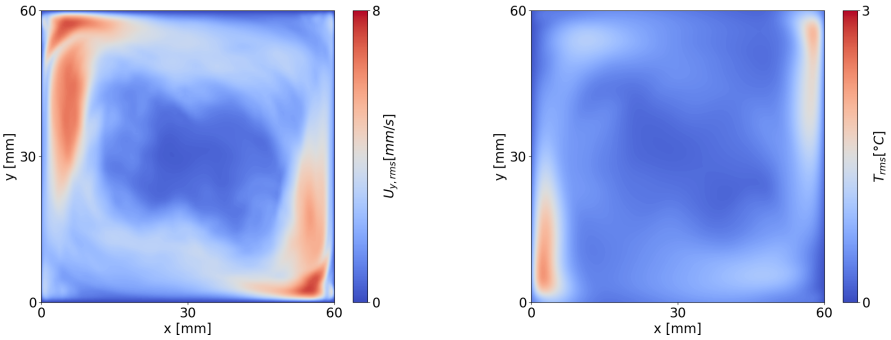

(a) U_y GaInSn (b) T GaInSn

Figure 4.11 - *Fields of the rms values for vertical component of the velocity and temperature calculated by CHT, adiabatic walls DNS simulations in GaInSn. Section in one of the measurement xy planes,* $z = 12\,\mathrm{mm}$.

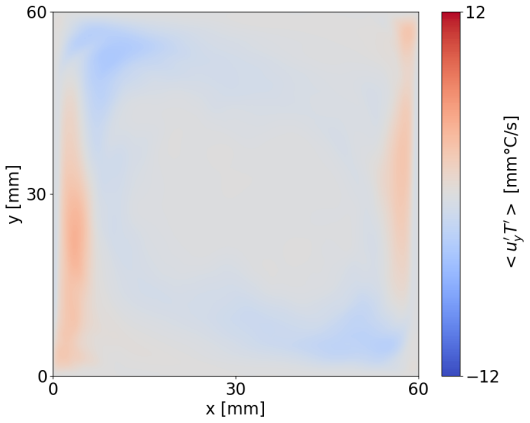

Figure 4.12 - *Turbulent heat flux field calculated by CHT, adiabatic walls DNS simulations in GaInSn. Section in one of the measurement xy planes,* $z = 12\,\mathrm{mm}$.

modifications made between the two simulations highlighted in Table 4.1, the primary trends of the turbulent heat flux (THF) remain consistent. This suggests that the assumptions underlying the experimental choices based on the DNS 1 of Table 4.1 are still valid and correct as they repeat in DNS 3.

However, a discernible difference in the magnitude of the THF values is evident, with Figure 4.12 exhibiting values approximately half of those shown in Figure 4.5. These results can be interpreted as indicative of a damping effect due to the solid

walls, which, when included in the simulation, tend to smooth the flow and produce a more uniform temperature distribution, thereby resulting in less intense turbulent and fluctuating characteristics.

4.6 Conclusions

This Chapter focused on the numerical setup employed in this work for the RANS and DNS simulations. Following a theoretical overview of the governing fluid equations in Section 4.1, the numerical domain used for the simulations was detailed in Section 4.2. Subsequently, the two different approaches, DNS and RANS, were described in Section 4.3 and Section 4.4, respectively, outlining the hypotheses and assumptions applied in each case and summarizing the test cases available for comparison. To conclude, a summary of the numerical results obtained was presented with field representations of various quantities in Section 4.5. The results demonstrate a generally good agreement between RANS and DNS in predicting average fields, confirming the reliability of RANS for this purpose, even in natural convection for low Pr fluids. However, the largest discrepancies between RANS and DNS are observed in regions where mixing and turbulent phenomena are more pronounced, highlighting the limitations of current RANS models in accurately predicting turbulent heat fluxes. Further research is crucial to improve the accuracy of RANS models in predicting these fluxes, particularly in more complex flow configurations where the current numerical settings may not be applicable due to increased flow complexity. Consequently, RANS will be used to support the analysis of averaged velocity and temperature fields in water and GaInSn, while DNS will serve as a more precise benchmark for fluctuations and spectral comparisons.

Chapter 5

Thermocouple and Fiber Bragg Gratings

After the choice of the techniques performed in Chapter 2, this Chapter focuses on the characterization of the temperature sensors, the thermocouple (TC) described in Section 2.3.1 and the fiber Bragg grating (FBG) of Section 2.3.2. The main purpose is to understand their performance and limitations under various conditions and experimental configurations. These sensors are integrated within the same Chapter due to the similarity in the preliminary work conducted with both.

Initially the working principles of both sensors are examined in greater detail in Section 5.1. Subsequently, the calibration process is addressed from a theoretical perspective, followed by a presentation of the tests performed in Section 5.2. In particular, the analysis focuses on the static calibration, including associated uncertainties, and the estimation of the actual response times of the sensors in different fluids, referred to as dynamic calibration. The results of each procedure are then discussed. Eventually, Section 5.3 addresses another aspect concerning the behavior of Fiber Bragg Gratings (FBG) in liquid metals. Most of the work reported in this Chapter was conducted in collaboration with Clemens Naumann as part of his Master's Thesis at the Von Karman Institute for Fluid Dynamics [153].

5.1 Working principle

In this section, the working principles of the two temperature sensors are explained in greater detail, emphasizing the aspects that may influence the interpretation of the final results.

5.1.1 Thermocouple

The working principle of a thermocouple (TC) is based on the Seebeck effect, discovered in 1826 by Thomas Johann Seebeck [209]. Seebeck discovered that if a temperature difference is present between two points of an electrically conducting material,

an electromotive force (EMF) proportional to the temperature difference develops between these points as a result of the variation of the electron density along the conductor. Therefore, in a homogeneous conductor A the Seebeck thermoelectric force is given by Equation (5.1) [36].

$$E_A(T_1, T_2) = \int_{T_2}^{T_1} \sigma_A(T) dT = E_A(T_1) - E_A(T_2) \tag{5.1}$$

where σ_A is the Seebeck coefficient of the homogeneous metal A. To be noticed that if the material is not perfectly homogeneous, also the dependence on the position x of $\sigma_A(T, x)$ should be taken into account.

In order to perform temperature measurements exploiting this physical principle, two wires of different metals A and B are welded together. This welded point is called hot junction or measuring junction and is in contact with the temperature to measure T_1. Their free ends are referred to as cold junction or reference junction, kept at a known temperature T_r. Following Equation (5.1), the resultant thermoelectric force can be as expressed in Equation (5.2), which, given the materials A and B is only a function of the temperatures T_1 and T_r.

$$E_{AB}(T_1, T_r) = [E_A(T_1) - E_A(T_r)] - [E_B(T_1) - E_B(T_r)] \tag{5.2}$$

If it is assumed that the temperature T_r of the reference junction is known and kept constant (usually 0 °C), the thermoelectric force of the circuit of the two metals is only a function of the measured temperature T_1 at the hot junction. In fact, $E_A(T_1, T_r = 0)$ is only dependent on the material properties and on known temperatures. Several standard thermocouple types are defined by the metal combination (A, B). The Seebeck coefficients can be calculated using specific databases of empirically determined polynomial functions [210].

As a direct consequence of Equations (5.1) and (5.2), three practical laws have been formulated for the description and the use of thermocouples:

1. *Law of the homogeneous temperature*: introducing a third metal C into a circuit of the two metals A and B does not alter the resulting EMF in the circuit if both ends of the third metal C are at the same temperature. This is useful in practice when wires made of a third metal are needed to connect the open ends to an EMF measuring device.

2. *Law of homogenous material*: If both conductors are made of the same metal A, the measured voltage $E_{AA}(T_1, T_r)$ will be zero, regardless of the temperature difference $T_1 - T_r$. Therefore, in practice, thermocouples are constructed using materials with significantly different Seebeck coefficients σ, in order to maximize the electromotive force (EMF) generated.

3. *Law of addition of thermoelectric signals*: for a series of thermocouples, the induced voltages are added. This is useful when the signal of the cold junction is not at the standard temperature of 0 °C and therefore needs to be corrected. This is normally called Cold Junction Compensation (CJC)

Practical applications of thermocouples, therefore, necessitate the precise implementation of the cold junction compensation (CJC), as improper CJC can introduce significant measurement errors [36]. Additionally, appropriate handling of the measured voltage, typically in the range of mV, is required. This includes signal amplification, shielding from electromagnetic interference, and noise rejection to ensure accurate measurements.

The hot junction of thermocouples can be designed in different ways. Figure 5.1 shows three main designs.

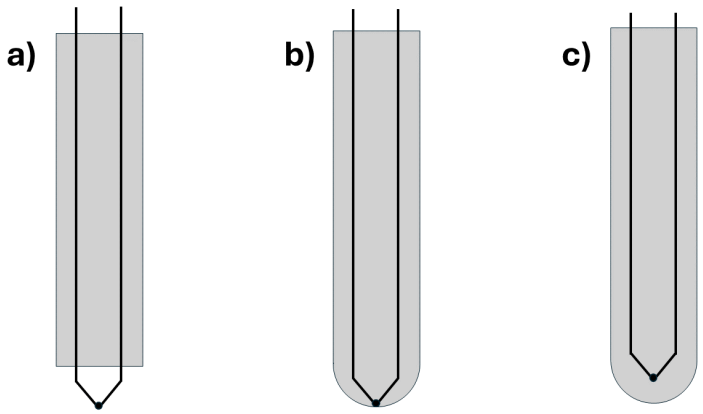

Figure 5.1 - *Different thermocouple junction designs: a) exposed junction; b) grounded junction; c) sheathed junction*

A thermocouple with an exposed tip exhibits superior dynamic behavior compared to other junction types due to its direct contact with the surrounding medium. However, this configuration also makes it the most fragile and sensitive type, as mechanical or chemical impacts can easily cause damage. In harsh environments, such as corrosive fluids, grounded thermocouples are often employed [12]. A stainless steel sheath provides not only resistance to heat, mechanical stress, or chemical impacts but also ensures good dynamic properties by directly connecting to the junction.

In electrically conductive fluids, such as electrolytes, molten salts, and particularly liquid metals, exposed and grounded thermocouples often cannot be used due to the risk of parasitic electric currents coupling into the thermocouple [12, 52]. The sheathed tip of the thermocouple offers electrical insulation between the junction and the surrounding medium, thus preventing these parasitic currents. Powdered magnesium oxide (MgO) is commonly used as an insulating material for this application. In addition to its high electrical resistivity of $1 \times 10^{13}\,\Omega\,\mathrm{m}$ to $1 \times 10^{16}\,\Omega\,\mathrm{m}$ [211], powdered MgO possesses a relatively high thermal conductivity of $0.5\,\mathrm{W/(m\,K)}$ to $55\,\mathrm{W/(m\,K)}$ [67], depending on its compression and sintering processes. Nevertheless, the thermal resistance introduced by this insulation negatively affects the dynamic behavior of sheathed thermocouples compared to exposed and grounded types.

Although thermocouples inherently measure temperature based on material prop-

erties, they still require periodic calibration to ensure accurate measurements. Over time, thermocouples can experience drift, caused either by the operating environment or simply by the passage of time [36]. For this reason, a section of this Chapter (section 5.2) is dedicated to the calibration of the temperature sensors.

5.1.2 FBG

The temperature measurement with FBG sensors is based on detecting changes in the wavelength of light reflected from a fiber-optic grating [70, 77]. The FBG sensor is an optical fiber with an integrated distributed Bragg reflector (DBR, also called Bragg mirror) in its core, which consists of a periodic and permanent modification δn of the core refractive index n_{eff} for a typical length L of 4 mm to 6 mm when the fiber is used for sensing, as shown in Figure 5.2. However, the length of the sensitive is customizable and different applications might require different grating lengths.

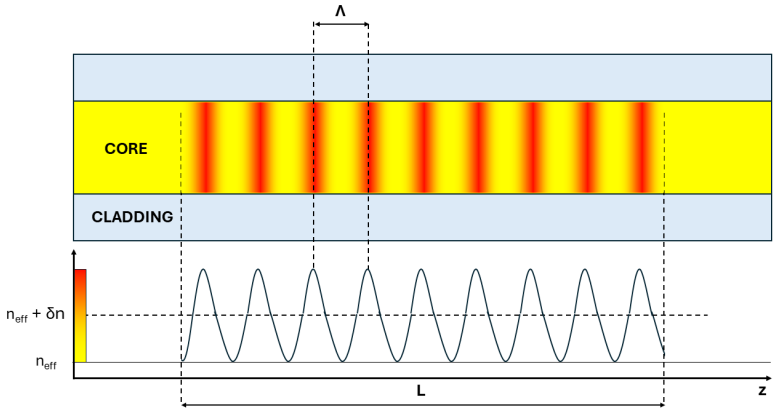

Figure 5.2 - *Schematic of the Bragg Gratings principle*

Such modulation is obtained in the fabrication process by lateral illumination of the fiber core using interfering ultraviolet laser beams thanks to the photosensitivity of single mode fibers. Because of the variation of the refractive index, small Fresnel reflections, distributed along the grating, add in phase for a specific wavelength called Bragg wavelength λ_B, defined as in Equation (5.3), where n_{eff} and Λ represent the effective refractive index and the grating period of the Bragg mirror, respectively.

$$\lambda_B = 2n_{\text{eff}}\Lambda \tag{5.3}$$

Both of these parameters are affected by changes in strain and temperature, resulting in a shift $\Delta\lambda_B$ in the Bragg grating center wavelength. This shift, using Equation (5.3), can be expressed as Equation (5.4), where the first term represents the strain effects and the second term represents the temperature effects. By tracking the wavelength at which Bragg reflection occurs, the magnitude of an external

perturbation can be determined, providing a readout mechanism directly inscribed in the fiber and able to retrieve the absolute value of the targeted quantities.

$$\Delta\lambda_B = 2\left[\Lambda\frac{\partial n_{\text{eff}}}{\partial l} + n_{\text{eff}}\frac{\partial\Lambda}{\partial l}\right]\Delta l + 2\left[\Lambda\frac{\partial n_{\text{eff}}}{\partial T} + n_{\text{eff}}\frac{\partial\Lambda}{\partial T}\right]\Delta T \tag{5.4}$$

Since the grating can be photo-imprinted into the fiber core without compromising the mechanical strength of the silica, multiple gratings can be inscribed into a single fiber, enabling quasi-distributed sensing [77]. For the sake of this work, only one grating was inscribed at the tip fiber used.

In particular, the strain effect term can be further expressed as in Equation (5.5) where $p_{11} + p_{12}$ are components of the strain optic tensor, ν_P is the Poisson ratio, and $\epsilon_s = \Delta l/l$ represents strain [212], giving an approximate strain sensitivity of $\approx 1\,\text{pm}/\mu\epsilon$.

$$\Delta\lambda_{B,\epsilon} = \lambda_B\left[1 - \frac{n_{\text{eff}}^2}{2}[p_{12} - \nu_P(p_{11} + p_{12})]\right]\epsilon_s \tag{5.5}$$

On the other hand, the temperature effect can be expressed as in Equation (5.6):

$$\Delta\lambda_{B,T} = \lambda_B(\alpha_\Lambda + \alpha_n)\Delta T \tag{5.6}$$

where

$$\alpha_\Lambda = \frac{1}{\Lambda}\frac{\partial\Lambda}{\partial T} \tag{5.7}$$

$$\alpha_n = \frac{1}{n_{\text{eff}}}\frac{\partial n_{\text{eff}}}{\partial T} \tag{5.8}$$

are respectively the thermal expansion coefficient of the fiber ($\approx 0.55\times10^{-6}\,1/\text{K}$ for silica) and the thermo-optic coefficient ($\approx 8.6\times10^{-6}\,1/\text{K}$ for germanium-doped silica-core fibers). The index change dominates, giving a typical temperature sensitivity of $\approx 10\,\text{pm}/^\circ\text{C}$ to $15\,\text{pm}/^\circ\text{C}$.

While it is theoretically possible to calculate the exact temperature sensitivity $\Delta\lambda_{B,T}$ for a given Λ and n_{eff}, it has been observed that this theoretical value varies slightly between FBG sensors, even from the same fabrication batch, due to manufacturing tolerances [213]. Therefore, a static calibration is required to determine the true sensitivity and the peak-wavelength-to-temperature dependence before conducting measurements. The calibration procedures adopted for this work are described in Section 5.2.

Furthermore, the theory above indicates that any change in wavelength due to an external perturbation to the grating is the sum of strain and temperature effects. Thus, in applications where only one perturbation is of interest, it becomes necessary to deconvolute temperature and strain This can be achieved through a separate calibration of the two effects [84], by encasing the fiber to isolate it from strain effects [214], or by combining different sensing systems for the two phenomena [83].

5.2 Calibration

As discussed in Section 5.1, calibration is a critical component in ensuring accurate and reliable temperature sensing. Even sensors that are based on physical properties, which theoretically do not require calibration, must undergo this process to meet stringent accuracy and reliability standards. For each sensor employed, two types of calibrations are generally performed:

- *Static calibration:* This is conducted to quantify the relation between the sensor's measured output and the actual temperature.
- *Dynamic calibration:* This provides information on how quickly the sensor responds to temperature changes.

The following section provides a detailed explanation of these essential calibration procedures for both types of sensors, including a description of the experimental equipment specifically used for this purpose.

5.2.1 Static calibration

The static calibration of temperature sensors is a process designed to verify and, if necessary, adjust the accuracy of a sensor's temperature readings. When this is performed through comparison with another (more accurate) temperature sensor under identical thermal conditions, it is referred to as a comparative calibration. For a successful static comparative calibration, the following elements are required:

- *Sensor and acquisition system:* The sensor to be calibrated along with its entire measurement chain.
- *Calibration environment:* A stable and controlled environment to minimize temperature fluctuations during the calibration process.
- *Reference sensor:* A temperature reference instrument or calibration source that has traceable accuracy superior to the sensor being calibrated.

The following section provides a detailed description of these components and presents the results in terms of calibration accuracy and uncertainty, which ultimately impact the final measurements in the cavity.

Experimental setup and procedures

For the purpose of the static calibration of the temperature sensors of this work, the components presented in Table 5.1 were used.

The sensors to calibrate are the sheathed type K thermocouple and the FBG described in Section 2.3.1 and Section 2.3.2 with their respective acquisition systems and used in the configuration shown in Figure 2.9. The reference sensor used is a class AA RTD by Omega (P-L-1/10-M30-150-0-P-1) with a maximum declared uncertainty of $u_{T_{ref}} = \pm 0.23\,^{\circ}\mathrm{C}$. The measurements of the RTD are acquired via a NI9216 acquisition card from National Instrument [215]. A climatic chamber WKL30/40

Table 5.1 - *Components used in the static calibration of TC and FBG*

Component	Function	Specifics
Sheathed type K TC	Sensor to calibrate	Ø250 µm, see Section 2.3.1
NI9212	Acquisition system for TC	see Section 2.3.1
FBG	Sensor to calibrate	Ø125 µm, see Section 2.3.2
BaySpec Interrogator	Acquisition system for FBG	see Section 2.3.2
RTD	Reference sensor	Ø3 mm
NI9216	Acquisition system for RTD	Accuracy 0.15 °C [215]
Climatic chamber	Controlled environment	WeissTechnik WKL30/40

by WeissTechnik is used to set the temperature and mantain all the sensors in a controlled environment. The climatic chamber and the three sensors as they are used in the calibration setup are shown in Figure 5.3(a) and Figure 5.3(b).

(a) Climatic chamber

(b) Temperature sensors and reference RTD

Figure 5.3 - *Experimental setup of the comparative static calibration for temperature sensors*

During the calibration, the maximum horizontal and vertical distance between the sensors are 3 cm and 1 cm respectively, which leads to a calibration volume that is much smaller than the volume of the climatic chamber. Therefore, the maximum temperature uncertainty of the calibration volume is considered as $u_{T_{cal}} = 0.2\,°C$ according to the calibration certificate of the climatic chamber. The humidity inside the chamber is set to 0% to prevent possible measuring uncertainties caused by moisture inside the chamber during the calibration process. All sensors were calibrated at seven distinct temperatures, ranging from 20 °C to 80 °C, with increments of 10 °C. This approach enabled coverage of the whole measurement range while allowing the entire calibration process to be completed within a single day.

The calibration procedure was carried out as follows:

- The desired temperature was set using the thermostat of the climatic chamber.
- Sensors inside the chamber were left to reach thermal equilibrium, defined as the point at which deviations from the average reading of the sensor across all samples stopped decreasing. This process typically required about one hour for each calibration point.
- Temperature data from each sensor were recorded over a 60 s period at a sampling rate of 1 Hz. This acquisition duration was chosen to ensure statistically independent measurements, while also maintaining a reasonable acquisition time and providing a sufficient number of samples to achieve a low standard deviation in the average, thus enabling a reliable temperature reading.
- This procedure was repeated for each calibration temperature, resulting in a comprehensive static calibration curve for every temperature sensor.

It is important to note that a calibration for strain for the FBG was not conducted in this case. During the temperature calibration procedure, maximum care was taken to ensure that the fiber was not bent or subjected to any type of stress, allowing any effects recorded in the calibration to be attributed solely to temperature. However, this does not imply that strain will not play a role during actual measurements. The hypothesis, later supported by experimental evidence, is that the strain effect resulting from the movement of the fluid in the facility will be minimal and negligible compared to the effect of temperature. This is a significant assumption, but it appears to be justified by the results presented in Chapter 8.

Results

The sensor readouts from the 60 samples are compared with the corresponding temperature readings from the reference thermometer at each calibration temperature. Consequently, the standard deviation offers insights into potential signal noise or other deviations of the sensors and their respective acquisition systems. However, the values from the reference RTD are assumed to remain constant over the 60 samples, thereby representing the actual temperature within the calibration volume. This assumption is made to simplify the uncertainty analysis of the static calibration. The resulting calibration datasets, presented in Table 5.2, are utilized in a regression model that establishes a relationship between the measured sensor quantities and the reference temperature.

The linear regression model shown in Equation (5.9) was used to fit the data:

$$T(X) = \frac{X - b}{a} \tag{5.9}$$

where X represents either the measured temperature of a thermocouple or the wavelength peak of the FBG sensor and a and b are the slope and the intersection at the y-axis of the linear regression. The regressions were carried out for both sensors using the *curve fit* function from the *scipy optimize* module in Python adopting the least square method and the results are shown in Figure 5.4.

Table 5.2 - *Static calibration results of the temperature sensors averaged over 60 samples, including their standard deviation and compared with the measured reference temperature*

RTD [°C]	TC 0.25mm [°C]	FBG Sensor [nm]
20.78	20.89 ± 0.06	1525.6790 ± 0.0041
29.93	29.97 ± 0.05	1525.7533 ± 0.0010
39.90	39.90 ± 0.03	1525.8426 ± 0.0008
49.87	49.91 ± 0.03	1525.9186 ± 0.0003
59.84	59.85 ± 0.03	1526.0060 ± 0.0007
69.79	69.70 ± 0.03	1526.0951 ± 0.0011
79.62	79.52 ± 0.04	1526.1824 ± 0.0026

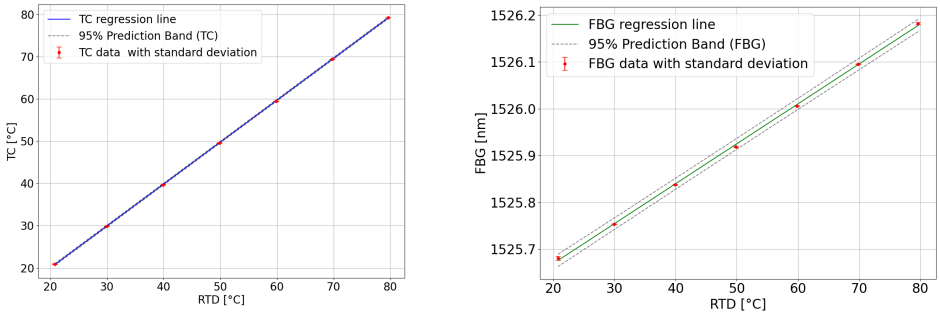

(a) TC calibration

(b) FBG calibration

Figure 5.4 - *Static calibration curves of the temperature sensors. The sensors are calibrated in a climatic chamber taking an RTD as a reference. The static calibration curves are plotted as a function of temperature. Both sensors acquired different points averaging each one over 60 samples. The standard deviation and the confidence band resulting from the fitting procedure of the regression line are also shown.*

The figure also displays the 95% confidence bounds of the linear regression. It is clear that the standard deviation of the sensor is significantly smaller than the deviation within the 95% confidence bounds of the linear regression at all calibration points. For further comparison, the fitting parameters a and b, including their 95% confidence bounds, are presented in Table 5.3.

Table 5.3 - *Intercept and slope of the linear regression of each sensor*

Sensor	Parameter a	Parameter b
TC	1.012 (0.994, 1.030) °C/°C	-0.952 (-1.936, 0.032) °C
FBG	0.00866 (0.00842, 0.00891) nm/°C	1525.49 (1525.48, 1525.50) nm

To quantify the quality of the regression, the root mean square error (RMSE) was used, determined by taking the square root of the average squared difference between the estimated and the measured value. This value, when divided by the sensors sensitivity a, quantifies the error of the corrected temperature and provides a reasonable estimation of the regression uncertainty $u_{T_{fit}}$, as shown in Table 5.4

Table 5.4 - *RMSE values and corresponding uncertainty $u_{T_{fit}}$ of each sensor*

Sensor	RMSE	Regression Uncertainty $\mathbf{u_{T_{fit}}}$
TC	0.3649 °C	± 0.36 °C
FBG	0.0049 nm	± 0.57 °C

To further evaluate the accuracy of the calibration, a plot of the deviations from the reference sensor is presented in Figure 5.5.

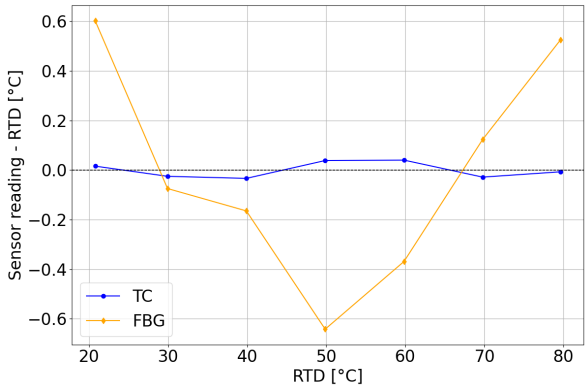

Figure 5.5 - *Difference between the sensors reading and the RTD reading plotted as a function of temperature to highlight possible second order effects*

The anticipated linearity of the sensors, as demonstrated in Figure 5.4, was generally confirmed. However, the primary focus shifted towards identifying and characterizing second-order effects. These deviations from linearity may be indicative of potential non-linearities or sensor drift as a function of temperature. Specifically, the thermocouple exhibited minimal deviation from the RTD, remaining within a narrow range of −0.05 °C to 0.05 °C after calibration, suggesting negligible drift across the entire calibration range. In contrast, the FBG sensor displayed considerably greater variability, with deviations ranging from −0.6 °C to 0.6 °C. While non-linearity, as documented in the literature [216, 217], could manifest as an increasing or decreasing consistent trend with temperature, such behavior was not observed within the limited temperature range of this study. Therefore, these deviations are likely attributable to other factors, such as sensor drift or minor measurement uncertainties. The impact of these discrepancies on the accuracy of the calibration fit will be carefully considered during the uncertainty analysis.

When combining $u_{T_{fit}}$ with the uncertainty of the reference thermometer $u_{T_{ref}}$ and the uncertainty due to the thermal gradient inside the calibration volume $u_{T_{cal}}$ through Equation (5.10) it is possible to retrieve the total uncertainty of the sensors $u_{T_{tot}}$ [218].

$$u_{T_{tot}} = \sqrt{u_{T_{fit}}^2 + u_{T_{ref}}^2 + u_{T_{cal}}^2} \tag{5.10}$$

The final values of the total uncertainty calculated for the sensors are reported in Table 5.5

Table 5.5 - *Total uncertainty of the two sensors*

Sensor	Total Uncertainty
TC	$\pm 0.47\,^{\circ}\mathrm{C}$
FBG	$\pm 0.64\,^{\circ}\mathrm{C}$

It is visible that the accuracy for the FBG sensor is lower compared to the one of the thermocouples, mainly due to its higher regression uncertainty. The potential influence of this can be attributed to the wavelength repeatability of the FBG interrogator used, which has a value of $u_{\lambda_B} = \pm 2\,\mathrm{pm}$ and the peak detection uncertainty, around $\pm 1\,\mathrm{pm}$. These are typical values for standard acquisition systems but previous studies have shown that the accuracy of temperature measurement systems with FBG sensors can be comparable with RTD when state-of-the-art systems are used [219–221]. Moreover, the total uncertainty of both sensors could be further reduced by using a high precision calibration RTD and an optimized calibration oven, possibly reducing $u_{T_{ref}}$ and $u_{T_{cal}}$ to $\approx \pm 0.05\,^{\circ}\mathrm{C}$ [222]. Despite these possible improvements, the achieved measurement accuracy with the performed static calibrations for all sensors respect the measurement requirements of Section 2.1 and it has therefore been decided to not go further.

All the procedure described is carried out according to the calculation of the type B uncertainty as presented in the Guide of Uncertainty in Measurements [223]. To calculate the final uncertainty associated to a measurement point, this uncertainty will be added to the type A uncertainty deriving from the standard deviation of the measured point.

5.2.2 Dynamic calibration

Dynamic calibration is the measurement of the response of a device to a controllable and reproducible input signal. For this specific case, the focus was on the time response of the sensors when a temperature step was provided. The dynamic response of most common temperature sensors, can be described by a model of a first-order system and it is analyzed as such [36] (see Appendix D). The results show that an individual dynamic characterization of temperature sensors is necessary for reliable temperature measurements with high temporal resolution because the response time of a temperature sensor depends not only on the sensor size but also on the heat transfer coefficient between the sensor and its surrounding, which is a priori unknown

and depends on the thermophysical properties of the sensor, the fluid, and on the flow parameters.

Experimental setup and procedures

The dynamic calibration of temperature sensors has been extensively addressed in the literature, employing various setups for diverse purposes, which have yielded differing and sometimes conflicting results. The primary setups identified in the literature for this purpose are summarized as follows:

- *Laser technique*: Previous studies have concentrated on dynamic characterization by heating the temperature sensor with a high-power laser and analyzing the thermal response of the sensor during the heating and/or cooling phases [224–226]. A significant advantage of this technique is that the temperature sensor can be calibrated in situ within transparent fluids [227, 228]. Furthermore, very high sensor temperatures can be attained, contingent on experimental conditions and laser power [229]. However, the heat transfer can be characterized by a step in heat flux rather than an actual temperature step, as the steady-state temperature is influenced by the radiation absorption characteristics of the sensor and the heat transfer to the surrounding medium. Consequently, the underlying physical phenomenon cannot be regarded as identical to that expected in the present measurements, despite some studies attempting to correlate the heat flux step to a temperature step through theoretical calculations [224]. Moreover, the laser calibration method is not applicable to opaque fluids such as liquid metals.

- *Conduction-based technique:* This technique involves direct contact between the tip of the thermocouple and a heating source, thus primarily relying on conduction for heat transfer [230]. Although it is feasible in various fluids, the primary aim of this technique is to provide a heat flux step rather than the temperature step required for this study.

- *LCSR (Loop Current Step Response):* In this method, the thermocouple is internally heated by applying an electrical current at its open ends, which is subsequently stopped. The output of the thermocouple is monitored as it returns to ambient temperature, and the transient response is analyzed to ascertain its time constant. A mathematical transformation is employed to convert this internal data into the response of the thermocouple to an external temperature change [231]. This technique has yielded satisfactory results and, once implemented, allows for high repeatability across different environments. However, the implementation and mathematical post-processing of the data require considerable time and resources, which were not deemed justifiable for this investigation. Moreover, due to the fundamental principle on which it is based, the technique cannot be directly applied to the FBG sensor.

- *Furnace:* This approach generates a temperature step by inserting the sensor into a furnace utilizing a moving cart [86, 232]. Depending on the velocity of the

cart, a temperature ramp may be employed instead of a temperature step. While this method has proven effective, it is primarily developed for measurements in air and gas, as its application in various fluids can be challenging.

- *Water droplet:* This specific technique is mainly utilized to determine the thermal product of surface coaxial thermocouples [233]. The temperature step for the droplet method is produced by a droplet that falls onto the sensitive part of the sensor, typically at a temperature lower than that of the initial sensor temperature. This setup is generally suitable for use with various fluids without introducing significant complications to the setup itself [45, 153]. This technique was also adopted in preliminary stages of this study. However, the results were less reliable, and issues related to sensor wetting arose. Consequently, it is not further discussed in this work. For more detailed information, a publication featuring the author as a co-author can be consulted [45, 153].

- *Hot air jet:* In this method, the sensor is placed in a hot air jet attached to a rotating element, allowing it to oscillate between a hot air stream and an ambient zone at variable frequencies [88]. By increasing the oscillation frequency, the rate of temperature change is regulated. However, this technique is only applicable to gases or air and is nearly impossible to implement with liquid metals.

- *Plunging:* This technique involves submerging the sensor in a bath maintained at a constant temperature different from ambient conditions, thereby recording the response of the sensor. If the immersion time is sufficiently short, i.e., shorter than the response time of the sensor, the heat transfer is primarily governed by forced convection, allowing for the retrieval of the response time of the sensor. This method is widely employed in both commercial and scientific applications, for fiber Bragg grating [234] and thermocouple [85, 235, 236] due to its simplicity and effectiveness. The plunging approach can vary, ranging from manual operations to highly controlled moving carts and systems. Its reproducibility and reliability depends on the setup, and its primary advantage lies in its relative simplicity and the capacity to be used with different fluids.

For this study, only the plunging method is considered due to its simplicity and applicability to water and GaInSn, the primary fluids involved in the project. The analysis was also extended to glycerin, paraffin oil, and molten salt to comprehensively assess the behavior of the sensors and obtain meaningful results. However, their results are not presented here, as the insights provided by the plunging technique are considered sufficiently broad and comprehensive to convey clear conclusions for the purpose of this work.

In Figure 5.6, the experimental setup for the plunging calibration technique is schematically drawn.

Before starting the plunging process, the calibration fluid is heated in a beaker using a heating plate to reach the temperature T_f, thereby generating a temperature step ΔT for the sensor, which is initially at ambient temperature. Following recommendations from the literature [237], the temperature difference between the fluid and the sensor was, whenever feasible, set to $\Delta T \approx 20\,\mathrm{K}$ for each calibration run.

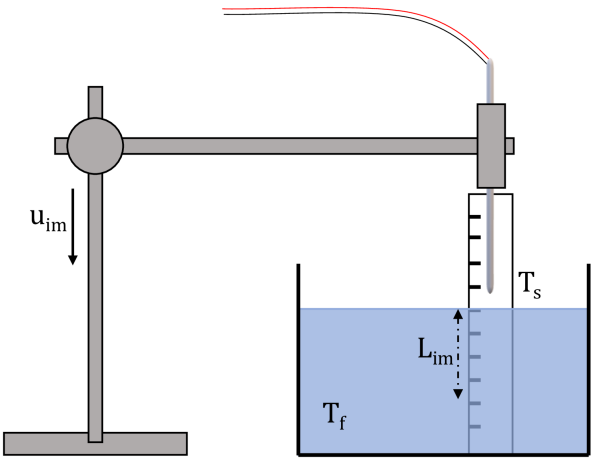

Figure 5.6 - *Schematic of the plunging method for the dynamic calibration of the temperature sensors [153].*

This value was determined to be optimal for reducing uncertainties, particularly for the thermocouples, which are influenced by the temperature dependence of the sensor material parameters, while still providing a sufficient temperature step to minimize measurement and evaluation uncertainties. Nevertheless, some tests were conducted to assess the impact of ΔT, which indicated that this parameter does not significantly affect the final time response [153].

For increased repeatability, the sensor is fixed to a positioning arm at a defined height to ensure that the immersion length is always the same between different calibration runs. Thus, the influence of possible thermal stratification can be neglected. The whole arm is lifted up manually over the beaker, and lowered until it is fully immersed and has reached its final position. After the sensor is in thermal equilibrium with the fluid, it is taken out of the fluid by lifting the positioning arm again. Then, the data acquisition is stopped, and the plunging calibration process is finished. To determine the influence of the immersion velocity u_{im} on the response time of the sensors, multiple calibration runs at different plunging velocities in the range of 10 mm/s to 500 mm/s are performed with every temperature sensor in all calibration fluids. To reduce immersion effects and conduction errors along the temperature sensor stems, the immersion length L_{im} was held constant at 10 mm throughout all calibration runs. In particular for the FBG it is important to notice that the because of the grating length < 1 mm of the FBG sensor, the immersion time for a plunging velocity of 500 mm/s is <2 ms, which is shorter than the shortest measured response times. Even though the influence on the response time measurements might increase for lower immersion velocities, this effect is not further investigated in the present study since the observed wetting process of the fiber tip during the immersion happens almost instantaneously. In addition, the sensor position during the immersion process is monitored by a Dantec SpeedSense M310 high-speed camera at an image rate of 100 Hz with a Nikkon Micro-Nikkor 105 mm macro lens and an image res-

olution of 1280 × 800 pixel. Using the known optical magnification, the plunging velocity and depth can be precisely determined with an uncertainty below 5 % for all calibration runs.

To get a complete analysis of the phenomenon, water, glycerin, paraffin oil, GaInSn and molten salt were used as calibration fluids. The latter consists of a ternary nitrate salt mixture (53 wt% KNO_3 + 40 wt% $NaNO_2$ + 7 wt% $NaNO_3$, also known as HITEC) with a melting point of 142 °C was chosen and it was heated up to 180 °C for the plunging calibration. The thermophysical properties of all calibration fluids are listed in Table 5.6.

Table 5.6 - *Thermal conductivity k, density ρ, specific heat capacity c_p, dynamic viscosity η, and Prandtl number Pr of all calibration fluids used. All properties are evaluated at 45 °C, except for the HITEC salt, which is evaluated at 200 °C.*

Parameter	**GaInSn** [23, 173]	**Water** [238]	**HITEC** [239, 240]	**Paraffin Oil** [241]	**Glycerin** [242]
k W/(m K)	16.500	0.635	0.571	0.133	0.295
ρ kg/m^3	6440	990	1937	832	1246
c_p J/(kg K)	296	4180	1439	1987	2486
μ mPa s	2.4	0.6	7.4	12.8	201.2
Pr [/]	0.04	3.92	18.65	189.76	1698

It should be noted that the property values may slightly vary during the calibration runs due to the temperature dependence of most parameters. However, for the sake of simplicity and after evaluating the minimal impact on the calibration value calculations, the provided values are considered at approximately the fluid temperature during the plunging calibration process.

For this test, the primary results will focus on the inertia of the sensors. While it was important to maintain the entire measurement chain during the static calibration, this is of secondary importance in this case since the main results pertain to the properties of the sensors and their behavior with the surrounding environment. Consequently, a different acquisition system was utilized for the thermocouple to achieve a higher acquisition frequency, thereby avoiding limitations imposed by the acquisition frequency of the NI9212. For this test, the HBM QuantumX MX440B universal amplifier was employed for the thermocouple, while the BaySpec WaveCapture interrogator, as shown in Figure 2.4(b), was used for the FBG. To ensure that the acquisition frequency was not a limiting factor, a sampling rate of 5000 Hz was employed for both sensors during each acquisition to adequately resolve the temperature step responses.

Results

In Figure 5.7, the response time of the FBG and the thermocouple are shown as a function of the immersion velocity u_{im} for the plunging process in different fluids.

The estimation of the response time was carried out by fitting the experimental

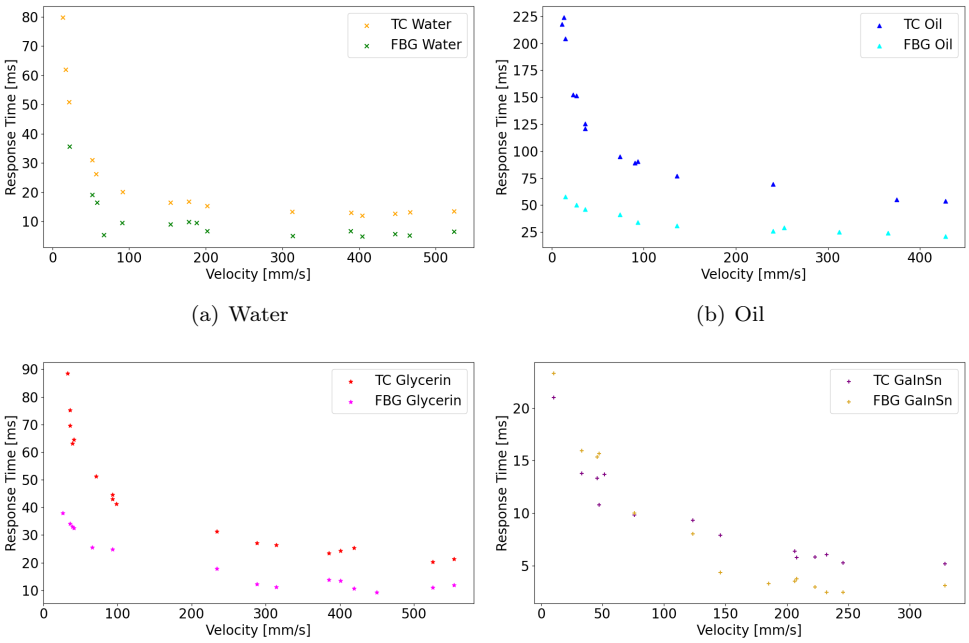

(a) Water (b) Oil

(c) Glycerin (d) GainSn

Figure 5.7 - *Response time τ of the investigated temperature sensors in dependence of the immersion velocity u_{im} for the plunging process in different fluids*

data to the form of the step response of a first order system and estimating τ using the least-squares method as explained in Appendix D. It should be noted that the test in molten salt was not conducted with the thermocouple; therefore, the comparison of the two sensors in molten salt is not presented.

Comparing the different graphs, the FBG sensor consistently demonstrates the shortest response times. This observation aligns with the theoretical foundations outlined in Appendix D, which states that the response time of a sensor decreases with a reduction in heat capacity, attributed to its lower mass and, consequently, lower thermal inertia. The larger sensor exhibits the longest response time; however, no second-order behavior in the response curve of the sheathed thermocouple was observed, which would have been expected due to the sheathing of the sensor.

In addition, it is also observable that the response time strongly depends on the immersion velocity. This is again in agreement with the theory, since the response time decreases for increasing immersion velocity, which is caused by an increased heat transfer at the surface of the sensor. To furthermore investigate the influence of different calibration fluids on the response time of the sensors, the response time was also measured in dependence of the immersion velocity u_{im} for the plunging process in GaInSn, water, glycerin, and oil at 45 °C and for the FBG also in molten salt at 180 °C. The results are shown in Figure 5.8

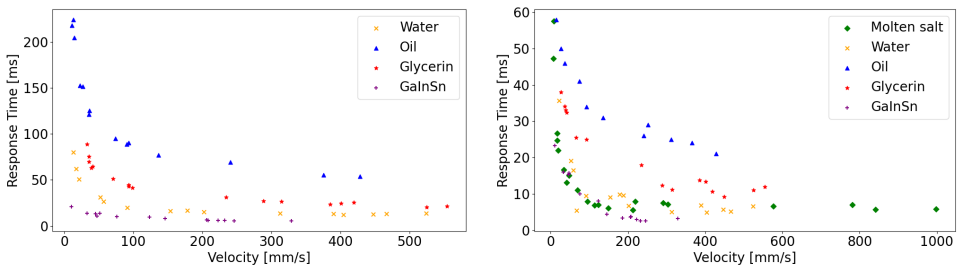

(a) TC dynamic calibration

(b) FBG dynamic calibration

Figure 5.8 - *Response time of the investigated sensors in dependence of the immersion velocity u_{im} for the plunging process in molten salt, GaInSn, glycerin, paraffin oil and water at* 45 °C *and HITEC at* 180 °C.

The graphs show that for both sensors, the longest response times are observed in oil, followed by glycerin, molten salt, water and GaInSn. Referring to the thermophysical properties of the fluids in Table 5.6, it can be concluded that the response time depends significantly on the thermal conductivity k of the fluid. The higher k, the better the heat transfer at the sensor surface, which leads to lower response times. A similar trend was also found in literature [68] when the time response of a coaxial type E thermocouple was estimated in water ($k \approx 0.6\,\mathrm{W/(m\,K)}$ and $\tau = 5.5\,\mathrm{ms}$) and in NaK molten salt ($k \approx 26\,\mathrm{W/(m\,K)}$ and $\tau = 0.63\,\mathrm{ms}$).

Additionally, the response time of the FBG sensor is significantly lower compared to the thermocouple, ranging from 20 % to 70 % less. The range of measured response times of the FBG in water is with 7 ms to 50 ms in good agreement with previous experimental studies carried out in water with the plunging technique [44, 85] that measured a time constant of 8.9 ms and 10.8 ms of a bare 125 µm FBG. However, the immersion velocity is not reported in neither of the two.

On the other hand, different studies in air performed with the laser technique showed time responses of $\tau \approx 77\,\mathrm{ms}$ [229], $\tau \approx 230\,\mathrm{ms}$ [225] and $\tau \approx 33\,\mathrm{ms}$ [88], the latter being carried out with a 14 µm FBG. It is clear that the obtained response times in the present studies are significantly shorter. The main reason for this discrepancy is that the heat-up process in the mentioned studies took place in air, which results in less effective heat transfer between FBG and surrounding. Hence, the response time is expected to be longer compared to measurements in liquids caused by a lower heat transfer coefficient. Furthermore, the temperature change in the fiber is generated by the laser assuming constant heat flux boundary condition in contrast to constant temperature conditions in the present study, which may also be a reason for differing results. All these differences show once again that comparability is limited due to many influencing experimental parameters.

Many studies in literature focus on regenerated and packaged FBGs for high temperature applications coherently obtaining higher respose times for coated and bigger sensors from $\tau \approx 50\,\mathrm{ms}$ [86] to $\tau \approx 9\,\mathrm{s}$ [87]. Only one paper was found evaluating

the dynamic analysis of the FBG used for strain sensing [243]. The obtained time response was $\tau \approx 1.4$ ms to 4.2 ms, interestingly lower than any time response registered when analyzing the temperature dependence. This difference suggests that varying the physical phenomenon responsible for the lengthening may lead to distinct time responses for strain and temperature measurements.

More considerations and comments about the trends of the time response and much more detailed analyses carried out with non-dimensional approaches about the transient heat transfer are shown in the published paper related to this work [45].

One final effect analyzed, which is useful for the purpose of this thesis, was the influence of the exposed length of temperature sensors from the ceramic tube (see Figure 2.9). It was possible to attach the sensors at any length outside the tube, necessitating an analysis to determine the optimal length. The exposed length must be sufficient to ensure that the sensitive parts of both sensors are uncovered, specifically exceeding 1 mm to ensure that the grating of the FBG is outside the tube. On the other hand, a shorter exposed length reduces the risk of bending the fiber due to fluid movement, thereby minimizing undesired strain effects, but also increases the effect of the thermal inertia given by the tube itself. The aim was to estimate the response time of the sensor for different exposed lengths and, once a stable value was reached, select the shortest exposed length among those tested. The tests were only conducted for the thermocouple, and the results are presented in Table 5.7.

Table 5.7 - *Response time of the thermocouple for different exposed lengths when plunged in water with an immersion velocity of* 150 mm/s.

Exposed length [mm]	**Time Response τ [ms]**
1	22.0 ± 4.6
2	15.4 ± 0.5
3	15.4 ± 0.5
4	15.0 ± 1.1
5	13.0 ± 0.9
10	13.2 ± 0.7
20	13.8 ± 2.2

It can be observed that the response time tends to stabilize at a constant value for exposed lengths between 2 mm to 5 mm. Therefore, the shortest possible length, i.e., 2 mm, was selected. Longer exposed lengths were excluded due to the potential for induced strain that could affect the reading of the fiber sensor, as explained above.

5.3 Effects of liquid metals on the FBG

Another issue worth noting is the atypical behavior exhibited by the FBG when employed in GaInSn, a subject covered in a publication by the author [244]. Notably, no damage to the gratings was detected when the fiber was utilized in molten salt at a temperature of 180 °C. Figure 5.9 displays the spectrum of the fiber in both

water and molten salt, while a spectrum in GaInSn is shown further in this Section in Figures 5.11 and 5.12.

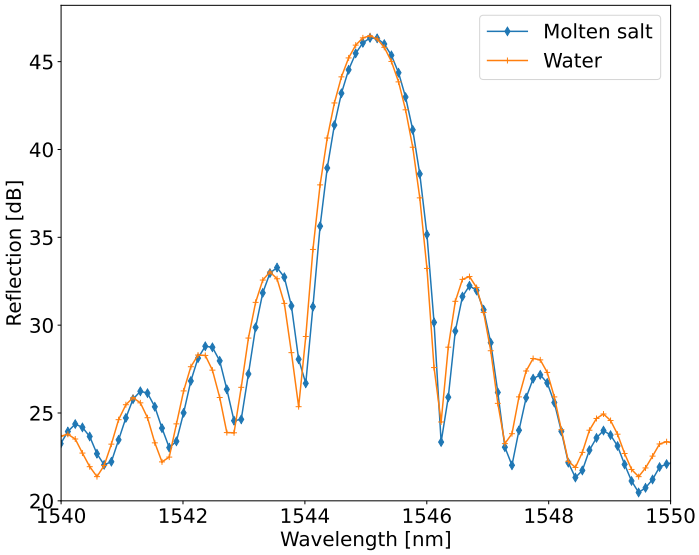

Figure 5.9 - *Comparison of the FBG spectra in molten salt and water. The molten salt spectrum was shifted in order to easen the comparison*

In Figure 5.9, the molten salt spectrum has been shifted so that its peak coincides with that of the water spectrum to facilitate a comparison of their shapes. The figure zooms in on the most relevant region, around the peak wavelength, where no significant differences can be observed between the two spectra, thereby confirming that the molten salt did not affect the spectral shape. This once again confirmed the suitability of the bare fiber at relatively high temperatures, theoretically allowing for its use in liquid metal environments like LBE. However, a peculiar behavior was observed when the fiber was used to measure temperature in GaInSn. The comparison between the time evolution of the temperature signals recorded by the fiber and the thermocouple at two different heights in the cavity along position 1 (see Figure 3.4) is presented in Figure 5.10.

More details about these profiles are provided in Chapter 8. At this point, they are presented solely to highlight the inconsistent behavior of the FBG in relation to the thermocouple. The figure demonstrates that the absolute value of the temporal evolution reveals discrepancies between the TC and FBG readings at certain points, such as at $y = 35\,\text{mm}$. Conversely, for other signals, such as at $y = 40\,\text{mm}$, the temporal evolution of the absolute values of the two signals aligns well.

Interestingly, when the average of the signals is removed, the fluctuations around the mean for both signals exhibit excellent agreement. This observation strongly

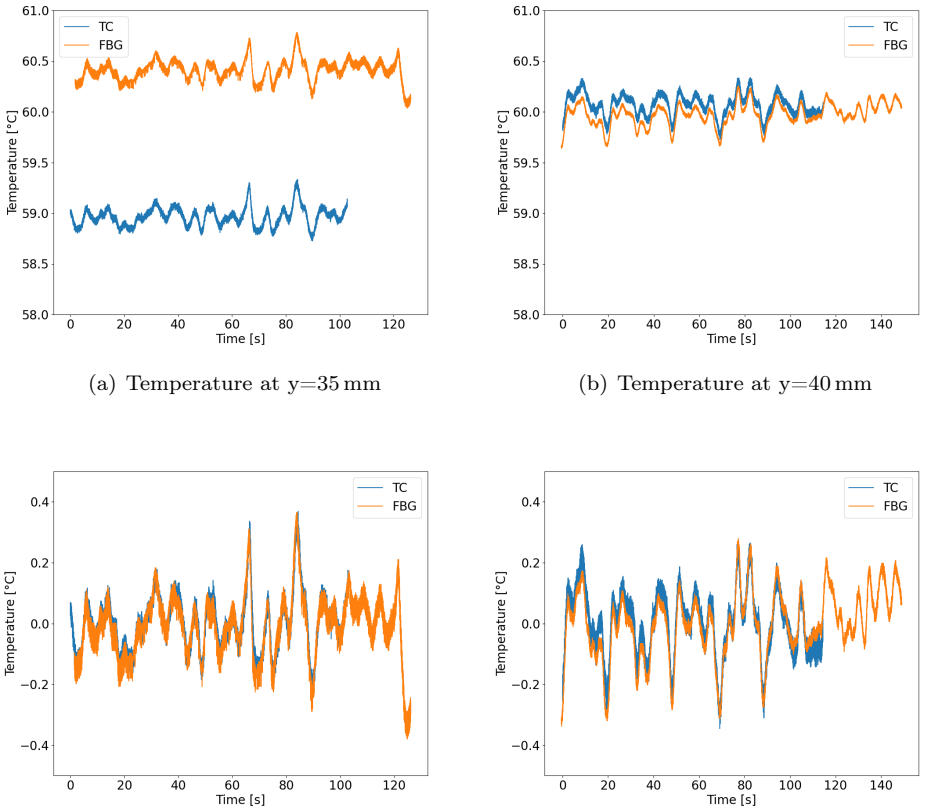

(a) Temperature at y=35 mm

(b) Temperature at y=40 mm

(c) Temperature fluctuations (mean removed) at y=35 mm

(d) Temperature fluctuations (mean removed) at y=40 mm

Figure 5.10 - *Time evolution of the signals of FBG and TC recorded at* y=35 mm *and* y=40 mm *of Position 1 in Figure 3.4. The cavity was filled with GaInSn. Despite the difference in the absolute value of the signals, the fluctuations around the mean are in very good agreement.*

suggests that both sensors are primarily capturing fluctuations of the same underlying phenomenon, namely temperature. This implies that strain-induced fluctuations are negligible compared to the temperature-induced ones. While a constant bending of the fiber could potentially introduce a constant offset in one of the signals, leading to the observed discrepancy in absolute values, this possibility is considered unlikely. The grating is situated near the neutral axis of the fiber, and the bendable length, i.e., the length extending beyond the tube, is approximately 2 mm. This minimizes the effect of bending on the signal, making temperature the predominant measured effect.

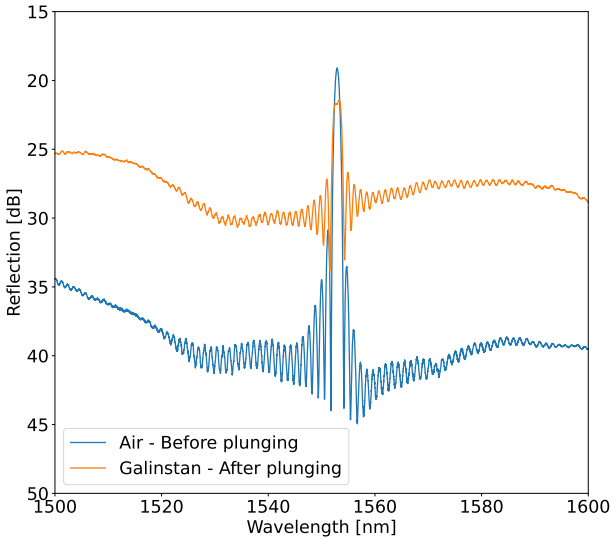

Figure 5.11 - *Effects of the liquid metal GaInSn on the FBG full spectrum*

To explore this phenomenon further, the spectra of the FBG were analyzed before and after the fiber was plunged in GaInSn without imposing any temperature change. The results are presented in Figure 5.11.

A notable initial observation is the increase of the power level of the reflection across the entire spectrum, indicative of increased noise. As temperature measurement relies solely on peak wavelength, this elevated noise may not inherently compromise temperature retrieval accuracy. However, a discernible flattening and a reduction in peak intensity are also observed. These peak alterations directly impact the final temperature measurement. To further investigate these phenomena, a magnified view of the peaks from various acquisitions is presented in Figure 5.12.

Two primary effects can be observed. The first, illustrated in Figure 5.12(a), is the flattening of the spectrum. It is evident that the shape of the spectrum becomes flatter and wider when submerged in the metal. The second effect, depicted in Figure 5.12(b), is the asymmetry of the spectrum, as demonstrated by the right secondary lobe, which is significantly higher than the left one. The combination of these two effects could, in principle, lead to the fitting algorithm failing to accurately retrieve the correct peak wavelength, thus resulting in incorrect temperature readings. This observation is consistent with the fact that temperature fluctuations are still detected correctly; once the peak is identified by the algorithm, it is reasonable to assume that the shift of the peak (even if inaccurately represented in absolute value) remains consistent, thereby providing reliable fluctuations.

Despite reaching out to the hardware provider, detailed information about the

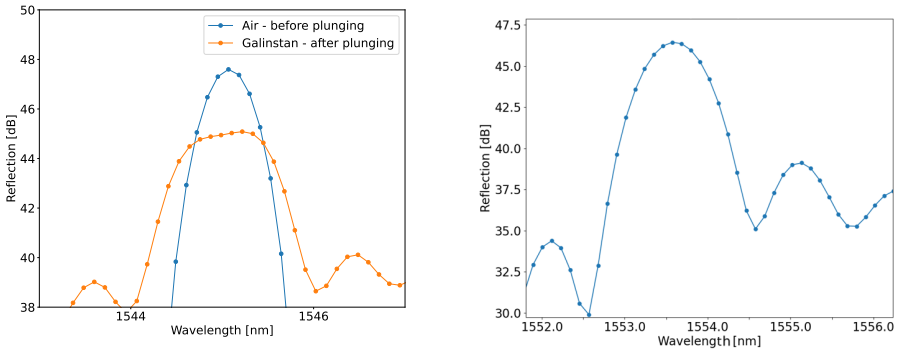

(a) Flattening

(b) Asymmetry, after plunging

Figure 5.12 - *Effects of the liquid metal GaInSn on the FBG spectra*

algorithm employed by the software was not obtained, preventing further investigation in this area. A preliminary estimation was attempted by exploring various peak-retrieving fitting algorithms available in the literature [220, 245, 246]. The approach involved considering for the fitting all points of the spectrum within a window of 3 dB, 6 dB, or 9 dB from the maximum value of the spectrum. The discrepancies between the peak wavelengths identified by different algorithms applied to the peak shown in Figure 5.12(b) and the value provided by the software were then compared in Table 5.8.

Table 5.8 - *Shift of the peak wavelength in respect of the value given by the Sense2020 software*

Shift of the peak wavelength in respect of the value given by the software *			
	3dB window	**6dB window**	**9dB window**
Gaussian fit	−0.74 pm	−0.30 pm	−1.58 pm
Polynomial fit	−2.24 pm	−6.24 pm	−113.10 pm
Center of gravity	−16.71 pm	−13.80 pm	−195.75 pm

It is evident that different algorithms are affected variably by the choice of the window, specifically by the number of points included in the analysis. Once again, due to the lack of details regarding the algorithm utilized by the Sense2020 software, it was impossible to draw further conclusions. However, it is possible to notice that some of the values reported in Table 5.8 are compatible with the temperature shift

*The conversion from the wavelength peak shift in pm to temperature in °C for this FBG is 8.66 pm/°C as reported in Table 5.3

observed in Figure 5.10(a).

Moreover, this effect exhibited inconsistent reproducibility. Spectral shape varied unpredictably when the fiber was immersed or even slightly moved within the metal. This variability made it challenging to conduct proper tests to investigate the phenomenon. However, several observations can be made:

- The issue is not temperature-dependent, as molten salts operating at 180 °C did not exhibit the phenomenon. Furthermore, the temperatures at which the phenomenon was detected never exceeded 80 °C.
- Reproducibility was inconsistent, making detection challenging and rigorous testing difficult to design.
- Tests with different fibers (all produced at the University of Mons as described in Section 5.1.2) and interrogators, achieving spectral resolution up to ≈ 1 pm, indicated fiber dependence but not interrogator dependence. Eventually, not all fibers exhibited the issue and, even when they did, the intensity of the spectrum shape change varied.

Following these considerations, one hypothesis is that reflections at the fiber tip cause the phenomenon. This aligns with several observations. The grating is inscribed at the fiber tip, minimizing the distance between the grating and the end and therefore making the reflections more likely to affect directly the zone with the grating. This scenario would render the phenomenon temperature-independent, as it would primarily depend on the reflectivity of the medium. This hypothesis also explains the occurrence of the phenomenon in GaInSn but not in other fluids or molten salt, a transparent, water-like fluid. The dependence on the fiber could be explained as an influence given by the cut on the fiber tip that could influence the mirror-like behaviour of the fiber and therefore the reflection intensity. As this issue was not previously reported in literature, the fiber cut was not consistently controlled during this work, limiting definitive conclusions.

Further investigation is necessary. However, the author believes that reflections at the fiber tip provide a plausible explanation for the observed phenomena. For future work, careful attention to the fiber tip cut is crucial when using the sensors in highly reflective fluids such as GaInSn.

5.4 Conclusions

This Chapter provided a detailed analysis of the performance of the temperature sensors to assess their behavior, particularly in terms of time response during the final measurements in liquid metals. The analysis was then expanded to include other fluids and the investigation of various effects, with the results subsequently published in a journal article [45].

The primary conclusion drawn from this study is the recognition of the impossibility of determining a singular value for the time response of a sensor, as this parameter

is not solely an intrinsic property of the sensor itself, but also depends on the environmental and experimental conditions. Nonetheless, the different values reported here align with the requirements specified in Section 2.1. In particular, Figure 5.7(d) illustrates a time response ranging from 10 ms to 15 ms for both sensors in the range of the expected velocities of the GaInSn under natural convection in the cavity. As a summary, Table 5.9 reports the values of the spatial and temporal resolutions expected by the sensors in the final measurements with the two working fluids.

Table 5.9 - *Spatial and temporal resolution of temperature sensors for water and GaInSn*

Sensor	**Spatial Resolution** $\mathbf{\Delta x}$ **[mm^3]**	**Temporal Resolution** $\mathbf{\Delta t}$ **[ms]**	
		Water	**GaInSn**
TC	2×10^{-2}	≈ 55	≈ 15
FBG	5×10^{-2}	≈ 35	≈ 10

The temporal resolution was derived from the analysis conducted in Section 5.2.2, considering the expected velocity ranges in both fluids. Although the values in water were slightly higher than initially estimated due to the low flow velocities, the temporal resolution of the sensor remains sufficient to conduct the final measurements. This is particularly true in GaInSn, where the slightly higher velocities and the higher thermal conductivity of the fluid contribute to maintaining a low response time for the temperature sensors. The spatial resolution of the sensors is solely determined by their dimensions and, as such, was not further addressed in this Chapter. The reported values are consistent with those presented in Chapter 2 and were only recalculated based on the dimensions of the selected sensors. These values are independent of the fluid medium.

Moreover, the uncertainty analysis carried out in Section 5.2.1 show total uncertainties of the sensors only slightly lower than the magnitudes of the temperature fluctuations estimated in Chapter 2. This effect will be therefore taken into account and further analyzed in Chapter 8.

Additional results encompass several key findings: firstly, the anticipated trend was confirmed, with the sensors exhibiting faster response times in high-conductivity fluids, such as liquid metals, compared to water. Secondly, it was observed that the rate of immersion, or plunging speed, demonstrates an inverse relationship with response time, where faster immersion leads to shorter response times. However, the ultimate effect on achieving a plateau in time response depends on the interaction with other considered parameters.

Finally, the influence of the length of the sensors outside of the ceramic tube was found to be negligible within the range of 2 mm to 5 mm, leading to the selection of 2 mm as the final value for the tests.

Eventually, Section 5.3 addresses the behavior of the FBG in GaInSn, as its unpredictable change in the peak shape was an unexpected side result of this analysis that could significantly affect the following measurements. However, a plausible ex-

planation has been found in the light reflection obtained by the fluid itself, strongly dependent on how the fiber is cut at the tip, and therefore highlighting the importance of this manufacturing aspect when using the fibers in highly reflective fluids. The final outcomes and implications of this behavior for the present work are presented in Chapter 8.

Chapter 6

Ultrasound Doppler Velocimetry

Ultrasound Doppler Velocimetry (UDV) is a velocity measurement technique particularly well-suited for opaque fluids such as liquid metals. Its primary advantage lies in its reliance on the propagation of sound waves, eliminating the need for optical access to the flow field. Furthermore, UDV is non-intrusive and enables simultaneous, distributed velocity measurements [99–101]. As one of the main drawbacks, the technique itself is inherently influenced by numerous parameters, and optimizing these variables poses a significant challenge [100, 247]. Furthermore, when applied in harsh environments such as liquid metals, its effectiveness is not always reliable, and the relationships between these parameters and successful measurement outcomes have yet to be fully elucidated [12, 51].

This Chapter focuses on analyzing the relationships between these influencing factors to better understand their impact on measurement outcomes. It begins by detailing the general working principle of UDV in Section 6.1, providing a foundation to identify where each parameter plays a role and how it affects the measurement process. A separate experimental setup adopted for the UDV characterization is then outlined in Section 6.2. Particular attention is given to the choice of the seeding particles and the uncertainty calculation, respectively in Sections 6.3 and 6.4. Eventually, the results obtained are presented in Section 6.5.

6.1 Working Principle

Ultrasound Doppler velocimetry (UDV) operates on the pulse-echo principle and relies on the presence of acoustic inhomogeneities within the fluid to provide velocity measurements. In molten metals, these inhomogeneities often occur naturally (typically as oxides), while in other fluids such as water, scattering particles must be artificially introduced. The simplest ultrasonic measurement configuration typically employs a single ultrasound transducer, functioning as both an emitter and receiver of

acoustic waves. This transducer, based on the piezoelectric effect, emits a short ultrasonic pulse composed of harmonic wave trains (N_{cycles}) at an emission frequency f_e within the range of 1 MHz to 10 MHz, which propagates as a longitudinal wave along the acoustic axis with the sound velocity of the medium. As the pulse propagates through the fluid, a portion of the acoustic energy is scattered by the inhomogeneities (or particles) moving at velocity U. As a convention, U is negative when the target is moving toward the transducer. Figure 6.1 shows the schematic of the measurement of the fluid velocity in a pipe taken as a reference for this explanation.

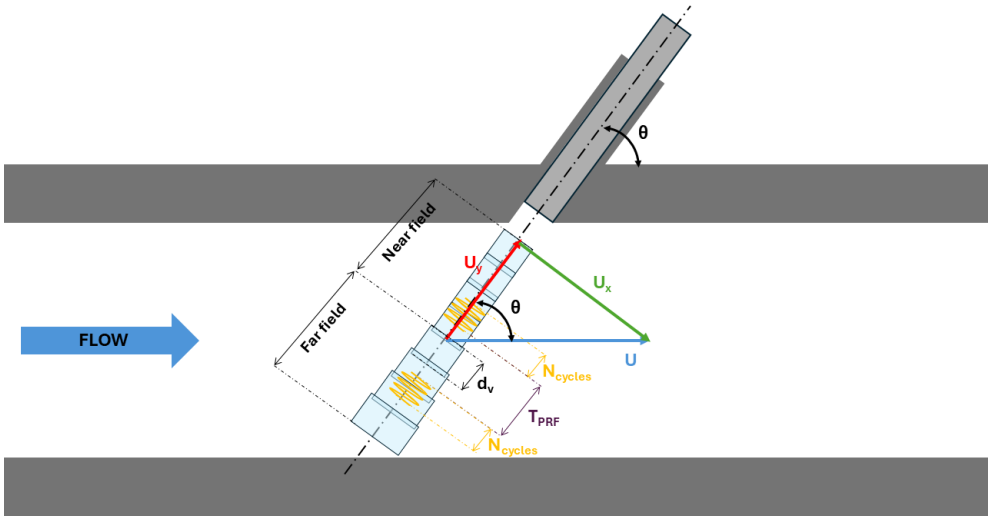

Figure 6.1 - *Schematic of the UDV velocity measurement in a pipe.*

Due to this movement, the frequency f_t perceived by the target particle is described by Equation (6.1), where:

- c = speed of sound in the medium,
- f_e = pulse emission frequency,
- θ = inclination of the sensor relative to the main flow direction.

$$f_t = f_e \left(1 - \frac{U \cos\theta}{c}\right) \tag{6.1}$$

The reflected echo signal, consisting of scattered echoes from all particles in the propagation zone, is received by the same transducer with a frequency f_r given by Equation (6.2):

$$f_r = f_e \left(1 + \frac{U \cos\theta}{c}\right) \tag{6.2}$$

The difference between these two frequencies, known as the Doppler frequency shift f_D, is expressed by Equation (6.3):

$$f_D = f_t - f_r = \frac{2 f_e U \cos\theta}{c} \tag{6.3}$$

In pulsed Doppler ultrasound, the probe does not work in continuous mode but emits short ultrasonic bursts with a time interval t_{PRF}, known as the Pulse Repetition Frequency (PRF), and continuously receives echoes from targets located within the path of the ultrasonic beam. By measuring the changes in phase between successive echoes, the shift in the scatterer positions along the full axis of the probe can be determined, thereby providing a complete axial velocity profile along the entire direction of pulse propagation [99, 248]. In fact, it is possible to relate the position of a particle in the ultrasonic beam to the time delay t_D between an emitted burst and the echo reflected by the particle via Equation (6.4).

$$P = \frac{c \times t_D}{2} \tag{6.4}$$

Through the knowledge of the time between pulses t_{PRF}, it is possible to estimate the particle displacement $P_2 - P_1$ using Equation (6.5), and then rearranging to retrieve the axial velocity of the fluid $U_y = U \times \cos\theta$, as shown in Equation (6.6).

$$P_2 - P_1 = U \times \cos\theta \times t_{\mathrm{PRF}} = U_y \times t_{\mathrm{PRF}} = \frac{c \times (t_{D,1} - t_{D,2})}{2} \tag{6.5}$$

$$U_y = \frac{P_2 - P_1}{t_{\mathrm{PRF}}} = \frac{c \times (t_{D,1} - t_{D,2})}{2 t_{\mathrm{PRF}}} \tag{6.6}$$

Given that $(t_{D,1} - t_{D,2})$ can be very small, typically in the order of microseconds, it is often more practical to replace it with the phase shift δ, given by Equation (6.7).

$$\delta = 2\pi f_e (t_{D,1} - t_{D,2}) \tag{6.7}$$

Therefore the particle axial velocity can be written as in Equation (6.8):

$$U_y = \frac{c \times \delta}{4\pi \times f_e \times t_{\mathrm{PRF}}} \tag{6.8}$$

δ represents the change in phase between successive pulse echoes. The phase shift arises due to the displacement of scatterers in the fluid relative to the transducer during the time between consecutive pulse emissions t_{PRF} and can therefore contain the same information of a Doppler frequency. From this analogy comes the name Ultrasound Doppler Velocimetry. Recalling also Equation (6.3), it is possible to see how Equation (6.8) and Equation (6.9) share the same mathematical form being both dependent on a phase shift.

$$U_y = \frac{c \times f_D}{2 f_e} \tag{6.9}$$

However, it is important to underline that the Doppler frequency f_D itself, is never directly measured and what allows us to measure the velocity U_y is the phase shift δ of the echo signal between two successive transmissions.

In order to obtain accurate measurements, not only the parameters in Equation (6.9) must be known, but several other parameters must also be configured within the acquisition software. Due to their interdependence and the influence of external conditions, optimizing these parameters is non-trivial. The literature commonly identifies four critical parameters [51, 102, 249, 250]:

- **Pulse repetition frequency (PRF)**: The inverse of PRF, t_{PRF}, is the time between two consecutive emissions and therefore one of the key parameters to be set by the operator in the acquisition software. The PRF determines the maximum detectable frequency shift, and thus the maximum velocity as well as the maximum detectable depth [152]. In fact, when sampling f_D at a frequency PRF, the maximum detectable f_D is half of PRF due to Nyquist limitations. Therefore, recalling Equations (6.4) and (6.9), these values are related by Equations (6.10) and (6.11):

$$U_{\mathrm{y,max}} = \frac{c}{4 f_e \times t_{\mathrm{PRF}}} \tag{6.10}$$

$$P_{\mathrm{max}} = \frac{c \times t_{\mathrm{PRF}}}{2} \tag{6.11}$$

  with:

$$P_{\mathrm{max}} U_{\mathrm{y,max}} = \frac{c^2}{8 f_e} \tag{6.12}$$

  While the constant $P_{\mathrm{max}} U_{\mathrm{y,max}}$ can be calculated for a given fluid and sensor, yielding a value of approximately $0.1\,\mathrm{m^2/s}$ for GaInSn, the other parameters are closely tied to the choice of the t_{PRF}. For the cavity measurements in GaInSn, however, $U_{\mathrm{y,max}}$ does not fall below $70\,\mathrm{mm/s}$, and P_{max} remains above $0.137\,\mathrm{m}$, thus allowing for the measurement of the expected velocities within the setup.

- **Emissions per profile EP**: it is the number of data pulses collected and processed by the acquisition system to calculate the final estimated velocity related to one profile. This parameter, together with the PRF, determines the real temporal resolution of the acquisition, i.e. its sampling frequency f_s. While increasing this value reduces variance, it also impacts temporal resolution, which is theoretically given by Equation (6.13).

$$f_s = \frac{1}{t_{PRF} \times EP} \tag{6.13}$$

  In reality, also delays of the electronics, the time lapse used to transfer data and a fixed number of EP used for internal computation (16) should also be taken into account when computing the real sampling frequency f_s which will be therefore always worse than the theoretical one

- **Axial resolution $\mathbf{d_v}$**: The axial resolution defines the distance between the centers of two consecutive sampling volumes as shown in Figure 6.1 but it does not affect their radial dimension, which mainly depends on the size of the piezoelectric sensor itself and is determined by the burst length N_{cycles} according to Equation (6.14):

$$d_{\text{v}} = \frac{cN_{\text{cycles}}}{2f_e} \tag{6.14}$$

- **Emitting power**: it is the power of the emitted US signal. Higher power improves signal-to-noise ratio but may introduce phase-shift errors and signal degradation due to increased ringing in the transducer and higher dissipated energy.

Given the strong interdependence of these parameters, the following sections focus on understanding their impact through practical experiments. Insights regarding other software settings are also discussed, but the emphasis remains on the aforementioned key parameters due to their direct influence on spatial and temporal resolution, as well as signal quality.

An important consideration when selecting the sensor is the shape of the ultrasonic beam. Ideally, the beam should remain as narrow as possible throughout the measurement depth to minimize the measuring volume and optimize the spatial resolution. However, the geometry of the acoustic field is governed by the diameter of the transducer D_{UDV} and the ultrasonic wavelength $\lambda_e = c/f_e$. The evolution of the ultrasonic field is illustrated in Figure 6.2, comparing the theoretical beam shape for sensors of the same external diameter ($D_{\text{UDV}} = 8\,\text{mm}$) at emitting frequencies f_e of 8 MHz and 10 MHz.

Two distinct regions are observed in Figure 6.2:

- **Near field**: A cylindrical region near the transducer whose length L_{NF} is given by Equation (6.15):

$$L_{\text{NF}} = \frac{D_{\text{UDV}}^2}{4\lambda_e} \tag{6.15}$$

  In this region, oscillations in the intensity of the acoustic beam can affect the Doppler measurements, and empirical tests are often required to assess their impact on the final measurements.

- **Far field**: Beyond the near field, the intensity decreases with distance, and the beam assumes a conical shape with divergence χ given by Equation (6.16):

$$\chi = 2\arcsin\left(\frac{1.22\lambda_e}{D_{\text{UDV}}}\right) \tag{6.16}$$

  Radial oscillations of the intensity are typically appearing in this region.

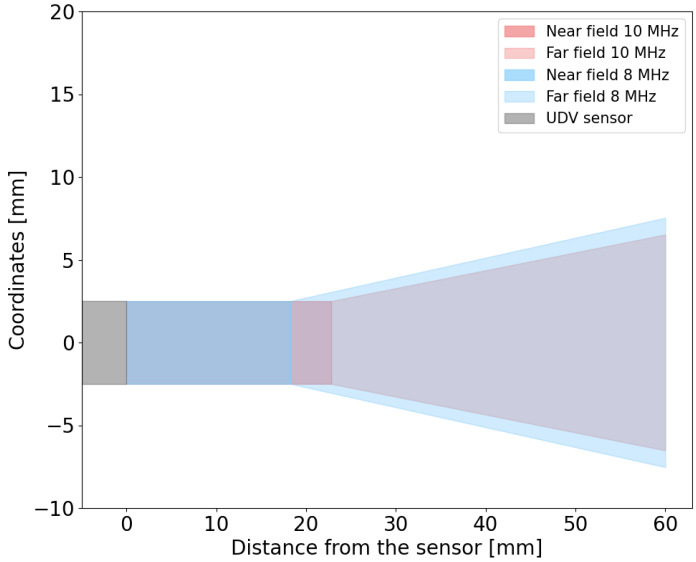

Figure 6.2 - *Comparison of the US cone shape for two different sensors. The higher the emitting frequency f_e, the longer is the near field. At the same time the divergence of the cone is smaller therefore providing an overall better spatial resolution.*

It is evident that these values are derived from theoretical calculations and only provide an estimation of the general shape of the ultrasonic beam. The significance of these regions will be further emphasized in the subsequent Sections of this Chapter and in Chapter 8, demonstrating their impact on the final measurements.

One final aspect to highlight, which is inherently part of the working principle of the sensor, is that the UDV technique does not require calibration. The velocity of particles U_y is determined based on the emission frequency f_e, the measured Doppler frequency f_D, and the speed of sound c. Once the speed of sound is known with sufficient accuracy, it directly provides the absolute value of the particle velocity, without the need for calibration against a reference sensor. However, uncertainties in the involved parameters can introduce inaccuracies in the velocity measurements, particularly in fluids like GaInSn, where the relationship between temperature and the speed of sound is not well established. Some previous studies therefore performed comparative calibrations of the sensor by testing it against a known flow [102, 251], consistently reporting errors of less than 5% even at velocities in the order of mm/s [102]. For the purpose of this thesis, it was decided not to perform additional sensor calibration, and to manage the uncertainties arising from this decision, as discussed in Section 6.4.

6.2 Water loop setup

Preliminary tests aimed at characterizing the UDV technique were conducted in a water closed forced convection loop, as illustrated in Figure 6.3.

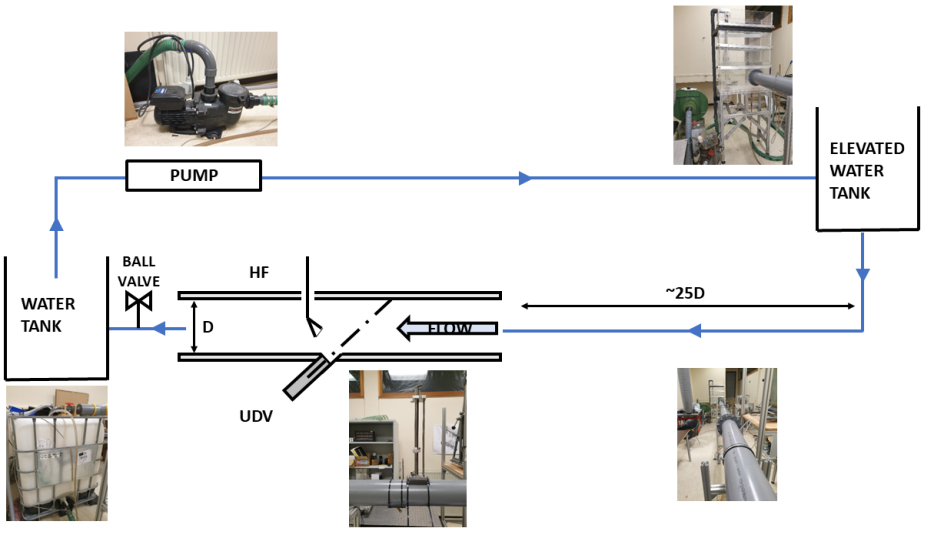

Figure 6.3 - *Schematic of the closed water loop, with pictures of each component included.*

The water is stored in a reservoir with a capacity of 1000 L and is pumped into an elevated tank connected to the main pipe, which has a diameter of 150 mm and a total length of 8 m. The water flows through this pipe for ≈ 4 m $= 25$D before reaching the section where the sensor is installed. Additionally, tests were performed using a hot film probe, and its placement is indicated in Figure 6.3; however, results obtained with this probe are presented in Chapter 7. The TR0408LS UDV sensor (4 MHz US, 8 mm diameter) was flush-mounted at the bottom of the pipe, inclined at an angle of $\theta = 45°$, allowing for direct contact with the water. At the end of the main pipe, the water naturally flows to the initial reservoir.

This experimental setup was chosen primarily to enable control over the velocity across a range of Reynolds numbers, $Re = 10$ to 40 000. However, fine control of the flow characteristics was imprecise, relying on a ball valve for adjustment. The well-established behavior of fully developed flow in a pipe allowed focusing the investigation on the influence of sensor settings without introducing the further complexity of an unknown flow configuration.

6.3 Seeding

As previously mentioned, the presence of scatterers in the flow is crucial for successful measurements. In a facility such as the one described in Section 6.2, the large volume of water involved complicates the provision of the appropriate amount and type of scatterers. Additionally, since Particle Image Velocimetry (PIV) was conducted in the same facility prior to these tests, some residual particles remained in the pipes. Thus, the tests performed in the water loop facility of Section 6.2 relied on these existing particles, as well as on water impurities and microbubbles generated by the descent of the water, without the addition of any artificial tracers. The results presented in Section 6.5.1 indicate that this approach was effective.

Nevertheless, an extensive analysis of the optimal particle types for UDV measurements was conducted, keeping in mind that the final measurements were performed in a much smaller and controlled setup as the one described in Chapter 3. Four primary parameters must be considered when selecting the most suitable particles for UDV measurements [252, 253]:

- **Particle Dimensions**: The dimensions of the particles play a vital role in UDV measurements. The particle diameter should ideally be equal to or smaller than the wavelength of the ultrasound wave, defined as $\lambda_e = c_f/f_e$ with c_f being the speed of sound in the fluid. However, the diameter should not be excessively small, or else insufficient scattering will occur for detection by the transducer. Empirical guidelines suggest $d_p > 0.02\lambda_e$ [254] and $d_p \approx \lambda_e/4$ [248]. For a probe operating at a frequency of 10 MHz, this optimal value in water corresponds to $d_p \approx 39\,\mu m$, while for a frequency of 8 MHz, $d_p \approx 48\,\mu m$. For GaInSn, where the speed of sound is higher, these values increases respectively to $d_p \approx 68\,\mu m$ and $d_p \approx 86\,\mu m$

- **Stokes Number**: The Stokes number, defined as in Equation (6.17)

$$St = \frac{\tau_v}{t_c} \tag{6.17}$$

  is a non-dimensional parameter that represents the ratio of the viscous time lag of a particle (τ_v), i.e., its characteristic time, to the characteristic time of the flow (t_c). The former should be minimized to ensure accurate tracking of fluid motion. Ideally, the particle response time should be significantly lower than the time response of the sensors and the characteristic timescales of the flow phenomena under investigation. For this work, this typically translates to a target τ_v on the order of milliseconds. The latter is often calculated as the ratio between a characteristic length of the flow, e.g. the boundary layer thickness or the dimension of an obstacle, and the characteristic velocity of the flow, e.g. the freestream velocity. The relaxation time of the particle due to drag forces is given by Equation (6.18), where ρ_p and d_p are the density and diameter of the particle, respectively, and μ_f is the dynamic viscosity of the fluid. The Stokes number gives an indication of the lag of the particles in following the fluctuations of the fluid.

$$\tau_v = \frac{\rho_p d_p^2}{18\mu_f} \tag{6.18}$$

- **Density Ratio**: The density ratio, defined as $R_\rho = \frac{\rho_p}{\rho_f}$, represents the ratio of the particle density ρ_p to the fluid density ρ_f. This ratio provides an estimate of how well the particle can capture the amplitude of velocity fluctuations in the fluid.

- **Acoustic Impedance**: The acoustic impedance $Z = \rho c$ is the product of the density ρ and the speed of sound c. It is a critical parameter, as the amplitude of the energy of the signal scattered by the particle is given by:

$$\Omega = \frac{Z_f - Z_p}{Z_f + Z_p} \tag{6.19}$$

  A greater difference in acoustic impedance between the particle and the medium results in better quality scattered signals.

The inter-dependence of these parameters provides critical insights for selecting the optimal particles. In particular, it can be interesting to study the mechanics of a single particle regulated by Equation (6.20) in the non-dimensional form [255, 256] where the term on the left hand side is related to the inertia of the particle, the first term on the right hand side to the viscous drag and the last term to the added mass term.

$$St\,\frac{\partial U_p}{\partial t} = \frac{(U_f - U_p)}{t_c} + \frac{3}{2R_\rho}St\,\frac{\partial U_f}{\partial t} - \frac{St}{2R_\rho}\frac{\partial U_p}{\partial t} \tag{6.20}$$

Considering harmonic oscillation of the fluid velocity $U_f(t)$, it is possible to solve the linear ODE with constant coefficient in Equation (6.20) to obtain Equation (6.21) as solution for the ratio of the fluctuations amplitude U_p/U_f in the oscillation [255, 257] where $s = 2\pi i$ is the complex frequency used as variable for the Laplace transform.

$$r = \frac{U_p}{U_f} = \frac{1 + \frac{3\,St}{2R_\rho}s}{\left(St + \frac{St}{2R_\rho}\right)s + 1} \tag{6.21}$$

Therefore, it is possible to see that if $R_\rho = 1$, the particles can, in principle, follow any frequency of the fluid since $r = U_p/U_f = 1$. However, achieving a perfect density match between particles and fluid is often challenging, if not impossible. In such cases, it is advisable to maintain a low Stokes number to effectively follow the fluctuations. Therefore, when achieving $R_\rho = 1$ is unfeasible, keeping $St \to 0$ is beneficial. A graphical representation of the analysis is provided in Figure 6.4, where the ratio of amplitude r is shown as a function of the St number for various particle types in water [255].

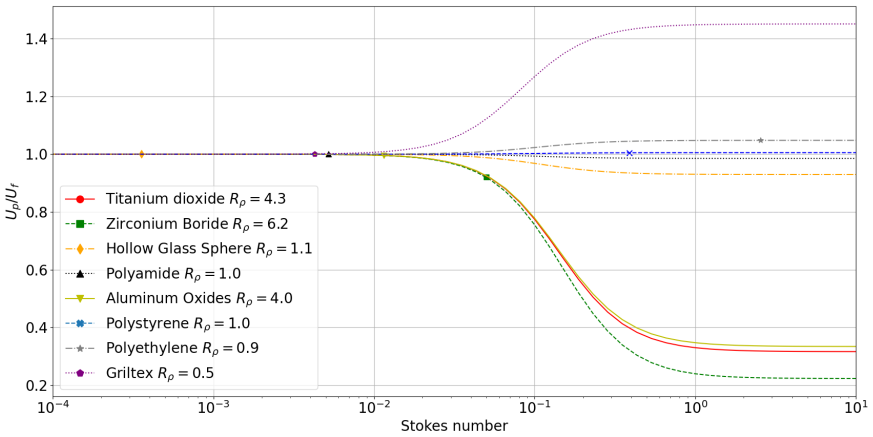

Figure 6.4 - *Ratio of velocity fluctuation amplitudes as a function of the Stokes number in water. Each line represents a different material, with markers indicating specific particle sizes available on the market.*

In particular, for a given particle with $R_\rho \neq 1$, it is also possible to estimate the maximum frequency of the flow $f_{cut-off}$ that the particle can follow as in Equation (6.22) recalling Equation (6.17) where St_p is the St number for the given particle.

$$f_{cut-off} = \frac{St_p}{\tau_v} \tag{6.22}$$

In liquid experiments, buoyant forces may also play a significant role. Therefore, it is important to consider the terminal velocity U_T, expressed in Equation (6.23):

$$U_T = \frac{(\rho_f - \rho_p) g d_p^2}{18 \mu_f} \tag{6.23}$$

It is advisable to maintain the ratio $\frac{U_T}{U_f} \ll 1$. However, even if this condition is satisfied, the deposition effects in the absence of flow must be considered. Additionally, lift forces should be taken into account when operating in regions with high velocity gradients.

Following this theoretical overview, the particles considered for the cavity experiments are summarized in Table 6.1. The characteristic frequency of the fluids was taken as a reference $f = 100\,\text{Hz}$, consistently with Chapter 2 and the characteristic velocities of the fluids were taken from the DNS simulations of Chapter 4.

Table 6.1 - *Comparison of the different particles analyzed for water and GaInSn for a US emitting frequency of* 10 MHz

Particle Material	d_p [µm]	$\frac{\mathbf{D}}{\lambda_e/4}$ [/]	St_p [/]	τ_v [µs]	R_ρ [/]	Ω [/]	r [/]	$f_{cut-off}$ [Hz]
				Water				
Titanium dioxide	0.2	0.01	5.4×10^{-7}	5.42×10^{-3}	4.25	1	1	All
Zirconium Boride	50	1.3	5.0×10^{-2}	4.98×10^{2}	6.25	NA	0.92	46
Hollow Glass Sphere	10	0.26	3.6×10^{-4}	3.55×10^{0}	1.11	1	1	All
Polyamide	40	1.04	5.2×10^{-3}	5.22×10^{1}	1.02	1	1	All
Aluminum oxides	30	0.78	1.2×10^{-2}	1.15×10^{2}	4	1	1	All
Polystyrene	350	9	0.4	3.88×10^{3}	0.99	1	1	All
Polyethylene	925	24	2.5	2.54×10^{4}	0.93	0.99	1.05	39
Griltex	50	1.3	4.3×10^{-3}	4.25	0.53	0.99	1	All
				Galinstan				
Titanium dioxide	0.2	< 0.01	5×10^{-7}	5.03×10^{-3}	0.66	1	1	All
Zirconium Boride	50	0.73	4.6×10^{-2}	4.6×10^{2}	0.97	NA	1	All
Hollow Glass Sphere	10	0.15	3.3×10^{-4}	3.28×10^{0}	0.17	1	1	All
Polyamide	40	0.58	4.8×10^{-3}	4.82×10^{1}	0.16	1	1.02	1.4
Aluminum oxides	30	0.44	1.1×10^{-2}	1.06×10^{2}	0.62	1	1	All
Polystyrene	350	5.1	3.6×10^{-1}	3.58×10^{3}	0.15	1	2.28	6
Polyethylene	925	13.50	2.3	2.35×10^{4}	0.15	0.99	2.32	1
Griltex	50	0.73	3.9×10^{-3}	3.9×10^{1}	0.08	0.99	1.05	1
Optimal value	/	1	$\ll 1$	$\ll 1$	1	1	1	$\gg 100$

Once again, it is important to highlight that these parameters only give an indication and do not give absolute rules about the performances of the particles as scatterers. More than one type of particle is in principle suitable for measurements in water and GaInSn. For the focus of this work, i.e., fluctuations of the velocities, priority has been given to the dynamic parameters, e.g., the cut-off frequency, the viscous time lag, and fluctuations amplitude ratio. In the end, following also suggestion of the manufacturer, Griltex particles made of copolyamide by Signal Processing with a diameter of 40 µm to 60 µm were used for the water measurements in the cavity.

A similar analysis was carried out for GaInSn. As shown in the bottom part of Table 6.1, the signal quality in GaInSn was found to be acceptable without the addition of any external particles. This is likely due to the presence of naturally occurring gallium oxide Ga_2O_3particles within the fluid. Gallium oxide forms spontaneously when the liquid metal is exposed to oxygen, resulting in the formation of particles with a density close to that of GaInSn ($\rho = 6440\,\mathrm{kg/m^3}$). Therefore, these particles effectively follow the flow fluctuations, providing a suitable scattering medium for the UDV measurements. However, the formation of these particles is a complex process, involving the agglomeration of the oxide layer that forms on the free surface of the liquid metal due to fluid motion. This makes it difficult to predict the exact size and distribution of these naturally occurring particles, which in turn can introduce uncertainties into the UDV measurements. Nevertheless, no external particles were added during the GaInSn measurements within the cavity, and the results obtained in this configuration are presented in Chapter 8.

One last key point not covered by these theoretical considerations is the concentration of particles needed to achieve a good quality of the signal. The exact value also depends on the emitting frequency f_e and the expected exploration depth P_{max} [254], so that a unique value is difficult to find. Moreover, adding too many particles could lead to changes of the fluid properties and to the presence of impurities in the fluid that in the framework of this work could cause damage to other fragile probes, e.g. the hot-film. The best practice for deciding the amount of particles to be put in a flow is to continuously record the UDV signal of the flow and stop when the quality of the signal is not improving. This has been said to the author by different researchers and sensor manufacturers. However, an empirical rule says that a concentration of 50 mg/L is usually a good first attempt value to try. Moreover, successful measurements have been carried out with a concentration of 30 % in mud and 50 % in blood [254]. For this project, during the water measurements in the cavity, a concentration of 250 mg/L was found to be empirically the best despite being higher than the aforementioned values. The final choices made for the different experimental setups are therefore summarized in Table 6.2.

6.4 Uncertainty calculation

The calculation of uncertainty is made following the guidelines of the Guide to the Expression of Uncertainty in Measurement (GUM) by the Joint Committee for Guides in Metrology (JCGM) [223], therefore calculating separately type A and type B uncertainty. Type A uncertainty is the one deriving from the statistical analysis of a

Table 6.2 - *Summary of particles used in different setups*

Setup	Working fluid	Particles	Concentration
Loop	Water	Impurities PIV particles Microbubbles	NA
Cavity	Water	Griltex 50 µm	250 mg/L
Cavity	GaInSn	Gallium Oxides	NA

series of observations and it decreases as the number of measurements increases. For statistically independent data, it can be generally expressed by Equation (6.24):

$$u_{A,U} = \frac{k \times \sigma}{\sqrt{N}} \tag{6.24}$$

where σ is the standard deviation, N is the number of measurements performed and k is a parameter related to the confidence interval associated with the measurement. For the current work, $k = 2$ in order to achieve a confidence interval of 95 % [223]. It might be interesting to highlight that, as it will be extensively mentioned in Chapter 8, the evolution in time at points along the measured profile had values where the signal was below the minimum threshold, and therefore they were registered as zero. The calculation of the type A uncertainty was carried out after removing such zeros from the profiles. Type B uncertainty is related to means other than statistical analysis, e.g., with the use of estimates from previous measurements, specifications from the manufacturer, handbooks, calibration certificates, etc. In the case of the UDV, only a few papers in the literature address this specific issue [249, 258]. In particular, the work of Nauber *et al.* (2020) [249] was taken as the main reference for this calculation. Therefore, type B uncertainty is calculated considering the general equation for the velocity as reported in Equation (6.9). The considered parameters are:

- f_D, the Doppler frequency shift. Recalling Equation (6.3) and knowing the order of magnitudes of the targeted velocities, it is possible to estimate its value and its dependencies on the other parameters for the propagation of uncertainty.
- f_e, the US emitting frequency depending on the sensor used and subjected to the uncertainties due to the electronics of the system.
- θ, the angle between the main direction of the flow and the axis of the sensor. The value of the angle changes with the experimental setup, varying from $\theta = 0°$ in the main setup of Chapter 3 and $\theta = 45°$ in the water loop of Section 6.2. Its uncertainty is also dependent mainly on the building of the setup.
- c is the speed of sound in the fluid. Since c can be expressed as a function of temperature, its uncertainty has been reported to the uncertainty of temperature. In particular, for water, the third order fit polynomial given by Equation (6.25a)

was obtained by fitting the experimental data by [259], and the uncertainty over the speed of sound was calculated with the law of propagation of uncertainty starting from the uncertainty on the temperature measurement.

$$c = C_1 T^3 + C_2 T^2 + C_3 T + C_4 \tag{6.25a}$$
$$C_1 = 0.0001\,\mathrm{m/(sK^3)}, \tag{6.25b}$$
$$C_2 = -0.0455\,\mathrm{m/(sK^2)}, \tag{6.25c}$$
$$C_3 = 4.7456\,\mathrm{m/(sK)}, \tag{6.25d}$$
$$C_4 = 1404.3\,\mathrm{m/s}. \tag{6.25e}$$

However, to the knowledge of the author, the same dependence is currently not existing for GaInSn. Only a few papers cite the values $c = 2730\,\mathrm{m/s}$ and $\partial c/\partial T = -0.3\,\mathrm{m/(s\,K)}$ [166, 249, 258] which have also been used for this thesis. Another way to approach this issue would be to use the function provided by the software UDOP4000, able to retrieve the speed of sound in the medium. With this function, the user can set the distance s between the sensor and the wall and the probe sends an US pulse and measures the time t_0 that it takes for the pulse to come back to the probe. The speed of sound is therefore retrieved as in Equation (6.26):

$$c = \frac{2s}{t_0} \tag{6.26}$$

Using again the law of propagation of uncertainty, Equation (6.27) expresses the relative uncertainty u_c/c of the speed of sound:

$$\frac{u_c}{c} = \sqrt{\left(\frac{\partial c}{\partial s}\frac{u_s}{c}\right)^2 + \left(\frac{\partial c}{\partial t_0}\frac{u_{t_0}}{c}\right)^2} = \sqrt{\left(\frac{2}{t_0}\frac{u_s}{c}\right)^2 + \left(2s\frac{u_{t_0}}{c}\right)^2} \tag{6.27}$$

Considering that such a test would take place in the cavity with $s = 60 \times 10^{-3}\,\mathrm{m}$ and with $c_{\mathrm{GaInSn}} \approx 2740\,\mathrm{m/s}$, it is obtained $t_0 \approx 2 \times 10^{-5}\,\mathrm{s}$. It is therefore possible to estimate the sensitivities of the two contributions, obtaining $1/s \approx 10^3$ and $t_0 = 10^{-5}$, leading to extremely high relative uncertainties over the measured speed of sound. For this reason, it has been preferred to adopt the literature values. However, it is the belief of the author that this could be a viable solution in different setups and with different equipment.

Moreover, for a full calculation of the uncertainty, it is important to remember that the position of the particle, i.e., the center of the measurement volume of the UDV, is also a function of the speed of sound and the Doppler frequency shift, as mentioned in Equation (6.4). Therefore, the uncertainty on the latter propagates also to the location where the velocity is measured. Intuitively, the bigger the gradient of velocity along the measuring line $\partial U/\partial P$, the higher will be this uncertainty on the final value of velocity.

The final type B relative uncertainty $u_{B,U}$ of the velocity U can therefore be expressed as in Equation (6.28):

$$\frac{u_{B,U}}{U} = \sqrt{\left(\frac{\partial U}{\partial f_D}\frac{u_{f_D}}{f_D}\right)^2 + \left(\frac{\partial U}{\partial f_e}\frac{u_{f_e}}{f_e}\right)^2 + \left(\frac{\partial U}{\partial \theta}\frac{u_\theta}{\theta}\right)^2 + \left(\frac{\partial U}{\partial c}\frac{u_c}{c}\right)^2 + \left(\frac{\partial U}{\partial P}\frac{u_P}{P}\right)^2} \tag{6.28}$$

where the terms express respectively the uncertainty due to the Doppler frequency, to the emitting frequency, the speed of sound, and the position along the measurement line. In particular, the last two terms can be further developed as in Equations (6.29) and (6.30) using the law of the propagation of the uncertainty.

$$\frac{\partial U}{\partial c}u_c = \frac{\partial U}{\partial c}\frac{\partial c}{\partial T}u_T \tag{6.29}$$

$$u_P = \sqrt{\left(\frac{\partial P}{\partial c}\frac{\partial c}{\partial T}u_T\right)^2 + \left(\frac{\partial P}{\partial f_D}u_{f_D}\right)^2} \tag{6.30}$$

An overview of the impact of the different parameters on the relative uncertainty is reported in Table 6.3.

Table 6.3 - *Relative uncertainties of measured quantities and their impact on the total uncertainty of the velocity*

Quantity	**Relative uncertainty**	**Contribution to the velocity uncertainty**
f_D	$\approx 1\,\%$	$\approx 1\,\%$
f_e	$\approx 1\,\%$	$< 1\,\%$
c	$\approx 1\,\%$	$\approx 1\,\%$
θ	$\approx 1\,\%$	$< 1\,\%$
P	$\approx 0.1\,\%$	$< 1\,\%$
Total $u_{A,U}$	/	$< 1\,\%$
Total $u_{B,U}$	/	$1\,\%$ to $2\,\%$
Total $u_{tot,U}$	/	$1\,\%$ to $3\,\%$

The relative uncertainties for f_D and f_e were provided directly by the sensor manufacturer during a customer service inquiry. As explained in Section 6.1, it is not the Doppler frequency f_D itself that is directly measured, but rather the phase shift of the echo signal between successive transmissions. Consequently, while the uncertainty for f_D is expressed as a percentage of f_D for consistency with the principles outlined in Section 6.1, it actually represents the uncertainty associated with the measured phase shift. The uncertainty in the angle θ was estimated based on the specific configuration of the experimental setup.

For the purpose of the calculation, a nominal value of each one of these parameters has to be adopted. In this table, it is not relevant to provide such values as the change of the setup, the sensor, and the fluid makes it different for each case. Some of the relative uncertainty values were provided by the manufacturer directly since they

depend on the electronics and on parameters that are not accessible to the user. The final values of uncertainty are in agreement with what has been found in the literature [249] and what has been communicated by the manufacturer of the probe and the acquisition system.

It is important to underline other two main sources of uncertainties highlighted by the manufacturer:

- Beam shape and volume: the measurements performed with the UDV are always averaged over the volume of the US beam, according to what was shown in Figure 6.2. Despite the possibility of theoretically calculating this volume, its boundaries will never be sharp and clear, leading to significant uncertainties when strong gradients in the flow are present. In the framework of this work, the measurements will be compared, as explained in Chapter 8, with numerical simulations that are also averaged in the same volume of the UDV sensor, therefore limiting the impact of such influence. It is interesting to notice that when taken into account by Nauber *et al.* (2020) [249], this uncertainty contributed by far the highest value, 13.9 %, due to the high velocity gradient in the measured volume.
- Particles: the big assumption of the UDV measurements is that the particles perfectly follow the flow and that all the particles in the same sampling volume move in the same direction with the same velocity. Despite the accurate analysis done in Section 6.3, it is impossible to completely eliminate and also to quantify this uncertainty and account for it in the calculation.

The total uncertainty, as reported in Table 6.3, is eventually calculated as in Equation (6.31):

$$u_{tot,U} = \sqrt{u_{A,U}^2 + u_{B,U}^2} \tag{6.31}$$

6.5 Results and discussion

This section presents the results acquired with the UDV sensor across various setups and for different purposes. Initially, the findings from the water pipe, focusing on both turbulent and laminar flow measurements, are detailed. A parametric study examining factors affecting UDV measurements was conducted in the same facility, and the results are presented alongside a similar study performed in the differentially heated cavity. Finally, the section includes results from tests conducted in the cavity to assess the actual impact of obstacles in the final configuration.

6.5.1 Water loop

The results obtained from measuring the velocity profile within the pipe are analyzed in this section. Two distinct Reynolds numbers were investigated: one representing fully turbulent flow and the other in the laminar regime. This comparison aims to assess the response of the sensor to varying velocity magnitudes and their fluctuations. Additionally, a comparison is made with direct numerical simulation (DNS) results

[260] and particle image velocimetry (PIV) experimental profiles, which are available only for the higher Reynolds number. The PIV measurements were conducted previously in the same facility as part of an earlier project [261]. A comparison with the well-known $1/7^t h$ law for turbulent mean velocity profiles in pipes is also shown in the same figure [198]. The results pertaining to turbulent flow are illustrated in Section 6.5.1, depicting the average velocity profile U and the turbulence intensity (TI), respectively. The latter is calculated as in Equation (6.32) where the rms value is given by Equation (4.17).

$$\mathrm{TI} = \frac{u'_{rms}}{U_{mean}} \tag{6.32}$$

While the considered velocity component is the axial flow direction, determined from the projection of the measured velocity, it can be considered representative of the overall flow characteristics within the pipe. This is because the other velocity components (radial and tangential) typically contribute relatively minor contributions to the overall velocity magnitude and turbulent intensity in a circular pipe.

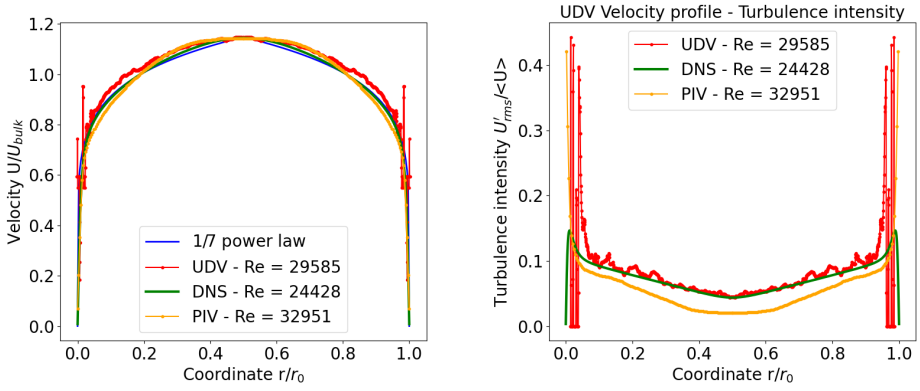

(a) Average velocity profile

(b) Turbulence Intensity (TI) profile

Figure 6.5 - *Fully developed turbulent profiles of average velocity and turbulence intensity in a water pipe. Comparison between UDV, PIV, DNS and theoretical estimations.*

The experimental profiles are mirrored, indicating that only the first half of the profile was measured and subsequently copied for the remaining half. This assumption relies on the known symmetry of such profiles, in addition to the observed decrease in UDV signal strength further from the sensor, which rendered the second half of the profile less reliable. As mentioned in Section 6.2, precise control of the velocity in the facility posed challenges. Consequently, the velocity during measurements was adjusted to be as close as possible to that used in the existing PIV experimental results for comparison purposes. Nevertheless, it was not possible to achieve a difference in the Reynolds number smaller than approximately 10 % between the two

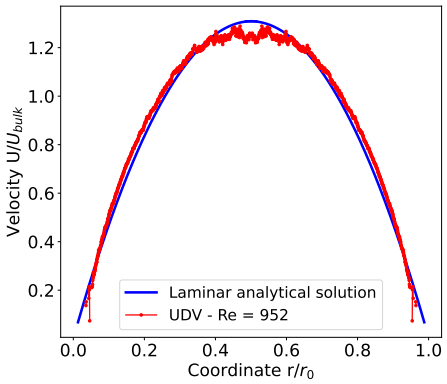

Figure 6.6 - *Laminar profiles of average velocity in a water pipe. A comparison is carried out between UDV and the analytical solution of the Poiseuille flow.*

datasets. Subsequently, the DNS results with the closest available Reynolds numbers were selected for further comparison. Although slight differences in Reynolds numbers remain, all profiles considered are fully turbulent, making them suitable for comparative analysis. All profiles are presented in a non-dimensionalized form, utilizing the bulk velocity defined in Equation (6.33) as the non-dimensionalization velocity for the experimental profiles, valid for axisymmetryc circular pipes with radius r and diameter D [198]:

$$U_{bulk} = \frac{4}{\pi D^2} \int_0^{\frac{D}{2}} U(r) 2\pi r \, dr \tag{6.33}$$

For the tests of Section 6.5.1, $U_{bulk} \approx 210\,\mathrm{mm/s}$. Additionally, the coordinates are non-dimensionalized with respect to the pipe diameter. A strong agreement is observed among all profiles, particularly in relation to the turbulence intensity measurements, which hold greater significance for this study. Notably, the core value of the TI aligns with the theory of fully developed flows in pipes, represented as $TI = 0.16\, Re^{-0.125} \approx 0.06$ [262].

As anticipated, the UDV exhibits reduced performance in close proximity to the sensor, specifically within a length approximately corresponding to the near field, consistent with the explanations provided in Section 6.1. This phenomenon is also reflected in the TI profile, where several zero values occur within the first mm. A spike in turbulence intensity is observed in both experimental profiles, likely resulting from the abrupt transition between the zero value at the wall and the peak TI in its vicinity, which could not be accurately captured by the resolution of these experimental techniques. Nonetheless, an excellent agreement with the DNS results is attained toward the center of the profile.

A comparable analysis was conducted for a laminar profile with $U_{bulk} \approx 7\,\mathrm{mm/s}$, with the results presented in Figure 6.6.

In this instance, experiments at such low Reynolds numbers were not conducted using PIV, precluding an experimental comparison. Furthermore, DNS data for laminar Reynolds numbers were not found in available databases. Consequently, the comparison was made against the laminar solution of Poiseuille channel flow [198] and good agreement was observed between the measured average velocity profile and that predicted by the analytical solution. However, comparing turbulence intensity (TI) profiles was infeasible. The analytical solution for purely laminar flow lacks TI information, as TI is inherently null over the entire section. Additionally, even with minor turbulence present in the experiments at these low velocities, the signal noise would likely mask the true TI, rendering comparison impractical. Therefore, performing a dedicated DNS at the exact experimental Reynolds number was deemed unnecessary and the comparison at low velocities was limited to the average profiles. Nevertheless, valuable insights into the performance of the UDV at low velocities can still be deduced from this analysis.

6.5.2 Parametric study

This section outlines the procedures employed to conduct tests in both the experimental facilities described in Section 6.2 and Chapter 3, with the goal of optimizing the sensor measurement settings. As previously mentioned, the profiles measured in Section 6.2 represent the classical turbulent or laminar profiles in a pipe and do not present innovation in themselves. However, their established characteristics facilitated a comprehensive sensitivity analysis of the UDV parameters, encompassing both internal instrument settings and external environmental factors. Understanding the interaction of these factors is essential for optimizing measurement outcomes and ensuring precision in the experiments. Consequently, this enabled to extend the analysis in the differentially heated cavity, leading to the retrieval of optimized measurement settings.

The parameters analyzed include those identified in Section 6.1 as critical parameters, as well as additional factors related to software settings and environmental conditions.

- $\mathbf{T_{PRF}}$: This parameter varies according to each flow configuration and velocity. Its initial value should be estimated using Equations (6.10) and (6.11), considering the characteristics of both the setup and the flow to be measured. Subsequently, an empirical parametric study is essential to identify an optimal value that ensures high signal quality along with the desired sampling frequency. Additional adjustments may be necessary with the initiation of each new test campaign.

- **Emissions per profile**: A lower value is preferred to achieve a higher acquisition frequency, though this may result in increased sample variance. To strike an optimal balance, low values were chosen to ensure the best achievable acquisition frequency without significantly degrading signal quality. In most practical applications, 8 to 100 pulse emissions are typically necessary to measure a single velocity profile, compensating for the often very low signal-to-noise ratio.

- **Number of cycles**: This parameter defines the length of the emitted burst. A higher value results in lower spatial resolution but improves signal strength. A default value of 4 peaks per burst is established, as no significant improvement in the signal was observed with longer bursts; therefore, this default value was retained.

- **Spatial resolution**: This refers to the axial spatial resolution that influences the final volume where the signal is averaged. Once the number of cycles is set and the sensor selected, there is limited scope for the operator to enhance it. However, the axial resolution consistently remained below 0.5 mm, rendering the real issue the transversal resolution, which primarily depends on the sensor size. Generally, an increase in spatial resolution can lead to a reduction in the total measurable depth. This was not a concern for the final setup due to its small dimensions. Nonetheless, performing an analysis of the actual performance of the sensor in this regard was of paramount importance.

- **Emitting power and Time Gain Control (TGC)**: These two parameters jointly determine the power of the signal received and processed by the transducer. While the emitting power represents the actual power of the emitted signal, the TGC amplifies the received signal and can be set by the operator or automatically detected by the software. An overly high combination of these two can cause saturation, while a low combination may result in a signal too weak to register. In scenarios where seeding the flow is not possible, the received signal could be very weak, making a high TGC value ideal. Conversely, excessive emitting power can quickly lead to saturation, especially in proximity of the sensor. As a general rule, when dealing with a weak signal, it is advisable to increase the TGC rather than the emitting power to avoid undesirable effects, such as ringing within the transducer.

- **Sensitivity**: This parameter defines the threshold allowing the user to disregard the computation of the Doppler frequency if the signal energy level falls below a user-defined value. It is recommended particular care in adjusting this parameter, as increasing sensitivity may incorporate more noise into the calculations, potentially cancelling out turbulent fluctuations. Unfortunately, the software does not provide a quantitative indication of this value.

- **US frequency**: The emitting frequency of the ultrasound (US) is determined solely by the sensor. For this project, three sensors operating at 8 MHz and 10 MHz were compared. In theory, a higher US frequency enhances spatial resolution due to the narrower angle of the ultrasound cone. However, higher frequency ultrasounds also experience greater attenuation in the fluid, typically limiting the maximum measurable depth. Given the compact nature of the setup, a reduction in maximum depth was not a concern, and the highest commercially available US frequency was preferred to maximize spatial resolution. To facilitate simultaneous acquisitions in the cavity, both 8 MHz and 10 MHz sensors were utilized.

- **Gravity effects**: The objective of these tests was to evaluate how changing the orientation of the sensor relative to gravity influences its interaction with the flow. While gravity does not directly affect ultrasound, it can impact the interaction of the sensor with the flow medium. For instance, when positioned at the top of the setup, air bubbles in the flow might accumulate around the tip of the sensor, whereas placing it at the bottom could result in sediment or particle settling, both of which could negatively affect the measurements. Ideally, the sensor should be positioned on the side. However, practical constraints often take precedence, leading to positioning decisions based on these considerations.

It was considered that presenting the complete outcomes of the parametric study for each parameter and setup would not contribute significant value to the work. Therefore, only a summary of the optimal values identified for the measurements across various setups and fluids is provided in Table 6.4.

Table 6.4 - *Summary of the optimal values of the analyzed UDV parameters for each setup. The number of tests carried out in the water loop for the full parametric study is also reported.*

Parameter	**# of tests**	**Water**		**GaInSn**
		Water loop	**Cavity**	**Cavity**
t_{PRF}	17	250 µs	4064 µs	500 µs
Emissions per profile	12	150	150	30
# of cycles	4	4	4	4
Axial Resolution	3	0.099 mm	0.128 mm	0.233 mm
Emitting power	11	High	Medium	Medium
Tgc	3	40 dB	Auto	Auto
Sensitivity	7	High	Medium	Medium
US frequency	3	8 MHz to 10 MHz	8 MHz to 10 MHz	8 MHz to 10 MHz
Gravity effects	10	bottom, $\theta = 51°$	bottom, $\theta = 0°$	bottom, $\theta = 0°$

The table presents the parameters selected for this study. Although a parametric study is always essential when conducting UDV measurements under new conditions, it is evident that some parameters, such as axial resolution, are highly dependent on the fluid, specifically the speed of sound in the medium. In contrast, other parameters, such as emitting power and sensitivity, are more related to the setup, as their optimal values remain unchanged with different fluids. However, it is crucial to emphasize that this technique is extremely sensitive to unpredictable environmental factors. Consequently, slight adjustments to the parameters should be performed regularly, ideally every day before commencing the tests.

6.5.3 Preliminary results in the cavity

In addition to the settings optimization analysis described in Section 6.5.2, further preliminary tests were conducted in the differentially heated cavity using water as the working fluid. Since these tests are part of the investigation into the parameters affecting UDV performance, they are included in this Chapter. The primary aim of these tests was to assess the influence of the experimental setup walls on the UDV and to evaluate how the measurements respond when obstacles obstruct the ultrasound beam. It has been demonstrated that UDV can measure low velocities ($\approx$ mm/s), such as those anticipated in the cavity [99, 247]. However, artifacts arising from echoes generated by interfaces or nearby walls can interfere with these measurements. Specifically, velocity profiles were obtained along position 1 (refer to Figure 3.4) under three different configurations depicted in Figure 6.7.

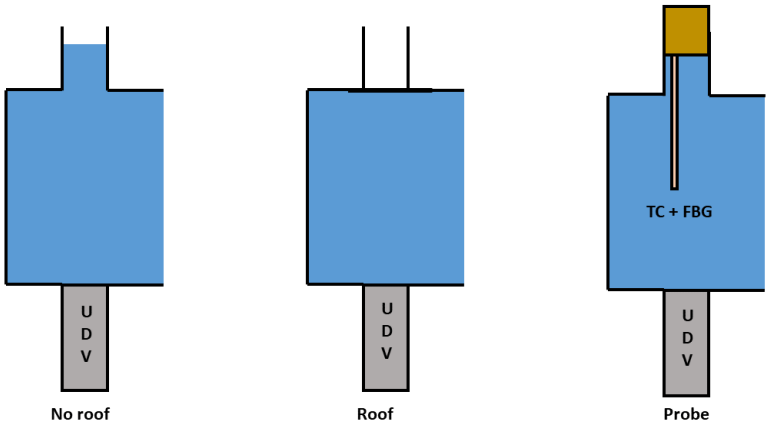

Figure 6.7 - *Cavity configurations adopted for UDV characterization. The goal is to test the effect of obstacles along the ultrasound beam.*

In the three illustrations, the left side of the cavity, as shown in Figure 3.4(a), is depicted, with the UDV sensor flush-mounted at the bottom. In all three configurations, the blue area indicates the water, indicating the location of the free surface. The top wall features three different configurations:

- No roof: the stainless steel tube used for the temperature sensor ingress is left open.
- Roof: the stainless steel tube used for the temperature sensor ingress is closed, simulating a flat wall on the top. The temperature sensors are not inside the cavity.

- Probe: the temperature sensors are inserted into the cavity with their supports. This configuration closes the tube but does not create a flat closure like the second case. Additionally, the probes, inserted at different heights within the cavity, are expected to affect the measurements and create artifacts.

These three configurations were used to conduct the tests outlined in Table 6.5 with both 8 MHz and 10 MHz UDV sensors.

Table 6.5 - *Tests performed to assess the effects of obstacles on the UDV velocity measurements*

Test	**ΔT°C**	**Configuration**	**TC+FBG position**
1	51.0	No roof	NA
2	51.0	No roof	NA
3	51.3	No roof	NA
4	51.2	Roof	NA
5	51.3	Roof	NA
6	51.3	Probe	y=28 mm ; y=48 mm
7	51.3	Probe	y=28 mm ; y=48 mm

All the tests tried to keep the same temperature difference in the cavity so that the flow was not influenced by it. The temperature sensors were not inserted in the cavity in the first four tests while they were place at two different heights in Test 6 and 7, therefore simulating the real conditions of the measurements.

One first parameter that can be useful to analyze to see if artifacts are created is the US echo profile. This parameter gives the evolution of the echo envelope of the ultrasonic signal received by the transducer. It informs on the presence of high reflective structures and on a possible saturation of the receiver. Its module does not have any unit as it is expressed as relative numbers and covers a range from 1 to 2048. The results are shown in Figure 6.8.

These results demonstrate that the echo profiles are influenced by the various configurations. Initial saturation of the echo profile is typical and consistently occurs near the sensor. For Test 1 (UDV 10 MHz, without roof), the echo shows no spikes and diminishes with distance from the sensor. In Test 4 (UDV 10 MHz, with roof), the wall presence is distinctly visible at $y = 60$ mm, indicating sufficient coupling between the fluid and sensor with no evident wetting issues. In Test 6, the probes visibly alter the echo at both positions.

The effect of the four configurations on the velocity profile is shown in Figure 6.9 for the 10 MHz UDV sensor.

The picture illustrates a trough in all cases near the opposite wall, even if slightly less pronounced in the presence of the roof. Chapter 8 will show that this same feature is also captured by adequately averaged DNS and RANS simulations. Furthermore, the overall profile appears to be minimally influenced by the different configurations. The most significant differences arise when the opposite wall is present, as anticipated

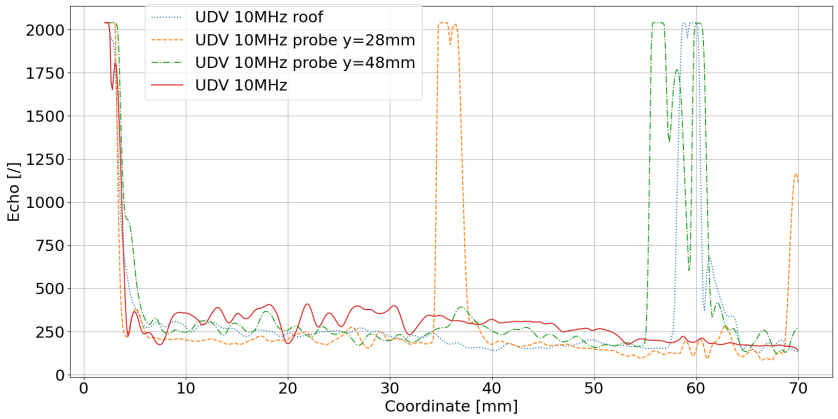

Figure 6.8 - *Echo modules of the UDV* 10 MHz *shown for different configurations*

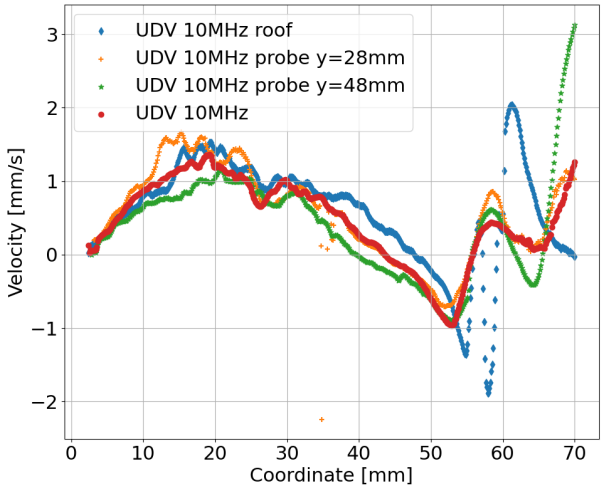

Figure 6.9 - *Velocity profiles along position 1 in the cavity for the* 10 MHz *UDV sensor in four different configurations*

due to the higher back echo received from the wall itself. However, the differences in the echoes depicted in Figure 6.8 suggest a much larger discrepancy between the profiles that is not reflected in the velocity profiles.

6.6 Conclusions

This Chapter presented the primary results obtained concerning the characterization of the UDV sensor. Initially, the key parameters involved in the measurements were discussed in Section 6.1. Subsequently, the specific setup utilized for sensor characterization, which consisted of a closed-loop water pipe, was described in Section 6.2.

Particular emphasis was then placed on the selection of particles in Section 6.3 and the calculation of uncertainty in Section 6.4. For the particle selection, Griltex particles with an average diameter of 50 µm were ultimately chosen for water measurements in the cavity while in the water loop satisfactory measurements were achieved mainly relying on water impurities. Therefore, in the case of GaInSn, reliance was placed on the gallium oxides that inevitably form when the fluid is exposed to oxygen. As for the uncertainty calculation, a comprehensive and detailed procedure was outlined for both type A and type B uncertainty assessments, with results that can be directly applied to the final measurements.

Following this, the results obtained in the closed water loop were presented and discussed in Section 6.5.1, demonstrating overall good agreement with DNS and previous experimental data for fully developed forced convection flows. However, while further comparisons at lower velocities were generally successful, they were limited to average profiles. In fact, data at even lower velocities, such as those expected within the cavity, were not available due to the limitations of the facility. The same facility was subsequently employed to conduct a parametric study on various parameters in Section 6.5.2, many of which are intrinsic to the probe, while others depend on environmental factors. This analysis was then extended to the GaInSn case in the differentially heated cavity, leading to the identification of an optimal set of parameters for the final measurements. A summary of the achieved spatial and temporal resolutions across the various facilities and fluids is presented in Table 6.6.

Table 6.6 - *Summary of spatial and temporal resolutions obtained with the* 10 MHz *UDV*

Case	**Axial resolution d_v**	**Volumetric resolution Δx**	**Temporal resolution Δt**
Water in the loop	0.099 mm	1.5 mm^3 to 3.2 mm^3	43 ms
Water in the cavity	0.128 mm	2.5 mm^3 to 4.2 mm^3	1000 ms
GaInSn in the cavity	0.233 mm	4 mm^3 to 18 mm^3	23 ms

First, it should be noted that a range is provided for the volumetric resolution, as the ultrasound beam from the sensor expands in a conical shape. Although the axial resolution d_v is quite fine, the volumetric resolution of the sensor quickly worsen due to the substantial averaging width resulting from the size of the sensor. However, the smaller volumes, i.e., those closer to the sensor, are still close to the resolution requirements outlined in Chapter 2. Moreover, the real impact of the averaging volume can be really assessed only when the radial velocity gradient of the flow to be

measured is known. As previously mentioned, this issue could be partially addressed by performing a proper averaging of the numerical simulations, at least for the purpose of comparing experimental and numerical results. Furthermore, while the temporal resolution presented do not cover the entire range of expected velocities fluctuations, they can still provide valuable insights into the part of the energy spectrum. One important aspect to emphasize is that the UDV measurements will be restricted to capturing only the vertical component of the velocity. However, as illustrated in Chapter 4, the configuration of the setup suggests that this component should provide a reliable representation of the overall velocity magnitude.

A final series of tests presented in Section 6.5.3 was conducted directly in the cavity to evaluate the influence of obstacles along the measurement line, such as walls or other probes. Although these obstacles were detected by the echo signal, the final results regarding the fluid velocity did not appear to be significantly impacted by their presence or the potential echo bounces created by them, likely due to their small size. Consequently, the repeatability of the results under varying conditions confirmed the suitability of chosen probe configuration within the experimental setup.

Chapter 7

Hot wire - hot film anemometry

This Chapter addresses the characterization of Hot Film Anemometry as the last velocity measurement technique, with a focus on calibration procedures and the challenges encountered when utilizing this probe in conductive fluids such as water and GaInSn.

The Chapter begins with a description of the underlying physical working principle in Section 7.1, also addressing specific issues related to film probes used in conductive fluids. Subsequently, the core focus of the Chapter, namely the calibration of the probe, is discussed in detail. Section 7.2 elaborates on the theory of static and dynamic calibration, as well as the description of different setups used to tackle the problem of simultaneous calibration with respect to temperature and velocity.

Sections 7.4 and 7.5 present the results obtained using the described setups and provide a detailed explanation of two distinct calibration methodologies, the $Nu - Re$ approach and the Hollasch method. The application of these methodologies to the datasets for water and GaInSn, along with the corresponding results, are presented.

In conclusion, the influence of the heated probe on the surrounding environment, specifically on temperature sensors, is examined in Section 7.6, while Section 7.7 addresses the issue of streamwise spatial resolution through a more detailed calculation.

7.1 Working principle

In this Section, the operating principle of Hot Wire-Film Anemometry is outlined. The term *wire* is used in this Section when referring to the probe to keep the discussion as general as possible but the same principle is applied to Hot Film probes, being the structure of the probe the only difference between the two, as explained in Section 2.3.4. The probe works based on the cooling effect of a flow on a heated body, usually the wire with a cylindrical shape, subjected to the general cooling law of Newton reported in Equation (7.1), where Q is the heat transferred from the wire to the flow, h is the convective heat transfer coefficient, A is the frontal area of the wire, T_w is the temperature of the wire and T_f is the temperature of the measured flow:

$$Q = hA(T_w - T_f) \tag{7.1}$$

The wire is connected to one arm of a Wheatstone bridge* and heated by an electrical current I_w as shown in Figure 7.1.

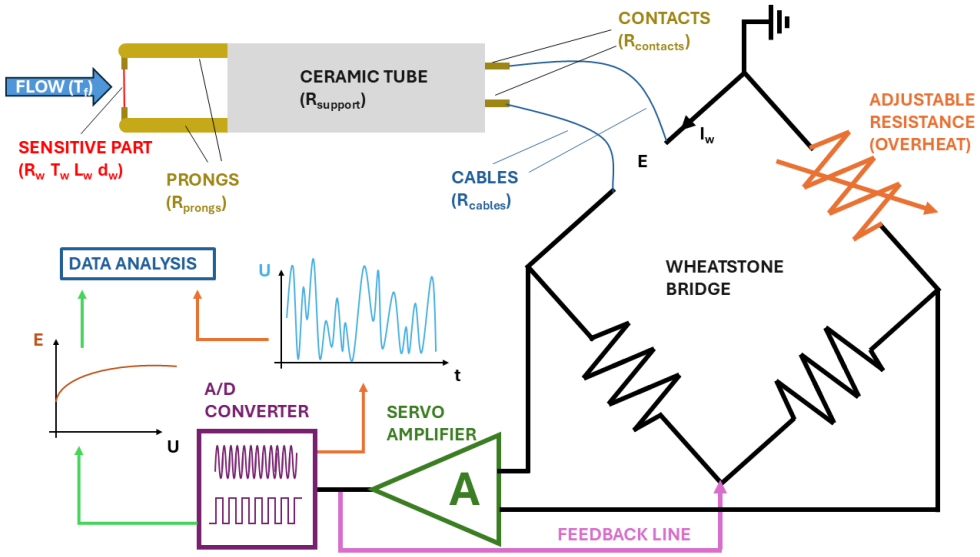

Figure 7.1 - *Measurement chain of the Hot Wire - Hot Film Anemometry when used in Constant Temperature Anemometry mode.*

The voltage E measured across the wire can therefore be expressed through Equation (7.2) [263]:

$$E = R_{tot} I_w \tag{7.2}$$

with R_{tot} being the series of resistance shown in Figure 7.1 and reported in Equation (7.3):

$$R_{tot} = R_w + R_{prongs} + R_{support} + R_{contacts} + R_{cables} \tag{7.3}$$

In particular the resistance of the wire R_w is temperature dependent according to Equation (7.4) where R_{ref} indicates the wire resistance at the reference temperature T_{ref} and α_w is the temperature coefficient of resistance:

$$R_w = R_{ref} \left[1 + \alpha_w \left(T_w - T_{ref}\right)\right] \tag{7.4}$$

*A Wheatstone bridge is an electrical circuit designed to measure an unknown resistance by balancing two legs of the bridge circuit. It consists of four resistive arms, where two arms have known resistances, while the remaining arms include an unknown resistance and an adjustable, variable resistance.

The operating wire resistance therefore depends only on the material, the wire dimensions (both constant once that the probe is chosen) and the operating temperature.

The heat q generated by Joule effect in the wire is given by Equation (7.5):

$$Q = R_w I_w^2 \tag{7.5}$$

Therefore, the steady-state energy balance for the wire can be expressed as in Equation (7.6), where D_w is the wire diameter and L_w is its active length.

$$R_w I_w^2 = \pi D_w L_w h (T_w - T_{ref}) \tag{7.6}$$

Defining the Nusselt number relative to the wire Nu_w as in Equation (7.7), with k_f being the thermal conductivity of the fluid, it is possible to rewrite Equation (7.6) as Equation (7.8), and therefore extract the expression of Equation (7.9) for the current I_w flowing in the wire.

$$Nu_w = \frac{hD_w}{k_f} \tag{7.7}$$

$$R_w I_w^2 = \pi L_w k_f (T_w - T_{ref})\, Nu_w \tag{7.8}$$

$$I_w = \sqrt{\frac{\pi L_w k_f (T_w - T_{ref})\, Nu_w}{R_w}} \tag{7.9}$$

Eventually, recalling Equation (7.2), the output voltage E measured by the system can be related to flow characteristics through Equation (7.10):

$$E = R_{tot} I_w = R_{tot} \sqrt{\frac{\pi L_w k_f (T_w - T_{ref})\, Nu_w}{R_w}} \tag{7.10}$$

The response of the probe is therefore dependent on the Nusselt number Nu_w, which, through dimensional analysis, can be expressed as a function of $Nu_w = f(Re_w, Pr, Gr_w)$ for incompressible, well-guided flows [264]. This relationship connects the hot-wire voltage to several flow parameters, including density, temperature, viscosity, thermal conductivity, and flow angle. The sensitivity of the probe to flow angle could pose a challenge for three-dimensional velocity vector measurements, and consequently, turbulent heat flux measurements. However, in the present work, the measured velocity y-component is the dominant component of the flow, as demonstrated in Chapter 4, effectively minimizing the influence of the other component perpendicular to the wire. It is important to note that the cooling effect of the fluid passing over the wire results in the same voltage output for flows of equal speed approaching from opposite directions. Consequently, the probe is unable to discern flow orientation or direction.

This sensitivity necessitates accurate calibration to eliminate dependencies on non-relevant parameters and the issue will be deeply discussed in the further Sections. In summary, the bridge voltage E, represents the heat transfer and can be directly related

to the flow velocity through an accurate calibration. The sensor measures pointwise and provides continuous voltage time series, which can be converted into velocity and processed into amplitude and time-domain statistics, e.g., mean velocity, turbulence intensity, higher order moments, auto-correlations, and power spectra.

From Equation (7.10), two different working philosophies can be adopted:

- **Constant Current Anemometry (CCA)**: I_w is kept constant and it is therefore the resistance of the wire to change according to the cooling power of the flow. In this case, the frequency response is limited by the thermal inertia of the wire itself.

- **Constant Temperature Anemometry (CTA)**: R_w (and therefore R_{tot}) is kept constant, meaning that recalling Equation (7.4) the temperature of the wire remains constant. Thus, a servo amplifier maintains the bridge balance by regulating the current to the sensor I_w (i.e., the heating power) through a feedback line, ensuring a constant temperature of the wire despite the cooling effects of the fluid. In this approach, the thermal inertia of the wire can be neglected, resulting in a significantly improved frequency response. Additionally, since the temperature of the wire does not change, the fluid properties can be considered constant. For these reasons, nearly all modern anemometers operate based on this principle.

In this study, the CTA principle is adopted. The circuitry of such configuration is the one shown in Figure 7.1. One key parameter of the Wheatstone bridge is the adjustable overheat resistance, able to set the overheat ratio (OHR) and therefore the over temperature of the wire. According to the definition of Dantec Dynamics [265] adopted for this thesis, this parameter is defined by Equation (7.11), where $R_{w,ref}$ is the value of the resistance of the hot wire at the temperature $T_{w,ref}$, usually the ambient temperature.

$$\mathrm{OHR} = \frac{R_w - R_{w,ref}}{R_{w,ref}} = \alpha_w (T_w - T_{w,ref}) \tag{7.11}$$

Equation (7.11) can therefore be used to calculate the operating temperature of the wire by Equation (7.12):

$$T_w = \frac{\mathrm{OHR}}{\alpha_w} + T_{w,ref} \tag{7.12}$$

For the current work a value of OHR = 0.21 was adopted leading to an operating wire temperature of $T_w = 82\,^{\circ}\mathrm{C}$, higher than the temperature imposed at the active hot wall and therefore higher than any flow temperature encountered during the measurements. On the other hand, a too high value of OHR was avoided as the adopted 0.21 was already 3 times higher than the suggested 0.08 [59]. The probe described in Section 2.3.4. More details about the settings used in the Streamware Pro software are given in Appendix A.2.

7.1.1 Measurements in conductive fluids

In electrically conductive fluids such as water or liquid metals, specific challenges require careful consideration. To address these, the probe selected for measurement is the specific probe described in Section 2.3.4, which comprises a quartz fiber core with a diameter of 70 µm, a nickel thin-film layer of approximately 0.1 µm forming the sensitive part, and an additional quartz layer with a thickness of 2 µm to ensure electrical insulation and oxidation protection. This section introduces these challenges and outlines the solutions applied in this work.

One issue is related to the *grounding* of the liquid. The liquid must be grounded as close to the probe as possible, for example, by using an electrode plate connected to the signal ground of the anemometer. If no grounding is provided, the thin protective quartz coating may break down due to voltage differences caused by electric charges building up in the liquid or through direct conduction in electrically conductive liquids. Proper grounding also reduces the amount of electrical noise that can be coupled dielectrically from the liquid to the CTA circuits [59].

Another issue that could affect the sensor are *contaminants* in the flow. Contaminants, such as dust in air, chemicals in water and oxides in liquid metals, may adhere to the sensor and significantly alter the heat transfer. The influence of dirt generally increases with decreasing diameter. For fiber probes in liquids, particle contamination can be a serious problem, and it may often be necessary to filter the liquid for particles down to a few micrometers in size. Even then, regular cleaning of both fiber and film probes used in liquids is recommended. Film probes used for extended periods in water may accumulate calcium carbonate deposits, which tend to nucleate around the wire due to the elevated temperature, thereby reducing probe sensitivity. The deposition increases with sensor operating temperature causing drifting in the calibration or damaging of the probe. In the case of liquid metals, oxides in the order of micrometers could form, potentially damaging the probe. This issue will be discussed further in Section 7.4.

Also, *chemical reactions* in the form of electrolysis may occur with film probes used in water if the liquid is not properly grounded or if the quartz coating has been damaged. Electrolysis corrodes the sensor film near the damaged area, leading to increased sensor resistance and decreased sensitivity. If electrolysis continues, the sensor will eventually fail. Liquid metals are known to be harsh and corrosive environments, which could pose additional challenges. While there is no inherent reason to believe a hot film designed for water should fail in liquid metals, the conditions are much more demanding. Electrolysis can still occur, and the liquid metal itself could erode the protective layer, exposing the sensitive film directly to the metal.

To conclude, in liquids, dissolved gases may form *bubbles* on the heated sensor. If the sensor element is partly covered with bubbles, the resulting temperature gradients can damage the thin protective quartz coating. These bubbles could be removed mechanically by means of a soft marten hair brush. Shaking the probe from the stem has also proven effective in this work. In the specific case of water, bubbles can also be prevented by letting the water sit still for some time to allow air to escape or by boiling it beforehand. Additionally, the sensor temperature should be kept as low as possible to avoid bubble formation. Not all these solutions are directly applicable

to liquid metals; however, applying similar precautions as those used for water is recommended whenever feasible.

7.2 Calibration

As discussed in Section 7.1, the hot film probe is sensitive to multiple flow parameters. Accurate measurements therefore require a thorough calibration process capable of distinguishing the effects of these parameters. This section introduces the fundamental concepts of static and dynamic calibration for hot film probes, followed by an overview of the various calibration setups and methods employed. The results of these calibrations are presented in Sections 7.4 and 7.5.

7.2.1 Static calibration

The static calibration of the hot film is intended to retrieve the transfer function relating velocity and output voltage. For hot films and hot wires, this relationship is known to be strongly non-linear due to the heat transfer dynamics of a body in a flowing stream [266].

First of all, it is important, especially for this work, to address the problem of the lower limit of the use of the hot film, i.e., the minimum measurable velocity. In fact, if the flow is fully dominated by the natural convection generated by the heating effect of the probe, it becomes impossible to exploit the measuring principle itself. The limit is then reached when natural convection dominates over the convection imposed by the flow [115]. The condition expressed in Equation (7.13) must be satisfied to ensure the proper operation of the hot film [264, 266, 267]:

$$\Psi = \frac{Re_w}{Gr_w^{1/3}} > 1 \tag{7.13}$$

where

$$Re_w = \frac{U D_w}{\nu_f} \tag{7.14}$$

$$Gr_w = \frac{g\beta_f (T_w - T_f) D_w^3}{\nu_f^2} \tag{7.15}$$

are, respectively, the Reynolds number and the Grashof number calculated with the characteristic dimensions of the wire and the velocity estimated by the DNS simulations in Chapter 2, i.e., $U_{\mathrm{GaInSn}} \approx 30\,\mathrm{mm/s}$ and $U_{water} \approx 3\,\mathrm{mm/s}$. In particular, this condition allows for defining Equation (7.16), i.e., a minimum flow velocity U_{min} above which the natural convection phenomena generated by the probe can be ignored and the flow velocity can be correctly resolved [115]:

$$U_{min} = [g\beta(T_w - T_f)\nu_f]^{\frac{1}{3}} \tag{7.16}$$

Table 7.1 - *Hot film velocity limitations in water and GaInSn*

Fluid	Re_w	Gr_w	Re_w / $Gr_w^{1/3}$	U_{min}
Water	0.34	0.119	0.7	4.3 mm/s
GaInSn	7.3	0.114	15	2 mm/s

A summary of these values in flows of water and GaInSn is reported in Table 7.1 where $T_w = 82\,^{\circ}\mathrm{C}$ as explained in Section 7.1 and $T_f = 50\,^{\circ}\mathrm{C}$, taken as a reference of the average temperature of the fluid in the cavity.

It should be noted that Gr_w remains similar in both cases, as the only fluid-dependent parameter in its calculation is the kinematic viscosity, ν_f, which is nearly identical for water and GaInSn. In contrast, the Re_w differs by an order of magnitude, corresponding to the variations in velocity values employed for the estimation. In the case of water, the ratio Ψ is slightly below unity, indicating that velocities at the lower end of the expected range may not be accurately captured by the probe. Specifically, the minimum resolvable velocity in water is approximately 4 mm/s, posing a risk of either entirely obscuring the velocity field or, more likely, failing to detect the anticipated low-amplitude fluctuations. Conversely, the minimum resolvable velocity in GaInSn suggests the necessity for cautious measurements of fluctuations, yet remains within a range that enables velocity measurements.

Nevertheless, this lower limit can be further reduced by decreasing the sensor overtemperature, thereby lowering the Gr_w number. Moreover, if a probe is calibrated in the same orientation with respect to the gravitational field as it is subsequently used, it may operate even at lower velocities [59].

It is clear that the working range of this study approaches the limits of the operating conditions of the probe, necessitating careful consideration of the influence of natural convection flows induced by the probe itself. This is strictly related to the temperature and velocity sensitivity of the probe that can be assessed through sensitivity analysis methods developed for hot wire probes [268]. However, these methods were primarily developed for transonic and supersonic flows and often require the use of multiple probes with distinct sensitivities to various flow parameters. This allows for the formulation of a closed system of equations and a more comprehensive understanding of the flow field. Furthermore, the complete computation of these sensitivities typically requires experimental measurements of the voltage response of the probe to variations in different flow parameters and cannot be done a priori. Given these considerations, a sensitivity analysis was not deemed compatible with the scope of the present study. The solutions adopted are presented in Section 7.5.2.

On the other hand, when working in a fully forced convection regime, dimensional analysis indicates that $Nu = f(Re, Pr)$, thereby shifting the problem of calibration to finding a satisfying relationship describing this dependence.

Typical mathematical forms of the relationships used to relate these parameters for the cooling law of cylinders are presented in Equations (7.17) and (7.18) [266], where A and B are constants depending on the wire dimension, wire resistance, and

fluid properties (e.g., temperature and Pr).

$$E^2 = A + BU^n \tag{7.17}$$

$$E = a_0 + a_1 U + a_2 U^2 + a_3 U^3 + a_4 U^4 \tag{7.18}$$

In Equation (7.17), the index n depends on the chosen heat-transfer law for describing the flow, and for $n = 0.5$, King's law is retrieved [269]. Equation (7.18) represents a standard polynomial fit, with experience showing that a fourth-order polynomial provides the best fit for these applications [266].

In this context, it is crucial to consider the maximum measurable velocity. Wire and fiber film sensors are typically designed to withstand the aerodynamic forces encountered in practical scenarios, including supersonic speeds. The upper velocity limit specified in the data sheet is determined by the velocity that induces a stagnation temperature exceeding a critical value, depending on the specific probe characteristics [59]. For the probe used in this study, the declared velocity limit is 10 m/s (see Table 2.5), and velocities approaching this upper limit are very unlikely to be reached, rendering this limitation of secondary significance for this work.

As a final point, it is crucial to emphasize that, as seen in Equation (7.3), the hot film probe essentially consists of a chain of resistances. Consequently, when one of these resistances changes, the entire calibration of the probe is affected. For this reason, not only must the probe be carefully calibrated, but it is also essential to calibrate the entire measurement chain (and not only the probe) while avoiding shuffling cable connectors or plugging and unplugging the probes, as contact resistances could change dramatically. It is therefore advisable to calibrate the probe more than once during the same test campaign, as the resistance values could vary due to unpredictable and uncontrollable environmental factors. For this study, calibrations and measurements were performed on the same day whenever possible, or at least on consecutive days, with particular care taken to avoid any modification to the probe cabling and electronics.

7.2.2 Dynamic calibration

In addition to the static calibration, performing a dynamic calibration is essential. The dynamic response of the system is determined by the properties of the wire and the associated electronics. The most widely used and recognized method for evaluating the time constant of the system, and thereby its temporal resolution, is the square wave test. This procedure involves injecting a current pulse (square wave) at the wire terminal, which results in additional heat dissipation by the wire. The response of the system, typically monitored via an oscilloscope, follows the characteristic shape depicted in Figure 7.2.

The shape of the response enables the optimization and measurement of the characteristic time of the system τ_w, and thus its cut-off frequency $f_{cut-off}$, as expressed in Equation (7.19) for hot film probes [270, 271].

$$f_{cut-off} = \frac{1}{\tau_w} \tag{7.19}$$

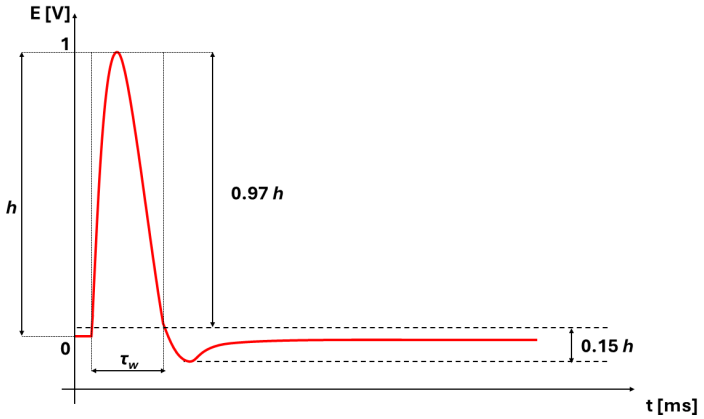

Figure 7.2 - *Typical dynamic response of a hot film probe subjected to a square wave test*

The optimization of the feedback loop in the Dantec System used in this study involves adjusting the gain and filter settings of the feedback amplifier, as well as the cable compensation to balance the capacitance and inductance in both legs of the Wheatstone bridge. During the dynamic calibration, the sensor should be subjected to a flow condition corresponding to the highest velocity encountered, as this represents the most demanding situation. Under such conditions, heat is removed from the probe most rapidly, requiring the sensor to respond with maximum efficiency.

7.3 Calibration setups

To satisfy the requirements outlined in Section 7.2 regarding control over all potential influencing parameters, various setups were identified and tested in this study. The calibration apparatuses employed were as follows:

- **Tank setup:** The hot film was positioned in the center of a tank filled with fluid, which could be drained through a valve located at the bottom. This setup is straightforward to implement and can, in principle, be used with both water and GaInSn. However, achieving temperature control was not possible, and the relationship between the valve opening and the velocity experienced by the probe was nontrivial. Consequently, the final results were not highly successful, and a summary of the main conclusions is reported in Appendix A.3.
- **Closed loop setup:** This setup is the same as that used for the characterization of the UDV described in Section 6.2 with some modifications highlighted in Section 7.3.1. Although this setup cannot be used with GaInSn and lacks proper temperature control, it offered an excellent opportunity to compare the hot film with the UDV velocity sensor, yielding valuable insights into the use of the hot film for velocity measurements.

- **Oil bath calibration setup:** This setup utilizes a linear translational stage and a temperature-controlled oil bath. In this configuration, the hot film is mounted on a movable platform, i.e., the translational stage, allowing it to traverse at various velocities through a stationary fluid. The fluid can be either the oil bath medium itself, with temperature control, or a different fluid contained within a vessel placed inside the bath. This setup provided precise control over velocity and temperature and is discussed in greater detail in Section 7.3.2.

7.3.1 Water loop setup

As noted in Section 7.3, the closed water loop setup yielded valuable results in the calibration and comparison of the hot film probe. The description of the facility was previously detailed in Section 6.2. This Section elaborates on the implementation of the hot film measurements within the described setup. The hot film was positioned inside the pipe as illustrated in Figure 7.3.

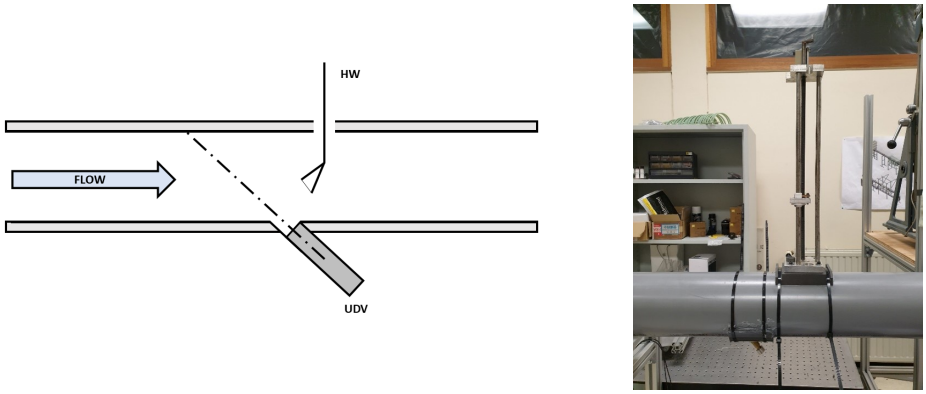

(a) Schematic (b) Picture

Figure 7.3 - *Configuration of the hot film and UDV in the closed water loop setup*

The hot film was inserted from the top and manually adjusted using a screw, enabling positioning with a precision of 0.1 mm.

During the calibration phase, the hot film was positioned at the center of the pipe, and the average velocity from the central point of the UDV profile was used as the reference calibration velocity. The flow velocity was subsequently varied by adjusting a ball valve, allowing a full calibration range up to 250 mm/s. The hot film was positioned downstream of the UDV to avoid flow disturbances. Thanks to the non-intrusive nature of the UDV, independent measurements were obtained from the two sensors at the same point.

Despite some benefits, the setup presented several challenges during the calibration process:

- **Lack of temperature control:** Attempts to implement temperature control, such as using electric heaters, proved impractical. Results from these tests indicated a strong temperature influence, especially closed to the wall as discussed in Section 7.4. This finding led to the development of an alternative calibration setup.

- **Flow direction:** In this setup, the fiber-film probe was exposed to a flow parallel to its prongs, while in the cavity, the flow would arrive perpendicularly, either from the top or bottom. In addition to the not good practice of calibrating with a different prong orientation than that expected in the actual flow, this difference can also influence the vibrations induced by the flow on the probe. Vibrations are generally higher when the prongs are mounted perpendicular to the main flow direction, introducing further uncertainty and noise that should be taken into account also in the calibration phase. Therefore, calibrations performed in this facility may be considered unreliable for the final application.

- **Velocity range:** The velocity range explored in the calibration was higher than that expected in the cavity, leading to reduced precision in the lower range, which is of primary interest for the final measurements.

Although some issues remained unresolved, the facility successfully provided useful results. Following the described calibration procedure, a comprehensive experimental campaign was conducted, comparing the measurements obtained by the hot film and the UDV over a full profile. The hot film was incrementally traversed across multiple points along the pipe diameter, with measurements taken after allowing flow disturbances to subside. Simultaneously, the UDV probe captured a complete profile, and the data corresponding to the position of the fiber-film probe were used for comparison. The results obtained from this setup are discussed in Section 7.4.

7.3.2 Oil bath setup

The final setup used for the proper calibration of the hot film probe was ultimately capable of precisely controlling both temperature and velocity, allowing sweeping within the desired ranges for both quantities.

Figure 7.4 presents a schematic of the setup utilized.

The setup consists of an Isotech Hyperion 4936 oil bath, whose temperature is controlled through electrical resistances and PT100 sensors connected in a feedback loop. The temperature range was limited between $-25\,^{\circ}\mathrm{C}$ to $140\,^{\circ}\mathrm{C}$, which is more than adequate for the purposes of this study. Inside this bath, a cylindrical stainless steel container with a diameter $D = 100\,\mathrm{mm}$ and a height $H = 200\,\mathrm{mm}$ was placed to contain the fluid where the actual measurements took place. Several factors motivated this configuration choice:

- The internal container enabled the use of a different fluid inside it, allowing the flexibility to employ any desired fluid during the calibration, independent of the original bath oil.

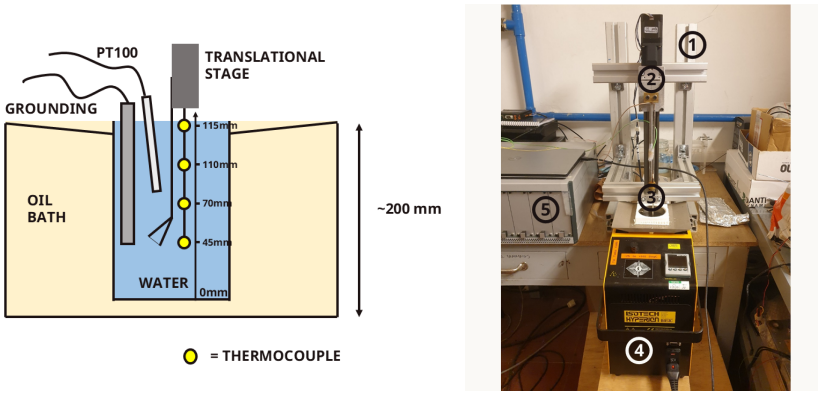

(a) Schematic (b) Picture with legend

Figure 7.4 - *Schematic and picture of the oil bath calibration setup. 1) Support made of Bosch profiles 2) Linear translational stage with its motor and controller 3) Probes 4) Oil bath 5) Dantec anemometer.*

- The physical separation between the two fluids mitigated potential influences from natural convection motions caused by oil heating through the electrical resistance, thereby minimizing disturbances in voltage readings.
- The smaller container facilitated a more uniform temperature throughout the entire working environment.

Inside the smaller container, multiple temperature sensors were installed. A DANTEC PT100 was employed to measure the average fluid temperature. Additionally, a rack of four Omega K-type thermocouples with tip dimension of 1 mm was used to monitor potential temperature stratification and to account for the temperature gradient during post-processing. A maximum gradient of 0.03 °C/mm was observed, with a maximum average temperature difference of 0.4 °C between different runs conducted at the same temperature. Consequently, the temperature inside the smaller container was considered constant and homogeneous.

The fiber-film probe was mounted on the linear translational stage SLW-0630 DS8x15 by Igus motors, driven by a stepper motor and a D1-type motor controller. This motor allowed for a velocity range up to 30 mm/s, thereby enabling a comprehensive calibration that covered the entire measurement range. During calibration, the fluid remained stationary while the probe was moved at various velocities. The probe trajectory was defined to remain entirely within the fluid during each run and to avoid proximity to the bottom wall to prevent potential damage and unwanted wall effects.

Moving the fiber-film probe instead of the fluid also presented a significant advantage, particularly relevant to this type of probe, by helping to prevent bubble formation around the probe. In water, small air bubbles adhering to the probe were visibly formed, potentially causing issues described in Section 7.1.1. To mitigate this,

tapping on the probe stem prior to starting the run proved effective in dislodging bubbles, and the use of boiled distilled water helped eliminate air from the fluid in advance. In GaInSn, where optical access was unavailable and boiling the fluid was not feasible within the setup, periodic tapping of the stem was deemed the most effective precautioneven although its effectiveness could not be visually confirmed.

7.4 Results in the water loop

This Section presents the results obtained in the closed-loop water facility described in Section 6.2 with the modifications made in Section 7.3.1. The results are divided into two parts:

- The first part pertains to the calibration of the fiber-film probe, performed through a comparison with the UDV sensor.
- The second part presents and discusses the results obtained by measuring a complete profile with both probes in the water pipe.

7.4.1 Calibration

For the calibration of the probe, the UDV was employed as the reference sensor, given that the results presented in Chapter 6 demonstrated its reliability in measuring average profiles in the same setup. Since the UDV measures a complete profile while the hot film probe only provides pointwise measurements, the reference velocity was taken as the velocity at the point in the UDV profile corresponding to the position of the hot film probe in the pipe. The resulting calibration is depicted in Figure 7.5.

Despite the relatively low velocity range swept in this setup, i.e., up to 300 mm/s, an accurate fit was achieved using King's law. This outcome serves as an initial validation of the suitability of the probe even at low velocities, providing experimental evidence supporting the calculations presented in Section 7.2.1. A similar fit was attempted using a polynomial function, but since the results were comparable, King's law was selected due to its foundation in physical principles, as outlined in Section 7.2.1.

The final calibration equation employed is given by Equation (7.20) where E is expressed in V and U in m/s:

$$E^2 = 3.78 + 0.93 \times U^{0.4} \tag{7.20}$$

This setup also allowed for a proper dynamic calibration of the probe. When setting the maximum velocity reachable with the setup, i.e., approximately 230 mm/s, the result shown in Figure 7.6 was retrieved.

First of all, it is evident that the expected shape of the curve was retrieved (see Figure 7.2). The value automatically calculated by the software can be seen at the top part of the figure, and it is approximately 80 kHz. This value is consistent with previous studies carried out in air [263] with hot wire probes having diameters of approximately 5 µm to 10 µm. However, for the probe used in this work, such a value

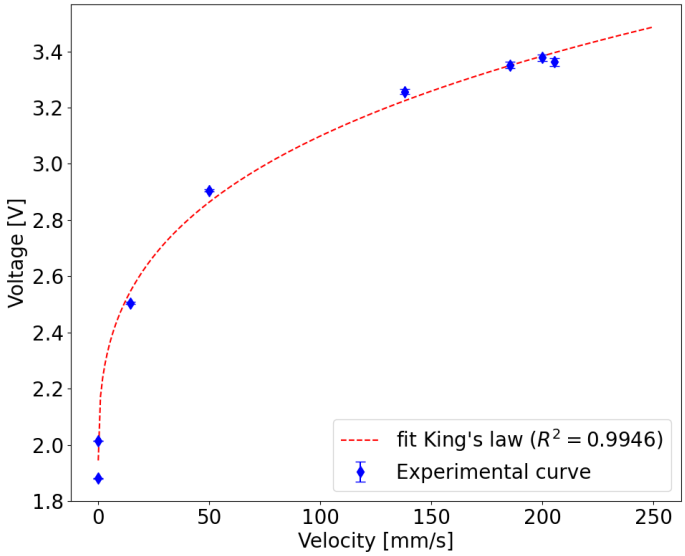

Figure 7.5 - *Velocity-voltage calibration of the hot film probe using the UDV as a reference sensor for velocity estimation. The fit was performed with King's law and its coefficient of determination R^2 is shown.*

appears to be an overestimation of its actual capabilities. In fact, the values declared by the provider are around 30 kHz [59] and were actually lowered to a more realistic range of 5 kHz to 10 kHz after a consultation with customer service[†].

At this point, it is also worth mentioning that there is disagreement in the literature on whether the square wave test is truly equivalent to the imposition of a velocity perturbation on the wire. Previous attempts to validate this type of test through direct testing with flow perturbations produced contradictory results, leading to cut-off frequency estimations up to an order of magnitude lower [272, 273], which are closer to the expected performance of the probe. In constant temperature anemometry operating conditions for film probes, the theoretical bandwidth is solely limited by the control loop, given the negligible thermal inertia of the thin-film sensor. However, in practice, the bandwidth is influenced by the damping effect of the backing substrate, the protective quartz coating, and the boundary layer flow around the wire. Therefore, the maximum bandwidth retrieved by the software closely represents the optimal bandwidth of the servo loop rather than the actual bandwidth of the sensor when used for flow measurements. For this reason, an autonomous in situ dynamic calibration is always recommended when a precise value must be retrieved. Nonetheless, this value

[†]The customer support of Dantec confirmed the correctness of the procedure carried out with the system to retrieve the cut-off frequency. However, the value given by the software was considered unreliable because it was too high. The minutes of this call are available on request.

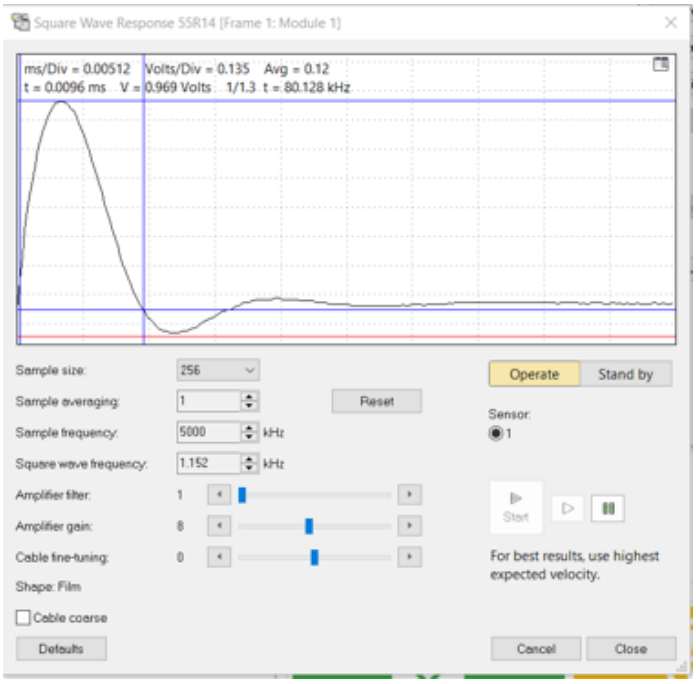

Figure 7.6 - *Measured dynamic response of the hot film. The typical overshoot with an oscillatory behavior, as depicted in Figure 7.2, is clearly appearing. Through the use of Equation* (7.19)*, the value of the cut-off frequency of the probe is retrieved.*

was not further investigated, as the acquisition frequencies targeted in this research are significantly lower than the kHz range, which is a value easily achievable by any probe of this manufacturing type, according to Dantec customer service[†].

7.4.2 Velocity measurements

After obtaining a complete calibration curve that covers the entire expected velocity range during the measurements, this curve was subsequently used to convert the acquired voltage across the entire profile into velocity. Figure 7.7 presents the profile measured using this procedure. Although measurements could be limited to half of the diameter due to the symmetry of the pipe, the complete set of measurements is reported here for the sake of completeness.

The non-dimensionalized comparison demonstrates a reasonably good agreement between the two sensors. The velocity used for non-dimensionalization is the bulk velocity, as defined in Equation (6.33), yielding values of $U_{\text{bulk,HF}} = 140\,\text{mm/s}$ and $U_{\text{bulk,UDV}} = 129\,\text{mm/s}$ for the hot film and UDV, respectively.

The uncertainty for the UDV was calculated according to Section 6.4, while the uncertainty for the hot film takes into account only type A uncertainty, as reported in Equation (6.24), along with a conservative estimation of uncertainty due to the

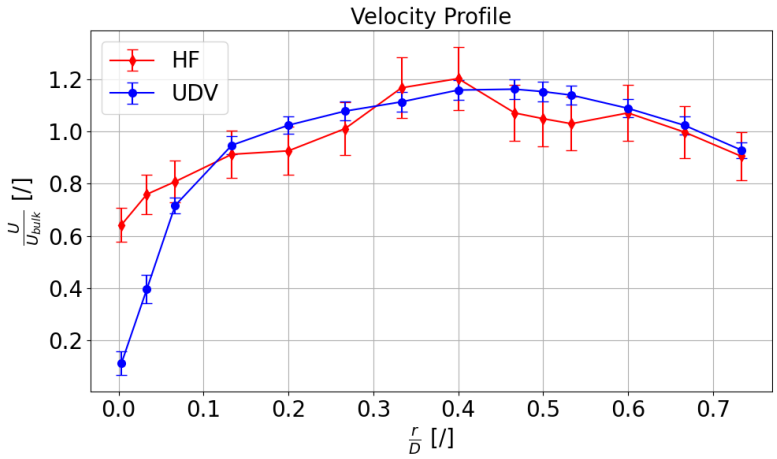

Figure 7.7 - *Comparison between the velocity profiles measured by the UDV and the fiber-film probe. A general good agreement can be found with the highest differences appearing close to the wall.*

temperature dependence of the probe. In fact, the manufacturer specifies that film probes can be affected by temperature variations, leading to errors of up to 10 % per °C. In this case, the bulk temperature was measured solely in the elevated tank using a PT100 sensor, confirming that the frictional heating from the pump and variations in ambient temperature did not increase the temperature of the entire water volume by more than 1 °C. Therefore, in addition to the calculated type A uncertainty, an uncertainty of 10 % was added to the hot film measurements.

It is observed that the largest difference between the two profiles occurs near the walls. This finding is consistent with previous literature, where hot wire measurements close to the walls reported velocities up to one order of magnitude higher than reference values, increasing with the conductivity and the thickness of the walls [274]. The higher thermal inertia of the wall compared to that of the fluid can create a cooling effect, resulting in increased measured voltage and consequently higher velocity readings near the wall. Moreover, as proximity to the wall increases, conduction becomes a more significant factor in the overall heat transfer process of the probe.

Lastly, it is important to mention the degradation of probe condition during the measurements. As noted in Section 6.2, the water used had previously been employed for PIV measurements, and complete removal of all seeding particles was not feasible. These particles were advantageous for the UDV measurements as they served as effective scatterers. However, they were small enough to pose minimal risk to the probe. Nonetheless, they could adhere to the sensitive components and prongs, potentially affecting measurement outcomes in unpredictable ways. Figure 7.8 illustrates the difference between a new/clean probe and the same probe following its usage in the facility.

Such phenomenon is difficult to quantify and even taking it into account in the

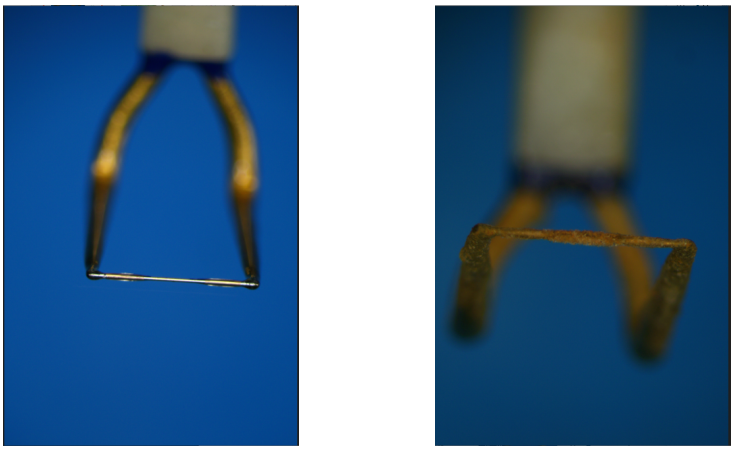

(a) Clean probe

(b) Probe after ≈ 200 h in the water

Figure 7.8 - *Comparison between the conditions of the fiber-film probe before and after its usage in the closed water loop. Such condition is believed to be also a factor affecting the final measurement*

uncertainty calculation is difficult in practice. Fortunately, the probe could be restored at the original conditions after cleaning with a soft marten hair brush and distilled water, allowing further tests to run smoothly.

7.5 Results in the oil bath

This Section presents the results obtained in the oil bath facility described in Section 7.3.2. This Section is further divided into different parts:

- **Acquisition procedure:** Section 7.5.1 describes how the signal is acquired and processed to extract the desired information, as a simple average of the entire acquired signal is insufficient for this setup.
- **Calibration post-processing:** Section 7.5.2 details the procedure used to treat the data and generate a calibration curve that accounts for both temperature and velocity.
- **Calibration results:** Section 7.5.3 describes and comments on all the results obtained with this setup in water and GaInSn, highlighting common points and differences, and evaluating the feasibility for use in the final cavity setup.

7.5.1 Acquisition procedure

The zero reference was set at an arbitrary point below the fluid surface, allowing for a total run of 150 mm. The probe was then traversed at different velocities ranging

from 0 mm/s to 30 mm/s with an acceleration of 100 mm/s^2 to minimize the portion of the run where the probe was moving at a non-constant velocity.

The acquisition of a single calibration data point followed these steps:

- Setting the desired calibration temperature
- Allowing all disturbances to dissipate until a stable zero-velocity voltage was recorded with the hot film
- Initiating temperature acquisition with the temperature sensors
- Starting a continuous movement of the probe following these phases:
  - Acceleration phase from 0 to the desired calibration velocity directed downward
  - Constant velocity phase (going downward) for the whole available run
  - Deceleration phase from the constant velocity to 0
  - Acceleration phase from 0 to the desired calibration velocity directed upward
  - Constant velocity phase (going upward) for the whole available run
  - Deceleration phase from the constant velocity to 0
  - Repetition of the process for several runs, depending on the chosen velocity
- Simultaneously, starting data acquisition with a sampling frequency of 100 Hz, i.e. the sampling frequency adopted in the final measurements.
- Stopping the runs waiting for the translational stage to return to the initial position
- Repeating for different velocities
- Repeating for different temperatures

This process leverages the fact that the probe cannot distinguish different flow directions, as discussed in Section 7.1, resulting in identical voltage measurements during both the upward and downward runs. A visualization of the process is reported in Figure 7.9(a) for an acquisition performed at $T = 52\,^{\circ}\mathrm{C}$ and $U = 25$ mm/s, therefore giving a total duration of 1 run of 6 s.

The signal exhibits a stabilization period during the initial runs, as the probe, subjected to a constant velocity flow, gradually reaches thermal equilibrium with its surroundings. To extract a meaningful average value, the acquired signal was processed as follows:

- **Segmentation**: The signal was divided into segments, each representing a single upward and downward probe movement, as illustrated in Figure 7.9(b). This segmentation was facilitated by the identification of local minima and maxima in the signal. Each segment exhibits a distinct pattern: an initial

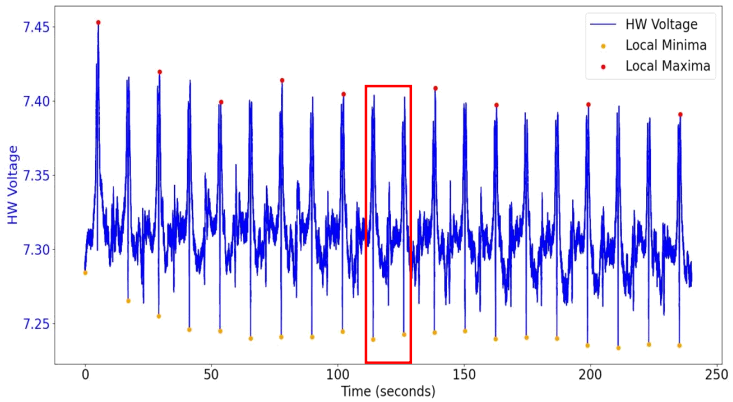

(a) Original raw voltage signal acquired by the hot film.

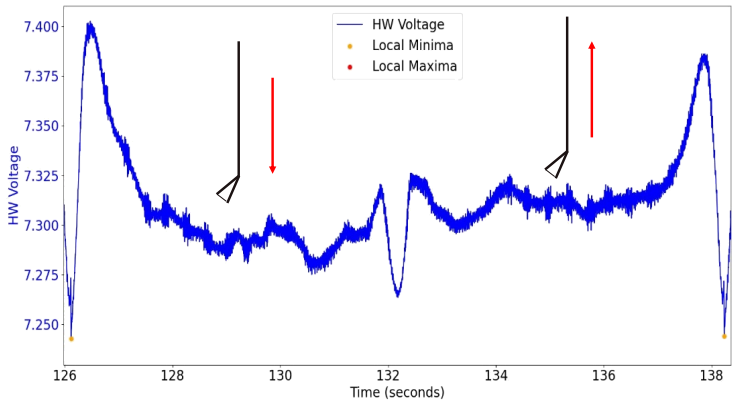

(b) Zoomed view of the original raw voltage signal. The two phases of the probe motion, upwards and downwards, are clearly discernible by identifying local maxima and minima in the signal.

Figure 7.9 - *Original raw voltage signal acquired by the hot film and zoomed view with the probe motion.*

phase characterized by a rapid change in signal amplitude corresponds to the acceleration of the probe. Following this, the signal stabilizes around a constant value, indicating steady-state motion of the probe. Subsequently, a drop in the signal marks the deceleration and reversal of the direction of the probe at the end of the downward run. The signal then exhibits a similar pattern during the upward movement of the probe, with an initial acceleration phase followed by a period of steady-state motion and a final deceleration phase to return at the starting point.

- **Constant Velocity Selection**: within each segment, only the portions corresponding to constant probe velocity were considered. These portions were identified based on the precise control of the motor driving the probe.
- **Segment Averaging**: the selected portions within each segment were averaged to obtain a single average value for that particular run.
- **Run Averaging**: this process was repeated for all segments, yielding an average value for each individual run.
- **Final Averaging**: the average of these individual run averages, denoted as E_{nm}, was considered the most representative value of the behavior of the probe under the specific conditions defined by velocity U_m and temperature T_n.

At the end of the whole process, the following vectors were retrieved to be processed:

$$T = [T_0, T_1, \ldots, T_N]$$
$$U = [U_0, U_1, \ldots, U_M]$$
$$E = \begin{bmatrix} E_{00} & E_{01} & \ldots & E_{0M} \\ E_{10} & E_{11} & \ldots & E_{1M} \\ \vdots & \vdots & \ddots & \vdots \\ E_{N0} & E_{N1} & \ldots & E_{NM} \end{bmatrix}$$

with $N = 5$ and $M = 18$ for water and $N = 5$ and $M = 14$ for GaInSn. These data were then processed with different methods to find a calibration curve suitable for the measurement campaign.

7.5.2 Processing methodologies

Once the vectors of temperature, voltage, and velocity measurements are collected and processed to obtain meaningful and organized values, the challenge becomes how to combine them to create a mathematical relationship linking the three vectors. This relationship can then be used as a transfer function to derive the physical value of the velocity from the voltage measured by the hot film. This Section presents the two different methods adopted in this study:

- **Nu-Re calibration [264]:** this method consists in the use of an effective wire temperature to eliminate the dependency of the calibration on the flow temperature allowing to establish a unique Nu-Re non-dimensional calibration curve.
- **Hollasch method [118]**: this method was originally developed by Hollasch and Gebhart [118] for low velocities calibrations in non-isothermal water flows. The main idea is to divide the calibration range in two regions, where the bottom one allows a dedicated treatment of mixed convection region.

After the detailed explanation of the two methods, the results obtained are presented in Section 7.5.3.

Nu-Re calibration

This method is based on a data reduction technique developed in literature [264]. Recalling Equation (7.10), it is possible to express the Nu number as in Equation (7.21):

$$Nu_w = \frac{E^2}{k_f(T_w - T_{ref})} \frac{R_w}{\pi L_w R_{tot}^2} \tag{7.21}$$

Defining also the Re number relative to the probe as in Equation (7.22), where ρ_f and μ_f are respectively the density and the dynamic viscosity of the fluid, it is possible to identify an effective wire temperature $T_{w,eff}$ defined as the wire temperature which collapses a set of Nu-Re data obtained at different flow temperatures on a single curve. The procedure is graphically shown in Figure 7.10.

$$Re_w = \frac{\rho_f U D_w}{\mu_f} \tag{7.22}$$

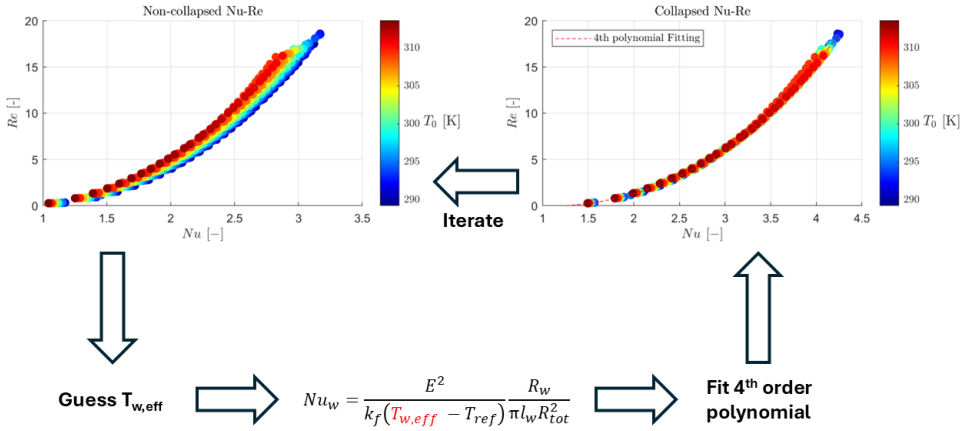

Figure 7.10 - *Iterative procedure to retrieve the wire effective temperature and perform the Nu-Re calibration. The data shown are taken from another work carried out at the Von Karman Institute [275].*

The selection criterion for $T_{w,eff}$ involves the use of a 4^{th} order polynomial fit. The wire temperature defined in this manner effectively represents the convective heat transfer process from the wire to the flow. Referring to the first step of Figure 7.10, it can be seen that when plotted in terms of voltage and velocity, distinct curves emerge for each temperature level. However, when plotted in terms of Re and Nu numbers with the inclusion of the effective wire temperature, all the data points collapse onto a single curve. This method is now well established in literature for high speed flows

and air measurements [263, 276] and its applicability in different conditions like the ones presented by this project is tested.

Hollasch method

This method was originally developed in the 1970s for the calibration of constant-temperature hot-wire anemometers at low velocities in water with variable fluid temperature. As shown in Section 7.2.1, when the involved velocities are very low, natural convection effects start to have a noticeable influence on the collected data. For this study, Table 7.1 illustrates how such limitations could impact the measurement of fluctuations. For this reason, the acquired dataset is divided into two distinct regions: the forced convection region and the mixed convection region. In the former, natural convection effects can be neglected, whereas in the latter, both natural and forced convection effects contribute significantly to the heat transfer process from the wire. Therefore, the two regions require a separate analytical treatment.

In the forced convection region, Equation (7.17) proved to provide a satisfactory linear relationship between E^2 and $\sqrt{U}$, but it did not account for temperature as a variable. In the reference study [118], based on experimental evidence, deviations from the linear behavior of Equation (7.17) were found to emerge when $\Psi = Re_w \,/\, Gr_w^{1/3} \approx 1$, i.e. around a threshold value of the velocity identified as U_t. As mentioned in Section 7.2.1, some of the interesting fluctuations for this study could occur around this range, and for this reason, this work was taken into consideration for the analysis.

In the statistical analysis of the two regimes, the following variables were considered:

- $\sqrt{U_m}$: the square root of velocity, treated as the dependent variable because it was imposed during the calibration process;
- E_{nm}^2: the voltage acquired with the probe, treated as an independent variable;
- T_n: the fluid temperature, treated as an independent variable;
- E_{n0}^2: the voltage acquired with the probe at the temperature T_n at $U_0 = 0$.

To simplify the analysis, the two voltage variables were combined into a single non-dimensional independent variable:

$$B_{nm} = \left(\frac{E_{nm}^2}{E_{n0}^2} - 1 \right)$$

Thus, a relationship of the form given by Equation (7.23) could be retrieved:

$$\sqrt{U_m} = f(B_{nm}, T_n) \tag{7.23}$$

The $\sqrt{U_m}$ was then expanded in a Taylor series with respect to the independent variables, and various combinations of different order terms were tested in the reference study to find the best fit with experimental datasets. More details about this procedure can be found in the reference study [118]. The optimal forms retrieved for

the two regions of interest were those reported in Equations (7.24) and (7.25) where the subscripts n, m are dropped:

$$\sqrt{U} = K_1 B + K_2 BT + K_3 \qquad \text{for the forced convection region,} \tag{7.24}$$

$$\sqrt{U} = C_1 B + C_2 B^2 + C_3 T + C_4 T^2 \qquad \text{for the mixed convection region.} \tag{7.25}$$

Here, K_1, K_2, K_3, C_1, C_2, C_3, and C_4 are coefficients to be determined during the calibration procedure.

A summary of the entire procedure is shown in Figure 7.11, taking into account both the calibration procedure previously explained and the measurement procedure of a point with general values E_f, E_{f0}, and T_f within the calibration range of velocity and temperature.

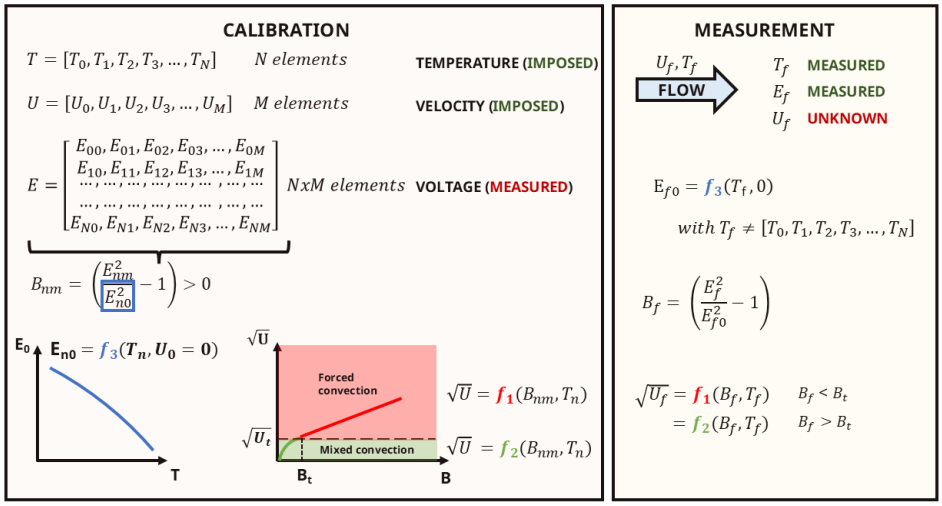

Figure 7.11 - *Graphical summary of the Hollasch method. The left panel summarizes the calibration procedure, while the right panel explains the procedure to determine the correct velocity value from a general measurement of $E_{0,x}$ and T_x.*

Significant attention must be directed toward the parameter denoted as E_{f0}. In Figure 7.11, the blue curve labeled f_3 illustrates the fitting function that establishes the relationship between this parameter and the temperature. It is evident that, to determine velocity accurately, E_{f0} is an indispensable parameter. However, it is practically unfeasible to obtain a measurement temperature T_f that exactly matches one of the calibration temperatures $[T_0, T_1, \dots, T_N]$. Therefore, to determine the corresponding E_{f0} for a given T_f, a fitting function expressed as $E_{f0} = f_3(T_f, 0)$ is necessary.

Although this approach may seem complex at times, to the best knowledge of the author, it is the only method in the literature specifically tailored for the calibration of

low velocities in conductive fluids. Moreover, despite utilizing a Taylor approximation and requiring the optimization of several coefficients, the method remains grounded in physical principles, with the mathematical formulation refined based on experimental data.

7.5.3 Calibration results

The results of each data processing method of the calibration acquired in the oil bath are reported here discussing in parallel the main outcomes obtained for water and GaInSn.

Nu-Re calibration

This section presents the results obtained with the application of the $Nu - Re$ calibration method to the acquired dataset. Figure 7.12 shows the different calibration curves for the fiber-film at different temperatures for the two fluids, corresponding to the first step (upper left corner) of Figure 7.10.

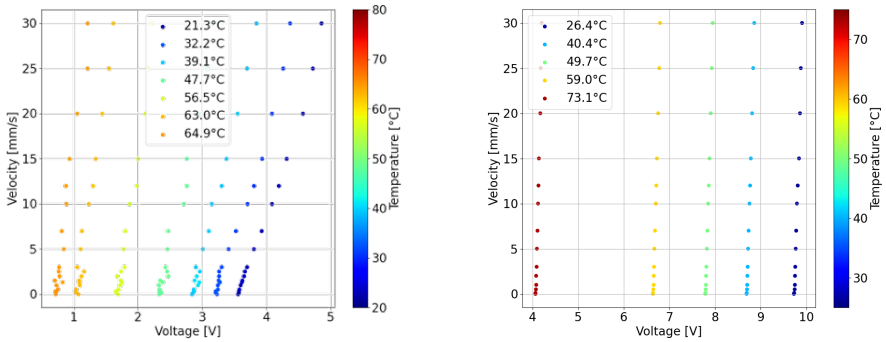

(a) Water (b) GaInSn

Figure 7.12 - *Velocity-temperature calibration results in water and GaInSn*

It is possible to observe that certain attributes of the curves align with the expectations. For example:

- Lower temperatures result in higher voltages, which is in line with what was anticipated in Section 7.1. This trend is consistent across all the curves, demonstrating the proper operation of the probe under constant temperature conditions.
- The relationship between velocity and voltage exhibits a trend reminiscent of the initial portion of a King's law curve, which aligns with prior understanding of the behavior of the probe. This observation reaffirms our existing knowledge regarding how the probe responds under varying conditions.

However, other aspects should be emphasized to get a full understanding of the graph:

- The trend at low velocities is less clear, especially in water, and in both cases the limit velocity where the King's law trend start to appear can be identified in the minimum velocities measurable retrieved for the two fluids in Table 7.1, i.e. when $\Psi = 1$.
- It is clear the strong sensitivity of the probe to temperature, which is much higher than the sensitivity to velocity. In fact, for a given temperature, the whole velocity curve lies in a range of $\approx 1\,\mathrm{V}$ in water and $\approx 0.2\,\mathrm{V}$ in GaInSn, therefore giving sensitivities of $\approx 30\,\mathrm{mV/(mm/s)}$ and $\approx 7\,\mathrm{mV/(mm/s)}$ respectively. On the other hand, for both fluids the full voltage range covered is $\approx 5\,\mathrm{V}$ corresponding to a temperature range of $60\,^{\circ}\mathrm{C}$, therefore giving a sensitivity to temperature $\approx 85\,\mathrm{mV/^{\circ}C}$. The probe therefore results to be much more sensitive to temperature than to velocity, at least in the range of the two quantities where it is used in this work. Moreover, consistently with what was said in Section 7.1, the sensitivity to velocity tends to decrease when the temperature of the fluid increases, i.e. when the over-temperature of the film decreases.

As a consequence, attempts to perform the second step of the $Nu - Re$ calibration collapsing the curve using the effective wire temperature did not yield positive outcomes. The curves remained significantly separated, similar to those shown in Figure 7.12, making it impossible to identify a single best-fit curve that could eliminate the temperature dependence. Even with attempts to manipulate some parameters of Equation (7.21), the curves did not collapse, highlighting a strong mathematical and physical limitation to this method. This approach has been well established in air [263, 264], where wire probes are used in different flow regimes up to the supersonic one with typically smaller temperature differences of approximately $30\,^{\circ}\mathrm{C}$, and where probes exhibit temperature sensitivities in the range of $10\,\mathrm{mV/K}$ to $15\,\mathrm{mV/K}$ [268].

In the present work, it is believed that the strong temperature dependence of the probe is a primary limitation contributing to the non-applicability of the method. Previous studies also emphasize the temperature dependence of film probes as a significant source of error [117]. Interestingly, increasing the wire temperature could potentially mitigate this issue by enhancing the sensitivity of the probe to velocity while reducing its sensitivity to temperature, as discussed in Section 7.1. However, elevating T_w results in an increased minimum measurable velocity U_{min} due to enhanced convective flow around the wire, thereby jeopardizing the increased sensitivity when targeting low velocities.

Hollasch method

The results of the application of the Hollasch method to the acquired datasets are shown in Figure 7.13.

First, it is possible to distinguish the two different flow regions, i.e., mixed convection (green) and forced convection (red). The threshold was chosen based on the limitations given in Table 7.1. Data points are plotted according to temperature,

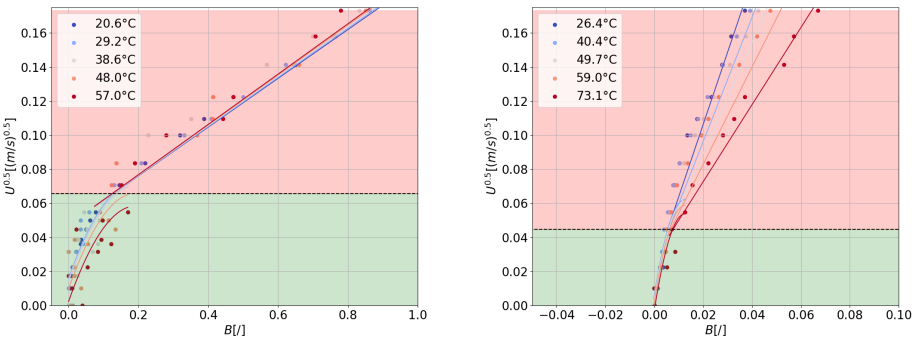

(a) Water

(b) GaInSn

Figure 7.13 - *Application of the Hollasch method to the dataset for water and GaInSn. The red and green regions respectively indicate the forced convection and mixed convection regions. The curve of different colors are the representation of Equations* (7.24) *and* (7.25) *for different temperatures.*

and the best-fit curves derived from Equations (7.24) and (7.25) are shown with temperature-based color-coding. Continuity between the two segments of the curves was not explicitly enforced in the model, leading to noticeable discontinuities, particularly for water at certain temperatures. Ideally, the constant K_3 in Equation (7.24) should be defined as $K_3 = \sqrt{U_t}$ to ensure smooth transitions between the curves. However, this constraint was not explicitly included in the original model [118], and the same approach was adopted in the present study to avoid overconstraining the model. Consequently, achieving proper continuity between the curves relies heavily on the quality and accuracy of the experimental data used for model fitting.

To retrieve the velocity value from the graph, an inverse approach to Equations (7.24) and (7.25) is employed, as illustrated in Figure 7.11. The first challenge involves computing the zero-velocity voltage value, E_{f0}, at the measured temperature, T_f, and therefore retrieving the function $E_{f0} = f_3(T_f, 0)$ for each dataset. These functions are illustrated in Figure 7.14.

Using the Least Squares Method (LSM) criteria, a second-order polynomial fit was determined to best describe the relationship between the hot film voltage and temperature. This trend remains consistent across different velocities and in both fluids. Additionally, it is insightful to extend this plot to all velocities, yielding the results shown in Figure 7.15.

Visualizing the data in this manner makes even more evident, as highlighted in Figure 7.10, that the dependence of the probe on temperature is significantly higher than its dependence on velocity. Indeed, the influence of velocity on the fitting is minimal, resulting in nearly identical fitting curves when considering all velocities or only the zero-velocity condition. This outcome suggests that while the velocity influence on the probe is present, it is not sufficiently pronounced to be accurately

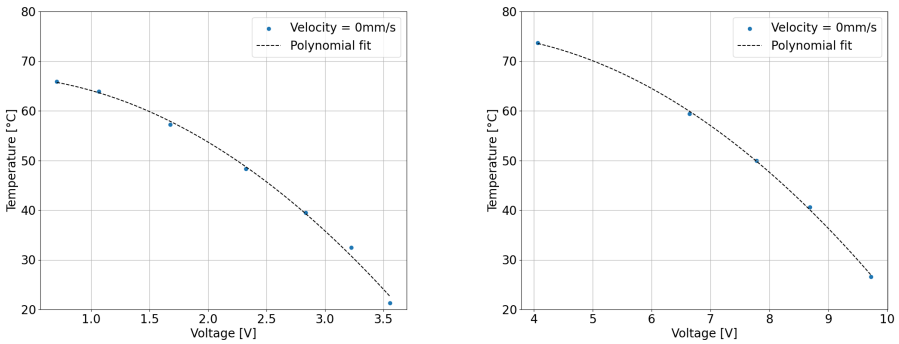

(a) Water (b) GaInSn

Figure 7.14 - *Hot film voltage vs Temperature at velocity $U = 0$. A second order fit was found to be the best and adopted for the relationship*

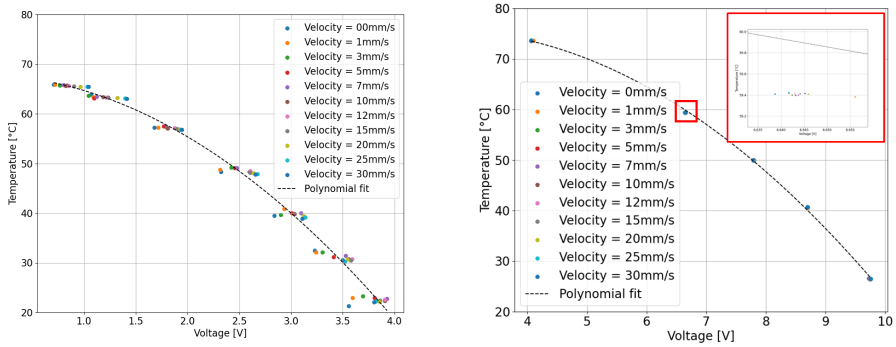

(a) Water (b) GaInSn

Figure 7.15 - *Voltage vs Temperature at different velocities. A second order fit was found to be the best and adopted for the relationship*

measured and risks being obscured by noise, with the probe primarily responding to temperature variations.

7.6 Effect of the hot film on the surroundings

It is foreseeable that heating the hot film probe during measurements could perturb its surroundings, and the significance of this effect must be assessed to evaluate the effective countermeasures to be implemented. The primary impact lies in the al-

teration of the local flow temperature. The heated probe functions as a volumetric heat source within the fluid, thereby inducing a localized increase in temperature. Section 7.2.1 has already discussed how this phenomenon affects the velocity field surrounding the wire. However, a non-negligible impact is also observed on temperature sensors, necessitating temperature corrections to account for this effect. This issue is particularly pronounced in fluids with higher thermal conductivity, such as liquid metals, as demonstrated in Figure 7.16.

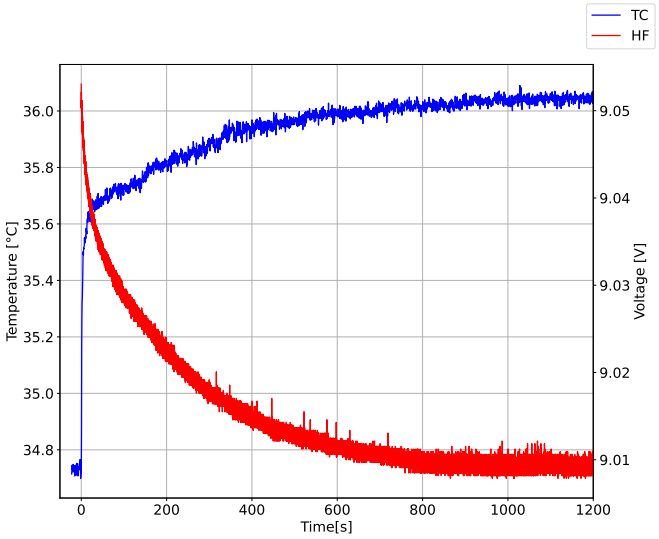

Figure 7.16 - *Effect of the hot film probe on the temperature measurements. Upon activation, the probe induces an increase in the fluid temperature, resulting in a corresponding decrease in the voltage measured by the probe.*

In Figure 7.16, both the thermocouple and the hot film were maintained within the GaInSn bath at an initial temperature of approximately 35 °C. At $t = 0$, the hot film probe was activated, thereby initiating the heating of its surroundings. It is evident that as the fluid temperature begins to increase, the voltage measured by the hot film correspondingly decreases. This effect cannot be attributed to the formation of a natural convection flow around the wire, as such a phenomenon would lead to an increase in the voltage measured by the hot film due to the associated rise in velocity. Thus, the only plausible explanation for this observation is the localized temperature increase in the fluid induced by the probe itself. Consequently, prior to performing all acquisitions, sufficient time was allocated to ensure the establishment of thermal equilibrium before commencing each run. Equilibrium was considered to be reached when both the voltage and temperature measurements, averaged over a 1-minute interval through a moving average, exhibited differences of less than 1 %. This averaging time was chosen because it represented the approximate duration of a single measurement point within the cavity. Furthermore, the time required to reach

equilibrium in Figure 7.16, approximately 15 min, was used as a reference for the waiting time between subsequent measurements in the cavity.

More insights on this effect can be given by Figure 7.17.

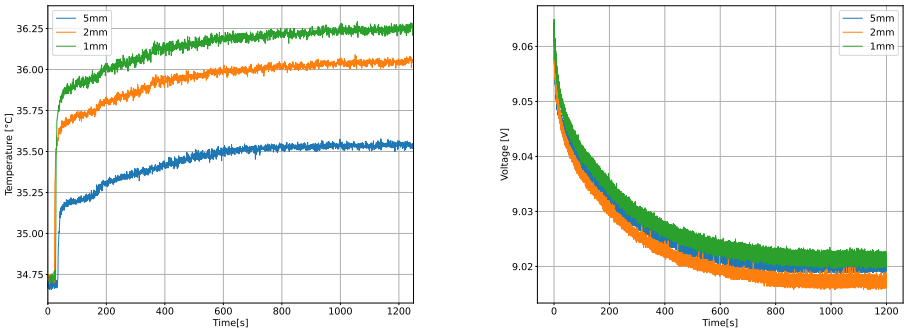

(a) Temperature reading by the TC

(b) Voltage reading by the hot film

Figure 7.17 - *Effect of the distance between the hot film and the thermocouple. On the left, the temperature increase of the thermocouple decreases when the sensor is placed at a higher distance from the heat source, i.e., the hot film. On the right, the hot film voltage recorded with the three different positions of the temperature sensors. The thermocouple position is not affecting the hot film reading.*

The two images illustrate the impact of varying the distance between the hot film and the thermocouple. Figure 7.17(a) demonstrates that the closer the thermocouple is to the hot film, the greater the observed temperature increase. This observation is logical, considering that the power dissipated by the wire diffuses spherically around it, resulting in a lower power received by a point in space as the distance from the heat source increases. Conversely, Figure 7.17(b) indicates that the voltage reading of the hot film remains unchanged regardless of the position of the thermocouple. This confirms that the thermal effect is unidirectional, with the hot film influencing the thermocouple, but not the other way around.

The analysis of this effect is crucial for several reasons. Primarily, it provides more insights into the positioning of the sensors defined in Section 2.4.2. In fact, it is evident that even at the chosen distance of 1 mm, the influence of the hot film on the thermocouple is significant. Positioning the sensors far enough apart to eliminate this influence is not feasible, as the final measurement volume would become too large for the scope of this analysis. Consequently, it is necessary to account for this thermal interaction by correcting the temperature readings accordingly. A full representation of the tests carried out is shown in Figure 7.18 where the ΔT_{TC} induced by the hot film on the surroundings is shown as a function of the distance between the sensors and the average fluid temperature.

As expected, the ΔT_{TC} is higher when the sensors are closer and the fluid temperature is lower. In the configuration used for the final measurements, i.e. distance

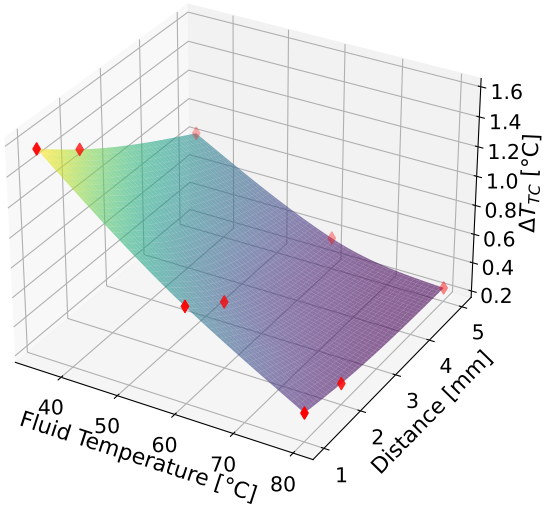

Figure 7.18 - *Effect of the hot film probe on the reading of the thermocouple. The steady-state temperature difference recorded by the thermocouple upon activation of the hot film is represented as a function of the distance between the TC and HF and the average GaInSn temperature. The temperature of the hot film is kept at* $T_w = 82\,^{\circ}\mathrm{C}$.

of 1 mm, the trend shown between ΔT_{TC} and the fluid temperature is linear and therefore a linear correction has been implemented for the final measurements. These tests have enabled a comprehensive understanding of the phenomenon, allowing for corrections to the temperature readings when the hot film is active. Additionally, measurements can be compared with those obtained when the hot film is inactive, facilitating a robust and meaningful comparison.

7.7 Spatial resolution

The spatial resolution of the hot film sensor was initially approximated in Section 2.2 as the volume of the entire cylindrical sensor. However, given the specific characteristics of the sensor, a more precise estimation can be achieved. Notably, while the resolution in directions perpendicular to the flow is determined by the wire length, the streamwise resolution length l_x depends on the sampling frequency f_s and the characteristic flow velocity U_c [265] as expressed by Equation (7.26)

$$l_x = \frac{U_c}{2f_s} \tag{7.26}$$

Considering for this calculation the velocity taken from the maximum estimated by the DNS simulations in GaInSn, i.e. $U \approx 30\,\mathrm{mm/s}$ and adopting the lowest sampling frequency used for the measurements, $f_s = 100\,\mathrm{Hz}$, the resulting streamwise resolution length is approximately $l_x \approx 150\,\mu\mathrm{m}$. This value is approximately twice than the probe diameter used for estimating the volumetric spatial resolution in Section 2.2. Consequently, recalling the length of the wire $L_w = 1.25\,\mathrm{mm}$ and adopting l_x as spatial resolution for the two directions perpendicular to the wire, the corrected volumetric resolution is $3 \times 10^{-2}\,\mathrm{mm}^3$, still respecting the requirements of Section 2.1.

7.8 Conclusions

This Chapter presented the work conducted for the characterization of the Hot Film probe in conductive fluids, primarily focusing on the issue of simultaneous calibration with respect to velocity and temperature.

The results reported in Section 7.4 demonstrated that the probe can reasonably measure velocity in water, maintaining good agreement with the UDV probe for velocities as low as 10 mm/s. However, the strong dependence on temperature introduced high uncertainty in the measurements at lower velocities, particularly near the pipe wall where the thermal effect is more pronounced. This finding emphasized the necessity for a calibration method that accounts for temperature effects. Consequently, an oil bath setup was implemented, enabling calibration across a wide range of temperatures and velocities within the measurement range. Despite employing specific methodologies for low-velocity measurements, the probe demonstrated significantly higher sensitivity to temperature fluctuations compared to velocity variations. This resulted in velocity effects being almost entirely masked by the dominant temperature signals. Consequently, while initially envisioned as a velocity probe as stated in Chapter 2, the probe was ultimately calibrated and utilized as a temperature sensor. Velocity effects were treated as a secondary, noise-like contribution, and the primary focus shifted towards temperature measurements.

Eventually, Section 7.7 addresses a more detailed calculation of the spatial resolution of the probe, which is summarized in Table 7.2 along with the sampling frequency used for the different experimental setups.

Table 7.2 - *Summary of spatial resolution and sampling frequency achieved with the Hot Film probe across various experimental setups.*

Case	$\mathbf{U_c}$	$\mathbf{f_s}$	**Streamwise resolution** $\mathbf{l_x}$	**Volumetric resolution** $\mathbf{\Delta x}$
Water in the loop	140 mm/s	1.5 kHz	70 µm ‡	5×10^{-3} mm^3
Water in the cavity	3 mm/s	0.1 kHz to 1 kHz	70 µm ‡	5×10^{-3} mm^3
GaInSn in the cavity	30 mm/s	0.1 kHz to 1 kHz	150 µm	3×10^{-2} mm^3

‡The direct calculation of the streamwise spatial resolution would deliver a value smaller than the diameter of the wire itself. For this reason, the wire diameter has been taken as reference value.

Chapter 8

Results in the differentially heated cavity

This Chapter presents the experimental and numerical results obtained in the differentially heated cavity, as detailed in Chapter 3, addressing the main issue introduced in Chapter 1, namely the measurement of turbulent heat flux in liquid metals. To achieve this, all the aspects discussed and analyzed throughout the thesis are revisited and recontextualized, with a focus on the phenomena occurring in natural convection within liquid metals. The spatial and temporal resolution of the sensors is further examined, alongside an evaluation of the performance of the setup and a comparison of the numerical simulation results with the experimental data.

First, the introductory remarks in Section 8.1 establish a framework for understanding common elements that facilitate the reading of the entire Chapter. Section 8.2 then presents the results with water as the working fluid, beginning with an examination of average profiles, followed by an analysis of fluctuations and instantaneous measurements, and highlighting key insights gained for the setup at this stage. The analysis proceeds with GaInSn in Section 8.3, following a similar structure, starting with average profiles and then focusing on fluctuations. Finally, Section 8.3.5 presents the turbulent heat flux calculation in GaInSn.

8.1 Introductory remarks

As demonstrated in Chapter 3, four positions were designated for experimental measurements. Figure 3.4 illustrates the symmetry of the cavity with respect to the plane $z = 30\,\text{mm}$. Due to this symmetry, the profiles at positions 1 and 2 are expected to be identical, as are the profiles at positions 3 and 4. This expectation was verified experimentally, as shown in Appendix E.1, and further confirmed by numerical simulations as shown in Section 4.5. Consequently, only two profiles, relative to the plane $z = 12\,\text{mm}$, are presented hereafter: position 1 at $x = 4\,\text{mm}$, parallel to the hot copper plate and referred to as the "hot profile," and position 3 $x = 56\,\text{mm}$, parallel the cold copper plate and referred to as the "cold profile."

The results presented in this Chapter, are obtained under the conditions outlined in Table 8.1, providing a summary of the experimental setup detailed in Chapter 3. These conditions apply to both the experimental and numerical analyses of the cavity.

Table 8.1 - *Temperatures and non-dimensional parameters tested in this work for the different working fluids*

	Temperature [°C]				Gr [$\times 10^8$]	Pr	Ra [$\times 10^6$]
	T_{hot}	T_{cold}	T_{mean}	ΔT			
Water	78.8	26.5	52.7	52.3	1.8	3.4	610
Galinstan	79.5	37.5	58.5	42.0	1.4	0.022	3.0

As outlined in Chapter 3, the temperature differences achieved vary between the two fluids due to limitations of the experimental setup, particularly in the cooling system, which constrained the minimum attainable temperature preventing in both cases to reach the targeted $T_{cold} = 20\,°C$. However, the target hot temperature of $T_{hot} = 80\,°C$ was successfully reached. Despite these limitations, the target range of Gr and Ra numbers, as specified in Chapters 2 and 3, was achieved.

These temperature differences are crucial for the analysis, as they represent the maximum values attainable with the current setup, making them the most favourable to observing turbulence or transition to turbulence regime in natural convection.

The settings and main spatial and temporal resolution for all sensors used in obtaining these results are detailed in the conclusion Sections of each respective Chapter, specifically Sections 5.4, 6.6 and 7.8 for the temperature sensors, UDV, and HF.

8.2 Water

This Section presents the experimental and numerical results obtained in water within the differentially heated cavity. The average profiles for temperature and velocity are provided in Sections 8.2.1 and 8.2.2, respectively. Subsequently, the velocity and temperature fluctuations are analyzed together in Section 8.2.3.

Regarding the numerical simulations, Table 4.1 indicates that the only DNS simulations performed in water (DNS 2) adhere to the initially targeted boundary conditions, i.e. $T_{hot} = 80\,°C$ and $T_{cold} = 20\,°C$, but do not include the cavity walls (no conjugate heat transfer implemented), rendering it unsuitable for a reliable comparison with the experiments conducted under the conditions specified in Table 8.1. Consequently, the only available comparison for water carried out in this Section is with the RANS simulations. Specifically, the RANS simulations in water considered in this Chapter are those detailed in Table 8.2.

The rationale behind the choice of these settings and boundary conditions is discussed throughout this Chapter.

Table 8.2 - *Characteristics of the RANS simulations used for the comparison with the experimental study in water.*

Simulation	CHT	BC - T Active Walls	BC - T Passive Walls	BC - U	Turbulence model
RANS 1	No	$T_{hot} = 78.8\,°C$ $T_{cold} = 26.5\,°C$	Adiabatic	No slip	$k-\omega$ SST
RANS 2	Yes	$T_{hot} = 78.8\,°C$ $T_{cold} = 26.5\,°C$	Adiabatic	No slip	$k-\omega$ SST
RANS 3	Yes	$T_{hot} = 78.8\,°C$ $T_{cold} = 26.5\,°C$	$h = 35\,\frac{W}{m^2K}$	No slip	$k-\omega$ SST

8.2.1 Average temperature

The results obtained in terms of average temperature profiles in water at position 1 (hot profile) and position 3 (cold profile) in the cavity, under the conditions specified in Table 8.1, are reported and explained here.

Figure 8.1 presents a comparison between the experimental profiles acquired with the thermocouple, the fiber Bragg grating, and the hot film, and the RANS 1 simulation from Table 8.2.

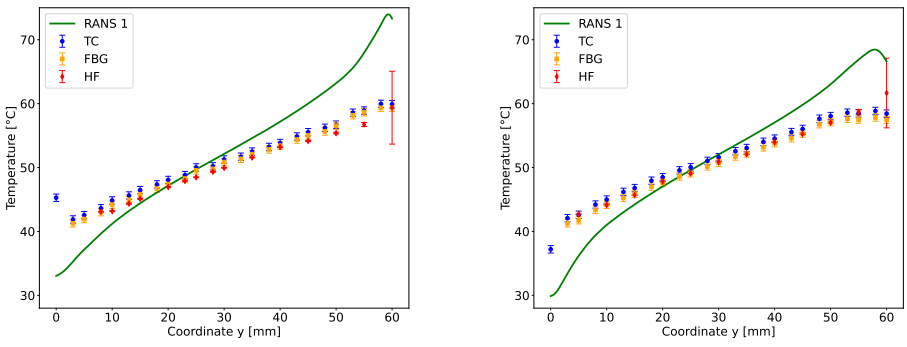

(a) $x = 4\,\text{mm}$ (b) $x = 56\,\text{mm}$

Figure 8.1 - *Average temperature profiles in water along the y direction parallel to the hot wall (position 1) and to the cold wall (position 3). Comparison between TC, FBG and RANS. In the RANS simulations, the cavity walls are excluded, and conjugate heat transfer effects are not accounted for.*

First, it is notable that there is very good agreement among the three experimental sensors. Particularly interesting is the outcome of the hot film, which, although originally designed to measure velocity, was ultimately found to be more suitable for temperature measurements. All uncertainties are implemented as described in the respective Chapters of each technique, and the measurements from the three sensors are generally within the uncertainty bars of each other. However, the point at $y = 60\,\text{mm}$ of the hot film profile exhibits an uncertainty significantly higher than the other points. This is likely due to the fact that this point corresponds to the interface between the fluid in the cavity and the cylindrical stainless steel tubes used for instrumentation access, as shown in Figure 3.5. In this configuration, it is possible that unexpected fluid recirculation is occurring, which could increase the velocity at this location. Given the sensitivity of the hot film to velocity, and the fact that it is being used to measure temperature, these velocity fluctuations are interpreted by the sensor as noise, thereby increasing the uncertainty.

The overall trend is as expected, with temperature increasing towards $y = 60\,\text{mm}$, i.e., near the roof of the cavity. The linear slope suggests heat transfer dominated by conduction, indicating that convection and circulation effects play a minor role and the fluid tends towards thermal stratification. However, given the thin boundary layer in water (see Figure 4.6) and the measurement location, this behavior was anticipated.

However, the steepness of both the experimental and numerical curves differs significantly, despite the boundary conditions being the same. To address this discrepancy, the simulation RANS 2, presented in Table 8.2, was performed. This simulation incorporated the cavity wall, i.e., implemented conjugate heat transfer, making the numerical domain more representative of the experimental conditions. The result of this modification is shown in Figure 8.2.

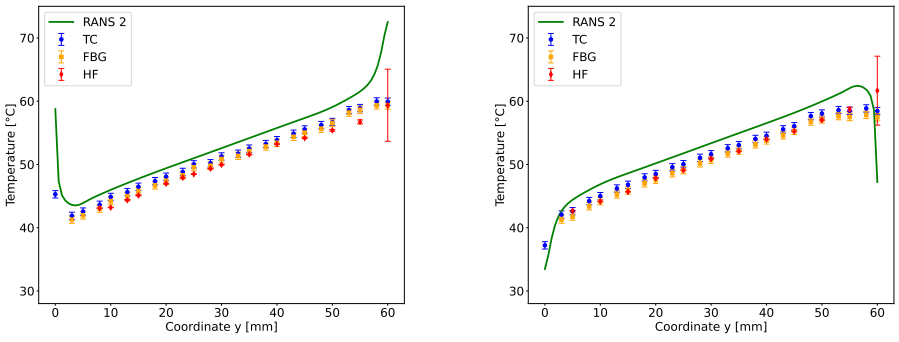

(a) $x = 4\,\text{mm}$ (b) $x = 56\,\text{mm}$

Figure 8.2 - *Average temperature profiles in water along the y direction parallel to the hot wall (position 1) and to the cold wall (position 3). Comparison between TC, FBG, HF and RANS. In the RANS simulations, the walls are included but considered adiabatic.*

It is evident that the experimental slope is perfectly matched after this implementation. In particular, the trend near the edge, close to $y = 0\,\text{mm}$, is also respected in both profiles. The first experimental point at $y = 0\,\text{mm}$ is measured with a thermocouple flush-mounted in the wall, and it perfectly follows the trends observed in the simulations, where a temperature jump tends to occur near the wall at the hot (cold) profile, corresponding to the higher (lower) temperature of the wall itself in respect of the fluid, due to the different thermal conductivities. Therefore, the conjugate heat transfer contributed significantly to correcting the slope of the entire profile, enabling a good match with the experimental data.

On the other side of the profile, near $y = 60\,\text{mm}$, the trend between experimental and numerical data differs noticeably. This can again be explained by the fact that, in the experimental setup, there is no wall at this point, as this is where the instrumentation access is located. Therefore, in the experiments, this region is in contact with the nitrogen filling the cavity, which provides very different local thermal boundary conditions, affecting the behavior of the fluid near the wall.

However, it is clear that the numerical simulations slightly overpredict the experimental results in both cases. As shown in Chapter 3, the walls of the cavity cannot be considered perfectly adiabatic, but a global heat transfer coefficient of $h = 15\,\text{W}/(\text{m}^2\text{K})$ was estimated. This feature was incorporated into the numerical simulations, accounting for heat losses from the passive walls of the cavity. Since the exact calculation of these losses is experimentally challenging, several values for the global heat transfer coefficient were analyzed to assess the sensitivity of the simulation to this parameter. The results are presented in Figure 8.3.

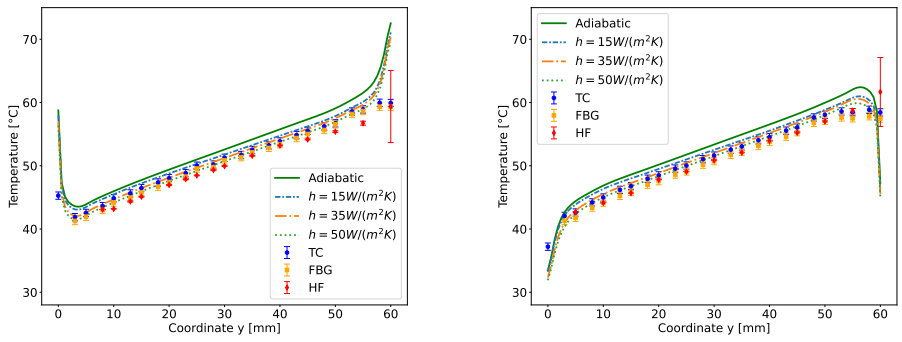

(a) $x = 4\,\text{mm}$ (b) $x = 56\,\text{mm}$

Figure 8.3 - *Average temperature profiles in water along the y direction parallel to the hot wall (position 1) and to the cold wall (position 3). Comparison between TC, FBG, HF and RANS simulations performed with different entity of the losses from the passive walls.*

The different RANS simulations presented are all variations of RANS 3 as it is outlined in Table 8.2, but with different heat losses implemented, as indicated in the

legend. The walls were in fact set to exchange heat by convection with a constant ambient temperature of 20 °C and a variable global heat transfer coefficient h ranging from adiabatic ($h = 0$) to 50 W/(m^{2}K).

It is evident that the differences due to the heat losses are minimal, as was already demonstrated in the average flow fields predicted by the numerical simulations in Chapter 4. However, it was possible to estimate the best fit with the experimental results by calculating the least mean square error between the numerical curves and the thermocouple experimental points, taken as the reference due to the inclusion of a measurement point at the wall. The results of this operation led to an optimal value of $h = 35\,\mathrm{W/(m^2K)}$, which is significantly higher than the value of $h = 15\,\mathrm{W/(m^2K)}$ found in Section 3.4. The results of the chosen RANS simulation, i.e., RANS 3 from Table 8.2, are shown in Figure 8.4.

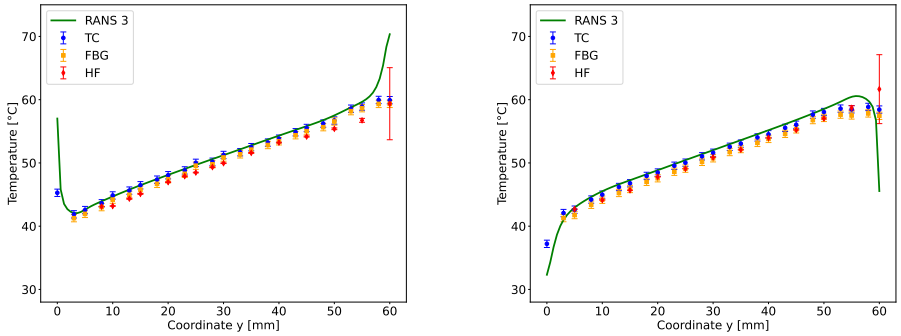

(a) $x = 4\,\mathrm{mm}$ (b) $x = 56\,\mathrm{mm}$

Figure 8.4 - *Average temperature profiles in water along the y direction parallel to the hot wall (position 1) and to the cold wall (position 3). Comparison between TC, FBG, HF and RANS.*

While tuning numerical simulations is generally discouraged, it was deemed necessary in this specific case due to several factors. Firstly, the simulation mesh was not generated directly from a CAD model of the experimental setup but created independently. This resulted in several discrepancies between the numerical domain and the actual experimental setup, as evident when comparing Figure 3.2 and Figure 4.1. Notably, the mesh did not incorporate the access points for instrumentation (numbers 2 and 7 in Figure 3.2), which can significantly contribute to heat losses. In fact, the effective exchange surface area of the actual cavity was almost double that of the simulated domain, due to the inclusion of these instrumentation access points. Considering the total real surface area of 0.0442 m^2, an average fluid temperature of 50 °C, an ambient temperature of 20 °C, and the experimentally retrieved heat transfer coefficient $h = 15\,\mathrm{W/(m^2K)}$, an estimation of the total heat losses from the cavity can be calculated as approximately 20 W. However, in the numerical simulation, the simulated surface area is significantly smaller, at only 0.0216 m^2. To achieve

the same level of heat losses with this reduced surface area, the heat transfer coefficient in the numerical model would need to be increased to a value of approximately $h \approx 30\,\mathrm{W/(m^2K)}$.

Secondly, the turbulence model employed in the simulations inherently introduces uncertainties, particularly in predicting near-wall behavior where the heat transfer coefficient h plays a crucial role. Given the complexity of accurately modeling turbulence effects, especially with the simplifications made in the mesh, minor adjustments to the heat transfer coefficient were deemed justifiable to improve the agreement between numerical results and experimental observations leading to the final adopted value of $h = 35\,\mathrm{W/(m^2K)}$. This approach aims to partially compensate for the limitations of the turbulence model in capturing the precise thermal behavior at the walls.

It is noteworthy that an analysis of the influence of the losses was also carried out with the velocity profiles, as it is presented in Appendix E.2. The influence of the losses was found to be negligible, or at least undetectable by the UDV sensor, thereby justifying the choice of the optimal value for the losses based solely on the thermal profile.

A key finding of this Section is that the implementation of conjugate heat transfer plays a crucial role in ensuring a meaningful comparison between experimental and numerical results. Moreover, accounting for heat losses from the passive walls can help compensate for minor discrepancies in the numerical modeling.

8.2.2 Average velocity

The results obtained in terms of average velocity profiles in position 1 (hot profile) and position 3 (cold profile) in the cavity under the conditions outlined in Table 8.1 are presented and discussed here.

The comparison for the velocity profiles is conducted exclusively with the vertical component of the velocity, U_y, as it is the component measured during the experiments. As explained in Chapter 4, this choice was primarily justified by the fact that, close to the active walls, U_y represents the dominant contribution to the velocity magnitude.

Figure 8.5 presents a comparison between the UDV measurements and RANS 3 of Table 8.2 near the cold wall (position 3).

The results show extremely low velocities and, consequently, very high relative uncertainties of the UDV sensor, primarily due to the significant number of zero values in the time evolution profile. In fact, if the backscattered signal is lower than the sensor sensitivity threshold, the recorded value is set as zero. It is important to note that the velocity measurements were taken slightly beyond the limits of the cavity at $y = 60\,\mathrm{mm}$, as the aperture made for the instrumentation access allowed some fluid to enter the stainless steel cylinder, enabling the measurements to extend until that point. However, the results beyond $y = 60\,\mathrm{mm}$ should be considered irrelevant for the comparison.

The experimental profile near the cold wall exhibits a trough at $y = 60\,\mathrm{mm}$, in the region where the flow coming from the hot side intersects with the flow cooled by the active wall and directed downwards. This feature, however, does not appear

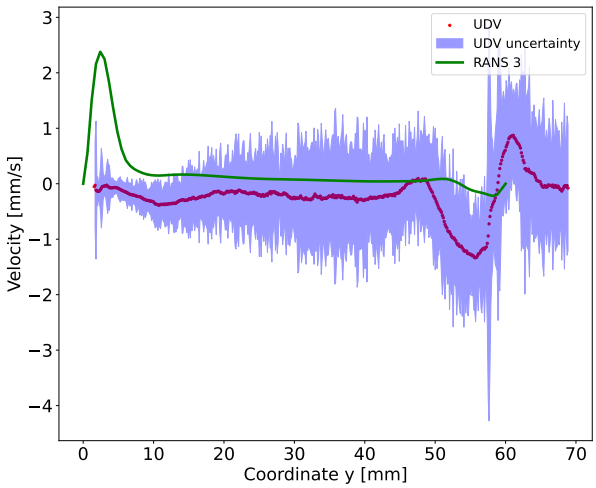

Figure 8.5 - *Average velocity profile U_y along the y direction parallel to the cold wall (position 3). Comparison between UDV and RANS.*

to be captured by the RANS simulation. To gain a better understanding of the phenomenon, Figure 8.6 presents a schematic where the ultrasound cone of the UDV is superposed with the full U_y field calculated by the RANS simulation.

In particular, the numerical profile previously shown in Figure 8.5 only takes into account the U_y along the green line shown in Figure 8.6. It is evident that the volume over which the UDV sensor averages is considerably larger, and averaging over the entire volume has a significant impact on the velocity output of the sensor. Specifically, the nearly zero velocities recorded up to approximately $y = 45\,\text{mm}$ can be explained by the fact that the sensor volume is largely outside the high-velocity region shown in Figure 8.6. The measured velocity becomes non-zero only when the measurement cone starts to expand, i.e., when the thin boundary layer near the wall is included in the measurement. However, in general, the high proportion of very low velocity values is expected to significantly lower the averaged measurement values over the cone volume of the sensor also affecting the reliability of the overall measurement.

It is therefore evident that, to make a proper comparison with the experiments, the numerical simulations must also be averaged over the same volume. The results of this operation are shown in Figure 8.7.

In this case, it is clear how the averaging process delivered results that fit much better with the experimental values, making the averaging process a key feature for obtaining meaningful comparisons. Additionally, the peak near $y = 0\,\text{mm}$ in the RANS simulation, which is not present in the experimental data, was reduced after the averaging process. This, combined with the fact that measurements close to the sensor are typically less reliable due to the potential saturation effects from the proximity

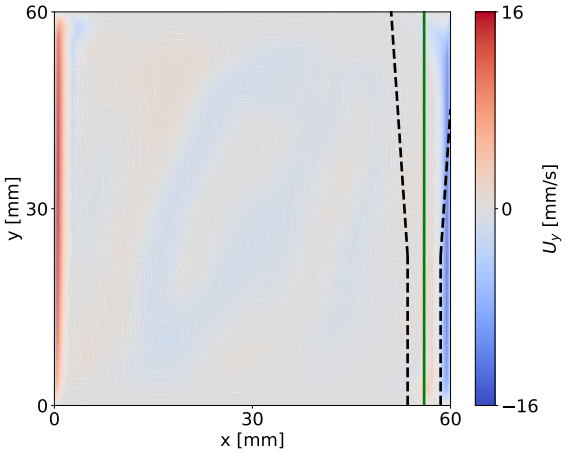

Figure 8.6 - *Average velocity field of RANS 3 of Table 8.2. The UDV ultrasound (US) cone for the* 10 MHz *sensor is represented close to the cold wall. The green vertical line shows its axis, i.e. the position 3 of the measurement from Figure 3.4.*

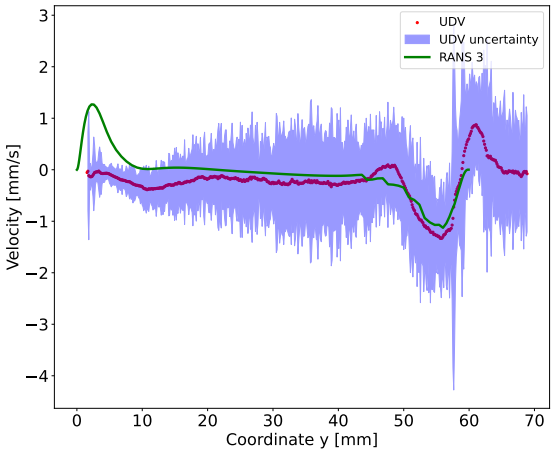

Figure 8.7 - *Average velocity profile U_y along the y direction parallel to the cold wall (position 3). Comparison between UDV and RANS. The RANS profile is averaged over the averaging cone of the UDV sensor.*

to the emitter, could explain why this feature is not captured in the experimental UDV profile. To conclude, it is noteworthy that the hot profile is only presented in Appendix E.3, as all recorded velocities were significantly affected by uncertainty,

preventing any discernible trend. This observation could still be attributed to the averaging process of the UDV, which may have smoothed out velocity variations. A similar phenomenon is also evident in the results of the numerical simulations.

As a key finding of this section, it is important to emphasize that cone averaging of the numerical simulations is a crucial feature for a meaningful comparison with the experimental UDV results, particularly in high-gradient zones. The drawback is of course given by the loss in terms of spatial resolution, which may affect the final results. From this point onward, for the rest of this Chapter, all velocity measurements are presented averaged over the cone unless otherwise specified.

8.2.3 Fluctuations

The results obtained in terms of fluctuations in water in the cavity under the conditions of Table 8.1 are reported and explained here.

The analysis of the fluctuation results in water suggested that the flow remained laminar and turbulence had not been triggered. Consequently, most of the meaningful measurements in water concerned average temperature and velocity fields, which were shown in the previous Sections. For the sake of completeness, the energy spectrum of the temperature signals recorded by the three different temperature sensors is shown in Figure 8.8 for $y = 35\,\text{mm}$ at position 3.

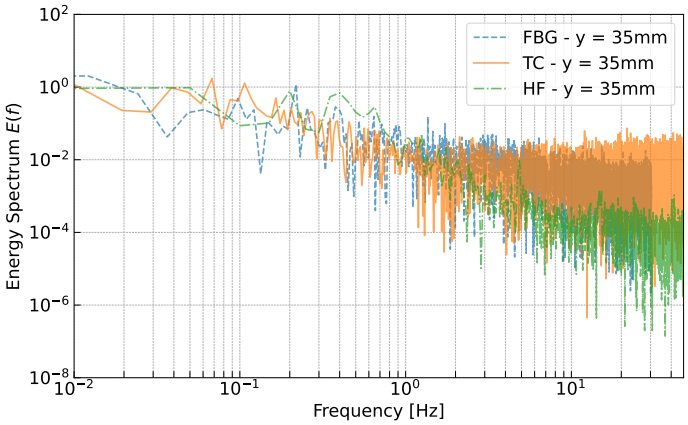

Figure 8.8 - *Energy spectrum of the temperature signal of the TC, FBG and HF at* $y = 35\,\text{mm}$ *along the cold profile (position 3).*

The energy spectrum represents the distribution of the energy of the signal across different frequency components. Mathematically, for a time-dependent signal $\phi(t)$, the energy spectrum $E(f)$ is expressed as in Equation (8.1) where $\mathcal{F}[\phi(t)]$ denotes the Fourier transform of $\phi(t)$.

$$E(f) = \left|\mathcal{F}[\phi(t)]\right|^2, \tag{8.1}$$

This analysis is particularly useful in identifying dominant frequencies and understanding the behavior of the signal in the frequency domain. In this case, despite the good agreement among the three sensors, the spectrum exhibits a flat trend across all frequencies and does not display any peaks that would indicate a possible natural frequency of the flow related to potential turbulent effects. Furthermore, this trend implies the absence of significant energy cascading across the different flow scales, which is characteristic of turbulent flows, and therefore likely suggests a laminar flow.

Additional analysis has been performed using the FBG sensor as a reference to investigate the flow behaviour at different positions along y. The results are presented in Figure 8.9 for positions 1 and 3.

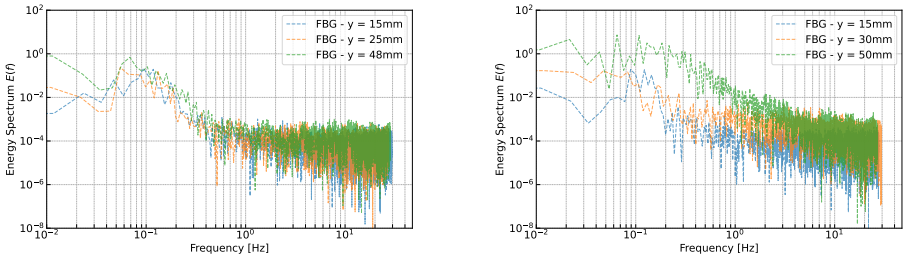

(a) $x = 4\,\text{mm}$ (b) $x = 56\,\text{mm}$

Figure 8.9 - *Energy spectrum of the temperature signal in GaInSn along the y direction parallel to the hot wall (position 1) and to the cold wall (position 3). Comparison between FBG profiles.*

Despite the change in height, and consequently the potential development of the boundary layer, no significant differences are observed in the energy content of the flow at different positions, particularly at $x = 4\,\text{mm}$. Figure 8.9(b) illustrates a slightly higher energy content in the low-frequency range for the signal at $y = 50\,\text{mm}$. Although this observation is physically plausible, as increased thermal mixing on the cold side is expected near the top of the cavity, this feature does not correspond to a discernible trend over the whole profile and cannot be retrieved in the hot profile at $x = 4\,\text{mm}$. Consequently, the analysis of fluctuations in water at different positions did not yield additional insights into the possibility of turbulent flow, rendering the calculation of the turbulent heat flux unnecessary. It is important to acknowledge that the RANS simulations presented in this work were conducted using a turbulence model. Given the potentially laminar nature of the flow in water within the considered operating range, the use of a turbulence model may not be the most appropriate approach. However, to maintain consistency with the overall analysis with GaInSn, the RANS simulations were performed using this methodology.

8.3 Galinstan

This Section presents the experimental and numerical results obtained in GaInSn in the differentially heated cavity. First, the average profiles are reported in Sections 8.3.1 and 8.3.2 for temperature and velocity, respectively. Afterwards, the fluctuations are treated separately in Sections 8.3.3 and 8.3.4 again for temperature and velocity, respectively. The calculation of the turbulent heat flux with the available data is then attempted in Section 8.3.5.

The numerical simulations adopted here for comparison with the experimental results are the DNS 3 from Table 4.1 and the RANS described in Table 4.3, the same used for the grid independence study in Chapter 4. The insights gained from the water analysis are therefore implemented, as both simulations include the conjugate heat transfer and the cone averaging for the UDV velocity comparison. However, only the RANS simulation implements the losses from the passive walls. Despite their importance highlighted in Section 8.2, the comparison of the adiabatic DNS with experimental results remains valuable.

8.3.1 Average temperature

The results obtained in terms of average temperature profiles in GaInSn at position 1 (hot profile) and 3 (cold profile) in the cavity under the conditions of Table 8.1 are reported and explained here.

Figure 8.10 presents a comparison between the TC and HF experimental sensors and the DNS and RANS numerical simulations. Due to the effect of the liquid metal on the fiber spectrum, as discussed in Chapter 5, the FBG data is not included in the average profiles. However, the sensor performance for the fluctuations analysis will be further discussed.

The thermocouple measurements are corrected based on the tests performed in Section 7.6 to account for the heating effect induced by the hot film. The two sensors exhibit good agreement.

In contrast, the numerical results exhibit a different slope of the temperature profiles. It is notable that the RANS and DNS results only show minor discrepancies, despite the fact that the losses from the passive walls were not implemented in the DNS. However, Section 8.2.1 demonstrates that the impact of these losses is relatively small. Moreover, the region where the discrepancies are most pronounced corresponds to the area of highest thermal mixing, i.e., where turbulence is more pronounced (see Section 8.3.3), indicating that RANS results may not be fully reliable in this region.

However, the numerical profile appears much steeper than the experimental one, suggesting that the experiments were conducted with a smaller temperature difference between the two walls. In fact, a further analysis carried out in Figure 8.11 shows the same results in a non-dimensionalized form.

The conventional non-dimensional form employed is the one of Equation (8.2) where T is the temperature in dimensional form, T_{cold} is the temperature of the cold wall and $\Delta T = T_{\text{hot}} - T_{\text{cold}}$ is the temperature difference across the cavity.

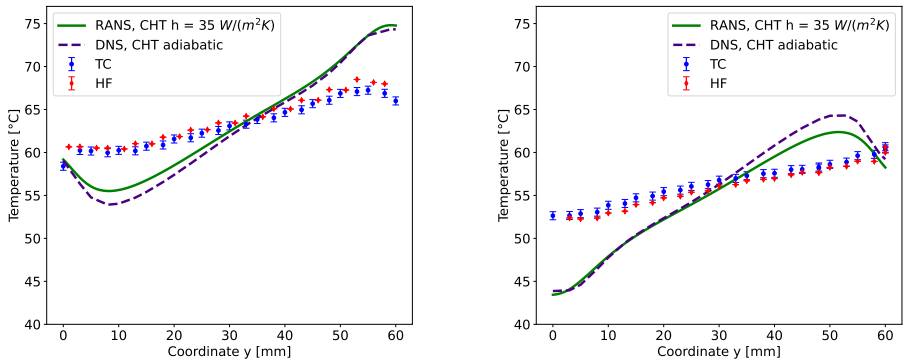

(a) $x = 4\,\mathrm{mm}$ (b) $x = 56\,\mathrm{mm}$

Figure 8.10 - *Average temperature profiles in GaInSn along the y direction parallel to the hot wall (position 1) and to the cold wall (position 3). Comparison between TC, HF, RANS and DNS.*

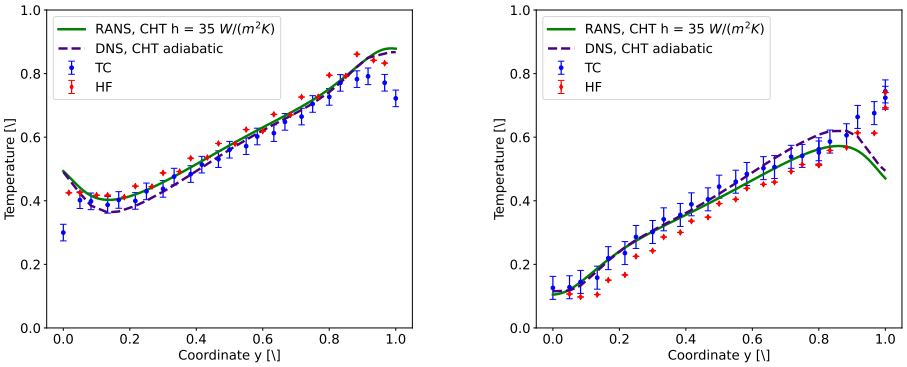

(a) $x = 4\,\mathrm{mm}$ (b) $x = 56\,\mathrm{mm}$

Figure 8.11 - *Average temperature profiles in GaInSn along the y direction parallel to the hot wall (position 1) and to the cold wall (position 3). Comparison between TC, HF, RANS and DNS. The passive walls in the DNS simulations are adiabatic.*

$$T_{\text{non-dim}} = \frac{T - T_{\text{cold}}}{\Delta T} \tag{8.2}$$

However, the values employed for such non-dimensionalization are different for numerical and experimental results. While for the numerical results the values of

the imposed boundary conditions, i.e. the ones reported in Table 8.1, are used, for the experimental profiles the values $T_{\text{hot}} = 68\,^{\circ}\text{C}$ and $T_{\text{cold}} = 52\,^{\circ}\text{C}$ were employed. Such values were artificially found by a least square method, trying several values and employing the ones that were giving the best fit with the numerical results for both profiles. The employment of such values will be further justified in the following sections.

These assumptions are reasonable, as the differing characteristics of GaInSn could render some of the boundary condition assumptions made in water experiments no longer fully valid. For instance, the boundary conditions were measured only at the central point of the copper plate, assuming temperature uniformity based on the tests carried out in water and shown in Appendix B.1. However, these assumptions might not hold true in GaInSn, where the faster fluid motion could create a more variable temperature distribution across the copper plate. Furthermore, non-perfect wetting of the GaInSn on the wall surface could introduce an additional thermal resistance, potentially influencing the temperature perceived by the fluid. These phenomena could consequently lead to slightly different boundary conditions and, as a result, slightly altered flow fields and temperature distributions, such as the one shown in Figure 8.10.

8.3.2 Average velocity

The results obtained in terms of average velocity profiles in GaInSn at position 1 (hot profile) and position 3 (cold profile) in the cavity, under the conditions outlined in Table 8.1, are reported and explained here.

The results from Section 8.2.2 emphasized the importance of performing a cone average when comparing numerical results with experimental ones. A visualization of this operation for GaInSn is shown in Figure 8.12(a).

In this case, the averaging process still has an impact, but it is relatively lower than the one observed in water. In fact, the entire volume of the sensor is located within a region of relatively low gradient, and despite the loss of some information due to the reduced spatial resolution, the overall impact on the average profile is not significant, as demonstrated further in Figure 8.12(b). This result is reasonable, as the gradient within this region is lower than the gradient encountered in water.

Considering this, a comparison between the numerical and experimental results is presented in Figure 8.13.

The experimental profiles indicate upward velocities near the hot wall and downward velocities near the cold wall, with the velocity magnitude increasing as the flow develops, which is consistent with the expected behavior. It should be noted that these measurements were conducted using two different sensors: the 10 MHz sensor near the hot wall and the 8 MHz sensor near the cold wall. The 10 MHz sensor exhibits a less noisy signal and generally provides better performance due to its finer spatial resolution.

Regarding the numerical profiles, both DNS and RANS simulations exhibit relatively good agreement. Discrepancies can be attributed to the absence of loss models in the DNS simulations and to differences in the cone averaging process resulting from the distinct mesh refinements employed in the two simulations. However, the impact

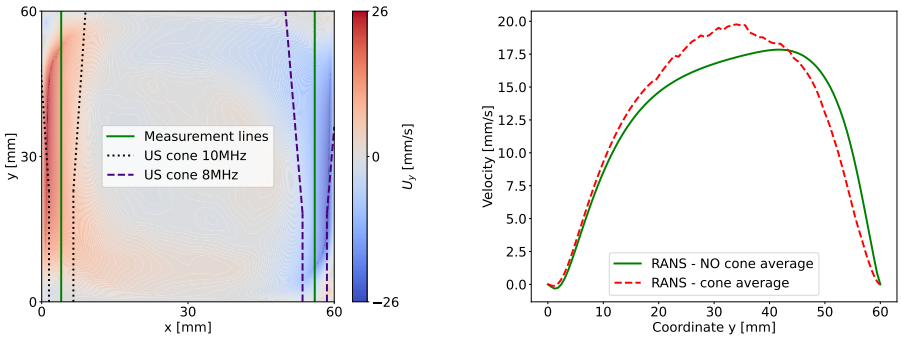

(a) Ultrasound cones of two UDV sensors

(b) Impact of the cone average on the velocity U_y profile in position $x = 4\,\text{mm}$

Figure 8.12 - *Average U_y velocity field of DNS 2 of Table 4.1. The UDV ultrasound (US) cones for the* 10 MHz *and the* 8 MHz *sensors are represented respectively close to the hot and cold wall. The green vertical lines show the measurement positions of the experiments, corresponding to the axes of the two sensors. The velocity U_y profiles are compared when plotted only along the axis of the sensor and when the cone average is considered.*

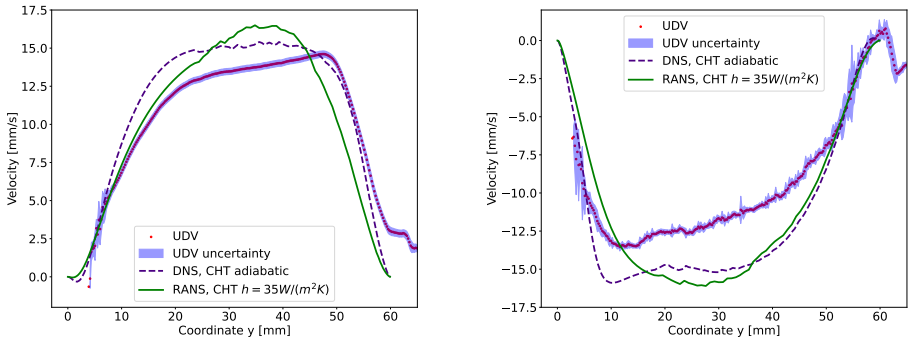

(a) $x = 4\,\text{mm}$

(b) $x = 56\,\text{mm}$

Figure 8.13 - *Average velocity profile U_y along the y direction parallel to the hot wall (position 1) cold wall (position 3). Comparison between UDV, RANS and DNS. The RANS profile is averaged over the averaging cone of the UDV sensor, while the DNS is not. Heat losses from the walls is also not implemented in the DNS.*

of losses, particularly the magnitude of the heat transfer coefficient, appears to be minimal on the velocity profiles, as demonstrated in Appendix E.2.

The comparison between experimental and numerical profiles is also satisfactory, particularly near the hot wall. However, a slightly lower velocity is observed, which may again suggest that the actual temperature difference in the experimental setup is smaller than initially expected. Given that the velocity field is directly influenced by the temperature field in natural convection, it is expected that $U \propto \sqrt{\Delta T}$, according to Equation (2.1). However, in this case, such a correction did not yield the expected match between experimental and numerical results.

8.3.3 Fluctuations of temperature

The results obtained in terms of temperature fluctuations in GaInSn at position 1 (hot profile) and 3 (cold profile) in the cavity under the conditions of Table 8.1 are reported and explained here.

The comparison is made between the thermocouple, fiber Bragg grating, hot film, and DNS 2 of Table 4.1. The DNS results are presented only at the experimental points to facilitate the comparison. In fact in these points numerical probes were placed, allowing the recording of the full time evolution of the signal. The RANS simulations, being steady state, do not provide insights into temperature fluctuations and, therefore, are not considered in this Section.

First, the root mean square (rms) values of the fluctuations, calculated as in Equation (4.17), are reported in Figure 8.14 to evaluate the magnitude and trend of the fluctuations.

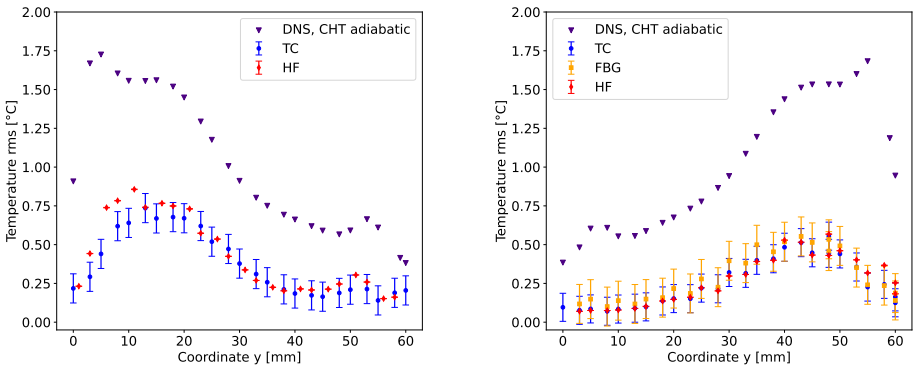

(a) $x = 4\,\text{mm}$ (b) $x = 56\,\text{mm}$

Figure 8.14 - *Root mean square (rms) temperature profiles in GaInSn along the y direction parallel to the hot wall (position 1) and to the cold wall (position 3). Comparison between TC, FBG, HF and DNS.*

The experimental uncertainty $u_{\phi_{\text{rms}}}$ over the rms value ϕ_{rms} of the generic quantity ϕ is calculated as in Equation (8.3), starting from the uncertainty u_ϕ over the quantity

ϕ itself, using the law of propagation of uncertainty [218], where N represents the length of the entire measurement vector of ϕ.

$$u_{\phi_{\text{rms}}} = \frac{u_\phi}{\sqrt{N}} \tag{8.3}$$

The values of the experimental fluctuations are perfectly in the range predicted in Chapter 2, i.e. 0.5 °C to 1 °C as reported in Table 2.9, therefore supporting the accuracy of the estimations made. Moreover, all the sensors, FBG included, are once again in very good agreement with each other.

The results also show consistency with the expected trends of the flow. The fluctuation values are higher in the first half of the profile, close to the hot wall, while the opposite occurs near the cold wall. As previously mentioned, this phenomenon can be explained by considering that these zones are where the flow at different temperatures mix during circulation in the cell. Despite this qualitative agreement, it is noticeable that the numerical values are generally higher than the experimental ones, even though they follow similar trends. This observation is somewhat consistent with the hypothesis presented in Section 8.3.1, as a lower temperature difference in the cavity would lead to lower turbulence, and consequently, lower fluctuations. To further verify this aspect, Figure 8.15 shows the temperature rms value, non-dimensionalized by the temperature difference ΔT, where for the experiments the ΔT retrieved in Section 8.3.1 was used, while for the numerical simulations, the boundary conditions of Table 8.1 were adopted.

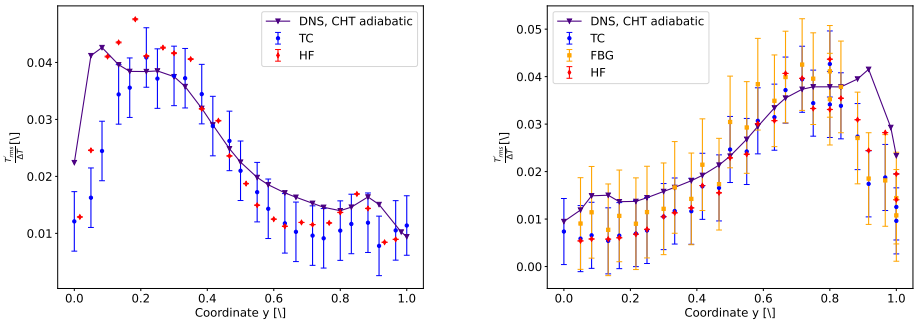

(a) $x = 4\,\text{mm}$ (b) $x = 56\,\text{mm}$

Figure 8.15 - *Non-dimensionalized root mean square (rms) temperature profiles in GaInSn along the y direction parallel to the hot wall (position 1) and to the cold wall (position 3). Comparison between TC, FBG, HF and DNS.*

The non-dimensionalized values in this case are approximately matching the expected temperature fluctuation intensity of Table 2.1, as given by the first DNS simulations performed in GaInSn.

As already demonstrated in Section 8.3.3, the comparison between the different profiles shows excellent agreement when proper non-dimensionalization is applied,

not only qualitatively but also quantitatively. Therefore, this further supports the hypothesis presented in Section 8.3.1 regarding the potential variation in experimental boundary conditions.

To further investigate the characteristics of the fluctuations, a comparison of the energy spectra of the temperature fluctuations signal at $y = 10\,\text{mm}$, i.e. where the temperature rms proved to be higher along the hot profile (position 1) is shown in Figure 8.16.

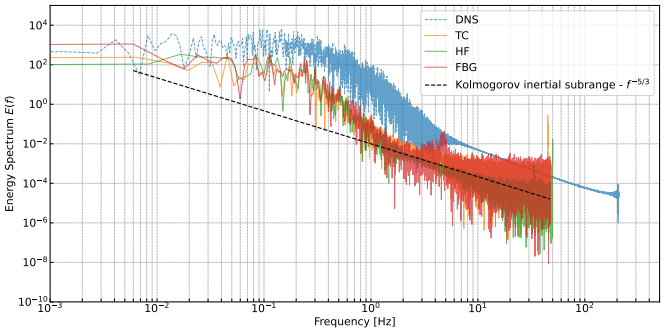

Figure 8.16 - *Energy spectrum of the temperature signal of the TC, FBG, HF and DNS at* $y = 10\,\text{mm}$ *along the hot profile (position 1). The -5/3 slope of the Kolmogorov cascade is also shown.*

The spectrum shows a very good agreement among the experimental sensors, as all three profiles exhibit the same trend and frequency contents. The comparison with the numerical simulations is also satisfactory, as the trend shown by the DNS is respected by the experimental sensors. However, these slopes have not been found to match the well-known Kolmogorov turbulence scale (slope -5/3). Moreover, as a direct consequence of what was shown in Figure 8.14, the experimental profiles are systematically lower in magnitude than the numerical ones. Despite this discrepancy, some conclusions can still be drawn.

Firstly, it is evident that, contrary to the observations in water, the profiles exhibit a slope, suggesting an energy cascade potentially associated with turbulent effects. This would be reasonable, as due to the coarser boundary layer present in GaInSn, bigger and higher energy vortices would enhance more turbulence at larger scales. Moreover, due to the similarity of the slope, and consequently the similar energy transfer across the different flow scales, the turbulent regime simulated numerically can be closely related to the one measured experimentally. Therefore, it is reasonable to assume that, when properly non-dimensionalized, the results align, as the flow behavior is qualitatively expected to be similar.

However, these slopes have not been found to match the well-known Kolmogorov turbulence scale (slope -5/3), previously retrieved by Cioni et al. [28] in a natural convection mercury flow. This discrepancy is possibly attributable to the fact that the Ra number analyzed was $Ra = 2.7 \times 10^9$, significantly higher than the one used in

this work, as detailed in Table 8.1. Therefore, this could suggest that a fully turbulent flow has not been achieved.

To further extend the analysis, a comparison of the DNS and the hot film (used as the reference sensor) energy spectra of the temperature fluctuations is presented in Figure 8.17 for both the hot and cold profiles at different heights.

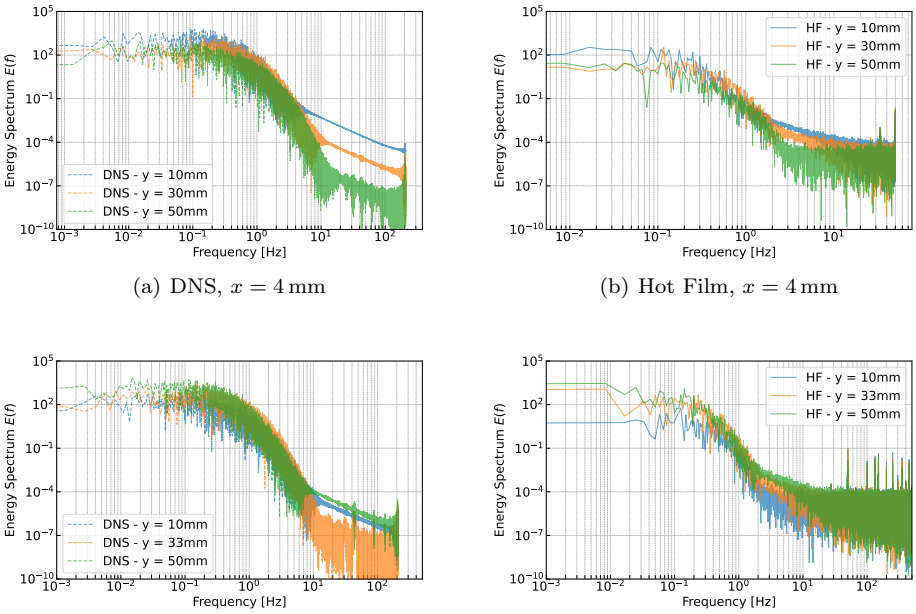

(a) DNS, $x = 4\,\text{mm}$

(b) Hot Film, $x = 4\,\text{mm}$

(c) DNS, $x = 56\,\text{mm}$

(d) Hot Film, $x = 56\,\text{mm}$

Figure 8.17 - *Energy spectrum of the temperature signal of the HF and DNS in GaInSn at different heights along the hot profile (position 1) and the cold profile (position 3).*

The experimental profiles in Figures 8.17(b) and 8.17(d) show a consistent agreement in the increase of frequency content as the boundary layer develops along the active wall, i.e., moving upwards near the hot wall and downwards near the cold wall. This same trend is captured by the DNS near the hot wall but is less consistent near the cold wall. However, it is noteworthy that both numerical and experimental results consistently do not indicate a significant high-frequency content in the flow, with most of the frequency content being limited to approximately 20 Hz to 30 Hz, which is lower than the estimated 60 Hz reported in Chapter 2. This overall agreement suggests that the temporal resolution of the chosen sensors was adequate for measurements in this flow regime.

To conclude this Section, it is interesting to note that no specific frequency peak was observed in the analysis, thereby not indicating the presence of any particular natural frequency of the flow.

8.3.4 Fluctuations of velocity

The results obtained in terms of velocity fluctuations u'_y in GaInSn at position 1 (hot profile) and position 3 (cold profile) in the cavity, under the conditions of Table 8.1, are reported and explained here.

The comparison is carried out among the UDV, the DNS 2 from Table 4.1, and the RANS simulation of Table 8.2. In fact, despite the RANS simulations being steady-state, it is still possible to compare their outcomes with the velocity fluctuation results. By recalling the definition of Turbulent Kinetic Energy (TKE) in Equation (4.16), it is possible to retrieve $u'_{\mathrm{y,rms}}$ under certain assumptions. Specifically, assuming isotropic turbulence, i.e., $u'_{\mathrm{y,rms}} = u'_{\mathrm{x,rms}} = u'_{\mathrm{z,rms}} = u'_{\mathrm{rms}}$, Equation (4.16) simplifies to Equation (8.4), and a single component of the fluctuations, u'_{rms}, can be retrieved using Equation (8.5).

$$TKE = \frac{3 \times u'_{\mathrm{rms}}}{2} \tag{8.4}$$

$$u'_{\mathrm{rms}} = \frac{2 \times TKE}{3} \tag{8.5}$$

The assumption is strong, as Chapter 4 showed that the turbulence phenomena in the cavity can exhibit strong 3D anisotropic characteristics. However, this remains the best approach to compare RANS results with experimental fluctuations.

The result of the comparison is shown in Figure 8.18.

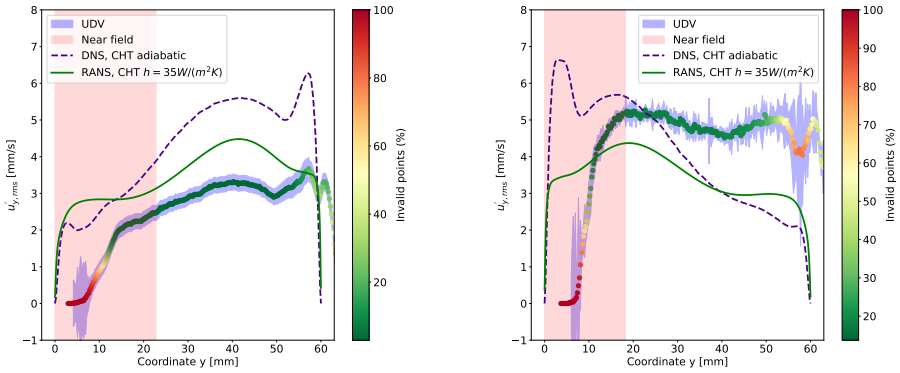

(a) $x = 4\,\mathrm{mm}$ (b) $x = 56\,\mathrm{mm}$

Figure 8.18 - *Root mean square (rms) values of the velocity fluctuations $u'_{y,rms}$ in GaInSn along the y direction parallel to the hot wall (position 1) and to the cold wall (position 3). Comparison between UDV, DNS and RANS.*

The experimental results are presented with the UDV experimental points, and their uncertainty is indicated by the blue area around each point. Additionally, each

point is colored according to the percentage of invalid vectors retrieved at each location. As previously highlighted in Section 8.2.2, one of the main challenges encountered with the UDV was the high percentage of invalid vectors, i.e., values interpreted by the sensor as zero because the reflected signal falls below the sensitivity threshold, meaning the signal from the flow scatterers is too weak to be detected. Estimating these invalid vectors is crucial to assess the reliability of the overall signal. It is evident that the higher concentration of invalid vectors occurs closer to the sensor, where the emitting power is high, and the risk of signal saturation is greater. However, this phenomenon does not appear to be directly related to the extension of the Near Field, highlighted in red in the figures, where measurements can sometimes be suboptimal for the reasons explained in Chapter 6. Nevertheless, the number of invalid vectors seems to correlate with the frequency, with the 10 MHz UDV showing a higher proportion of invalid vectors as well as a longer near field. Another region with a high number of invalid vectors is near the opposite wall, where echoes and resonances from the wall itself can affect the signal quality.

The overall rms value is generally very high, resulting in a turbulence intensity (TI) as defined in Equation (6.32), ranging between 20 % to 50 %, providing estimates much higher than those predicted in Table 2.1 by DNS simulations. However, the profile, particularly near the cold wall, does not exhibit a clear trend, suggesting that noise may have a significant influence on the rms value and casting some doubt on the reliability of the entire rms profile.

Regarding the numerical simulations, the profiles show a trend consistent with the fields presented in Chapter 4, with fluctuations being higher near the hot (cold) wall when the flow is directed upwards (downwards) and impinges on the roof (floor) of the cavity after reaching its maximum velocity. Notably, the RANS simulations provide a surprisingly good estimate of the order of magnitude of the fluctuations, despite the strong assumptions made. Although they are unable to capture all the nuances observed in the DNS simulations, the first approximation of the fluctuating quantities can be considered reasonably accurate.

To conclude the section, the energy spectra of the velocity fluctuations u'_y at different heights is presented in Figure 8.19.

It is evident that no discernible trend can be identified in the experimental data. The flatness of the spectrum indicates the dominance of noise over the turbulent or fluctuating characteristics of the flow. This observation supports the previously stated hypothesis and casts doubt on the reliability of the data concerning the fluctuations. Conversely, numerical results exhibit a spectrum comparable to that observed for the temperature fluctuations in Figure 8.17, with the frequency content of the flow again remaining below 20 Hz to 30 Hz. This outcome aligns with the predictions detailed in Chapter 2. Given the plausible physical origin of this spectrum, the results of this analysis further question the validity of the velocity data obtained using the UDV technique. However, the time response of the sensor looks once again suitable for liquid metals measurements in this flow regime.

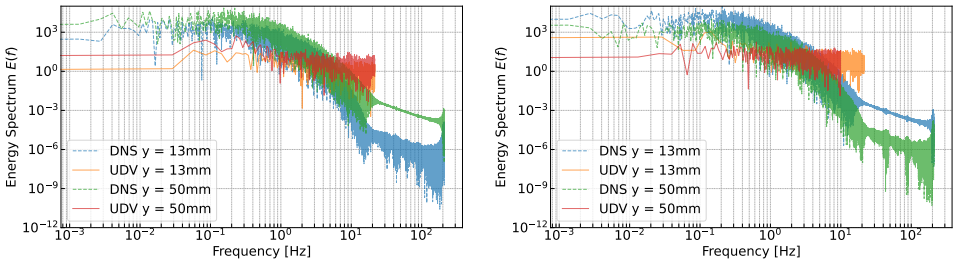

(a) $x = 4\,\mathrm{mm}$ (b) $x = 56\,\mathrm{mm}$

Figure 8.19 - *Energy spectrum of the velocity fluctuations signal in GaInSn along the y direction parallel to the hot wall (position 1) and to the cold wall (position 3). Comparison between UDV and DNS profiles.*

8.3.5 Turbulent heat flux calculation

The results obtained in terms of turbulent heat flux in GaInSn at position 1 (hot profile) and position 3 (cold profile) in the cavity, under the conditions outlined in Table 8.1, are presented and discussed here.

Building upon the results presented in Sections 8.3.3 and 8.3.4, an attempt is made to calculate the final goal of this thesis, i.e., the turbulent heat flux, as defined by Section 1.2. Since this quantity is a direct consequence of the velocity and temperature fluctuation measurements, its result is highly sensitive to the outcomes of Sections 8.3.3 and 8.3.4. In particular, while the temperature fluctuations provided meaningful insights, the velocity fluctuations should be regarded as less successful, thus impacting the final calculation of the turbulent heat flux. Nonetheless, for completeness, this Section presents and discusses the obtained values.

It is crucial to first explain how this value is calculated. As explained in Chapter 2, although sensor synchronization was ensured, not all sensors were acquiring data at the same sampling frequency due to setup limitations. Consequently, when the velocity and temperature signals were combined for the turbulent heat flux calculation, a solution was required for the matching of the two signals. In this work, the signal acquired at the higher frequency (temperature) was undersampled to match the time stamps of the signal at the lower acquisition frequency (velocity). While this resulted in a loss of information, this approach avoids interpolation (which would occur if the lower frequency signal were oversampled), thus preventing the introduction of additional uncertainty into the signal.

The results of this operation are presented in Figure 8.20 for the two positions analyzed. The results are shown in a non-dimensionalized form, where the average of the product of the temperature and velocity fluctuations is divided by the product of the rms values of temperature and velocity, as calculated in Sections 8.3.3 and 8.3.4.

The experimental values are reported without uncertainty bars, as the calculation of the uncertainty propagation resulted in uncertainties ranging from 20 % to 100 % of

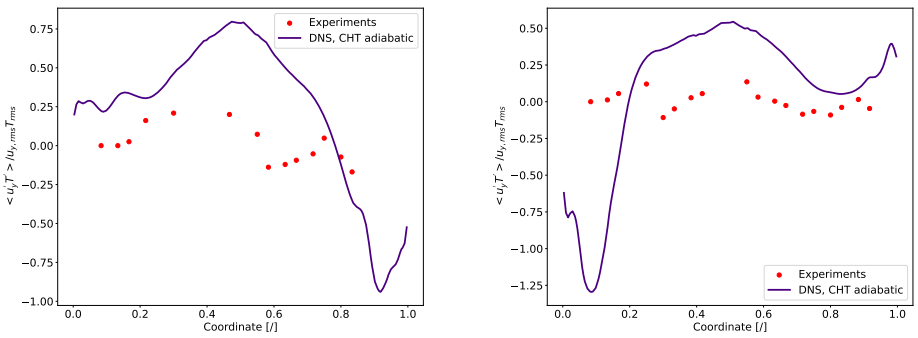

(a) $x = 4\,\text{mm}$ (b) $x = 56\,\text{mm}$

Figure 8.20 - *Turbulent heat flux (THF) profiles in GaInSn along the y direction parallel to the hot wall (position 1) and to the cold wall (position 3). Comparison between available experimental data and DNS.*

their absolute values, further compromising their reliability and the data visualization.

Some trends in terms of increasing and decreasing values in the profile may align with the DNS simulations. For instance, in the hot wall profile, a peak value around $y = 0.5$ can be observed, as well as certain characteristics in the second half of the cold profile. However, due to the high uncertainties, these values should be considered only as proof of concept, demonstrating that a methodology capable of retrieving turbulent heat flux values has been developed. Nonetheless, the current limitations of the available data restrict its full implementation.

In this context, making further conclusions regarding the quality of synchronization and the spatial scales of the sensors beyond those discussed in the previous Sections would be redundant, as these values would only be meaningful in the context of a reliable turbulent heat flux measurement.

8.4 Conclusions

This Chapter presented the measurements conducted in the differentially heated cavity with the temperature and velocity sensors characterized throughout the thesis. Additionally, a comparison with the available numerical simulations (DNS and RANS) was carried out.

Initially, the results obtained in water were presented in Section 8.2. While these results did not introduce significant innovations, particularly in terms of turbulent measurements, they facilitated the development of a robust methodology for utilizing the same experimental setup and procedures with GaInSn. Simultaneously, key insights were gained regarding the necessary modifications for the simulations, which allowed for a more accurate representation of the experimental conditions. These

insights were also applicable to the GaInSn case. Notable findings included:

- Implementation of conjugate heat transfer, i.e., simulating the cavity walls and conduction phenomena.
- Consideration of heat losses from the passive walls.
- Use of the cone average for a successful comparison with the UDV velocity profiles.

Building on this, the same approach was applied to GaInSn, as detailed in Section 8.3. Measurements of the temperature profiles revealed deviations from the numerical simulations, potentially indicating uncertainties in the experimental boundary conditions. This hypothesis is supported by the observation that an appropriate non-dimensionalization of the profiles yielded good agreement between experimental and numerical results. Furthermore, the frequency analysis indicated that, despite these discrepancies, the experiments and simulations likely represent the same flow regime, characterized by similar turbulent phenomena. Thus, comparisons between them are deemed valid when properly non-dimensionalized.

The average velocity profiles exhibited reasonable trends. However, the slight overestimation of velocity magnitude in the DNS and RANS simulations, particularly near the cold wall, again suggested a potentially lower temperature difference in the experimental setup. Notably, the estimated temperature difference inferred from the temperature profiles did not exhibit the expected proportionality of $U \propto \sqrt{\Delta T}$. Moreover, measurements of velocity fluctuations were not entirely successful, likely due to elevated noise levels and a significant proportion of invalid vectors in certain regions of the profiles. Consequently, these limitations substantially affected the estimation of the turbulent heat flux. Although results for the latter were obtained, their reliability remains uncertain.

Chapter 9

Conclusions

The main conclusions derived from this work are discussed in this Chapter. The primary objective of the study was to develop an experimental technique suitable for turbulent heat flux measurements in liquid metals. Specific conclusions about each part of the work are reported in the Conclusions Section at the end of each Chapter. This Chapter presents the concluding remarks, structured into three main Sections. In Section 9.1, the objectives outlined in Section 1.3 are revisited, highlighting the accomplishments and contributions of this work. Section 9.2 provides suggestions for future research, informed by the insights gained throughout this study. Each one of this Sections is further divided in four separate parts to address separately each aspect of the work: measurement techniques, experimental setup, numerical simulations, and experiments in liquid metals. Lastly, Section 9.3 explores potential directions for adpating the analysis to Lead Bismuth Eutectic (LBE).

9.1 Objectives: achievements and contributions

In the framework of this thesis, several objectives were identified in Section 1.3. A review of the main outcomes obtained is detailed in this Section.

9.1.1 Measurement techniques

Regarding the measurement techniques, two objectives were specifically identified in Section 1.3:

- **Evaluate the state-of-the-art of the measurement techniques**

  Initially, a review of the turbulence phenomenon in liquid metals was conducted to identify in detail the scales of the phenomena involved. Such estimations were derived from a combination of literature review, theoretical estimations, and preliminary Direct Numerical Simulations (DNS). Despite the approximate nature of these preliminary estimations obtained using different approaches, a good level of agreement was observed between the results.

The primary issues were identified in two key aspects: the spatial and temporal scales of the turbulence, which directly relate to the spatial and temporal resolutions of the sensors. The synchronization and positioning of the sensors were also critical factors for the turbulent heat flux measurements, as analyzed thoroughly in Chapter 2. While some of these aspects have been addressed individually in the literature, a comprehensive overview that takes into account all these aspects together represents an innovative contribution of this work.

For the progression of the work, the main outcome of this Section was the selection of the suitable measurement techniques: Ultrasound Doppler Velocimetry (UDV) and Hot Film Anemometry (HFA) for velocity measurements, and sheathed type K thermocouples (TC) and fiber Bragg gratings (FBGs) for temperature measurements. All of these techniques met, in principle, the spatial resolution, time resolution, and measurement range requirements established by literature studies and numerical simulations.

- **Characterize all the chosen techniques when used in liquid metals**

  Preliminary tests and calibrations were performed in various fluids and setups to assess the performance of the techniques, specifically to characterize their behavior in liquid metals. These tests were useful to confirm the practical performance and limitations of each technique. The main outcomes of each characterization are discussed in the Conclusions Section of each Chapter and are only briefly recalled here. This Section, therefore, focuses more on a final evaluation of their overall performance compared with the initial expectations.

  - *Thermocouple*

    The sheathed type K thermocouple selected met the expectations throughout the entire work, and no novelty or unexpected results emerged from its analysis. Its temporal resolution was found to be strongly dependent on several environmental factors, and its performance in the cavity confirmed its suitability, successfully addressing the fluctuations in GaInSn. Its selection was, therefore, correct, and its performance corroborates previous successful experiments in liquid metals.

  - *Fiber Bragg Gratings* Non-sheathed Fiber Bragg Gratings (FBGs) were successfully deployed in molten salt at high temperatures, demonstrating their viability up to at least 180 °C without damage. Furthermore, they effectively captured temperature fluctuations in GaInSn, as detailed in Chapter 8. However, as discussed in Section 5.3, the presence of GaInSn significantly altered the FBG spectrum, compromising the accuracy of absolute temperature measurements as explained in Chapter 5. The underlying physical cause of this phenomenon was identified as light reflections from the fiber end due to the high reflectivity of the liquid metal, exacerbated by the sensitive part of the FBG being located at the fiber tip. This explanation is consistent with the observed lack of temperature dependence and the absence of the effect in transparent fluids like molten salt. Preliminary tests conducted by the author suggest that this issue

could potentially be mitigated by applying glue to the fiber tip to minimize reflections. In general, roughening the fiber surface, for instance by creating a less clean cut, also appears to reduce this effect.

– *Ultrasound Doppler Velocimetry*

The UDV was tested in both water and GaInSn, under forced and natural convection conditions. The results generally show good performance when the sensor is used for velocities in the order of the cm/s. This is likely due to the number of scatterers present in a given volume of fluid, which is related to the backscattered signal and, consequently, the quality of the signal. As detailed in Chapter 6, the issue of seeding the flow was analyzed in depth, providing a complete overview and guide for particle selection. Lower velocities in the order of a few mm/s, such as those related to the flow fluctuations in the natural convection setup in GaInSn, were not successfully measured by the sensor. In particular, instantaneous profiles were sometimes discontinuous due to a high percentage of non-zero values, especially close to the sensor and the opposite wall, thus affecting the quality of turbulence estimations. Therefore, as highlighted in the literature, the UDV technique is sensitive to a wide range of parameters, making it challenging to obtain high-quality measurements. This work focused on characterizing the lower operating range of the sensor, establishing its limitations. Furthermore, this study contributes by identifying a methodology for the implementation of UDV measurements that can be followed by future researchers, including a comprehensive analysis encompassing parametric studies, particle selection, and uncertainty quantification.

– *Hot Film Probe*

The hot film was considered the most innovative and ambitious attempt in this work in terms of utilizing measurement techniques in liquid metals. The probe worked fairly well in a forced convection, fully developed water flow. However, when used in liquid metals, the main limitation encountered was its extremely high sensitivity to temperature, which tended to overwhelm the velocity signal. Despite promising results reported in the literature [58, 64] and initial analyses presented in Chapter 7, the velocity measurements attempted within the scope of this thesis were unsuccessful. Nonetheless, the probe responded very well to temperature, providing another reliable source of temperature measurements that aligned perfectly with the other temperature sensors.

9.1.2 Experimental setup

Design and develop a natural convection setup and the related procedures where liquid metals can be used and controlled under different conditions.

A natural convection setup was designed and manufactured for this thesis. Although the concept of the differentially heated cavity is not particularly innovative per se, practical ideas and procedures were implemented in this work regarding the use of GaInSn. Despite not completely avoiding its oxidation, the vacuum cycle and filling

procedure implemented provided adequate precautions to minimize it, and eventual oxidation did not seem to have a significant impact on the final measurements. Nevertheless, several questions arose during the work regarding the performance of the setup. The thick stainless steel walls were a source of heat losses that could not be neglected, and the Peltier elements and copper plates used to set the constant temperature boundary conditions raised concerns based on the outcomes observed in liquid metals.

Despite these challenges, the full experimental campaign was carried out, thanks to the use of two fluids, water and GaInSn. The former ultimately proved to be a key component in the success of the work. In fact, the results obtained with GaInSn in natural convection, representing the main innovation of this work, were made possible only because of the solid foundation laid during the water-phase experiments.

9.1.3 Numerical simulations

Conduct numerical simulations to elucidate their limitations and identify the conditions under which experimental approaches may provide useful insights.

Numerical simulations were conducted using two different approaches: DNS and RANS. DNS exhibited trends consistent with the expected physics of the flow, aligning well with some experimental observations. These results confirm DNS as the most reliable numerical tool currently available for simulating liquid metal flows. RANS simulations demonstrated reasonable agreement with DNS and experiments, particularly in capturing the trends of the average temperature and velocity fields. This outcome, while not entirely expected for natural convection in liquid metals, constitutes a noteworthy finding of this work. However, as anticipated, larger discrepancies were observed in regions with more intense turbulence.

For the fluctuations analysis, the comparison of rms velocity values derived from the TKE calculation, under the assumption of isotropic turbulence, indicated deviations from DNS results in the range of 10 % to 50 %. These discrepancies were more pronounced in regions of stronger turbulence. Consequently, RANS simulations may serve as a practical tool for obtaining initial estimates of natural convection flows in liquid metals, provided the application and required precision allow for such an approach. Nonetheless, validation and comparison with reliable experimental datasets remain essential for ensuring the accuracy and reliability of both numerical methods.

9.1.4 Experiments in liquid metals

Perform experimental tests in the designed setup to evaluate the thermo-hydraulic behaviour of low-Prandtl number fluids and compare the results with the numerical simulations.

Despite the possible uncertainties in the experimental boundary conditions previously mentioned, the main characteristics of the flow in the differentially heated cavity indicate that the flow regime was no longer laminar and was approaching turbulence. The targeted flow regime therefore appeared to have been effectively reached. The rms and frequency analyses exhibited trends and characteristics similar to those

obtained from DNS simulations, suggesting that the simulated flow regime could closely correspond to the experimental one. This qualitative agreement facilitated an appropriate non-dimensionalization of the experimental results guided by the DNS, highlighting the complementary nature of these methods. After these adjustments, the experimental and numerical approaches showed good agreement, particularly in terms of temperature fields, enabling a consistent interpretation of the main features of the flow. Regarding velocity measurements, the experiments faced the limitations previously discussed and did not yield reliable results in terms of fluctuations. Consequently, in this framework, DNS simulations are considered more reliable, as they exhibited reasonable physical trends. Further reseach should therefore focus on this aspect for the achievement of a full turbulent heat flux measurement.

9.1.5 Primary objectives of the work

In particular, the achievement of the different objectives mentioned above was finalized to the attainment of the two main objectives of this thesis, as outlined in Chapter 1.

1. **Develop an advanced experimental technique suitable for the measurement of turbulent heat flux in liquid metals.**

   The temperature measurements in liquid metals can be considered overall successful. However, the velocity measurements, while providing reasonable average results, did not yield the expected outcomes in terms of rms values and fluctuations. The development of the turbulent heat flux measurement technique was inherently dependent on the combination of both measurements and, as a result, cannot be considered fully successful at this stage. Nonetheless, the development process involved more than merely combining the two measurement sets, addressing several additional aspects of its implementation. For example, the analysis of the spatial and temporal resolution of the techniques proved effective. A methodology was also developed for sensor synchronization, positioning, and data processing. However, a definitive assessment of their effectiveness can only be made with a fully reliable THF measurement.

2. **Provide reference data for the study of natural convection in liquid metals, with a particular focus on the transitional and turbulent regimes. These data will serve as a valuable reference dataset as well as for the improvement of numerical models.**

   A dataset of temperature and velocity profiles, including averages and fluctuations, has been produced in the framework of this thesis. However, the results are limited by the issues already mentioned. While the temperature results align with physical expectations and, at least qualitatively, with numerical predictions, the velocity results exhibit significant limitations and cannot be considered fully reliable, particularly when fluctuations are taken into account. For this reason, the data provide useful insights into the behavior of liquid metals, but further research is necessary to assess their reliability. The use of the provided data as a reference dataset for tuning numerical simulations should

be approached with caution, acknowledging the limitations of the experimental results.

9.2 Recommendations for future works

The work carried out in this thesis allows for some recommendations for future research in this field. This thesis represents a contribution to the state-of-the-art regarding possible approaches to the turbulent heat flux measurement, but further research is needed to implement a fully functional experimental technique. The possibilities for extending the scope of the present work, with particular attention to Lead Bismuth Eutectic (LBE) applications, are also discussed in Section 9.3.

9.2.1 Measurement techniques

The development of a reliable velocity measurement technique for liquid metals is a priority, as it was the main limitation in this work for achieving a complete turbulent heat flux measurement. The Ultrasound Doppler Velocimetry (UDV) technique demonstrated its limitations but also proved to be a valid approach for measuring velocity in fluids where optical access is impossible. Further research could focus on the use of different techniques, e.g. the ones mentioned in Chapter 2.

Reliable temperature measurements appear to be feasible even with standard sheathed type K thermocouples, and if no special requirements are necessary, there may be no need to incorporate Fiber Bragg Gratings or hot film sensors into the analysis. However, further analysis of the FBG and hot film sensors would be beneficial. The effect of liquid metals on the FBG should be further investigated to support the conclusions provided in this thesis. In fact, FBGs could provide a reliable, in-situ, real-time sensors for temperature and strain measurements in liquid metals, with time responses that could, in principle, be superior to those of thermocouples. A quick solution to the problem could involve sheathing the fiber to protect the grating from direct contact with the metal, although this would degrade the time response. In more recent times, Raman scattering-based fibers have also demonstrated suitability for high-temperature measurements up to 680 °C. However, these sensors currently exhibit limited spatial resolution (0.5 m) and temporal resolution (5 s). Despite these limitations, they may still find applications in specific experimental facilities with different measurement objectives [277]. Another promising technology for future applications is based on optical frequency domain reflectometry (OFDR). Although a distributed measurement technique, OFDR has demonstrated spatial resolutions as fine as 1 cm while maintaining temperature uncertainties within 0.7 °C. Furthermore, advanced data processing techniques have enabled spatial resolutions as high as 0.5 mm to be achieved in 25 m-long optical fibers [278]. Furthermore, recent studies have demonstrated the potential of Fiber Bragg Gratings (FBGs) for velocity measurements. These techniques, based on principles similar to Constant Current Anemometry (CCA) as described in Chapter 7, have shown promise for measuring velocities as low as 0.02 m/s, offering the possibility of simultaneous temperature and velocity measurements with a single sensor [279, 280]. In these approaches, two grat-

ings are inscribed onto the same fiber. One grating is coated with a high thermal conductivity layer, which is heated by the radiation passing through the fiber itself, effectively creating a hot wire. The second, uncoated grating serves as a reference for ambient temperature measurements. The inherent advantages of FBG sensors, such as their excellent robustness and chemical inertness, make them particularly attractive for overcoming some of the limitations associated with conventional hot-film anemometry techniques.

Regarding the hot film probe, previous literature has demonstrated the feasibility of its use for velocity measurements in liquid metals [58, 64], and further research should be conducted to repeat and validate these findings. Alternative calibration setups could be explored, such as utilizing a controllable rotating container with a stationary probe. Ideally, calibration could be performed with a forced convection flow of liquid metal in a pipe or jet, similar to conventional calibration methods for air or water flow measurements. Furthermore, contacting different suppliers of hot-film anemometry probes could provide access to alternative probe designs, even though most commercially available probes for conductive liquids applications exhibit similar structural characteristics to those used in this study. However, different probes could present different sensitivities to temperature and velocity, possibly solving some of the issues raised in this work. Furthermore, it is anyway interesting to highlight that existing literature is also using hot film probes as temperature sensors for liquid metals [28], therefore validating also the use made in this work. In conclusion of this Section, it is worth noting the potential of Permanent Magnet Probes (PMPs) [52, 53], which are considered by many researchers to be a highly promising technique for velocity measurements in liquid metals. While significant practical challenges remain, successful implementations of PMP-based systems with thermocouples have been reported in the literature. Although a complete turbulent heat flux measurement using PMPs has not yet been achieved, the author believes this technology holds significant promise for future investigations. Due to the limited expertise in this specific area, providing detailed recommendations for future research utilizing PMPs is beyond the scope of this work. However, further exploration of this technique is strongly encouraged.

9.2.2 Experimental setup

The differentially heated cavity proved to be a suitable choice, providing a relatively simple flow configuration while still offering important insights into the flow behavior. For this reason, future research could continue using this setup with potential improvements. For instance, the author advises against using Peltier elements for constant temperature boundary conditions unless temperature differences sensitively smaller than the ones of this work wants to be achieved across the cavity. In fact, this work highlighted the difficulties in cooling down the hot side of the Peltier element when the temperature difference between its two faces was in the order of 30 °C to 40 °C. A more efficient solution would likely involve using heat exchangers with a controlled temperature loop to maintain the desired temperature difference, even though it could increase the setup complexity.

Further turbulence could be generated by increasing the temperature difference,

ΔT, and the characteristic length of the setup, L, as the Gr number scales as $\propto \Delta T$ and $\propto L^3$. A larger setup would also provide higher velocities, as the characteristic velocity scales with $\propto \sqrt{\Delta T}$ and $\propto \sqrt{L}$, which would be easier to measure with the sensors. Additionally, a higher volume-to-surface ratio would minimize the influence of thermal losses on the flow. Employing a cavity wall material with lower thermal conductivity would also be beneficial. For example, Inconel, with a thermal conductivity approximately 30 % lower than 316L stainless steel, would offer improved thermal insulation. While several polymers could be considered for cavity wall construction, their suitability is often limited by the maximum operating temperature and compatibility with the working fluid.

On the other hand, scaling up the cavity dimensions would necessitate a proportional increase in the working fluid volume ($\propto L^3$), significantly increasing the cost of experiments, particularly for expensive fluids like GaInSn. Furthermore, a larger cavity would require a correspondingly larger heated/cooled surface area, increasing the complexity and cost of the experimental setup. One potential solution to this challenge is to modify the aspect ratio of the cavity, increasing its size in only one direction. Previous literature studies [155, 281] have identified the cavity height (i.e., the height of the active walls) as the primary characteristic length, as it governs the development and transition to turbulence of the flow. This approach could potentially reduce costs and complexity while still allowing for the achievement of the desired Gr and Ra numbers. However, it is important to note that altering the aspect ratio can significantly influence the flow behavior, including the stability regimes exhibited by the system [281]. Furthermore, the accessibility of instrumentation can be significantly impacted by changes in the aspect ratio, potentially increasing the intrusiveness of the sensors that could alter the flow behavior. In fact, the probe may necessitate longer support structures, different access points, or, in the case of UDV, increased power for the emitted signal to ensure adequate ultrasound propagation for full profile measurements. Therefore, the optimal aspect ratio for future experiments should be carefully considered based on the specific research objectives.

If these parameters are constrained, turbulence could, in principle, also be induced artificially by triggering it with sinusoidal temperature boundary conditions or by inducing sinusoidal volume forces with external magnetic fields. Numerical works in this sense have already been carried out [30] but the experimental implementation of such features would of course increase the setup complexity. The change of the cavity aspect ratio or its orientation in respect to gravity can also help to enhance turbulent effects [26, 155].

Further modifications could involve alternative instrumentation strategies. For example, providing central top or horizontal access from a passive wall would enable measurements of bulk quantities or facilitate access to different profiles and consequently different information about the flow. Ideally, a profile perpendicular to the active wall would provide valuable information about temperature gradients and, consequently, the heat transfer occurring between the fluid and the cavity. Additionally, increasing the number of thermocouples embedded in the walls would enhance the understanding of the experimental boundary conditions, thereby facilitating more accurate comparisons with numerical simulations. Furthermore, if feasible during the

design phase, the integration of distributed optical fiber sensing techniques in the walls could provide valuable and detailed boundary conditions measurements.

Eventually, alternative configurations for studying natural convection could also be considered, such as a pool-type configuration to mimic real reactor conditions, a heated channel flow setup for potential forced convection studies, or an annular channel with a heating rod. Each configuration presents its own set of advantages and challenges, and further constraints and requirements will be needed in each case to determine the optimal setup.

9.2.3 Numerical simulations

Future studies on natural convection in liquid metals could initially focus on RANS simulations to estimate the involved quantities at least at an average level. Such simulations might also provide a preliminary approximation of velocity fluctuations, as shown in this work. While these results may not suffice for purely numerical investigations, they could serve as a foundation for designing and initiating further experimental studies.

Further improvements could be achieved by implementing turbulence models that account for the anisotropy of turbulent stresses. Reynolds Stress Models (RSMs), which directly solve transport equations for each component of the Reynolds stress tensor, offer the potential for enhanced accuracy. However, RSMs are known to be relatively unstable and computationally expensive compared to simpler models. Moreover, for a comprehensive understanding of the flow, it is crucial to recognize the strong interdependence between thermal and momentum turbulence. Consequently, accurate predictions of both phenomena are essential, and neglecting either aspect can lead to significant inaccuracies in the overall flow solution. Further efforts could investigate the application of URANS to natural convection flows in liquid metals. This approach may offer additional insights into the periodic behavior of large-scale mean structures, serving as an initial estimation.

However, achieving higher precision would require the use of Direct Numerical Simulations (DNS), which remain the most reliable approach for simulating liquid metal flows. The validation of such simulations against experimental data necessitates precise knowledge of the experimental boundary conditions, as well as the spatial and temporal resolution of the sensors, which are crucial for robust validation. The dataset provided in this work can certainly contribute to the validation and refinement of numerical models for natural convection. However, further experimental studies with improved instrumentation and measurement techniques are still required. Similar considerations have been emphasized in previous works combining experimental data and Large Eddy Simulations (LES) for low-Prandtl-number fluids [144].

9.2.4 Experiments in liquid metals

For a comprehensive understanding of the diverse turbulent behavior of liquid metals, future experiments could explore a broader range of flow regimes, from natural convection to forced convection, or, within the natural convection regime, investigate different Gr numbers, representing various turbulent regimes. This would enhance

the understanding of the full development of the flow, highlighting the different characteristics that arise as the flow regime develops. For example, further insights into the emergence of soft, hard, or ultrahard turbulence in natural convection, as previously discussed in the literature [27, 28], could be obtained. Such experiments would allow for more efficient adjustments of the experimental boundary conditions, rather than relying on several computationally expensive simulations. DNS could then be employed selectively, targeting specific regimes or phenomena observed in the experimental setup. Such an approach would also facilitate a deeper understanding of the current results, providing a more comprehensive interpretation of the observed turbulent phenomena within the cavity once a more complete picture of the transition process is obtained.

Additionally, consistent with previous numerical studies [30], the results suggest a relatively smooth transition from laminar to turbulent flow within the differentially heated cavity, occurring gradually across the entire boundary layer along the cavity walls. Consequently, no distinct natural frequency was identified in the spectral analysis, a characteristic typically observed in the developing boundary layer of a vertical flat plate, and generally a lower turbulence level was identified in the flow. However, these analyses were limited to a specific flow configuration, probably constrained by the limitations highlighted regarding the imposed boundary conditions. A more comprehensive investigation, encompassing previously discussed modifications to the experimental setup or incorporating measurements at different locations, e.g. positions closer to the wall, and exploring a wider range of flow conditions, could provide further insights into the nature of the transition process.

Before delving into these aspects, it is essential to emphasize that the immediate priority is to reliably establish functioning and reliable instrumentation. Only once this is achieved should attention shift to a comprehensive analysis of the flow regimes. Given the inherent limitations of experimental techniques in liquid metals, it is belief of the author that numerical simulations should always be conducted alongside experiments, starting with RANS simulations during the experimental design phase and progressing to DNS once the setup and its parameters are well-defined.

9.3 LBE adaptation

Chapter 1 introduced the main framework of this project, which focuses on the MYRRHA reactor that uses LBE as coolant. This Section presents some final remarks on possible adaptations of the setup and measurement techniques for use with LBE. Although the analysis conducted in this work did not involve LBE as a working fluid, it leveraged the thermohydraulic similarities between LBE and GaInSn to provide insights relevant to LBE and, more broadly, to low Pr number fluids. However, other properties, e.g. the thermal diffusivity, can be significantly different between the two, almost of a factor 2 due to the higher density of LBE and the lower thermal conductivity. According to the analysis carried out in Chapter 5, this could lead to slower response time of the sensors, which therefore should be characterized beforehand in LBE. Similar response times could anyway be obtained slighlty increasing the flow velocity. Moreover, this characteristic, combined with the similar thermal expansion

coefficients of the two materials, might indicate the presence of steeper temperature gradients within the fluid, especially close to the heat source/sink, necessitating the use of temperature sensors with higher spatial resolution.

The considerations outlined in Section 9.2 regarding potential improvements to the setup are still valid for LBE. Of course, the temperatures must be adjusted to avoid any points in the setup falling below the melting point of LBE (125±1°C [12]). In this context, RANS simulations could provide useful insights by identifying hot and cold spots in the setup.

Material compatibility is another crucial consideration. While stainless steel is widely used and well-established for working with LBE, other materials, such as copper, which can pose compatibility issues with LBE, may be coated as was done in this work. The coating used for the copper plates, in fact, was originally developed for bearings used in LBE.

Regarding the measurement techniques, future research could adapt the instrumentation for applications in LBE facilities, supporting the development of the future MYRRHA reactor. This includes developing appropriate coatings or modifications to ensure that the equipment can withstand the corrosive and high-temperature conditions of LBE.

- *Thermocouples*
  Sheathed thermocouples have been shown to work effectively in LBE [12]. Once the appropriate type is selected based on the application and the temperature range, no special precautions are necessary.

- *Fiber Bragg Gratings*
  Ceramic-coated fiber Bragg Gratings have proven effective for vibration measurements in fuel pins when used in LBE [282]. However, studies have demonstrated that type I gratings experience significant decay at temperatures around 300 °C, suggesting that casing is necessary. Nonetheless, such a solution would typically increase the size of the sensor and degrade its time response. This work demonstrated the effectiveness of uncoated fibers without degradation up to 180 °C when used in molten salt for temperature measurements. Given that silica is chemically inert to LBE, uncoated fibers should, in principle, be usable in LBE, as long as the temperature does not significantly exceed the melting point. However, the issue encountered in GaInSn regarding spectrum deformation could be expected to recur in LBE if, for example, it is related to the reflection properties of the metal. Further investigation into the root causes of this phenomenon would be necessary and tests in LBE would also be beneficial in this sense.

- *Ultrasound Doppler Velocimetry*
  For UDV, the primary limitation for its direct use in LBE is the high temperature. Previous tests conducted at SCK CEN and HZDR (Helmholtz-Zentrum Dresden-Rossendorf) have led to the development of a commercially available waveguide capable of withstanding temperatures up to 600 °C. This device consists of a protective stainless steel casing that can be directly immersed in the

molten metal. The main challenge with such casing devices is ensuring adequate acoustic coupling between the sensor and the melt, i.e., achieving proper wetting. Several solutions have been adopted to address this, such as using gels, pre-wetting the sensor to prevent oxide formation, and polishing the casing surface. However, using this device introduces additional complexities, particularly by adding new parameters that need to be optimized, such as the geometry and characteristics of the casing.

- *Hot Film*
  A primary limitation for the use of hot-film anemometry in liquid lead-bismuth eutectic (LBE) is the operating temperature. The sensor is typically rated for ambient temperatures up to 150 °C, with the wire temperature also limited to a maximum of approximately 150 °C to prevent damage to the quartz coating. In this work, the hot film was tested in environments up to 80 °C with wire temperatures reaching approximately 90 °C. In theory, the sensor should be usable in LBE as long as the melting temperature of the metal is not significantly exceeded. However, practical issues arise due to the fact that the probe always requires an overtemperature. Since LBE must remain above its melting point of approximately 130 °C to stay liquid, and the wire can operate up to 150 °C, there may be insufficient overtemperature to accurately sense either temperature or velocity, rendering the probe unusable. Furthermore, the lifetime of the probe will likely be significantly reduced when operating at its maximum temperature capabilities. Additionally, unknown chemical reactions could occur between LBE and the probe, exacerbated by high temperatures, with a risk of damaging the quartz coating and causing the nickel-sensitive element to degrade. Possible adaptations may include finding an alternative coating material, as proposed in Appendix A.1, or making the existing quartz coating thicker. However, the practical challenges in manufacturing such a probe could limit this approach, and it would also increase the sensor size, potentially degrading its time response.

These additional implementations could lead to the development of LBE facilities and instrumentation capable of addressing various challenges across different flow regimes. Such advancements would contribute to the progress of MYRRHA, fourth-generation nuclear reactors and small modular reactors (SMR), thereby supporting the growing energy demand while addressing the challenges posed by climate change.

Appendix A

Specifics on the Hot Film

A.1 Coating solutions for the hot film

The coating of the hot film when used in conductive fluids has always been an important part of the choice of the probe since the first tests were carried out in the 70s. The main purpose of the coat is to insulate, e.g., enamel or quartz, or to improve the wetting of the metals on the probe, e.g., nickel, copper or gold. In fact, electrical insulation in conductive fluids is necessary to have a sufficiently rapid response to allow turbulent measurements. Taking as a reference previous studies [58, 119, 121, 123, 283] the structural part of the wire is generally one order of magnitude bigger than conventional hot wires, i.e. 10 µm to 100 µm to grant structural strength. Sajben [119] explains in details the procedure used to coat the wire. In particular, the company Sigmund Cohn Inc., Mount Vernon, New Jersey is mentioned as the industry where the wire was purchased already coated with enamel and the industry still exists nowadays. The coating of the prongs with a pasty epoxy compound is also described in detail. White [121] particularly highlights the issue of the wetting of the probe in mercury due to the high surface tension of the metal. In particular it is stated that adding another metal coating to the probe *"cold resistance drift and erratic heat transfer (i.e. randomly variating) rates from hot film probes in mercury"* could be avoided. Therefore, a very thin gold coating obtained through a vapor deposition technique to promote wetting of mercury is proposed. Good results were obtained, even if the problems were not completely solved. Positive side effects of the gold layer were the longer life of the sensor and the increase resistance in harsh environment. The main disadvantage was that when one gold probe was removed and reinserted in the flow, it established a new calibration curve different from the first, thus preventing calibration in one facility and experiments in another. Further attempts made with silver didn't give better results. While copper is theoretically an option, it wasn't tested in this study. Other researchers have suggested that the only significant difference between copper and gold would be the latter's longer lifespan and give as further alternatives Columbium, Haynes 25 and nickel [119, 122]. Sajben et al. [119] tried with coatings made of gold, silver and nickel. The main conclusion was that the gold coating was

not desirable because the high cost was not compensated by the improvements given. The silver was removed by mercury right after inserting the probe in the metal while the nickel coating was found to be the best. Moreover, chemical deposition techniques like catalytic deposition were considered more suitable than other procedures because of their longer life time. Another solution suggested to improve wetting was to soak the probe for a few days in the mercury between the first insertion and the experimental runs [119, 121]. Another main concern in a conducting fluid is the electrical insulation needed without sacrificing the sensitivity of the probe [284]. White [121] talk about the availability of commercial techniques based on vapor deposition that allow to have quartz film deposited over the wire for electrical insulation with a thickness of 0.8-2 µm. Also in this case, the insulation of the prongs with epoxyor urethane is addressed as an important point. Malcolm [120, 123] also describes the sensor used as a *"hot-film sensor composed of a thin metallic film deposited on a glass or quartz substrate and electrical connections to the film to supply the heating current"*. The sensor was bought by Thermo-Systems Inc. St. Paul, Minnesota. The use of lacquer for electrical insulation is mentioned as ana alternative because of the difficulties in the manufacturing process with sputtered quartz. Their initial goal was in fact to create an in-house probe and for this reason they explore other alternatives, e.g. varnish and araldyte, but due to their high thickness (half the film radius) the solution was not considered suitable because of the high loss in terms of sensitivity of the probe. Anyway, it was considered suitable for the prongs insulation. Hill et al. [283] also give a description of the probe used as *"a quartz fiber covered with a thin film of platinum whose length is defined by a thicker plating of gold at either end"* but no details about the manufacturing process or even the dimensions of the probe are given. More recent studies tend to use commercially available probes that now seem to be able to achieve good performances [58, 64]. A summary of what has been reported here is given in Table A.1.

Table A.1 - *Characteristics of Coated Wires*

Core diameter	Core material	Coating thickness	Coating material
50 µm*	Tungsten	NA	NA
38 µm [119]	Tungsten	2.5 µm	Enamel (Sigmund Cohn Inc.)
55 µm† [285]	Tungsten	5 µm	Platinum
31 µm [120, 123]‡	Quartz	1.6 µm	Quartz
53.6 µm [283]§	Quartz	NA	NA
50.8 µm[121]‡	Quartz	1 µm	Quartz
51 µm[122] ‡	Quartz	1 µm	Gold/Silver/Nickel
50.8 µm[284] ‡	Quartz	2 µm	Gold/Silver/Nickel
25.4 µm [58]	Quartz	Unknown	Aluminum Oxides

*Made at the Von Karman Institute. Coating a hot wire was not possible in-house

†DISA 5501, now Dantec

‡The sensitive part is a film of 0.1 µm of Platinum placed in between the core and the protective coating layer, as in the probe used in this PhD

§Core in quartz with an exposed platinum film around

A.2 Settings

The Dantec System allows two different OHR settings for working in non-isothermal flows while accounting for temperature variations [265]:

- **Constant sensor temperature**: The overheat ratio is fixed at the beginning at a known ambient temperature. The *automatic overheat adjust* setting is disabled, allowing the sensor temperature to remain constant throughout the entire campaign. In this case, temperature correction of the data is usually required.
- **Constant sensor over-temperature**: The overheat ratio is adjusted at the beginning of each measurement based on the measured working temperature, ensuring a consistent over-temperature relative to the surroundings. The *automatic overheat adjust* setting is enabled, and temperature correction of the data is not required.

For this work, the first option was chosen by disabling the automatic overheat adjustment. The OHR value was set to 0.21, which, although higher than the recommended OHR of 0.08 [59], resulted in the wire operating at a constant temperature of $T_w = 82\,^{\circ}\mathrm{C}$, regardless of changes in the ambient temperature. This configuration ensures that the film temperature remains above the maximum temperature reached in the measurement setup. Furthermore, using the maximum allowable overheat ratio is advantageous for achieving the highest sensitivity to velocity (due to the enhanced heat transfer between the probe and the fluid) while minimizing sensitivity to temperature [263]. On the other hand, it can decrease the lifetime of the probe.

Therefore, with the constant temperature sensor setting, it is good practice to perform temperature corrections when the temperature variations are in the order of $2\,^{\circ}\mathrm{C}$ to $3\,^{\circ}\mathrm{C}$ [265]. Given the extensive temperature range covered in this work, a complete calibration with respect to temperature was necessary, as presented in Section 7.5 and no further temperature corrections were adopted.

To conclude, an image of the settings used in the StreamwarePro software is shown in Figure A.1:

The final temperature of the wire can be determined from this data. Additionally, the resistances of the various components of the system are reported.

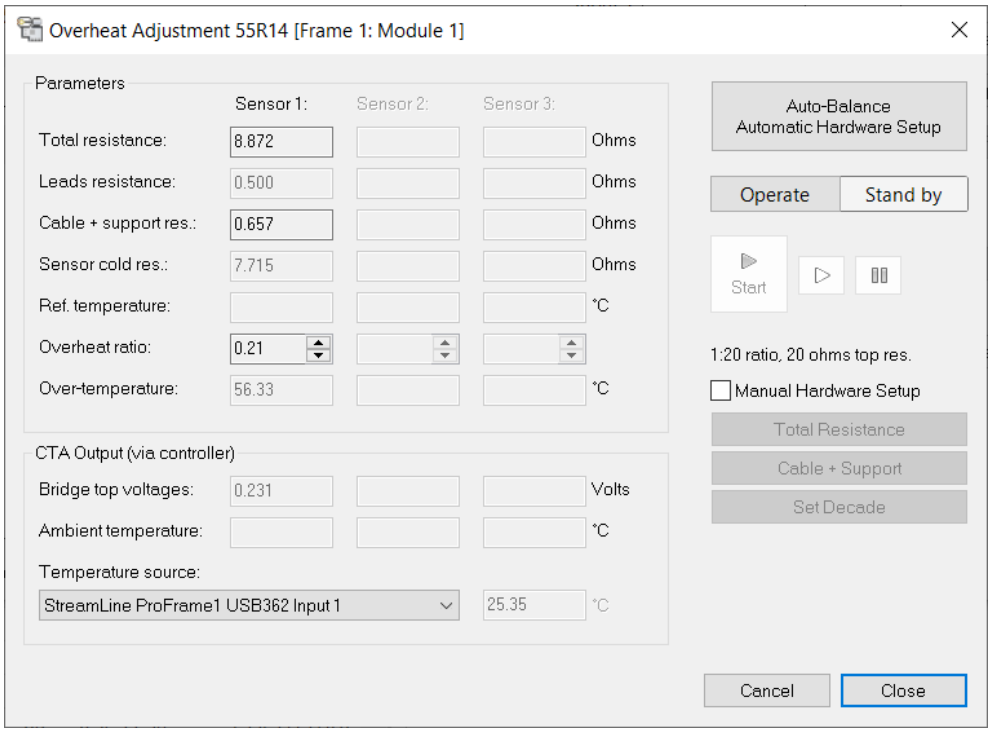

Figure A.1 - *Settings used in the StreamwarePro. The highlighted overheat ratio of 0.21 leads to a final wire temperature of approximately* 82 °C.

A.3 Hot film in the tank setup

This appendix reports the results obtained in the tank setup. Even though the outcomes were not particularly successful, it is still meaningful to examine this setup to describe the process that led to selecting alternative configurations. The setup consisted of a water tank with a bottom diameter of $D_{tot} = 120\,\text{mm}$ and a bottom valve with a diameter of $D_v = 4\,\text{mm}$, which was used to empty the tank. The hot film was held stationary in the center of the tank, positioned as far as possible from the lateral walls and the valve inlet to minimize secondary effects while the water level gradually decreased. A schematic of this configuration is shown in Figure A.2.

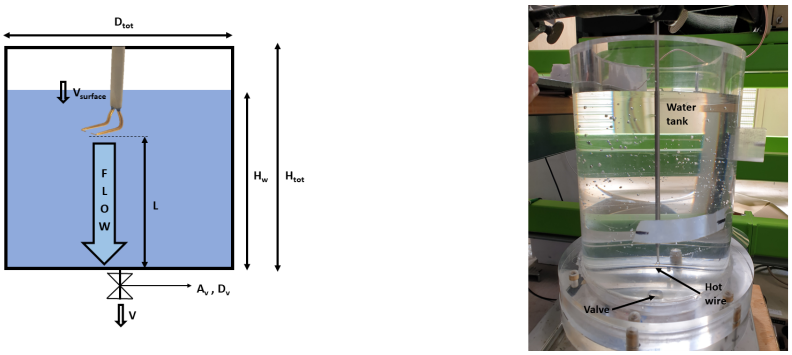

(a) Schematic (b) Picture

Figure A.2 - *Tank setup used for the hot film calibration*

Through Bernoulli's principle, it is possible to relate the velocity of the water as a function of the liquid height inside the tank using Equation (A.1):

$$U = C_v\sqrt{2gH_w(t)}, \tag{A.1}$$

where $C_v = 0.97$ [286] is a non-dimensional velocity coefficient depending on the fluid and the type of valve aperture, $H_w(t)$ represents the evolution over time of the water height in the tank, and g denotes the gravitational acceleration. In this case, $H_{w,0} = 230\,\text{mm}$. By recording the temporal evolution of the water height using a camera and a graduated scale positioned at the side of the tank, an estimation of the velocity was obtained. The resulting velocity was found to be approximately steady in a range around $U \sim 2\,\text{mm/s}$ to $10\,\text{mm/s}$, which may correspond to a significantly lower surface velocity, aligning more closely with the measurement of the sensor.

By adjusting the valve opening and the fluid height, it was possible to calibrate the hot film, albeit within a limited velocity range due to the fixed tank geometry. The choice of this setup was primarily driven by its simplicity. Moreover, this configuration offered several advantages, such as:

- the hot film is exposed to a flow that has the same direction as the flow that will be experienced in the cavity,

- this type of calibration can also be repeated inside the cavity, allowing for an ideal *in-situ* calibration.

This setup proved useful in understanding which parameters affect the measurements with the hot film, the sensitivity of the probe, the optimal hardware and software settings, and providing general insights into using the probe in a controllable environment. Figure A.3 displays a voltage and temperature acquisition performed with this setup.

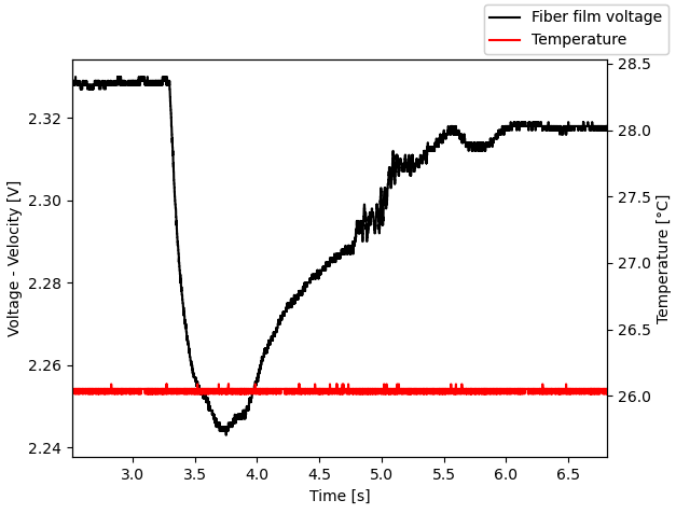

Figure A.3 - *Evolution in time of the voltage acquisition in the tank. At* $t = 3.3\,\mathrm{s}$ *the valve is open. The fluid then starts to accelerate until reaching a steady state value around* $t = 6\,\mathrm{s}$

In the figure, it is clear that the effect of the bottom valve opening at time $t = 3.3\,\mathrm{s}$ resulted in a drop in the voltage reading of the sensor. However, the cause of this voltage drop remains unclear. The fiber-film is only sensitive to the velocity magnitude, and any increase in velocity should correspond to a higher voltage. One hypothesis is that the probe was more affected by the pressure drop induced by the valve opening than by the minor surface velocity. As a reminder, temperature effects were not considered.

Moreover, these tests presented several additional issues:

- **Lack of reproducibility:** The tests were conducted twice per day for two consecutive days, but the results were not consistently reproducible. Although an effect of the valve opening on the fiber-film reading was consistently observed, the magnitude of this effect varied in each acquisition, making it impossible to establish a clear relationship between voltage and velocity.
- **Velocity range and control:** As previously mentioned, the velocity in this system was not easily controllable due to the manual adjustment of the bottom

valve. Additionally, the uncertainty in velocity estimation, based on the tank scale reading and Equation (A.1), was of the order of 1 mm/s, which was the same order of magnitude as the estimated velocities.

- **Temperature control:** Although the temperature remained relatively constant during each acquisition, the lack of temperature control prevented the establishment of relationships between voltage and temperature, rendering the procedure incomplete.

Furthermore, it was impossible to conduct a proper dynamic calibration and estimate the frequency response of the probe using this setup. Due to the poor control over velocity, even the worst-case condition corresponding to the highest velocity was difficult to set.

For these reasons, further tests with different setups were deemed necessary to achieve the desired calibrations.

Appendix B

Experimental tests

B.1 Infrared camera analysis of the copper plates

Separate and specific tests were conducted using an infrared camera to verify the validity of the isothermal assumption for the copper plate and to assess whether measuring the temperature only at the central point would provide a reliable estimate of the plate's overall temperature. To achieve this, an experimental setup consisting of an infrared camera, a copper plate, and a Peltier element was assembled. The copper plate was positioned vertically, with the infrared camera capturing one side, while the Peltier element, connected to a DC power supply, was placed on the opposite side as the heating element. A schematic of the setup is shown in Figure B.1.

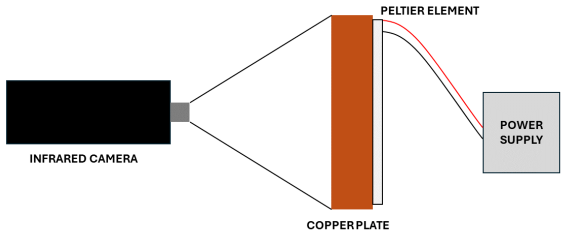

Figure B.1 - *Setup used for the infrared camera tests. The infrared camera is aimed at the copper plate, placed vertically and heated from the back by the Peltier element connected to a DC power supply.*

The copper plate was painted black, and the infrared camera was calibrated using a K-type thermocouple. A fine calibration was not necessary in this case, as the focus was on the temperature gradient across the plate rather than its absolute value. The tests were performed at different power levels of the Peltier element, with average temperatures of the plate ranging from 20 °C to 80 °C. Results for the two extreme temperatures (low and high) are presented in Figure B.2.

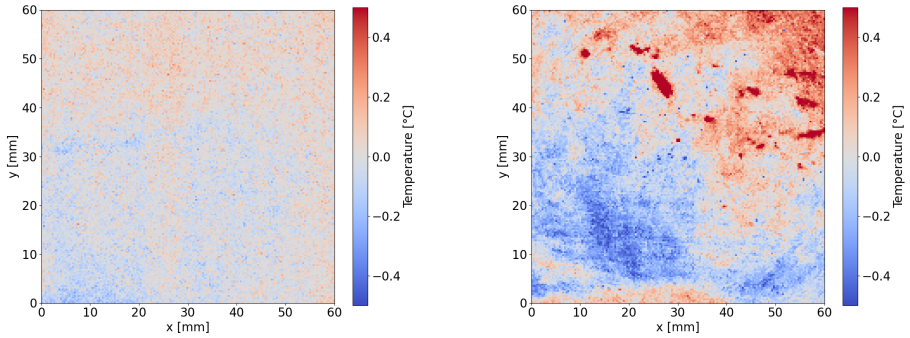

(a) $T_{mean} = 20.3\,^{\circ}\mathrm{C}$ (b) $T_{mean} = 79.6\,^{\circ}\mathrm{C}$

Figure B.2 - *Infrared camera images for two different average temperatures of the plates. The images represent the difference between the average temperature obtained by averaging 100 instantaneous images taken at a frequency of* 2 Hz *while heating with the Peltier element and the overall average plate temperature. This highlights the temperature differences across the plate.*

Some temperature non-uniformity can be observed across the plate. This is primarily because the Peltier element (54 mm edge length) is smaller than the copper plate (60 mm edge length), leading to uneven heating near the edges. Additionally, due to the vertical orientation of the plate, a typical temperature gradient expected for heated vertical surfaces was observed [238]. The plate was kept vertical during the tests to simulate conditions as closely as possible to those in the actual experiments. Moreover, certain hot or cold spots on the plate are visible at higher temperatures, corresponding to areas where the black coating was slightly damaged. This resulted in variations in emissivity, leading to incorrect readings from the infrared camera in those regions and therefore it cannot be interpreted as a real temperature gradient. In conclusion, a maximum temperature gradient of 0.8 °C was observed on the plate when heated to 80 °C, while a gradient of 0.2 °C was recorded at 20 °C. These results indicate that the plates are sufficiently isothermal, and a central point measurement can reliably represent the temperature of the entire plate. Additionally, since this test was conducted in air, it is expected that, in contact with a fluid of higher thermal conductivity (such as water or GaInSn), the temperature distribution across the plate would be even more uniform.

B.2 Leak tests in the cavity

Before operating the facility, preliminary tests were conducted to assess leakage behavior. As mentioned earlier, with water, it was sufficient to confirm that no liquid leakage occurred. For gas, the situation was more complex since the facility was not originally designed to be fully gas-tight. To address this, the test shown in Figure B.3 was performed.

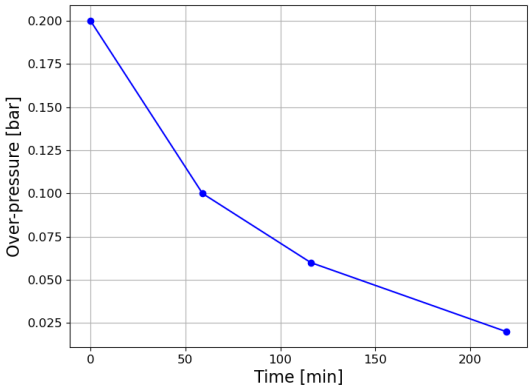

Figure B.3 - *The graph shows the evolution of pressure inside the cavity over time, expressed as overpressure relative to ambient pressure, i.e.,* 1 bar.

The cavity was initially filled with nitrogen at 1.2 bar, which corresponds to the operating pressure of the system, and was allowed to depressurize naturally until it reached ambient pressure. As seen in the graph, ambient pressure is restored after 4 hours to 5 hours, which is more than sufficient for a full test run. This indicates that no gas refill is needed during a typical one-day test. However, the cavity was refilled with gas before starting each new test day.

Appendix C

Physical properties of materials

This Appendix presents the primary properties of the various fluids and materials utilized in this thesis. Whenever feasible, these properties are provided at a reference temperature relevant to the study, specified accordingly. Additionally, the references for the values and the relationships considered are provided.

C.1 Water

Table C.1 - *Thermophysical properties of water at a temperature of* $T = 53\,^{\circ}\mathrm{C}$*, corresponding to the average of the operating conditions in the differentially heated cavity [259].*

Property	**Symbol**	**Unit**	**Value**
Density	ρ	$\mathrm{kg/m^3}$	987
Specific heat	c_P	$\mathrm{J/(kg\,K)}$	4182
Dynamic viscosity	μ	$\mathrm{mPa\,s}$	0.52
Thermal conductivity	k	$\mathrm{W/(m\,K)}$	0.64
Thermal expansion coefficient	β	$\mathrm{1/K}$	4.57×10^{-4}
Surface tension	γ	$\mathrm{mN/m}$	66.8
Thermal diffusivity *	α	$\mathrm{m^2/s}$	1.56×10^{-7}
Speed of sound	c	$\mathrm{m/s}$	1546
Prandtl number*	Pr	[–]	3.4

C.2 Galinstan (GaInSn)

Table C.2 - *Thermophysical properties of GaInSn at a temperature of* $T = 58.5\,^{\circ}\mathrm{C}$*, corresponding to the average of the operating conditions in the differentially heated cavity.*

Property	Symbol	Unit	Value
Composition [23, 173]	[-]	wt%	$Ga_{67}In_{20.5}Sn_{12.5}$
Melting point [23, 173]	T_m	°C	10.6
Density [23, 173]	ρ	kg/m^3	6323
Specific heat [23, 173]	c_P	J/(kg K)	325
Dynamic viscosity [23, 173]	μ	mPa s	1.79
Thermal conductivity [23, 173]	k	W/(m K)	26.5
Thermal expansion coefficient	β	1/K	1.23×10^{-4}
Surface tension [23, 173]	γ	mN/m	586
Thermal diffusivity *	α	m^2/s	1.29×10^{-5}
Speed of sound † [166]	c	m/s	2730
Prandtl number*	Pr	[–]	0.021

C.3 Lead-Bismuth Eutectic (LBE)

Table C.3 - *Thermophysical properties of LBE at a temperature of* $T = 220\,^{\circ}\mathrm{C}$*, corresponding to the core inlet temperature of MYRRHA.*

Property	Symbol	Unit	Value
Composition [12]	[-]	wt%	$Pb_{44.5}Bi_{55.5}$
Melting point [12]	T_m	°C	125±1
Density [12]	ρ	kg/m^3	10427
Specific heat [12]	c_P	J/(kg K)	147
Dynamic viscosity [12]	μ	mPa s	2.28
Thermal conductivity [12]	k	W/(m K)	10.7
Thermal expansion coefficient	β	1/K	1.24×10^{-4}
Surface tension [12]	γ	mN/m	409
Thermal diffusivity *	α	m^2/s	6.98×10^{-6}
Speed of sound [12]	c	m/s	1750
Prandtl number*	Pr	[–]	0.031

*Calculated from the other properties

†According to the literature, the speed of sound is the property for which the least information is available, particularly with respect to its temperature dependence.

C.4 Copper Cu-ETP

Table C.4 - *Thermophysical properties of Copper Cu−ETP at a temperature of* $T = 20\,°\mathrm{C}$ *[287].*

Property	Symbol	Unit	Value
Composition	[-]	wt%	$Cu_{>0.99}O_{<0.04}$ $Bi_{<0.0005}Pb_{<0.005}$
Melting point	T_m	°C	1083
Density	ρ	kg/m^3	8900
Specific heat	c_P	$J/(kg\,K)$	394
Thermal conductivity	k	$W/(m\,K)$	390
Thermal expansion coefficient	β	1/K	1.77×10^{-5}

C.5 Stainless steel 316L

Table C.5 - *Thermophysical properties of Stainless steel 316L at a temperature of* $T = 20\,°\mathrm{C}$ *[288].*

Property	Symbol	Unit	Value
Composition‡	[-]	wt%	$C_{=0.030}Si_{=1.00}Mn_{=2.00}P_{=0.045}$ $S_{=0.015}N_{=0.10}Cr_{16.50–18.50}$ $Mo_{2.00–2.50}Ni_{10.00–13.00}$
Melting point	T_m	°C	1375-1400
Density	ρ	kg/m^3	8000
Specific heat	c_P	$J/(kg\,K)$	500
Thermal conductivity	k	$W/(m\,K)$	15
Thermal expansion coefficient	β	1/K	1.6×10^{-5}

‡The percentages given represent the alloying elements added to the steel, while the remainder is iron (Fe)

Appendix D

Theory of 1st order systems

This appendix outlines the general behavior of first-order systems, commonly used to model various physical phenomena such as mass-damper systems, RC circuits, and mass heating systems. To explain some mathematical insights of this type of systems, the latter was chosen as an example, as it is most relevant to this work.

For temperature sensors, the temperature variation depends on energy transfer between the sensor and its environment, following Fourier's thermal equation and Newton's law as expressed in Equation (D.1) where ρ_s is the density of the sensor, $c_{P,s}$ its specific heat, V_s is the sensor volume, T_s is the sensor temperature, T_f is the fluid temperature, h is the convective heat transfer coefficient, and A_s is the sensor surface area.

$$\rho_s c_{P,s} V_s \frac{\partial T_s}{\partial t} = h A_s (T_f - T_s) \tag{D.1}$$

Thus, the sensor is modeled as a first-order system with a time constant τ, and the temperature evolution is described by Equation (D.2):

$$T_s(t) = T_f - (T_f - T_{s0}) e^{-\frac{t}{\tau}} \quad \text{with } \tau = \frac{\rho_s c_{P,s} V_s}{h A_s}. \tag{D.2}$$

The behavior of the response of the system, as shown in Figure D.1, is influenced by T_{s0} (the starting point), T_f (the asymptotic value), and τ (the speed at which the system reaches the steady-state value). The time constant τ is defined as the time required for the sensor to reach 63.2 % of the steady-state value following a step input. Several methods can be employed to estimate τ:

- Measure the time to reach the steady state, defined as when the system reaches 99.3% of the asymptotic value (approximately 5τ). However, this methodology can be challenging to implement in practice, as accurately identifying the 99.3% threshold can be difficult, particularly in the presence of noisy measurements.

- Determine τ by identifying the time corresponding to 63.2 % of the temperature difference between the initial and steady-state values.

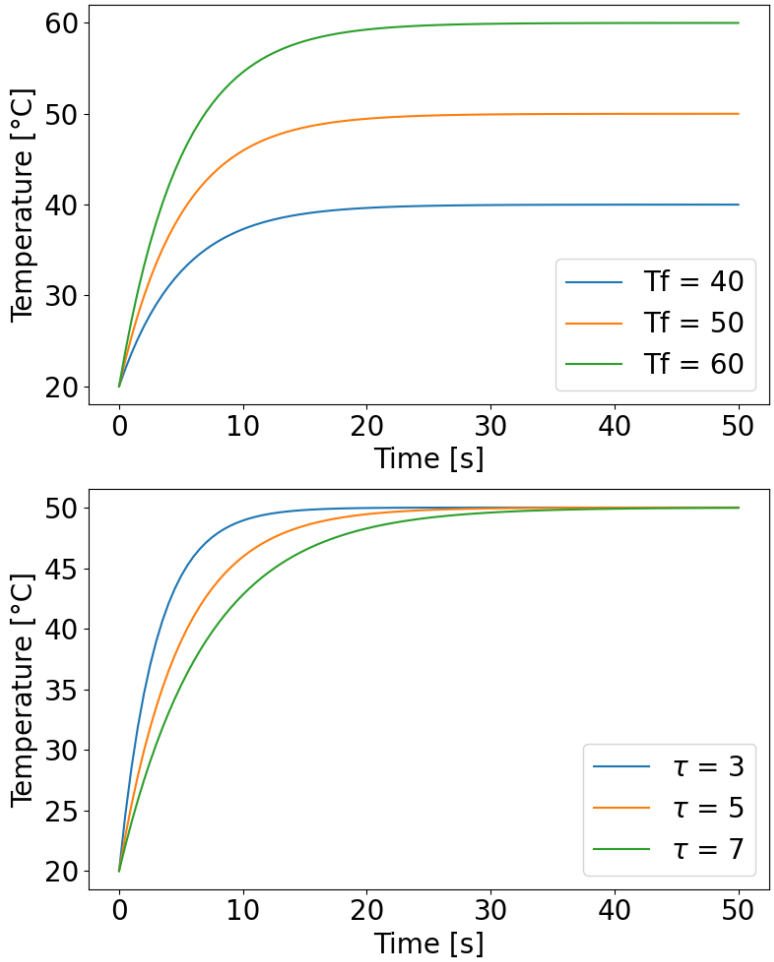

Figure D.1 - *Typical responses of a first order system to a step input. The influence of the various parameters involved in the response is analyzed.*

- Fit the experimental data to the form of Equation (D.2) and estimate τ using the least-squares method.
- Use the log-incomplete method by rewriting Equation (D.2) in the form of Equation (D.3), where the slope of $Z(t)$ is related to τ:

$$Z(t) = \ln\left(\frac{T_s(t) - T_f}{T_{s0} - T_f}\right) = -\frac{t}{\tau}. \tag{D.3}$$

For the purposes of this thesis, the described behavior is regarded as a reasonable approximation of the behaviour of the sensors, unless explicitly stated otherwise in the

text. However, in real systems, it may not be possible to generate an ideal step input. In such cases, the excitation signal $M(t)$ can be approximated by a step signal with a finite rise time, modeled as a ramp followed by a step. The ramp input, characterized by a rise time t_r, is described by Equation (D.4).

$$M(t) = \begin{cases} \frac{t}{t_r} & t < t_r \\ 1 & t \geq r \end{cases} \tag{D.4}$$

Applying this ramp signal to a first-order system might allow for a more precise estimation of τ through fitting.

Appendix E

Differentially heated cavity

E.1 Temperature measurements in water at different positions

Due to the symmetry of the cavity, the measurements performed in the planes $z = 12\,\text{mm}$ and $z = 48\,\text{mm}$ coincide, as demonstrated in Figure E.1. For this reason, Chapter 8 focuses on two out of the four positions to simplify the visualization of the results.

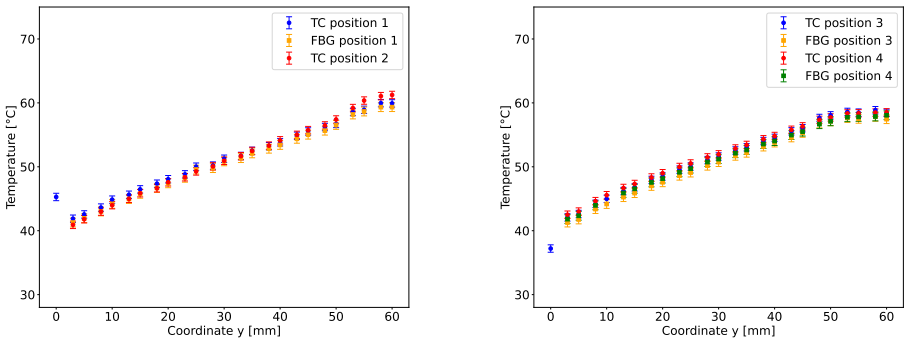

(a) $x = 4\,\text{mm}$ (b) $x = 56\,\text{mm}$

Figure E.1 - *Average temperature profiles in water along the y direction parallel to the hot wall (position 1-2) and to the cold wall (position 3-4). Comparison between FBG and TC measurements over the two possible measurement planes, i.e.* $z = 12\,\text{mm}$ *and* $z = 48\,\text{mm}$.

E.2 Impact of the losses on the RANS simulations

Impact on the CHT RANS simulations in water and GaInSn of the implementation of heat losses of different entity from the passive walls. Figures E.2 and E.3 show their effect on the velocity profiles of the numerical simulations.

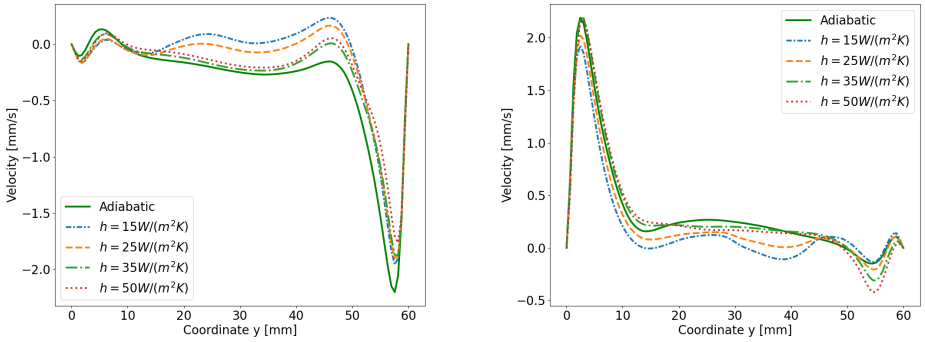

(a) $x = 4\,\text{mm}$ (b) $x = 56\,\text{mm}$

Figure E.2 - *Average velocity U_y RANS profiles in water along the y direction parallel to the hot wall (position 1) and to the cold wall (position 3). Comparison between RANS simulations performed with different losses from the passive walls.*

For the case of GaInSn, only the adopted heat transfer coefficient and the measured experimental coefficient are compared.

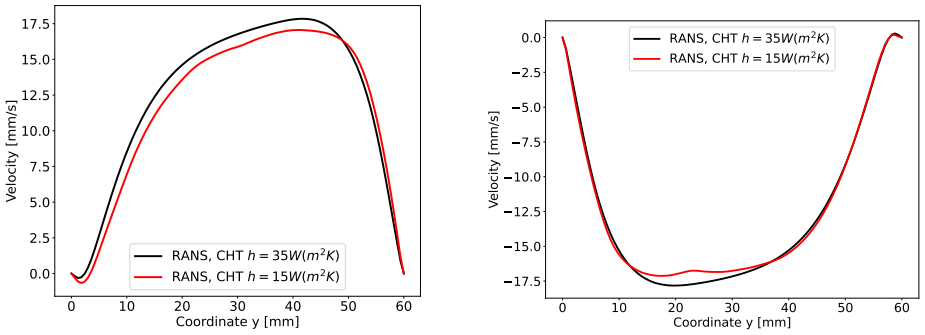

(a) $x = 4\,\text{mm}$ (b) $x = 56\,\text{mm}$

Figure E.3 - *Average velocity U_y RANS profiles in GaInSn along the y direction parallel to the hot wall (position 1) and to the cold wall (position 3). Comparison between RANS simulations performed with different losses from the passive walls.*

E.3 UDV velocity hot profile in water

The comparison between RANS and UDV of the velocity U_y profile in water in position 1, i.e. close to the hot wall, is reported in Figure E.4.

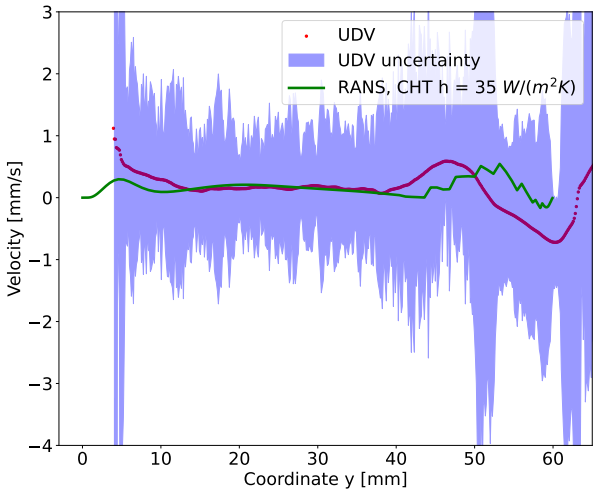

Figure E.4 - *Average velocity profile U_y along the y direction parallel to the hot wall (position 1). Comparison between UDV and RANS.*

Due to the cone averaging, the velocities predicted by the RANS simulations are extremely low, even in the final part of the profile. Consequently, the UDV sensor readings exhibit a high level of uncertainty, as the velocity measurements are dominated by noise. Therefore, this profile is not considered reliable.

Appendix F

Scientific outputs

The research carried out in this thesis led to the following publications and the creation of the following scientific outputs, presented in chronological order in each Section.

F.1 Journal Papers

- Naumann, C., Carlesi, T., Henning, O., Cierpka, C. and Laboureur, D. *Dynamic characterization of Fiber Bragg Grating temperature sensors.* Experimental Thermal and Fluid Science 156 (2024): 111222.

F.2 Conferences, workshops and symposia

- Carlesi, T., Laboureur, D., Pacio, J., Van Tichelen, K., Planquart, Ph. and Mégret, P.: *Selection of measurement techniques for turbulent heat flux measurements in liquid metals.* 12th Symposium of VKI PhD Research 2021, March 2021, Sint-Genesius-Rode, Belgium

  Poster at the 12th Symposium of VKI PhD Research 2021, March 2021, Sint-Genesius-Rode, Belgium

- Carlesi, T., Laboureur, D., Pacio, J., Van Tichelen, K., Planquart, Ph. and Mégret, P. (2021). *Experimental analysis of the dynamic behaviour of FBG temperature sensors.* 25th Annual Symposium of the IEEE Photonics Benelux Chapter, Mons, Belgium.

  Poster at the 25th Annual Symposium of the IEEE Photonics Benelux Chapter, Mons, Belgium

- Carlesi, T., Laboureur, D., Pacio, J., Van Tichelen, K., Planquart Ph. and Mégret, P.: *Characterization of measurement techniques for their use in liquid metals.* 13th Symposium of VKI PhD Research 2022, March 2022, Sint-Genesius-Rode, Belgium

Oral presentation at the 13th Symposium of VKI PhD Research 2022, March 2022, Sint-Genesius-Rode, Belgium

- Carlesi, T., Laboureur, D., Pacio, J., Van Tichelen, K., Planquart, Ph. and Mégret, P.: *Experimental and numerical analysis of natural convection in a differentially heated cavity.* 14th Symposium of VKI PhD Research 2023, March 2023, Sint-Genesius-Rode, Belgium

  Oral presentation at the 14th Symposium of VKI PhD Research 2023, March 2023, Sint-Genesius-Rode, Belgium

- Carlesi, T., Oder, J., Laboureur, D., Planquart, Ph., Pacio J., Van Tichelen, K. and Mégret, P.. *Experimental and numerical analysis of natural convection in a differentially heated cavity in water and GaInSn.* In International Heat Transfer Conference Digital Library. Begel House Inc., 2023.

  Oral presentation at the International Heat Transfer Conference (IHTC17), Cape Town, South Africa

- Carlesi, T., Laboureur, D., Pacio, J., Van Tichelen, K., Planquart, Ph., Mégret, P. *Experimental analysis of natural convection in a differentially heated cavity in GaInSn.* In EPJ Web of Conferences, vol. 288, p. 05002. EDP Sciences, 2023.

  Oral presentation at Advancements in Nuclear Instrumentation Measurement Methods and their Applications (ANIMMA2023), Lucca, Italy

- Carlesi, T., Laboureur, D., Pacio, J., Van Tichelen, K., Planquart, Ph. and Mégret, P.: *Experimental analysis of natural convection in a differentially heated cavity in water and GaInSn.* 15th Symposium of VKI PhD Research 2024, March 2024, Sint-Genesius-Rode, Belgium

  Oral presentation at the 15th Symposium of VKI PhD Research 2024, March 2024, Sint-Genesius-Rode, Belgium

- Carlesi, Tommaso, Delphine Laboureur, Philippe Planquart, Julio Pacio, Katrien Van Tichelen, and Patrice Mégret. *Factors influencing the behaviour of FBG sensors for temperature measurements.* In Integrated Photonics Research, Silicon and Nanophotonics, pp. JTu1A-9. Optica Publishing Group, 2024.

  Poster at Bragg Gratings, Photosensitivity and Poling in optical materials and waveguides (BGPP2024), Québec City, Québec, Canada

References

[1] Working Group, I. I. I. contribution to the, W. G. I. I. I. Sixth, and Assessment Report. Climate change 2022 mitigation of climate change. Technical report, Intergovernmental Panel on Climate Change, 2022. Cited on page 1.

[2] IEA. Net zero roadmap: A global pathway to keep the 1.5 °c goal in reach. Technical report, International Energy Agency, 2023. Cited on page 1.

[3] J. Rogelj, D. Shindell, K. Jiang, S. Fifita, P. Forster, V. Ginzburg, C. Handa, H. Kheshgi, S. Kobayashi, E. Kriegler, R. Séférian L. Mundaca, and M.V. Vilariño. *Mitigation Pathways Compatible with 1.5°C in the Context of Sustainable Development.* Cambridge University Press, 2018. Cited on page 1.

[4] IEA. Nuclear power and secure energy transitions. Technical report, International Energy Agency, Paris, 2022. Cited on pages 1 and 2.

[5] OECD. Introduction to generation iv nuclear energy system and the international forum. Online, 2010. URL `https://www.gen-4.org/`. Cited on page 2.

[6] Ferry Roelofs and Chloe Chavardes. Sesame thermal hydraulics simulations and experiments for the safety assessment of metal cooled reactors. Technical report, Horizon 2020, 2015. Cited on page 2.

[7] Horizon2020. Myrrha research and transmutation endeavour (myrthe), April 2015. Cited on page 2.

[8] Horizon2020. Partitioning and transmuter research initiative in a collaborative innovation action (patricia), 2020. Cited on page 2.

[9] Hamid Aït Abderrahim, Peter Baeten, Didier De Bruyn, and Rafael Fernandez. MYRRHA: A multi-purpose fast spectrum research reactor. *Energy Conversion and Management*, 63:4–10, November 2012. ISSN 0196-8904. Cited on pages 2 and 3.

[10] Hamid Aït Abderrahim. Realization of a new large research infrastructure in belgium: MYRRHA contribution for closing the nuclear fuel cycle making nuclear energy sustainable. *EPJ Web of Conferences*, 246:00012, 2020. Cited on pages 2, 3, and 4.

[11] Didier De Bruyn, Hamid Aït Abderrahim, Peter Baeten, and Paul Leysen. The MYRRHA ADS project in Belgium enters the front end engineering phase. *Physics Procedia*, 66:75–84, 2015. ISSN 1875-3892. Cited on pages 2 and 3.

[12] NEA. *Handbook on lead-bismuth eutectic alloy and lead properties, materials compatibility, thermal-hydraulics and technologies*. Nuclear Energy Agency, 2 edition, 2015. Cited on pages 2, 3, 14, 15, 19, 43, 83, 107, 199, and 214.

[13] Didier De Bruyn, Hamid Aït Abderrahim, and Marc Schyns. Recent progress and perspectives in the Belgian MYRRHA ADS programme. In *Proceedings of the 2019 International Conference on Advances in Nuclear Power Plants (ICAPP2019), Juan-les-pin, France, May 12-15, 2019*, 2019. Cited on page 3.

[14] Feynman R., Leighton R. B., and Sands M. The feynman lectures on physics, 1964. Cited on page 4.

[15] William M. Kays and Michael E. Crawford. *Convective heat and mass transfer*. McGraw-Hill, 3 edition, 1993. ISBN 0-07-033721-7. Cited on pages 5, 68, and 69.

[16] Akshat Mathur, Ferry Roelofs, Matilde Fiore, and Lilla Koloszar. State-of-the-art turbulent heat flux modelling for low-prandtl flows. *Nuclear Engineering and Design*, 406(112241), 2023. Cited on pages 5, 7, and 69.

[17] G. Grötzbach. Challenges in low-Prandtl number heat transfer simulation and modelling. *Nuclear Engineering and Design*, 264:41–55, 2013. ISSN 0029-5493. Cited on page 6.

[18] A. Shams, F. Roelofs, E. Baglietto, S. Lardeau, and S. Kenjeres. Assessment and calibration of an algebraic turbulent heat flux model for low-Prandtl fluids. *International Journal of Heat and Mass Transfer*, 79:589–601, 2014. ISSN 0017-9310. Cited on page 7.

[19] S. Manservisi and F. Menghini. A CFD four parameter heat transfer turbulence model for engineering applications in heavy liquid metals. *International Journal of Heat and Mass Transfer*, 69(0):312–326, 2014. ISSN 0017-9310. Cited on page 7.

[20] L.N. Carteciano, D. Weinberg, and U. Müller. Development and analysis of a turbulence model for buoyant flows. In *4th World Conference on Experimental Heat Transfer, Fluid Mechanics and thermodynamics*, Brussels, June 1997. Cited on page 7.

[21] Thermal-hydraulics of innovative nuclear systems (thins) european project. Seventh Framework Programme, January 2015. Cited on page 7.

[22] Horizon2020. Sesame thermal hydraulics simulations and experiments for the safety assessment of metal cooled reactors, 2015. Cited on page 7.

[23] Yuriy Plevachuk, Vasyl Sklyarchuk, Sven Eckert, Gunter Gerbeth, and Rada Novakovic. Thermophysical properties of the liquid Ga-In-Sn eutectic alloy. *Journal of Chemical & Engineering Data*, 59(3):757–763, March 2014. ISSN 1520-5134. Cited on pages 8, 52, 95, and 214.

[24] Pankaj Kumar Mishra and Mahendra K. Verma. Energy spectra and fluxes for Rayleigh-Bénard convection. *Physical Review E*, 81(5):056316, may 2010. ISSN 1539-3755. Cited on pages 14 and 15.

[25] Lilla Koloszár and Matilde Fiore. Assesment of low Prandtl heat transfer and its modeling. Technical Report DEMOCRITOS 3 Deliverable TR22, Von Karman Institute for Fluid Dynamics, 2020. Cited on pages 15 and 57.

[26] P. Frick, R. Khalilov, I. Kolesnichenko, A. Mamykin, V. Pakholkov, A. Pavlinov, and S. Rogozhkin. Turbulent convective heat transfer in a long cylinder with liquid sodium. *EPL (Europhysics Letters)*, 109(1):14002, jan 2015. Cited on pages 15 and 196.

[27] S. Cioni, S. Ciliberto, and J. Sommeria. Strongly turbulent Rayleigh-Bénard convection in mercury: comparison with results at moderate Prandtl number. *Journal of Fluid Mechanics*, 335:111–140, mar 1997. Cited on pages 15, 44, 45, and 198.

[28] S. Cioni, S. Ciliberto, and J. Sommeria. Experimental study of high-Rayleigh-number convection in mercury and water. *Dynamics of Atmospheres and Oceans*, 24(1-4):117–127, January 1996. Cited on pages 44, 45, 182, 195, and 198.

[29] F. Roelofs, editor. *Thermal hydraulics aspects of liquid metal cooled nuclear reactors*. Elsevier, 2019. Cited on pages 14 and 24.

[30] Mohammed Alsailani. Numerical simulation of transition in liquid metals. Master's thesis, Von Karman Institute for Fluid Dynamics, 2021. Cited on pages 14, 15, 17, 43, 47, 49, 64, 65, 66, 67, 196, and 198.

[31] J. Oder, M. Alsailani, L. Koloszar, W. Munters, and D. Laboureur. Direct numerical simulation of differentially heated cavity at low prandtl numbers. In *Eleventh International Conference on Computational Fluid Dynamics*, 2022. Cited on pages 15, 64, and 67.

[32] A. Aubert, S. Poncet, P. Le Gal, S. Viazzo, and M. Le Bars. Velocity and temperature measurements in a turbulent water-filled taylor-couette-poiseuille system. *International Journal of Thermal Sciences*, 2015. Cited on pages 15, 19, 34, 35, and 38.

[33] Janet D. Scheel and Jörg Schumacher. Global and local statistics in turbulent convection at low Prandtl numbers. *Journal of Fluid Mechanics*, 802:147–173, 2016. Cited on pages 15 and 43.

[34] D. Olivari and C. Benocci. Introduction to the modelling of turbulence - von karman institute for fluid dynamics. Notes from the 1998 to 2011 lectures, September 2014. Course Note 158. Cited on pages 15 and 17.

[35] J.P.A.J. van Beeck. Introduction to mechanics of turbulence spectral dynamics of turbulent flows, October 2019. Course Note 168. Cited on pages 15 and 17.

[36] L. Michalski. *Temperature measurement*. J. Wiley, Chichester New York, 2 edition, 2001. ISBN 0470846135. Cited on pages 17, 18, 19, 82, 83, 84, and 91.

[37] Katayoon Taherkhani, Esmat Sheydaeian, Christopher Eischer, Martin Otto, and Ehsan Toyserkani. Development of a defect-detection platform using photodiode signals collected from the melt pool of laser powder-bed fusion. *Additive Manufacturing*, 46, 2021. Cited on page 17.

[38] Alexander J. Myers, Guadalupe Quirarte, Francis Ogoke, Brandon M. Lane, Syed Zia Uddin, Amir Barati Farimani, Jack L. Beuth, and Jonathan A. Malen. High-resolution melt pool thermal imaging for metals additive manufacturing using the two-color method with a color camera. *Additive Manufacturing*, 73, July 2023. ISSN 2214-8604. Cited on page 19.

[39] Paul A. Hooper. Melt pool temperature and cooling rates in laser powder bed fusion. *Additive Manufacturing*, 22:548–559, May 2018. Cited on pages 18 and 19.

[40] Romain Monier, François Thumerel, Julien Chapuis, Fabien Soulié, and Cyril Bordreuil. Liquid metals surface temperature fields measurements with a two-colour pyrometer. *Measurement*, 101:72–80, April 2017. ISSN 0263-2241. Cited on pages 17 and 19.

[41] A. V. S. Oliveira, A. Avrit, and M. Gradeck. Thermocouple response time estimation and temperature signal correction for an accurate heat flux calculation in inverse heat conduction problems. *International Journal of Heat and Mass Transfer*, 185:122398, April 2022. Cited on pages 18 and 19.

[42] C. Gerardi, N. Bremer, D. Lisowski, and S. Lomperski. Distributed temperature sensor testing in liquid sodium. In *NURETH-16*, pages 819–828, September 2015. Cited on pages 18 and 20.

[43] Craig Gerardi, Nathan Bremer, Darius Lisowski, and Stephen Lomperski. Distributed temperature sensor testing in liquid sodium. *Nuclear Engineering and Design*, 312:59–65, February 2017. ISSN 0029-5493. 16th International Topical Meeting on Nuclear Reactor Thermal Hydraulics. Cited on pages 18 and 20.

[44] T. Carlesi, D. Laboureur, P. Planquart, J. Pacio, K. van Tichelen, and P. Megret. Experimental analysis of the dynamic behaviour of fbg temperature sensors. In *25th Annual Symposium of the IEEE Photonics Benelux Chapter*, 2021. Cited on pages 18, 21, and 97.

[45] Clemens Naumann, , Tommaso Carlesi, Henning Otto, Christian Cierpka, and Delphine Laboureur. Dynamic characterization of fiber bragg grating temperature sensors. *Experimental Thermal and Fluid Science*, 2024. Cited on pages 18, 21, 93, 98, and 103.

[46] Christiane Heinicke, Andre Thess, and Ilko Rahneberg. Towards local resolution measurements in turbulent liquid metal duct flows. In *Journal of Physics: Conference Series*, volume 318, 2011. Cited on pages 18 and 22.

[47] Christiane Heinicke. Spatially resolved measurements in a liquid metal flow with Lorentz force velocimetry. *Experiments in Fluids*, 54(6):1–8, 2013. ISSN 1432-1114. Cited on pages 18 and 22.

[48] N Krauter and F Stefani. Immersed transient eddy current flow metering: a calibration-free velocity measurement technique for liquid metals. *Measurement Science and Technology*, 2017. Cited on pages 18 and 22.

[49] Sven Franke, Sven Eckert, Thomas Gundrum, and Gunter Gerbeth. Channel flow profile measurements at hot liquid metal loops by the Ultrasound Doppler method. In *9th International Symposium on Ultrasonic Doppler Methods for Fluid Mechanics and Fluid Engineering*, 2014. Cited on pages 18, 22, and 23.

[50] Lukas Zwirner, Mohammad S. Emran, Felix Schindler, Sanjay Singh, Sven Eckert, Tobias Vogt, and Olga Shishkina. Dynamics and length scales in vertical and convection of liquid metals. *Journal of Fluid Mechanics*, 2022. Cited on pages 18, 22, 34, 35, and 44.

[51] Sven Eckert, Andreas Cramer, and Gunter Gerbeth. *Magnetohydrodynamics: historical evolution and trends*, chapter Velocity Measurement Techniques for Liquid Metal Flows, pages 275–294. Springer Netherlands, Dordrecht, 2007. ISBN 978-1-4020-4833-3. Cited on pages 18, 23, 107, and 110.

[52] Thomas Schaub, Sascha Wüstling, Joachim Konrad, and Michael Tasler. Design and calibration of permanent magnet probes for the local measurement of velocity and temperature in a liquid metal backward facing step flow. *Experiments in Fluids*, 62(10), sep 2021. Cited on pages 18, 19, 23, 34, 35, 38, 83, and 195.

[53] Thomas Schaub, Frederik Arbeiter, Wolfgang Hering, and Robert Stieglitz. Forced and mixed convection experiments in a confined vertical backward facing step at low-prandtl number. *Experiments in Fluids*, 63(1), dec 2022. Cited on pages 18, 23, and 195.

[54] R. Mitra, M. Sieger, V. Galindo, F. Schindler, F. Stefani, and T. Wondrak. Flow reconstruction in a rayleigh-bénard convection cell with an aspect ratio 0.5 by contactless inductive flow tomography. *Magnetohydrodynamics*, 58(1-2): 81–88, may 2022. Cited on pages 18 and 24.

[55] Ivan Glavinić, Vladimir Galindo, Frank Stefani, Sven Eckert, and Thomas Wondrak. Contactless inductive flow tomography for real-time control of electromagnetic actuators in metal casting. *Sensors*, 22(11):4155, may 2022. Cited on pages 18 and 24.

[56] T. Lappan, M. Sarma, P. Heitkam, S.and Trtik, D. Mannes, K. Eckert, and S. Eckert. Neutron radiography of particle-laden liquid metal flow driven by an electromagnetic induction pump. *Magnetohydrodynamics*, 56:167–176, 2020. Cited on pages 18 and 24.

[57] Tobias Lappan. *X-ray and neutron radiographyof optically opaque fluid flows: experiments with particle-laden liquid metals and liquid foams.* PhD thesis, Technische Universitat Dresden, 2021. Cited on pages 18 and 24.

[58] B. Xu and B. Q. Li. Hot-film measurement of temperature gradient induced natural convection in liquid gallium. *Experimental Thermal and Fluid Science*, 29(6):697–704, 2005. ISSN 0894-1777. Cited on pages 18, 19, 25, 54, 191, 195, 201, and 202.

[59] Dantec Dynamics. Probes for hot wire anemometry, 2014. Cited on pages 18, 25, 32, 33, 136, 137, 139, 140, 146, and 203.

[60] Morena Angelucci, Ivan Di Piazza, and Daniele Martelli. Experimental campaign on the HLM loop NACIE-UP with instrumented wire-spaced fuel pin simulator. *Nuclear Engineering and Design*, 332:137–146, jun 2018. Cited on page 19.

[61] Julio Pacio, Katrien Van Tichelen, Sven Eckert, Thomas Wondrak, Ivan Di Piazza, Pierdomenico Lorusso, Mariano Tarantino, Markus Daubner, Karsten Litfin, Gen Ariyoshi, Hironari Obayashi, and Toshinobu Sasa. Advanced thermal-hydraulic experiments and instrumentation for heavy liquid metal reactors. *Nuclear Engineering and Design*, 399:112010, dec 2022. Cited on pages 19 and 20.

[62] Thomas Schulenberg and Robert Stieglitz. Flow measurement techniques in heavy liquid metals. *Nuclear Engineering and Design*, 240(9):2077–2087, 2010. ISSN 0029-5493. Cited on pages 23 and 27.

[63] J. Zeiniger. *Turbulenter Wärmetransport in flüssigem Blei-Wismut an einem vertikalen Heizstab im Ringspalt.* phdthesis, University of Karlsruhe, 2009. Cited on pages 19 and 23.

[64] B. Xu, B.Q. Li, and D.E. Stock. An experimental study of thermally induced convection of molten gallium in magnetic fields. *International Journal of Heat and Mass Transfer*, 49(13–14):2009–2019, July 2006. ISSN 0017-9310. Cited on pages 19, 25, 191, 195, and 202.

[65] Laura Villafañe and Guillermo Paniagua. Aero-thermal analysis of shielded fine wire thermocouple probes. *International Journal of Thermal Sciences*, 65: 214–223, March 2013. ISSN 1290-0729. Cited on page 19.

[66] G. Paniagua, R. Denos, and M. Oropesa. Thermocouple probes for accurate temperature measurements in short duration facilities. In *ASME TURBO EXPO*, June 2002. Cited on page 19.

[67] Tobias Krille, Rico Poser, Markus Diel, and Jens von Wolfersdorf. Conduction and inertia correction for transient thermocouple measurements. part ii: Experimental validation and application. In *MTT*, 2022. Cited on pages 19 and 83.

[68] L. E. Hochreiter and Alexander Sesonske. Thermal turbulence characteristics in sodium-potassium. *International Journal of Heat and Mass Transfer*, 12(1): 114–118, jan 1969. ISSN 0017-9310. Cited on pages 19 and 97.

[69] J. H. Rust and Alexander Sesonske. Turbulent temperature fluctuations in mercury and ethylene glycol in pipe flow. *International Journal of Heat and Mass Transfer*, 9(3):215–227, mar 1966. ISSN 0017-9310. Cited on page 19.

[70] Gang-Ding Peng, editor. *Handbook of optical fibers*. Springer, 2019. ISBN 9789811070853. Cited on pages 20, 21, and 84.

[71] G. P. Agrawal. *Fiber-Optic Communication Systems*. Wiley, Hoboken, 4th edition, 2010. Cited on page 20.

[72] Gabriele Bolognini and Arthur Hartog. Raman-based fibre sensors: Trends and applications. *Optical Fiber Technology*, 19:678–688, 2013. Cited on page 20.

[73] Matthew Weathered and Mark Anderson. Development of optical fiber instrumentation for use in sodium cooled fast reactors. In *NURETH-16*, pages 1050–1059, 2015. Cited on page 20.

[74] Darius D. Lisowski, Craig D. Gerardi, and Stephen W. Lomperski. Thermal cycling testing of distributed fiber optic temperature sensors for high-temperature applications. In *Proceedings of the 16th International Topical Meeting on Nuclear Reactor Thermal Hydraulics (NURETH-16), Aug 30 - Sep 04, 2015, Chicago, IL, US*, January 2015. Cited on page 20.

[75] Alex K. Sang, Mark E. Froggatt, Dawn K. Gifford, Stephen T. Kreger, and Bryan D. Dickerson. One centimeter spatial resolution temperature measurements in a nuclear reactor using rayleigh scatter in optical fiber. *IEEE Sensors Journal*, 8(7), July 2008. Cited on page 20.

[76] Zujie Fang, Ken K. Chin, Ronghui Qu, and Haiwen Cai, editors. *Fundamentals of optical fiber sensors*. Wiley, 2012. ISBN 9780470575406. Cited on page 21.

[77] Andreas Othonos and Kyriacos Kalli. *Fiber Bragg Gratings*. Artech House Publishers, 2006. ISBN 9780890063446. Cited on pages 21, 84, and 85.

[78] Ben De Pauw, Alfredo Lamberti, Ali Rezayat, Julien Ertveldt, Steve Vanlanduit, Katrien Van Tichelen, Thomas Geernaert, and Francis Berghmans. Signal-to-noise ratio evaluation of fibre Bragg gratings for dynamic strain sensing at

elevated temperatures in a liquid metal environment. *Journal of Lightwave Technology*, 33(12):2378–2385, June 2015. Cited on page 21.

[79] Abd El-Naser A. Mohamed, Ahmed Nabih Zaki Rashed, Mohamed Z. Elsiefy, M. M. Zaky, and Ahmed I.Elsaket. Characterization of fiber bragg grating for applications in nuclear research reactors. *The Egyptian International Journal of Engineering Sciences and Technology*, 27:23–29, 2019. Cited on page 21.

[80] Andrei Gusarov and Stefan K. Hoeffgen. Radiation effects on fiber gratings. *Ieee Transactions on Nuclear Science*, 60(3), June 2013. Cited on page 21.

[81] Stephen J. Mihailov. Fiber bragg grating sensors for harsh environments. *Sensors*, 12(2):1898–1918, February 2012. ISSN 1424-8220. Cited on page 21.

[82] G. Pereira, M. McGugan, and L. P. Mikkelsen. Method for independent strain and temperature measurement in polymeric tensile test specimen using embedded FBG sensors. *Polymer Testing*, 50:125–134, apr 2016. Cited on page 21.

[83] Xueke Yu, Ningfang Song, and Jingming Song. A novel method for simultaneous measurement of temperature and strain based on EFPI/FBG. *Optics Communications*, 459:125020, mar 2020. Cited on page 85.

[84] I. Mckeeman, G. Fusiek, M. Perry, P. Niewczas, and M. Johnston. In-situ temperature calibration procedure for temperature and strain fibre bragg grating sensors for monitoring pre-stressing strands. In *EDF Nuclear Generation*, 2015. Cited on pages 21 and 85.

[85] Yuheng Pan, Junfeng Jiang, Kun Liu, Shuang Wang, and Tiegen Liu. Response time characterization of fiber Bragg grating temperature sensor in water medium. *Review of Scientific Instruments*, 87(11):116102, nov 2016. Cited on pages 21, 93, and 97.

[86] Paula Rinaudo, Ignacio Paya-Zaforteza, Pedro Calderóna, and Salvador SalesbaI. Experimental and analytical evaluation of the response time of high temperature fiber optic sensors. *Sensors and Actuators*, 243:167–174, 2016. Cited on pages 92 and 97.

[87] David Barrera, Vittoria Finazzi, Joel Villatoro, Salvador Sales, and Valerio Pruneri. Packaged optical and sensors based and on and regenerated fiber and bragg gratings and for high temperature applications. *IEEE Sensors Journal*, 12(1):107–112, January 2012. Cited on page 97.

[88] A Japie van Wyk, Pieter L. Swart, and Anatoli A Chtcherbakov. Fibre bragg grating gas temperature sensor with fast response. *Measurement Science and Technology*, 17:1113–1117, July 2006. Cited on pages 93 and 97.

[89] Dengpan Zhang, Jin Wang, Yongjie Wang, and Xing Dai. A fast response temperature sensor based on fiber Bragg grating. *Measurement Science and Technology*, 25:075105, 2014. Cited on page 21.

[90] Yang Zhang, Fang Wang, Zhihui Duan, Zexu Liu, Zigeng Liu, Zhenlin Wu, Yiying Gu, Changsen Sun, and Wei Peng. A novel low-power-consumption all-fiber-optic anemometer with simple system design. *Sensors*, 17(9):2107, sep 2017. Cited on page 21.

[91] Hong Gao, Feng Gao, Xianchao Zhao, Jie Chen, and Xuewu Cao. Transient flow analysis in reactor coolant pump systems during flow coastdown period. *Nuclear Engineering and Design*, 241(2):509–514, feb 2011. Cited on page 21.

[92] A. Thess, E. V. Votyakov, and Y. Kolesnikov. Lorentz force velocimetry. In *Physical Review Letters*, volume 96, 2006. Cited on page 22.

[93] André Thess, Evgeny Votyakov, Bernard Knaepen, and Oleg Zikanov. Theory of the Lorentz force flowmeter. *New Journal of Physics*, 9(8):299, 2007. Cited on page 22.

[94] André Thess and Thomas Boeck. Electromagnetic drag on a magnetic dipole interacting with a moving electrically conducting sphere. *IEEE Transactions on Magnetics*, 49(6), June 2013. Cited on page 22.

[95] Jincan Zheng, Runcong Liu, Xiaodong Wang, Guodong Xu, Ze Lyu, Yurii Kolesnikov, and Xianzhao Na. An online contactless investigation of the meniscus velocity in a continuous casting mold using lorentz force velocimetry. *Metallurgical and Materials Transactions*, January 2020. Cited on page 22.

[96] M. Ratajczak, D. Hernández, T. Richter, D. Otte, D. Buchenau, N. Krauter, and T. Wondrak. Measurement techniques for liquid metals. *IOP Conference Series: Materials Science and Engineering*, 228:012023, jul 2017. Cited on page 22.

[97] Jānis Priede, Dominique Buchenau, and Gunter Gerbeth. Single-magnet rotary flowmeter for liquid metals. *Journal of Applied Physics*, 110(3):034512, 2011. Cited on page 22.

[98] J Forbriger and F Stefani. Transient eddy current flow metering. *Measurement Science and Technology*, 26(105303), 2015. Cited on page 22.

[99] Yasushi Takeda. Measurement of velocity profile of mercury flow by Ultrasound Doppler Shift method. *Nuclear Technology*, 79(1):120–124, oct 1987. Cited on pages 22, 107, 109, and 128.

[100] Daniel Brito, Henri-Claude Nataf, Philippe Cardin, Julien Aubert, and Jean-Paul Masson. Ultrasonic Doppler velocimetry in liquid gallium. *Experiments in Fluids*, 31(6):653–663, dec 2001. ISSN 0723-4864. Cited on pages 22 and 107.

[101] S. Eckert and G. Gerbeth. Velocity measurements in liquid sodium by means of ultrasound doppler velocimetry. *Experiments in Fluids*, 32:542–546, 2002. ISSN 0723-4864. Cited on page 107.

[102] Brandon Ward. *Gravity stratified mixed convection in liquid metal pools: implications and experimental interpretation for LMFRs.* phdthesis, Kansas State University, 2020. Cited on pages 22, 110, and 112.

[103] Yoshitaka Ueki, Yuya Noguchi, Juro Yagi, Teruya Tanaka, Takehiko Yokomine, Masaru Hirabayashi, Kuniaki Ara, Tomoaki Kunugi, and Akio Sagara. Ultrasonic Doppler Velocimetry experiment of lead-lithium flow with Oroshhi-2 loop. *Fusion Science and Technology*, pages 1–7, June 2017. ISSN 1536-1055. Cited on page 23.

[104] S. Eckert, S. Franke, T. Gundrum, G. Gerbeth, and J.-C. Willemetz. Applications of Ultrasonic Doppler Velocimetry to flow measurements in hot liquid metals. In *8th International Conference on Electromagnetic Processing of Materials, Oct 2015, Cannes, France*, 2015. Cited on page 22.

[105] W. J. Seale. Turbulent diffusion of heat between connected flow passages part 1: outline of problem and experimental investigation. *Nuclear Engineering and Design*, 54(2):183–195, 1979. ISSN 0029-5493. Cited on page 23.

[106] J. Pacio, M. Daubner, F. Fellmoser, and T. Wetzel. Experimental study of the influence of inter-wrapper flow on liquid-metal cooled fuel assemblies. *Nuclear Engineering and Design*, 352:110145, 2019. ISSN 0029-5493. Cited on page 23.

[107] Uiju Jeong, Yun Ho Kim, Jong-Man Kim, Tae-Joon Kim, and Sung Joong Kim. Experimental evaluation of permanent magnet probe flowmeter measuring high temperature liquid sodium flow in the ITSL. *Nuclear Engineering and Design*, 265:566–575, 2013. ISSN 0029-5493. Cited on page 23.

[108] Thomas von Weissenfluh. Probes for local velocity and temperature measurements in liquid metal flow. *International Journal of Heat and Mass Transfer*, 28(8):1563–1574, 1985. ISSN 0017-9310. Cited on page 23.

[109] Ralf Kapulla. *Experimental investigation of thermal stratified and unstratified mixing layers in sodium and water.* phdthesis, ETH Zürich, 2000. In German (original title: Experimentelle Untersuchung von thermisch stratifizierten und unstratifizierten Mischunsschitchten in Natrium und Wasser). Cited on page 23.

[110] Frank Stefani, Thomas Gundrum, and Gunter Gerbeth. Contactless inductive flow tomography. *Physical Review E*, 70(056306), 2004. Cited on page 24.

[111] Nico Krauter. Preliminary measurements with the ECFM in GaInSn. Technical report, Helmholtz Zentrum Dresden Rossendorf, 2016. Cited on page 24.

[112] N. Takenaka, T. Fujii, A. Ono, Y. Motomura, and A. Turuno. Flow visualization of liquid metals by neutron radiography. *Fusion Engineering and Design*, 27: 607–613, 1995. Cited on page 24.

[113] M. Ščepanskis, A . Jakovičs, K. Thomsen, T. Beinerts, M . Sarma, P. Vontobel, R. Nikoluškins, and A. Bojarevičs. Dynamic neutron radiography for liquid metal applications. In *8th International Conference on Electromagnetic Processing of Materials*, Cannes sur Mer, France, 2015. Cited on page 24.

[114] P.C. Stainback and K.A. Nagabushana. Review of hot-wire anemometry techniques and the range of their applicability for various flows. *Electronic Journal of Fluids Engineering*, 1993. Cited on page 25.

[115] Giuseppe P. Russo. *Hot wire anemometer*, chapter 3, pages 67–98. Elsevier, 2011. ISBN 9781845699925. Cited on pages 25 and 138.

[116] H. Worthington and C.B. Malone. Measurements of velocities in water with hot wires. *J. Franklin Inst*, 184:115–117, 1917. Cited on page 25.

[117] Akis Tselentis. Application of hot-wire (-film) flowmeters to water velocity measurements in wells. *Journal of Hydrology*, 58:375–381, 1982. Cited on pages 25 and 157.

[118] K. Hollasch and B. Gebhart. Calibration of constant-temperature hot-wire anemometers at low velocities in water with variable fluid temperature. *Journal of Heat Transfer*, 94(1):17–22, feb 1972. Cited on pages 25, 152, 154, and 158.

[119] Miklos Sajben. Hot wire anemometer in liquid mercury. *Review of Scientific Instruments*, 36(7):945–949, jul 1965. Cited on pages 25, 201, and 202.

[120] David G. Malcolm. *Thermo-anemometry in magneto-hydrodynamics*. phdthesis, University of Warwick, 1968. Cited on page 202.

[121] Donald Henry White. *An experimental investigation of natural convection heat transfer from vertical flat plates in mercury*. phdthesis, Oregon State Universiry, 1971. Cited on pages 25, 201, and 202.

[122] John Calvin Hurt. The use of a hot film anemometer to measure velocities below five cm/sec in mercury. mathesis, Oregon State University, 1972. Cited on pages 25, 201, and 202.

[123] D. G. Malcolm. Some aspects of turbulence measurements in liquid mercury using cylindrical quartz-insulated hot-film sensors. *Journal of Fluid Mechanics*, 37(4):701–713, jul 1969. ISSN 0022-1120. Cited on pages 25, 201, and 202.

[124] C. B. Reed, B. F. Picologlou, P. V. Dauzvardis, and J. L. Bailey. Techniques for measurement of velocity in liquid-metal MHD flows. *Fusion Technology*, 10 (3P2A):813–821, nov 1986. Cited on page 25.

[125] C. B. Reed. Convective heat transfer in liquid metals. In Sadik Kakaç, Ramesh K. Shah, and Win Aung, editors, *Handbook of single-phase convective heat transfer*, chapter 8. John Wiley & Sons, Inc., 1987. Cited on page 25.

[126] L. Hasse, M. Dunckel, and R. Davis. *Air-Sea Interaction*, chapter Hot Wire and Hot Film Anemometers. Springer, 1980. Cited on page 27.

[127] National Instruments. Ni 9212 and tb-9212 datasheet, 2015. Cited on pages 28 and 37.

[128] BaySpec. Wavecapture fbg interrogation analyzers datasheet, 2011. Cited on page 30.

[129] BaySpec-testlab. *Sense 2020 User Guide*, 2020. Cited on page 30.

[130] Signal Processing. Ultrasonic doppler velocimeter dop4000, 2020. Cited on page 31.

[131] Dantec Dynamics. *StreamWare Pro Manual*, 2022. Cited on pages 32 and 33.

[132] National Instruments. Ni-9215 and sbrio-9215 specifications, 2024. Cited on pages 32 and 37.

[133] S. P. Das, S. Chakraborty, and P. Dutta. Natural convection in a two dimensional enclosure heated symmetrically from both sides. *International Communications of Heat and Mass Transfer*, 29(3):345–354, 2002. Cited on pages 34, 35, and 38.

[134] M. Leporini, F. Corvaro, B. Marchetti, F. Polonara, and M. Benucci. Experimental and numerical investigation of natural convection in tilted square cavity filled with air. *Experimental Thermal and Fluid Science*, 2018. Cited on pages 34, 35, and 38.

[135] Francis Godaux. An experimental study of the transition of natural convection flow adjacent to a vertical surface. *International Journal of Heat and Mass Transfer*, June 1973. Cited on pages 34 and 35.

[136] D. Saury A. Weppe, F. Moreau. Experimental investigation of a turbulent natural convection flow in a cubic cavity with an inner obstacle partially heated. *International Journal of Heat and Mass Transfer*, 194(123052), May 2022. Cited on pages 34, 35, and 38.

[137] Ronald du Puits. Time-resolved measurements of the local wall heat flux in turbulent Rayleigh–Bénard convection. *International Journal of Heat and Mass Transfer*, 188:122649, June 2022. ISSN 0017-9310. Cited on page 35.

[138] Tim Laube, Franziska Emmendörfer, Benjamin Dietrich, Luca Marocco, and Thomas Wetzel. Thermophysical properties of the near eutectic liquid Ga-In-Sn alloy. Technical report, Karlsruher Institut für Technologie (KIT), 2021. Cited on page 35.

[139] P. Belleoud, D. Saury, P. Joubert, D. Lemonnier, and F. Djanna. Experimental investigations in an air-filled differentially-heated cavity at large rayleigh numbers. In *Journal of Physics: Conference Series*, 2012. Cited on pages 34, 35, and 38.

[140] G. N. Ivey. Experiments on transient natural convection in a cavity. *Journal of Fluid Mechanics*, 144:389–401, 1984. Cited on pages 34 and 38.

[141] Tim Laube, Benjamin Dietrich, Luca Marocco, and Thomas Wetzel. Turbulent heat transfer in a liquid metal tube flow with azimuthally inhomogeneous heat flux. *International Journal of Heat and Mass Transfer*, 189:122734, jun 2022. Cited on page 34.

[142] M. E. Negretti T Caudwell, J.-B Flòr. Convection at an isothermal wall in an enclosure and establishment of stratification. *Journal of Fluid Mechanics*, 2016. Cited on pages 34, 35, and 38.

[143] G. C. Vliet and C. K. Liu. An experimental study of turbulent natural convection boundary layers. *Journal of Heat Transfer*, 1969. Cited on pages 34 and 38.

[144] Sophia Buckingham. *Prandtl number effects in abruptly separated flows: LES and experiments on an unconfined backward facing step flow.* phdthesis, Université catholique de Louvain, August 2018. Cited on pages 34, 35, 38, and 197.

[145] S. Bharti Omprakash, K. Saha Arun, K. Das Malay, and Sohil Bansal. Simultaneous measurement of velocity and temperature fields during natural convection in a water-filled cubical cavity. *Experimental Thermal and Fluid Science*, 2018. Cited on pages 34, 35, and 38.

[146] E. Reshotko K.H. Sohn, K.B.M.Q. Zaman. Turbulent heat flux measurements in a transitional boundary layer. Technical report, NASA, April 1992. Cited on page 34.

[147] M. Hishida and Y. Nagano. Structure of turbulent velocity and temperature fluctuations in fully developed pipe flow. *Journal of Heat Transfer*, 1979. Cited on pages 34 and 35.

[148] H.I. Abu-Mulaweh, B.F. Armaly, and Chen T.S. Turbulent mixed convection flow over a backward-facing step. *International Journal of Heat and Mass Transfer*, 2001. Cited on pages 34, 35, and 38.

[149] L. L. Eyler and A. Sesonske. Turbulent structure measurements in mercury pipe flow. *International Journal of Heat and Mass Transfer*, 23(11):1561–1572, nov 1980. Cited on pages 34 and 35.

[150] Ki-Hyeon Sohn and Eli Reshotko. Experimental study of boundary layer transition with elevated freestream turbulence on a heated flat plate. Technical report, NASA, February 1991. No citations.

[151] H. Hishida. Detailed design consideration on wire-spaced LMFBR fuel assemblies under the effects of uncertainties and non-nominal geometries. In *Specialists' meeting on thermodynamics of FBR fuel subassemblies under nominal and non-nominal operating conditions, Karlsruhe, Germany, F.R., 5-7 February 1978*. IAEA, 1978. Cited on pages 35 and 38.

[152] *DOP4000 series User Manual*. Signal Processing S.A., 1 edition, 2019. Cited on pages 37 and 110.

[153] Clemens Naumann. Unsteady temperature measurement in hot/cold heated cavity filled with liquid metal. Master's thesis, TU Ilmenau, 2022. Cited on pages 38, 81, 93, and 94.

[154] R. J. A. Janssen and R. A. W. M. Henkes. Influence of prandtl and number on and instability mechanisms and transition and in a differentially heated square cavity. *Journal of Fluid Mechanics*, 1994. Cited on pages 43, 44, and 65.

[155] S. Paolucci. *The differentially heated cavity*. Sadhana, 1994. Cited on pages 43, 44, 45, 57, and 196.

[156] Samuel Paolucci and Donald R. Chenoweth. Transition to chaos in a differentially heated vertical cavity. *Journal of Fluid Mechanics*, 201:379–410, December 1989. Cited on page 43.

[157] J. A. Glazier and A. Naert. Evidence against ultrahard thermal turbulence at very high Rayleigh numbers. *Nature*, 398:307–310, 1999. Cited on page 43.

[158] I.V. Miroshnichenko and M.A. Sheremet. Turbulent natural convection heat transfer in rectangular enclosures using experimental and numerical approaches: A review. *Renewable and Sustainable Energy Reviews*, 82:40–59, February 2018. ISSN 1364-0321. Cited on page 43.

[159] A. A. Mohamad and R. Viskanta. Transient natural convection of low-Prandtl-number fluids in a differentially heated cavity. *International Journal for Numerical Methods in Fluids*, 13(1):61–81, 1991. ISSN 1097-0363. Cited on page 43.

[160] Tohru Takeshita, Takehiko Segawa, James A. Glazier, and Masaki Sano. Thermal turbulence in mercury. *Phys. Rev. Lett.*, 76:1465–1468, February 1996. Cited on pages 45, 52, and 53.

[161] A. A. Mohamad and R. Viskanta. Modeling of turbulent buoyant flow and heat transfer in liquid metals. *International Journal of Heat and Mass Transfer*, 36 (11):2815–2826, July 1993. Cited on page 45.

[162] Katrien Van Tichelen, Fabio Mirelli, Matteo Greco, and Giorgia Viviani. E-SCAPE: A scale facility for liquid-metal, pool-type reactor thermal hydraulic investigations. *Nuclear Engineering and Design*, 290:65–77, August 2015. Cited on pages 45 and 69.

[163] Maxon. *Maxon motor specifications*. Maxongroup, 2021. Cited on pages 46 and 49.

[164] Thermal Systems Laird. *UltraTEC UT Series Thermoelectric Cooler*. Laird Thermal Systems, April 2022. Cited on pages 45 and 56.

[165] Elektro-Automatik. *PSI 9000 2U DC Laboratory Supply Manual*. EA Elektro-Automatik GmbH, 2018. Cited on page 45.

[166] N. B. Morley, J. Burris, L. C. Cadwallader, and M. D. Nornberg. GaInSn usage in the research laboratory. *Review of Scientific Instruments*, 79(5):056107, 2008. Cited on pages 47, 53, 54, 120, and 214.

[167] Q. Xu, N. Oudalov, Q. Guo, H. M. Jaeger, and E. Brown. Effect of oxidation on the mechanical properties of liquid gallium and eutectic gallium-indium. *Physics of Fluids*, 24(063101):063101–113, June 2012. Cited on pages 47 and 54.

[168] A. J. Bialous, P. H. Peters, and E. E. Stone. Leakage testing handbook. Technical Report NAS-69-1117, National Aeronautics and Space Administration, July 1969. Cited on page 51.

[169] Galinstan safety data sheet, September 2009. Cited on page 52.

[170] Michael Knoblauch, Julian M. Hibberd, John C. Gray, and Aart J. E. van Bel. A galinstan expansion femtosyringe for microinjection of eukaryotic organelles and prokaryotes. *Nature Biotechnology*, 17(9):906–909, sep 1999. ISSN 1087-0156. Cited on page 52.

[171] Yi Chen, Justin L. Wagner, Paul A. Farias, Edward P. DeMauro, and Daniel R. Guildenbecher. Galinstan liquid metal breakup and droplet formation in a shock-induced cross-flow. *International Journal of Multiphase Flow*, 106:147–163, 2018. ISSN 0301-9322. Cited on pages 54 and 55.

[172] Marc Hodes, Rui Zhang, Lisa Steigerwalt Lam, Ross Wilcoxon, and Nate Lower. On the potential of Galinstan-based minichannel and minigap cooling. *IEEE Transactions on Components, Packaging and Manufacturing Technology*, 4(1): 46–56, jan 2014. ISSN 2156-3950. Cited on page 52.

[173] Yuriy Plevachuk, Vasyl Sklyarchuk, Sven Eckert, Gunter Gerbeth, and Rada Novakovic. Correction to " thermophysical properties of the liquid Ga-In-Sn eutectic alloy". *Journal of Chemical & Engineering Data*, 2014. Cited on pages 52, 95, and 214.

[174] Stephan Handschuh-Wang, Tiansheng Gan, Muhammad Rauf, Weifa Yang, Florian J. Stadler, and Xuechang Zhou. The subtle difference between galinstan (r) and eutectic gainsn. *Materialia*, 26:101642, December 2022. ISSN 2589-1529. Cited on page 52.

[175] Tingyi Liu, Prosenjit Sen, and Chang-Jin Kim. Characterization of nontoxic liquid-metal alloy Galinstan for applications in microdevices. *Journal of Microelectromechanical Systems*, 21(2):443–450, apr 2012. ISSN 1057-7157. Cited on pages 52 and 54.

[176] Philip Geddis, Lijun Wu, Andrew McDonald, Steven Chen, and Bruce Clements. Effect of static liquid Galinstan on common metals and non-metals

at temperature up to 200 C. *Canadian Journal of Chemistry*, 98:787–798, 2020. Cited on pages 52 and 53.

[177] Zacharias Stelzer. *Experimental and numerical study of electrically-driven MHD flow.* phdthesis, ETH Zürich, 2014. Cited on page 52.

[178] Luca Marocco, André Loges, Thomas Wetzel, and Robert Stieglitz. Experimental investigation of the turbulent heavy liquid metal heat transfer in the thermal entry region of a vertical annulus with constant heat flux on the inner surface. *International Journal of Heat and Mass Transfer*, 55(23-24):6435–6445, 2012. ISSN 0017-9310. Cited on page 53.

[179] P. J. Hlavac, B. G. Nimmo, and O. E. Dwyer. Experimental study of effect of wetting on turbulent flow of mercury in annuli. *International Journal of Heat and Mass Transfer*, 15(12):2611–2631, 1972. ISSN 0017-9310. Cited on page 53.

[180] S.-K. Chen, Y.-M. Chen, and N. E. Todreas. The upgraded Cheng and Todreas correlation for pressure drop in hexagonal wire-wrapped rod bundles. *Nuclear Engineering and Design*, 335:356–373, 2018. ISSN 0029-5493. Cited on page 54.

[181] Michael D. Dickey. Emerging applications of liquid metals featuring surface oxides. *ACS Applied Materials & Interfaces*, 6(21):18369–18379, 2014. Cited on page 54.

[182] Mohamamd Karbalaei Akbari, Francis Verpoort, and Serge Zhuiykov. State-of-the-art surface oxide semiconductors of liquid metals: an emerging platform for development of multifunctional two-dimensional materials. *Jurnal of Materials Chemistry A*, 9:34–73, 2021. Cited on pages 54 and 55.

[183] Sarah Holcomb, Michael Brothers, Aaron Diebold, William Thatcher, David Mast, Christopher Tabor, and Jason Heikenfeld. Oxide-free actuation of gallium liquid metal alloys enabled by novel acidified siloxane oils. *Langmuir*, 32(48): 12656–12663, 2016. Cited on pages 54 and 55.

[184] M. J. Regan, H. Tostmann, Peter S. Pershan, O. M. Magnussen, E. DiMasi, B. M. Ocko, and M. Deutsch. X-ray study of the oxidation of liquid-gallium surfaces. *FAS Scholarly Articles*, 55(16), 1977. Cited on page 54.

[185] Jan M. Chabala. Oxide-growth kinetics and fractal-like patterning across liquid gallium surfaces. *Physical Review B*, 46(18):11346–11357, November 1992. Cited on page 54.

[186] Brad L. Cumby, Gerard J. Hayes, Michael D. Dickey, Ryan S. Justice, Christopher E. Tabor, and Jason C. Heikenfeld. Reconfigurable liquid metal circuits by Laplace pressure shaping. *Applied Physics Letters*, 101(17):174102, 2012. Cited on page 54.

[187] Anton Plech, Uwe Klemradt, Hartmut Metzger, and Johann Peisl. In situ X-ray reflectivity study of the oxidation kinetics of liquid gallium and the liquid alloy.

Journal of Physics: Condensed Matter, 10(5):971–982, feb 1998. Cited on page 54.

[188] Nahid Ilyas, Dennis P. Butcher, Michael F. Durstock, and Christopher E. Tabor. Ion exchange membranes as an interfacial medium to facilitate gallium liquid metal alloy mobility. *Advanced Materials Interfaces*, 3(9):1500665, 2016. Cited on pages 54 and 55.

[189] Daeyoung Kim, Peter Thissen, Gloria Viner, Dong-Weon Lee, Wonjae Choi, Yves J. Chabal, and Jeong-Bong (J. B.) Lee. Recovery of nonwetting characteristics by surface modification of gallium-based liquid metal droplets using hydrochloric acid vapor. *ACS Applied Materials & Interfaces*, 5(1):179–185, 2013. Cited on page 55.

[190] Mohammad Rashed Khan, Collin B. Eaker, Edmond F. Bowden, and Michael D. Dickey. Giant and switchable surface activity of liquid metal via surface oxidation. *Proceedings of the National Academy of Sciences*, 111(39):14047–14051, 2014. ISSN 0027-8424. Cited on page 55.

[191] Yang LiXiang, Zhao Xi, Xu Sjuo, Lu YongYu, Chang Hao, and Liu Jin. Oxide transformation and break-up of liquid metal in boiling solutions. *Technological Sciences*, 63:289–296, March 2019. Cited on page 55.

[192] Engineering Omega. Omegatherm thermally conductive silicone paste, 2021. Cited on page 56.

[193] R. Verzicco and K. R. Sreenivasan. A comparison of turbulent thermal convection between conditions of constant temperature and constant heat flux. *Journal of Fluid Mechanics*, 595:203–219, January 2008. ISSN 1469-7645. Cited on page 56.

[194] Iztok Tiselj, Elena Pogrebnyak, Changfeng Li, Albert Mosyak, and Gad Hetsronib. Effect of wall boundary condition on scalar transfer in a fully developed turbulent flume. *Physics of Fluids*, 13(4), April 2001. Cited on page 57.

[195] Iztok Tiselj and Leon Cizelj. Dns of turbulent channel flow with conjugate heat transfer at prandtlnumber 0.01. *Nuclear Engineering and Design*, 253:153–160, 2012. Cited on page 57.

[196] A. Mosyak and E. Pogrebnyak. Effect of constant heat flux boundary condition on wall temperature fluctuations. *Journal of Heat Transfer*, 2001. Cited on page 57.

[197] Frank M. White. *Viscous fluid flow*. McGraw-Hill series in mechanical engineering. McGraw-Hill, New York, 2nd edition, 1991. ISBN 0-07-069712-4. Cited on page 62.

[198] William M. Kays, Michael E. Crawford, and Bernhard Weigand. *Convective heat and mass transfer*. McGraw-Hill series in mechanical engineering. McGraw-Hill,

Boston, 4. ed., international ed. edition, 2007. ISBN 0-07-123829-8. Cited on pages 62, 123, 124, and 125.

[199] Szilveszter Feher. Differentially heated cavity simulation with conjugate heat transfer. Master's thesis, Von Karman Institute for Fluid Dynamics, September 2024. Cited on pages 65 and 67.

[200] Argonne National Laboratory. Nek5000 version 19, 2019. Cited on page 65.

[201] M. K. Prasad Pradyumna. *Comprehensive assessment of NEK5000 DNS capabilities*. PhD thesis, Delft University of Technology (TU Delft), 2016. Cited on page 65.

[202] P. F. Fischer. An overlapping schwarz method for spectral element solution of the incompressible navier-stokes equations. *Journal of Computational Physics*, 133:84–101, May 1997. Cited on page 65.

[203] Anthony T. Patera. A spectral and element method and for fluid dynamics: Laminar flow in a channel expansion. *Journal of Computational Physics*, 54: 468–488, October 1983. Cited on page 65.

[204] Aleksandr Obabko, Paul Fischer, Oana Marin, Elia Merzari, and Dave Pointer. Verification and validation of nek5000 for t-junction, matis , siberia, and max experiments. In *NURETH 16*, 2015. Cited on page 65.

[205] M. Breuer, S. Wessling, J. Schmalzl, and U. Hansen. Effect of inertia in Rayleigh-Bénard convection. *Physical Review E*, 69(2):026302, feb 2004. ISSN 1539-3755. Cited on page 65.

[206] David C. Wilcox. *Turbulence modeling for CFD*. DCW Industries, 3. ed. edition, 2006. ISBN 1-928729-08-8; 978-1-928729-08-2. Cited on pages 66 and 70.

[207] H. K. Versteeg and W. Malalasekera. *An Introduction to Computational Fluid Dynamics*. Pearson Education Limited, Edinburgh Gate Harlow Essex CM20 2JE England, second edition, 2007. ISBN 978-0-13-127498-3. Cited on page 68.

[208] F. R. Menter. Two-equation eddy-viscosity turbulence models for engineering applications. *AIAA Journal*, 32(8):1598–1605, 1994. Cited on page 69.

[209] T. J. Seebeck. Ueber die magnetische polarisation der metalle und erze durch temperaturdifferenz. *Annalen der physik*, 1826. Cited on page 81.

[210] Karen Garrity. Nist its-90 thermocouple database - srd 60, 2000. Cited on page 82.

[211] Hornak J, Trnka P, Kadlec P, Michal O, Mentlík V, Šutta P, Csányi GM, and Tamus ZÁ. Magnesium oxide nanoparticles: Dielectric properties, surface functionalization and improvement of epoxy-based composites insulating properties. *Nanomaterials*, 8(6:381), 2018. Cited on page 83.

[212] G. Meltz, W.W. Morey, United Technologies, and Research Center. Bragg grating formation and germanosilicate fiber photosensitivity. In *International Workshop on Photoinduced Self-Organization Effects in Optical Fiber*, 1991. Cited on page 85.

[213] R. Allil, F. de Nazaré, and M. Werneck. *Fiber Bragg Gratings: Theory, Fabrication, and Applications*. SPIE Press, Bellingham, 2017. Cited on page 85.

[214] Chuan Luo, Han Wang, Dacheng Zhang, Zhengang Zhao, Yingna LI, Chuan Li, and Ke Liang. Analytical evaluation and experiment of the dynamic characteristics of double-thimble-type fiber bragg grating temperature sensors. *Micromachines*, 12(16), 2021. Cited on page 85.

[215] National Instruments. *NI9216 specifications*, August 2023. Cited on pages 86 and 87.

[216] Gordon M. H. Flockhart, Robert R. J. Maier, James S. Barton, William N. MacPherson, Julian D. C. Jones, Karen E. Chisholm, Lin Zhang, Ian Bennion, Ian Read, and Peter D. Foote. Quadratic behavior of fiber bragg grating temperature coefficients. *Applied Optics*, 43(13), May 2004. Cited on page 90.

[217] R. Mahakud, J. Kumar, O. Prakash, and S. K. Dixit. Study of the nonuniform behavior of temperature sensitivity in bare and embedded fiber bragg gratings: experimental results and analysis. *Applied Optics*, 52(31), November 2013. Cited on page 90.

[218] JCGM. Guide to the expression of uncertainty in measurement —Part 6: Developing and usingmeasurement models. Guide JCGM GUM-6:2020, International Bureau of Weights and Measures, September 2020. Cited on pages 91 and 181.

[219] G. Palumbo, A. Iadicicco, D. Tosi, P. Verze, N. Carlomagno, V. Tammaro, J. Ippolito, and S. Campopiano. Fiber bragg grating for temperature monitoring during medical radiofrequency treatments. *Procedia Engineering*, 168:1308–1311, 2016. ISSN 1877-7058. Cited on page 91.

[220] S. Dyer, P. Williams, R. Espejo, J. Kofler, and S. Etzel. Fundamental limits in fiber bragg grating peak wavelength measurements. In *17th International Conference on Optical Fibre Sensors*, 2005. Cited on page 102.

[221] Wang C, Zhang Y, Sun J, Yang C, Ren X, Li J, and Zhang D. Research on a fiber bragg grating temperature measurement method for inter-satellite laser link. *Rev Sci Instrum.*, 91(015007), January 2020. Cited on page 91.

[222] Grayson King and Fukushima Toru. Rtd interfacing and linearization using an aduc8xx microconverter®. *AN709, Analog Devices*, 2004. Cited on page 91.

[223] JCGM. Evaluation of measurement data – guide to the expression of uncertainiy in measurement (GUM). Guide JCGM 100, Joint Committee for Guides in Metrology, September 2008. Cited on pages 91, 118, and 119.

[224] Yanfeng Li, Zhijie Zhang, Chenyang Zhao, Xiaojian Hao, Ningchen Dong, Wuliang Yin, and Zhihua Pang. Laser based method for dynamic calibration of thermocouples. *Applied Thermal Engineering*, 174:115276, jun 2020. Cited on page 92.

[225] Changrui Liao, Dong ning Wang, Yuhua Li, Tong Sun, and Kenneth T. V. Grattan. Temporal thermal response of type ii–irfiber bragg gratings. *Applied Optics*, 48(16), June 2009. Cited on page 97.

[226] B. Serio, Ph. Nika, and J. P. Prenel. Static and dynamic calibration of thin-film thermocouples by means of a laser modulation technique. *Review of Scientific Instruments*, 71(11):4306, 2000. Cited on page 92.

[227] A. Garinei and E. Tagliaferri. A laser calibration system for in situ dynamic characterization of temperature sensors. *Sensors and Actuators A: Physical*, 190:19–24, 2013. Cited on page 92.

[228] R. Budwig and C. Quijano. A new method for in situ dynamic calibration of temperature sensors. *Review of Scientific Instruments*, 60(12), December 1989. Cited on page 92.

[229] Tyson L. Lowder, Jason A. Newman, Wesley M. Kunzler, Jonathan D. Young, Richard H. Selfridge, and Stephen M. Schultz. Temporal response of surface-relief fiber bragg gratings to high temperature co2 laser heating. *Applied Optics*, 47(20), July 2008. Cited on pages 92 and 97.

[230] Rakesh Kumar and Niranjan Sahoo. Dynamic calibration of a coaxial thermocouples for short duration transient measurements. *Journal of Heat Transfer*, 135(12), sep 2013. ISSN 0022-1481. Cited on page 92.

[231] H. M. Hashemian, K. M. Petersen, D. W. Mitchell, M. Hashemian, and D. D. Beverly. In-situ response time testing of thermocouples. *ISA Transactions*, 29 (4):97–104, nov 1990. ISSN 0019-0578. Cited on page 92.

[232] Yanfeng Li, Zhijie Zhang, Xiaojian Hao, and Wuliang Yin. A measurement system for time constant of thermocouple sensor based on high temperature furnace. *Applied Sciences*, 8(12):2585, dec 2018. Cited on page 92.

[233] David R. Buttsworth. Assessment of effective thermal product of surface junction thermocouples on millisecond and microsecond time scales. *Experimental Thermal and Fluid Science*, 25:409–420, July 2001. Cited on page 93.

[234] Hui Wang, Chen Li, Lei Liang, Ke Jiang, Shu Dai, Huifeng Wu, and Xiaoling Tong. Fast response characteristics of fiber bragg grating temperature sensors and explosion temperature measurement tests. *Sensors and Actuators: A. Physical*, 354(114236), 2023. Cited on page 93.

[235] Sumit Agarwal, Niranjan Sahoo, and Rishikesh Kumar Singh. Experimental techniques for thermal product determination of coaxial surface junction thermocouples during short duration transient measurements. *International Journal*

of Heat and Mass Transfer, 103(Note):327–335, December 2016. ISSN 0017-9310. Cited on page 93.

[236] S.L.N. Desikan, K. Suresh, K. Srinivasan, and P.G. Raveendran. Fast response co-axial thermocouple for short duration impulse facilities. *Applied Thermal Engineering*, 96:48–56, 2016. Cited on page 93.

[237] F. Bernhard. *Handbuch der Technischen Temperaturmessung*. Springer Berlin Heidelberg, Berlin, Heidelberg, 2014. Cited on page 93.

[238] Theodore L. Berghman, Adrienne S. Lavine, Frank P. Incropera, and David P. Dewitt. *Fundamentals of heat and mass transfer*. John Wiley & Sons, Inc., 7 edition, 2002. ISBN 978-0470-50197-9. Cited on pages 95 and 210.

[239] Alexander Bonk, Salvatore Sau, Nerea Uranga, Marta Hernaiz, and Thomas Bauer. Advanced heat transfer fluids for direct molten salt line-focusing csp plants. *Progress in Energy and Combustion Science*, 67:69–87, July 2018. ISSN 0360-1285. Cited on page 95.

[240] A. G. Fernández, H. Galleguillos, E. Fuentealba, and F. J. Pérez. Thermal characterization of hitec molten salt for energy storage in solar linear concentrated technology. *Journal of Thermal Analysis and Calorimetry*, 122(1):3–9, May 2015. ISSN 1588-2926. Cited on page 95.

[241] Z. Li and E. Gariboldi. Review on the temperature-dependent thermophysical properties of liquid paraffins and composite phase change materials with metallic porous structures. *Material Today Energy*, 20(100642), 2021. Cited on page 95.

[242] Pezhman Ahmadi, Antonin Chapoy, and Rod Burgass. An investigation on the thermophysical properties of glycerol. *The Journal of Chemical Thermodynamics*, 178:106975, March 2023. ISSN 0021-9614. Cited on page 95.

[243] Alexandre de Almeida Prado Pohl and John Canning. Accessing the time response of FBG. In *2007 Conference on Lasers and Electro-Optics - Pacific Rim*. IEEE, aug 2007. Cited on page 98.

[244] Tommaso Carlesi, Delphine Laboureur, Philippe Planquart, Julio Pacio, Katrien Van Tichelen, and Patrice Mégret. Factors influencing the behaviour of fbg sensors for temperature measurements. In *Integrated Photonics Research, Silicon and Nanophotonics*, pp. JTu1A-9. Optica Publishing Group, 2024. Cited on page 98.

[245] Daniele Tosi. Review and analysis of peak tracking techniques for fiber bragg grating sensors. *Sensors*, 17(10):2368, October 2017. ISSN 1424-8220. Cited on page 102.

[246] Nazila Safari Yazd, Jennifer Kawakami, Alireza Izaddoost, and Patrice Mégret. Effect of peak tracking methods on fbg calibration derived by factorial design of experiment. *Sensors*, 2021. Cited on page 102.

[247] Kenji Kikuchi, Yasushi Takeda, Hiroo Obayashi, Masao Tezuka, and Hiroshi Sato. Measurement of LBE flow velocity profile by UDVP. *Journal of Nuclear Materials*, 356:273–279, 2006. ISSN 0022-3115. Proceedings of the Seventh International Workshop on Spallation Materials Technology. Cited on pages 107 and 128.

[248] Signal Processing. Frequently asked questions on udv applications, 2020. Cited on pages 109 and 114.

[249] Richard Nauber, Lars Büttner, and Jürgen Czarske. Measurement uncertainty analysis of field-programmable and gate-array-based and real-time signal processing for ultrasound flow imaging. *J. Sens. Sens. Syst.*, 2020. Cited on pages 110, 119, 120, and 122.

[250] A. Cramer, C. Zhang, and S. Eckert. Local flow structures in liquid metals measured by ultrasonic Doppler velocimetry. *Flow Measurement and Instrumentation*, 15(3):145–153, 2004. ISSN 0955-5986. Ultrasonic Flowmetering. Cited on page 110.

[251] R. Nauber, N.Thieme, H.Radner, H.Beyer, L.Büttner, K.Dadzis, O.Pätzold, and J. Czarske. Ultrasound flow mapping of complex liquid metal flows with spatial self-calibration. *Flow Measurement and Instrumentation*, 48:59–63, 2016. Cited on page 112.

[252] Philippe Schmitt, Anne Pallarès, Stéphane Fischer, and Marcus Vinicius de Assis. Suspended sediment and characterization by multifrequency and acoustics. In *10th International Symposium on Ultrasonic Doppler Methods for Fluid Mechanics and Fluid Engineering*, Tokyo, Japan, 28-30 September 2016. Cited on page 114.

[253] Mickaël Bricault. *Rétrodiffusion acoustique par une suspension en milieu turbulent : application à la mesure de profils de concentration pour l'étude de processus hydrosédimentaires.* PhD thesis, Grenoble INPG, 2006. Cited on page 114.

[254] Ubertone. How to choose my particles? Online, 2020. URL `https://ubertone.com/faq.html`. Cited on pages 114 and 118.

[255] M.A. Mendez, Simonini A., and D. Laboureur. An introduction to particle image velocimetry (piv). VKI Annual Lecture Series, 2019. Cited on page 115.

[256] A. Melling. Tracer particles and seeding for particle image velocimetry. *Measurement Science and Technology*, 8, 1997. Cited on page 115.

[257] Monson H. Hayes. *Schaum's Outline of Theory and Problems of Digital Signal Processing.* McGraw Hill, 1999. Cited on page 115.

[258] P S Popel, V E Sidorov, D A Yagodin, G M Sivkov, and A G Mozgovoj. Density and ultrasound velocity of some pure metals in liquid state, 2015. Cited on pages 119 and 120.

[259] Eric W. Lemmon, Ian H. Bell, Marcia L. Huber, and Mark O. McLinden. *NIST Chemistry WebBook, NIST Standard Reference Database Number 69*, chapter Thermophysical Properties of Fluid Systems. National Institute of Standards and Technology (NIST), Gaithersburg MD, 20899, October 2024. National Institute of Standards and Technology (NIST). Cited on pages 120 and 213.

[260] H. Kawamura, H. Abe, and K. Shingai. DNS of turbulence and heat transport in a channel flow with different Reynolds and Prandtl numbers and boundary conditions. In *3rd Int. Symp. on Turbulence, Heat and Mass Transfer*, 2000. Cited on page 123.

[261] Muhsin Can Akkurt, Marco Virgilio, Tony Arts, Delphine Laboureur, and Kevin M Van Geem. Ray tracing-based piv of turbulent flows in roughened circular channels. *Experiments in Fluids*, 63, November 2022. Cited on page 123.

[262] N.T. Basse. Extrapolation of turbulence intensity scaling to $re_\tau >> 10^5$. *Physics of Fluids*, 34(075128), 2022. Cited on page 124.

[263] Fabrizio Fontaneto. Hot wire anemometer, 2018. Cited on pages 134, 145, 154, 157, and 203.

[264] B. Cukurel, S. Acarer, and T. Arts. A novel perspective to high-speed cross-hot-wire calibration methodology. *Experiments in Fluids*, 53(4):1073–1085, jul 2012. Cited on pages 135, 138, 152, 153, and 157.

[265] Finn Ekman Jørgsen. How to measure turbulence with hot-wire anemometers. Technical report, Dantec Dynamics, 2002. Cited on pages 136, 163, and 203.

[266] J. Anthoine, T. Arts, H.L. Boerrigter, J.M. Buchlin, M. Carbonaro, G. Degrez, R. Dénos, D. Fletcher, D. Olivari, M.L. Riethmuller, and R.A. van den Braembussche. *Measurement techniques in fluid dynamics, an introduction.* Von Karman Institute for Fluid Dynamics, 3rd edition, 2009. Cited on pages 138, 139, and 140.

[267] P. Bradshaw. Thermal methods of flow measurement. *Journal of Scientific Instrument*, 1, November 1967. Cited on page 138.

[268] Elissavet Boufidi. *Development of Methods For the Characterization and Uncertainty Assessment of Turbulent Quantities in High Speed Compressible Flows by Hot Wires and Fast Response Pressure Probes.* phdthesis, Universite Catholique de Louvain Institute of Mechanics Materials and Civil Engineering, February 2021. Cited on pages 139 and 157.

[269] L. V. King. On the convection of heat from small cylinders in a stream of fluid: determination of the convection constants of small platinum wires with application to hot-wire anemometry. *Phil. Trans. Roy. Soc.*, 214:373–342, 1914. Cited on page 140.

[270] Peter Freymuth. Frequency response and electronic testing for constant-temperature hot-wire anemometer. *Journal of Physics E: Scientific Instruments*, 10, 1977. Cited on page 140.

[271] P. Freymuth. Calculation of square wave test for frequency optimised hot-film anemometers. *J. Phys. E: Sci. Instrum.*, 14, 1981. Cited on page 140.

[272] B C Khoo, Y T Chew, C J Teo, and C P Lim. The dynamic response of a hot-wire anemometer: Voltage-perturbation versus velocity-perturbation testing for near-wall hot-wire/film probes. *Measurement Science and Technology*, 10:152–169, 1999. Cited on page 146.

[273] N. Hutchins, J. P. Monty, M. Hultmark, and A. J. Smits. A direct measure of the frequency response of hot-wire anemometers: temporal resolution issues in wall-bounded turbulence. *Experiments in Fluids*, 56(1), January 2015. ISSN 1432-1114. Cited on page 146.

[274] F. Durst and E. S. Zanoun. Experimental investigation of near-wall effects on hot-wire measurements. *Experiments in Fluids*, 33:210–218, 2002. Cited on page 148.

[275] Federico Bertelli, Mizuki Okada, Sergio Lavagnoli, and Koen Hillewaert. An active turbulence grid for turbomachinery flow experiments. In *ASME Turbo Expo 2024: Turbomachinery Technical Conference and Exposition*, volume 4, London, United Kingdom, June 2024. Cited on page 153.

[276] E. Boufidi and F. Fontaneto. Towards a more reliable application of hot-wire anemometry in complex compressible flows. In *XXIII Biannual Symposium on Measuring Techniques in Turbomachinery Transonic and Supersonic Flow in Cascades and Turbomachines*, 2016. Cited on page 154.

[277] Byeongyeon Kim, Youngwoong Kim, YunSook Lee, Ki-Ean Nam, Jung Yoon, Yong-Hoon Shin, Hyeonil Kim, Jewhan Lee, and BongWan Lee. Experimental study on practical application of optical fiber sensor (ofs) for high-temperature system. *Nuclear Engineering and Technology*, 56(12):5182–5189, December 2024. ISSN 1738-5733. Cited on page 194.

[278] Seong-O Yang, Seungmin Lee, Seok Ho Song, and Jihyung Yoo. Development of a distributed optical thermometry technique for battery cells. *International Journal of Heat and Mass Transfer*, 194:123020, September 2022. ISSN 0017-9310. Cited on page 194.

[279] V.A. Klishina, S.V. Varzhel, and E.A. Loseva. Method for simultaneous measurement of velocity and direction of fluid flow using fiber bragg gratings. *Optical Fiber Technology*, 75(103215), 2023. Cited on page 194.

[280] Victoria A. Novikova, Sergey V. Varzhel, Ianina D. Tokareva, and Andrey A. Dmitriev. Liquid flow motion rate measuring method, based on the fiber bragg gratings. *Optical and Quantum Electronics*, 52(132), 2020. Cited on page 194.

[281] Chiara Spaccapaniccia, Philippe Planquart, and Sophia Buckingham. Experimental investigation of the thermal-hydraulic phenomena inside a pool-type nuclear reactor using water modeling. resreport DE/00/1D, von Karman Institute for Fluid Dynamics, 2015. Cited on page 196.

[282] Ben De Pauw. *Experimental analysis of flow-induced vibration in lead-bismuth cooled nuclear fuel assemblies.* phdthesis, Vrije Universiteit Brussel, October 2015. Cited on page 199.

[283] J. C. Hill and A. Sleicher. Convective heat transfer from small cylinders to mercury. *International Journal of Heat and Mass Transfer*, 12(12):1595–1604, dec 1969. ISSN 0017-9310. Cited on pages 201 and 202.

[284] Robert Gordon Colwell. *Experimental investigation of natural convection of mercury in an open, uniformly heated, vertical channel.* phdthesis, Oregon State University, 1974. Cited on page 202.

[285] R. P. Dring and B. Gebhart. Hot-wire anemometer calibration for measurements at very low velocity. *Journal of Heat Transfer*, 91(2):241–244, may 1969. ISSN 0022-1481. Cited on page 202.

[286] Arthur Newell Talbot, Fred B. Seely, and Virgil R. Fleming. *Hydraulic Experiments with Valves, Orefices, Hose, Nozzles and Orefice Buckets.* Kessinger Publishing, 1918. Cited on page 205.

[287] Aurubis Stolberg. Material datasheet cu-etp, June 2024. Cited on page 215.

[288] Thyssenkrupp Materials (UK) Ltd. Material data sheet - stainless steel 1.4404 (316l), November 2017. Cited on page 215.